UNIVERSITY OF SOUTHAMPTON

FACULTY OF PHYSICAL SCIENCES AND ENGINEERING

ELECTRONICS AND COMPUTER SCIENCES

SCREEN PRINTABLE SACRIFICIAL AND STRUCTURAL PASTES AND PROCESSES FOR TEXTILE PRINTING

By

Yang WEI

A thesis submitted for the degree of Doctor of Philosophy

Electronics and Computer Science,

University of Southampton,

United Kingdom.

August 2013

UNIVERSITY OF SOUTHAMPTON

<u>ABSTRACT</u>

FACULTY OF PHYSICAL SCIENCES AND ENGINEERING

ELECTRONICS AND COMPUTER SCIENCE

<u>Doctor of Philosophy</u>

SCREEN PRINTABLE SACRIFICIAL AND STRUCTURAL PASTES AND
PROCESSES FOR TEXTILE PRINTING

by Yang WEI

This thesis presents a new approach for fabricating free standing structures on flexible substrates using the screen printing technique. The research addresses electronic textile applications and is intended to provide a new method for realising sensors and complex structures on fabrics. Conventional smart fabric fabrication methods, such as weaving and knitting, are only able to achieve planar structures with limited functionality. Packaged discrete sensors can also be attached directly to fabrics but this approach is unreliable and unsuitable for mass production. The reported materials and the fabrication processes enable free standing structures to be formed by printing functional layers directly on top of the fabric. This reduces the fabrication complexity and increases wearer comfort and the flexibility of the fabric.

This research details an investigation into sacrificial materials suitable for use on fabrics. A plastic crystalline material (Trimetlylolethane (TME)) was identified as an appropriate sacrificial material because it sublimates which reduces the chance of stiction occurring. A screen printable TME paste has been achieved by dissolving TME powder in a solvent mixture of cyclohexanol (CH) and propylene glycol (PG). The TME sacrificial paste can be cured at 85 $^{\circ}$C for 5 minutes providing a solid foundation for subsequent printed layers. This sacrificial layer can be removed in 30 minutes at 150 $^{\circ}$C leaving no residue. EFV4/4965 UV curable dielectric material was identified as an appropriate structural material for use with TME. The feasibility of the sacrificial and structural materials has been demonstrated by the fabrication of free standing cantilevers and microfluidic pumps on fabrics and flexible plastic films. Printed cantilevers, with capacitive and piezoelectric sensing mechanisms, have been demonstrated as human motion sensors. A printed microfluidic pump with a maximum pumping rate of 68 μL/min at 3 kHz has also been demonstrated. Both the cantilever and micropump have been demonstrated, for the first time, on fabrics and polyimide substrates, respectively.

Contents

Chapter 3

Chapter 4

List of Figures

List of Tables

DECLARATION OF AUTHORSHIP

I, YANG WEI declare that the thesis entitled **Screen printable sacrificial and structural pastes and processes for textile printing** and the work presented in the thesis are both my own, and have been generated by me as the result of my own original research. I confirm that:

- o this work was done wholly or mainly while in candidature for a research degree at this University;
- o where any part of this thesis has previously been submitted for a degree or any other qualification at this University or any other institution, this has been clearly stated;
- o where I have consulted the published work of others, this is always clearly attributed;
- o where I have quoted from the work of others, the source is always given. With the exception of such quotations, this thesis is entirely my own work;
- o I have acknowledged all main sources of help;
- o where the thesis is based on work done by myself jointly with others, I have made clear exactly what was done by others and what I have contributed myself;
- o part of this work have been published as listed in section 1.5 of this thesis.

Signed: ……………………………………………………………………..

Date:……………………………………………………………………………

.

Acknowledgements

Abbreviations

3D	Three dimensional
AC	Alternating current
CAD	Computer aided design
CH	Cyclohexanol
CMOS	Complementary metal oxide semiconductor
CVD	Chemical vapour deposition
DAQ	Data acquisition
DC	Direct current
DI	Deionized
DSC	Differential scanning calorimetric
EC	Ethyl cellulose
ECG	Electro cardiography
EHD	Electro hydrodynamic
EO	Electro osmotic
FET	Field effect transistor
HF	Hydrofluoric acid
IC	Integrated circuit
IDE	Interdigital electrode
IPA	Isopropyl alcohol
KOH	Potassium hydroxide
LPCVD	Low-pressure chemical vapour deposition
LTCC	Low temperature co-fired ceramic
MEMS	Microelectromechanical systems
MHD	Magneto hydrodynamic
NI	National instrument
NPG	Neopentylglycol
PAA	Poly(acrylic acid)
PCB	Printed circuit board
PDMS	Polydimethylsiloxane
PE	Pentaerythritol

PECVD	Plasma enhanced chemical vapour deposition
PG	Propylene glycol
PMMA	Poly(methyl methacrylate)
PNB	Polynorbornene
PTFE	Polytetrafluoroethylene
PVA	Poly(vinyl alcohol)
PVDF	Polyvinylidene fluoride
PZT	Lead zirconate titanate
RMS	Root mean square
SEM	Scanning electron microscope
TGA	Thermogravimentric analysis
TME	Trimethylolethane
TMP	Trimethylolpropane
UV	Ultra violet

Nomenclature

$\bar{v}$	Velocity of the fluid at the throat
ΔP	Pressure drop
2θ	Diffuser divergence angle
A_e	Exit area
A_t	Throat area
C	Capacitance
C_p	Pressure recovery coefficient
C_x	Capacitance of the cantilever
d	Distance between two plates
E	Young`s modulus
ε	Relative permittivity
ε_0	Permittivity of free space
f	Frequency
fr	Resonant frequency
h	Height of the liquid
i_s	Current passing through the cantilever
i_s	Current of the sensor
K	Pressure loss coefficient
K_d	Pressure loss coefficient in diffuser direction
K_n	Pressure loss coefficient in nozzle direction
L	Length of the cantilever
R	Radius of the tube
t	Time
t_c	Thickness of the cantilever
v	Voltage
V	Volume
V_{pp}	Peak to peak voltage

W_1	Width of the throat
W_2	Width of the exit
η	Efficiency
λi	Clamping coefficient
ρ	Density
φ	Flow rate
ω	Angular frequency

Chapter 1

Introduction

1.1   Overview of the research

Fabrics represent an attractive supporting platform for electronic integration because they have been a fundamental component of our daily lives for hundreds of years. As a result, smart fabrics aim to integrate new sensing and actuating functionalities into fabrics. Smart fabrics are defined as conventional fabrics with integrated electronic functionality (e.g. sensors and actuators), potentially offering new functionality in the ubiquitous application of fabrics [1].

Conventionally, sensors manufactured by silicon microfabrication techniques on a rigid substrate, are attached onto the clothing [2]. However, since these sensors are rigid, they have the potential to cause the wearer discomfort. Additionally, each sensor must be individually mounted, which is time consuming and costly. Weaving and knitting of functional yarns are common methods for fabricating smart fabrics; however, with yarn-based manufacturing methods, the primary objective is to achieve the desired fabric structure and so the layout of the functional yarn(s) must be constrained to coincide with the fabric's structural layout. Further, since a yarn must follow the entire length of the garment, difficulties occur with complex designs in particular where functionalised yarns (e.g. conductors) need to cross. Therefore, it is notable that, to date, creating a three-dimensional (3D) free standing structure on fabric, using a yarn-based approach, has not previously been demonstrated in the literature and therefore this research creates new potential applications in this field.

Screen printing offers a method to achieve 3D free standing structures on the surface of the fabric in which functional pastes are deposited on fabric only where they are

required. Screen printing provides greater design freedom than the yarn approach in that the printed layers can have any orientation on the fabric and do not need to follow the yarn directions. In addition, screen printing provides the ability to produce arrays of the same or different devices in a single process; screen printing is inherently a batch process producing multiple devices from a screen design. A broad range of functional pastes are commercially available, which allow a variety of functionalities to be combined in a layered structure, as a result of which free standing structures can be obtained using a sacrificial process.

To achieve free standing structures on top of the substrate, the principle of surface micromachining is employed. Typically, materials are deposited onto the substrate either as the structural layer or as the sacrificial layer. The free standing structure is released as the sacrificial layer is removed. However, sacrificial materials and their deposition processes used in Micro-electromechanical systems (MEMS) are usually not compatible with most fabric applications. For instance, spin coated photoresist may be absorbed by the fabric resulting in poor deposition results (e.g. thickness reliability). Spin coating is also not compatible with the roll to roll process typically associated with fabric manufacturing. In addition, some of their removal mechanisms could damage the fabric, such as high temperatures and applications of aggressive solutions.

There are a number of challenges in this research concerning the development of the material and fabrication processes, and in demonstrating the feasibility of using the developed sacrificial material on fabrics. Firstly, the research requires a sacrificial material which must be compatible with the fabric. The sacrificial material must be screen printable and completely removed at the end of the fabrication process leaving no residue. The cured sacrificial layer must also have enough mechanical strength to support the printing of subsequent layers and the removal process must not damage the fabric properties. Secondly, a structural material should be identified; this must be screen printable, compatible with the sacrificial material and have suitable mechanical properties. Thirdly, a generic fabrication process using the developed materials should be evaluated so that a variety of free standing structures can be achieved directly by deposition on fabric. Finally, the capability to integrate electronic sensing and actuating mechanisms, such as capacitive or piezoelectric, with the developed fabrication process

needs to be evaluated so that the printed free standing structures can perform as active devices.

Other challenges of fabricating free standing structures on top of the fabric are:

- o Surface roughness

    The surface of the fabric is not smooth compared with the normal substrates used in screen printed electronics (e.g. alumina tile) or in MEMS fabrication (e.g. silicon wafer).

- o Flexibility

    Fabric is a highly flexible substrate compared with typical substrates in MEMS fabrication processes.

- o Stretchability

    Fabrics are commonly stretchable and the devices printed on top must be durable during substrate deformation. The functionality of the device may change whilst stretching.

This research was funded by the MICROFLEX project which was a framework program 7 EU integrated project, grant number CP-IP 211335-2 (01-11-2008 to 31-10-2012). The project aim was to develop MEMS processing capability for the production of flexible smart fabrics. It also aimed to develop new functional inks that were compatible with fabrics. Finally, the research aimed to produce prototypes demonstrating the functionality of the new inks.

1.2   Objective and scope of the research

The objective is to develop sacrificial and structural materials suitable for fabric applications. Materials need to be formulated into a paste, which can be deposited using standard screen printing technology. The formulation process requires the blending of functional particles with other additives in a suitable solvent system, the measurement of paste properties and the optimisation of deposition processes. In addition, the cured sacrificial paste should be completely removed using a process which does not damage the fabric. The final target of the project is to demonstrate functional devices on fabric substrates realised using the standard screen printing technique.

1.3 Research methodology

To formulate a suitable sacrificial material and a corresponding structural material, an iterative approach is used, shown in Figure 1-1.
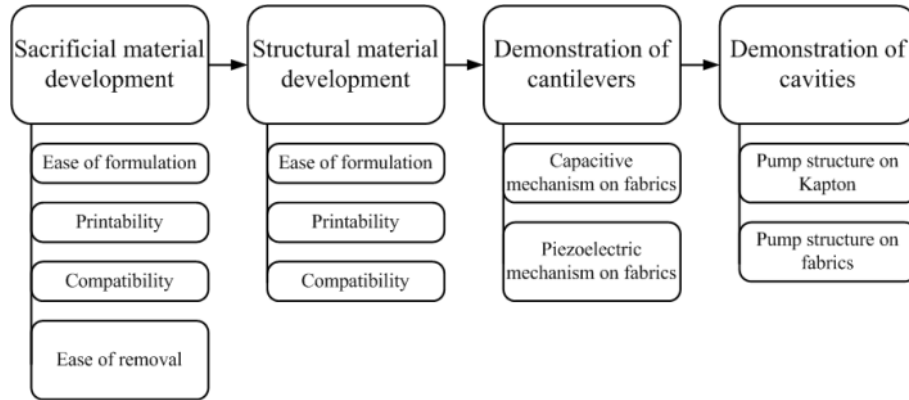
Figure 1-1: Research methodology.

The first stage of the research is defining suitable sacrificial materials having curing and removal processes that are compatible with fabrics. Since some of the candidate materials may not be available as a screen printable paste, the materials must then be formulated into a paste form. Viscosity and thixotropic properties of formulated pastes are examined in this stage.

Once a suitable sacrificial paste is achieved, the process moves to the second stage. In the second stage, structural materials will be evaluated in conjunction with the selected sacrificial material. The evaluation process is the same as the method used in the development of the sacrificial material. The optimisation of the formulation to improve printability of the material will be required if the materials are not in a paste form. If the materials are already screen printable, only their compatibility with the sacrificial material and the fabric is examined. The most important factor in this stage is the compatibility; any chemical reactions between the sacrificial and structural materials will result in poor printing. At the end of this stage, the materials and their compatibility with the fabrication process on fabrics will have been identified.

In the third stage, the feasibility of using the selected materials for the fabrication of free standing cantilevers is demonstrated. Then, by combining additional functional

materials, more complex cantilevers will be fabricated. In addition, the functionality of printed cantilevers as a sensing mechanism will be evaluated.

In the fourth stage, the feasibility of using the selected materials for the fabrication of cavities is demonstrated. A valveless micropump structure is used as an example because the pump contains complex free standing structures, such as cavities and channels.

1.4   Statement of novelty

- o   The development of a low temperature thermally curable (i.e. 85 $^{\circ}$C for 5 min) and removable (i.e. 150 $^{\circ}$C for 30 minutes) sacrificial material suitable for the fabrication of functional devices on fabric substrates (chapter 4).
- o   Removal temperature adjustment of the sacrificial material (section 4.5).
- o   The utilisation of a low temperature removable sacrificial material to fabricate fully screen printed cantilever structures on alumina and fabric substrates (Chapter 5).
- o   Identification of the optimum printing parameters to achieve a cantilever on fabrics (section 5.6).
- o   Using capacitive and piezoelectric mechanisms on printed cantilevers as the basis of smart fabric motion sensors (chapter 6).
- o   Using the developed fabrication method to obtain the first reported fully screen printed valveless micropump on Kapton (chapter 7).

1.5   Publications generated from this thesis

1)   Y. Wei, R. Torah, K. Yang, S. Beeby, and J. Tudor, '**A novel fabrication process to realise a valveless micropump on a flexible substrate**', Smart materials and structures, 2013. (In press)

2)   Y. Wei, R. Torah, K. Yang, S. Beeby, and J. Tudor, '**Screen Printable Sacrificial Fabrication Process to Realise a Cantilever on Fabric using a Piezoelectric Layer to Detect Motion for Wearable Applications**', Sensors and Actuators A: Physical, **203**, 2013, p 241-48.

3) Y. Wei, R. Torah, K. Yang, S. Beeby, and J. Tudor, '**A novel fabrication process to release a valveless micropump on a flexible substrate'**, in Transducers and Eurosensors Conference, Barcelona, Spain, 2013.

4) Y. Wei, R. Torah, K. Yang, S. Beeby, and J. Tudor, '**Screen printing of a capacitive cantilever-based motion sensor on fabric using a novel sacrificial layer process for smart fabric applications**', Measurement Science and Technology, **24**, 2013, p 1-11.

5) K. Yang, R. Torah, Y. Wei, S. Beeby, J. Tudor, '**Waterproof and durable screen printed silver conductive tracks on textiles**', Textile Research Journal, 2013. (Online). (doi: 10.1177/0040517513490063).

6) Y. Wei, R. Torah, K. Yang, S. Beeby, and J. Tudor, '**A Novel Fabrication Process to Realise Piezoelectric Cantilever Structures for Smart Fabric Sensor Applications'**, in IEEE Sensors Conference, Taipei, Taiwan, 2012.

7) Y. Wei, R. Torah, K. Yang, S. Beeby, and J. Tudor, '**Screen printed capacitive free standing cantilever beams used as a motion detector for wearable sensors'**, Procedia Engineering, **47**, 2012, p 165-169.

8) Y. Wei, R. Torah, K. Yang, S. Beeby, and J. Tudor, '**Screen printed capacitive free standing cantilever beams used as a motion detector for wearable sensors'**. in Eurosensors XXVI 2012: The 26th European Conference on Solid-State Transducers, Krakow, Poland, 2012.

9) Y. Wei, R. Torah, K. Yang, S. Beeby, and J. Tudor, '**A novel fabrication process for capacitive cantilever structures for smart fabric applications'**, in Symposium on Design, Test, Integration & Packaging of MEMS/MOEMS, Cannes, France, 2012.

1.6 Document structure

Chapter 1 provides an introduction to the smart fabric research area and a description of the aim and structure of the thesis. A statement of novelty is given and publications generated from this thesis are listed.

Chapter 2 reviews the common sacrificial and structural materials used in MEMS for the fabrication of free standing structures. For comparison, screen printed sacrificial and structural materials are also introduced. At the end of the chapter, sacrificial and structural materials which could be used for smart fabric applications are described.

Chapter 3 reviews existing smart fabrics and their fabrication processes. The fabrication processes of cantilever structures achieved in MEMS and by screen printing are detailed. The review of MEMS micropumps, emphasising the fabrication process, is provided at the end.

Chapter 4 evaluates potential sacrificial materials which are selected based on the literature. The most suitable sacrificial material is then optimised regarding its formulation, printability and the ease of removal.

Chapter 5 evaluates potential structural materials. The compatibility between the structural and sacrificial materials is examined. High importance is placed on compatibility in this chapter, as any chemical reactions between the sacrificial and structural materials will damage the entire printing results, such as structural deformation. The mechanical properties of the most suitable structural materials are evaluated at the end of the chapter.

Chapter 6 demonstrates the feasibility of using the sacrificial and structural materials for the fabrication of free standing cantilevers on fabrics. In addition to the sacrificial and structural materials, conductive and piezoelectric materials are introduced into the fabrication to achieve sensing mechanisms. The examination of the fabrication of these cantilevers is emphasised. At the end, the feasibility of using these cantilevers as a motion sensor is presented.

Chapter 7 explores the feasibility of using the selected materials to achieve more complex structures, such as micropumps. The challenge in achieving a pump on fabrics, such as the material removal and the membrane creation, is discussed. The problems which occurred during the fabrication are addressed. Finally, a preliminary test of the pump performance is given.

Chapter 8 gives the conclusions for this work. It summarises the development of the sacrificial material, the optimisation of the fabrication process and the fabrication and testing of functional devices. It also provides directions for future work to build on this research.

Chapter 2

Literature review: sacrificial and structural fabrication technologies

2.1 Introduction

Research in developing free standing structures on fabrics mainly involves sacrificial and structural material fabrication technologies. The principle explored in this thesis is a migration of surface micromachining techniques onto fabrics but the fabrication and material selection processes are completely different. This chapter will give an overview of all the fundamental knowledge necessary to direct this research.

This chapter is divided into two main parts, examining sacrificial and structural fabrication technologies. The first part (section 2.2) introduces the definition of sacrificial technology, a classification based on the removal mechanism, the sacrificial materials used in MEMS and existing screen printed sacrificial materials for the fabrication of free standing structures. Compatibility of these materials with fabrics will be discussed at the end of each section.

Sacrificial and structural materials are always presented together in the fabrication process because they cannot be used independently. Section 2.3 onwards describes the requirements of the structural material and common structural materials used in microfabrication. Next, screen printed structural materials are summarised along with

their applications. Finally, the challenges of using sacrificial technology on fabrics conclude the literature review.

2.2   Sacrificial fabrication technology

2.2.1   Definition of sacrificial technology

Sacrificial technology exploits a selective layer removal process to fabricate free standing overlying structures [3]. A sacrificial layer acts as a temporary supporting platform for subsequent layer deposition. This platform will be removed at the final fabrication stage to leave a free space and this temporary platform is commonly known as the sacrificial layer.

Sacrificial technology has been developed over the last three decades in MEMS fabrication processes, especially in surface micromachining [4]. Figure 2-1 shows a basic sacrificial process, which involves selective material removal to free an overlying layer resulting in the formation of either a cantilever or a bridge.
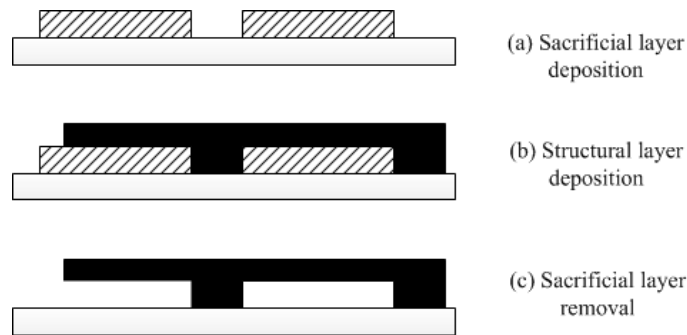
Figure 2-1: Schematic diagram of the sacrificial deposition and removal process.

In 1967, the sacrificial layer concept was first demonstrated by *Nathanson et. al.* [5] at the Westinghouse Research Laboratory using a 'metal spacer' to fabricate an overlaying beam which acted as the gate for a field effect transistor (FET). The beam was released by removing this metal spacer. In the early 1980's, *Howe et.al.* [6] found that micro scale cantilevers and bridges could be fabricated from polysilicon by using silicon dioxide as the sacrificial material. Silicon dioxide can be etched away by hydrogen fluoride (HF) without damaging the polysilicon layer. The simplicity of the fabrication process makes it attractive for the fabrication of free standing structures.

During the selection of materials used as the sacrificial layer on a rigid substrate, the following requirements should be carefully considered:

o   Ease of deposition

o   Ease of patterning

o   Strength: strong enough to prevent deformation during the subsequent processes

o   Compatibility: compatible with both the substrate and structural materials

o   Ease of removal without damaging the substrates and structure materials

2.2.2   Classification of removal methods

Sacrificial materials may be classified, by removal mechanism, into three categories:

o   Water removal

o   Acid and alkali removal

o   Organic solvent removal

o   Thermal removal

2.2.2.1   *Water removal*

The water removal mechanism works by dissolving the sacrificial material, forming a solution. The solubility between the material and water is the key to achieve this. The principle of solubility existing between the solute and the solvent is the '*like-dissolves-like*' rule [7, 8]. A solution is a mixture that contains solute (i.e. to be removed) and solvent (i.e. remover). The solubility of a material is the ability to dissolve into a solvent to form a homogenous solution at room temperature. It strongly depends upon the solvents, temperature and the pressure, but most materials are dissolved much quicker at higher temperatures because the temperature accelerates the movement of molecules. The solubility of the solute depends on not only the factors described above but also the properties of the solute. For instance, a polar solvent (e.g. water) is typically suitable for ionic and polar compounds. Conversely, a non-polar solvent (e.g. benzene) is often suitable for the dissolution of non-polar compounds, like wax [9]. If one solute is mixed with one solvent, a single phase is generated while the solute is completely dissolved, otherwise the solute suspension will be left at the bottom of the solution. From a solvent point of view, if two solvents are mixed together, a single phase is formed when they

are soluble with each other; otherwise two phases emerge and the low density solvent floats on top, such as a mixture of water and oil. Therefore, solutes and solvents should be carefully matched to achieve full dissolution.

For the removal process, water is a polar substance as it has an asymmetric molecular structure with one hydroxyl (–OH) group. Based on this principle, water removable materials must also have polarity. Material to be removed should have -OH group(s) with an asymmetric molecular structure. When a polar material is in contact with water, the hydrogen bonds begin to form because of the polar hydroxyl (-OH) groups existing in both water and the material. Once the bonds are formed, material molecules are broken away from the neighbours and surrounded by water molecules drifting into the solution. This formation is obtained easily due to an abundance of hydroxyl groups. Finally, the material is fully dissolved into water resulting in a removal mechanism.

2.2.2.2   Acid and alkali removal

The chemical reaction is the key factor when inorganic materials are in contact with corresponding inorganic liquid removers, such as an acid or alkali. The most common inorganic sacrificial material is silicon dioxide as it can be preferentially etched in HF solution with high selectivity to silicon [6]. Another common sacrificial material is polysilicon, which can be removed with potassium hydroxide (KOH) while the silicon nitride structural layer remains. Metallic materials, such as copper, can also be removed with appropriate inorganic removers, such as the mixture of $FeCl_2$ and HCl [10].

2.2.2.3   Organic solvent removal

Removal of organic materials has the same dissolution principle as water removal but different removers are used. Unlike inorganic materials, organic materials do not require aggressive solvents, such as acids and alkalis, as the remover. Instead, a variety of organic solvents or solvent systems are used as the removers to dissolve them from the substrate, such as the removal of uncross-linked SU-8 by acetone. This reduces the probability of damage to structural or substrate materials.

2.2.2.4   Thermal removal

Thermally removable sacrificial materials primarily concern the transformation of the sacrificial material due to a chemical or physical change caused by a change in

temperature. The key factors for thermally removable mechanisms are the temperature and time that the material is subjected to a specific temperature.

The chemical changes of a material include decomposition and oxidation resulting in new substance(s). Decomposition is regarded as a chemical reaction in which the material is broken down to simple structures or molecules due to the temperature. Oxidation is another chemical reaction in which oxygen is added to a substance to generate a new substance at a certain temperature [9]. In contrast, physical transformation only changes the phase of the material without modifying the chemical composition and new substances will not be produced. There are three physical phases, which are solid, liquid and gas. Transformations among three phases are possible by changing the temperature, shown in Figure 2-2.
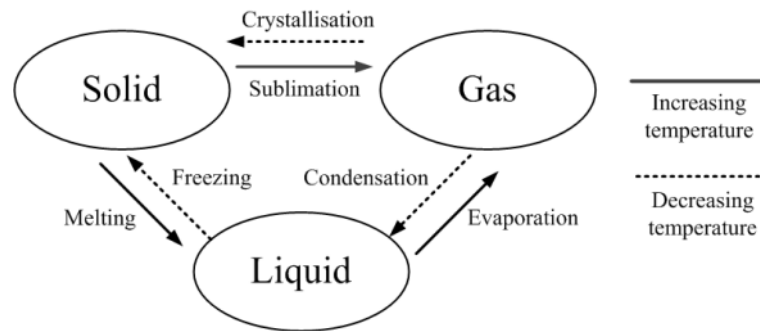
Figure 2-2: Phase changing diagram between solid, liquid, and gaseous phases.

The attractive forces between atoms in a material hold them together, whereas the movement of the atoms pushes them apart [7]. Temperature, in this case, accelerates the movement of the particle driving them further apart. At a certain temperature, a phase change could occur because the equilibrium is broken. However, some materials sublime directly without a liquid phase due to the high vapour pressure at a lower temperature (normally below its triple point at which three phases of a substance coexist at the same time). Vapour pressure is only a function of temperature and is independent of the volume of the system or the number of phases present [11]. Physical transformations do not require external substances involved and only the energy (e.g. heating and cooling) is required.

2.2.3 Sacrificial materials used in MEMS

There are a number of sacrificial materials reported in the literature in MEMS fabrication processes. They are based on inorganic materials, such as SiO_2, and organic materials, like SU-8. In terms of removal mechanisms, sacrificial materials used in MEMS can be separated into following categories.

Water removable sacrificial materials:

Not all water soluble materials can be used as the sacrificial material because the material must form a homogeneous film after deposition and be able to be removed by water after drying. Importantly, the material must not react with other materials during subsequent processes. Potential water soluble sacrificial materials for surface micromachining were studied by *Linder* [12]. They concluded that poly (acrylic acid) (PAA) and Dextran are the most appropriate materials for sacrificial applications as these materials have excellent film forming properties and are insoluble in most organic solvents. In this work, the maximum concentration of PAA and Dextran solutions were 19 wt% and 20 wt% resulting in viscosities of 3.67×10^{-1} Pa.s and 2.85×10^{-2} Pa.s, respectively. Both materials were spin coated onto planar substrates, such as silicon wafers and quartz substrates, and dried at 150 ^{o}C for 2 min. The maximum thickness of PAA layer was 9 μm, whereas Dextran only produced a 1.1 μm layer thickness due to its lower viscosity. To demonstrate the feasibility of using these materials for microfabrication, free standing SU-8 micro-scale structures were fabricated. PAA and Dextran were individually spin coated onto the substrate and dried. The SU-8 photolithography process was performed on top of the sacrificial layers. Finally, sacrificial layers were removed by rinsing the sample with deionized (DI) water. The results showed that PAA and Dextran layers did not react with SU-8 and the relevant solvents. In addition, despite the pattern geometry, the removal rate of PAA appears to be twice as fast as Dextran. Another study carried out by *Steager* [13] showed that Dextran can also be used as the sacrificial material for the fabrication of bacterial micro-robots as Dextran and its removal process are biocompatible.

Besides PAA and Dextran, several researchers have shown that poly (vinyl alcohol) (PVA) is also soluble in water and insoluble in most organic solvents, making it selectively removable during the sacrificial process. *Ferrell* [14] demonstrated that PVA

was suitable for the fabrication of microscale cantilever structures. The PVA ink was prepared by mixing DI water with PVA at a maximum concentration of 9 wt% and heating the solution to 70 ^{o}C to promote dissolution. The solution was then filtered through a filter paper to remove impurities. The sacrificial layer was formed by spin coating the PVA solution onto a silicon wafer followed by a baking step at 95 ^{o}C for 5min. A layer with 0.75 μm thickness was then formed. Later, it can be selectively removed by immersing the sample into DI water which dissolved the PVA layer [14]. However, it was found that the PVA layer would be dissolved during a subsequent photolithographic process and therefore a poly(methyl methacrylate) (PMMA) layer must be deposited on top of the sacrificial layer as a protective layer. More complex structures, such as SU-8 discs that are attached to a vertical cylindrical micro cantilever array [15] and worm shape nanoparticles [16], can also be achieved by using a PVA sacrificial layer.

Table 2-1: Summary of water soluble sacrificial materials in MEMS [12-14].

	PAA	Dextran	PVA
Maximum concentration	19 wt%	20 wt%	9 wt%
Viscosity	3.67×10^{-1} Pa.s	2.85×10^{-2} Pa.s	*
Deposition technique	Spin coating	Spin coating	Spin coating
Drying temperature	150 ^{o}C for silicon wafer 95 ^{o}C for polymer substrates	150 ^{o}C for silicon wafer 95 ^{o}C for polymer substrates	95 ^{o}C
Drying period	2 min	2 min	5 min
Maximum layer thickness	9 μm	1.1 μm	0.75 μm

*Information is undisclosed.

Table 2-1 summarises the fabrication parameters of water removable materials in MEMS. The advantages of water soluble sacrificial materials are that they are non-toxic, environmentally friendly and insoluble in most organic solvents. The solutions of these materials can be dried at temperatures below 150 ^{o}C in a short period (<10 minutes). Once dried, the layers are strong enough to support the fabrication of subsequent layers and are compatible with a number of polymer materials, such as SU-

8, Poly(methyl methacrylate) (PMMA) and Polydimethylsiloxane (PDMS). To release the structures, the samples were simply immersed in or rinsed by DI water so that these materials would be completely dissolved. However, the maximum concentration of the solution was 20 wt% resulting in a low viscosity so that only spin coating could be used. The layer thickness would be decreased once the water was evaporated giving a maximum layer thickness of approximately 10 μm. This makes it difficult to achieve a continuous and uniform coverage with these materials on an uneven surface, such as fabrics. There are further limitations on the substrate in that the surface must be flat, solid and relatively smooth for spin coating.

Organic and inorganic solvents removable materials:

The removers used in this section are chemicals, which are corrosive, oxidising, harmful or flammable. The removal rate is dependent on the temperature and the concentration of the remover. As these removal mechanisms have high selectivity, high throughput and are relatively inexpensive, they have been widely used in microfabrication processes. Table 2-2 summarises the common sacrificial materials used in microfabrication.

Table 2-2: Summary of common sacrificial materials removed by acids, alkalis, and solvent.

Sacrificial material	*Structural material*	*Removal reagent*	*Substrate*	*Ref*
Chromium	Gold	Cerium based etchant[4,5]	Glass	[17]
Zinc	Nickel	Alkaline liquor with H_2O_2[1,5]	Silicon	[18]
Copper	Gold	$FeCl_2$[1,5] and HCl[1,5]	Silicon	[10]
Polysilicon	Silicon Nitride	KOH[1,5]	Silicon	[19]
Silicon dioxide	Polysilicon	Hydrogen fluoride (HF)[1,5]	Silicon	[6]
SU-8*	NiFe	Acetone[4,5]	Silicon	[20]
PMGI	SU-8	MF-319[1]	Silicon	[21]
Polystyrene	SU-8	Toluene[4,5]	Glass	[22]

*Only uncured SU-8 can be removed by acetone. Cured SU-8 is difficult to remove.
[1]Corrosive, [2]Oxidising, [3]Harmful, [4]Flammable, [5]Toxic

Inorganic materials typically focus on oxides (i.e. SiO_2) and metals (i.e. copper), whereas organic materials are polymer materials which are removed by selective solvents. Silicon dioxide (SiO_2) can be deposited either by thermally growing it on top of the silicon wafer or through chemical vapour deposition (CVD) in which the SiO_2 is directly deposited onto the surface of the substrate. However, for most processes, oxides are usually deposited by CVD because the deposition is faster than thermal growth [23]. Silicon dioxide deposited by CVD processes below 500 ^{o}C (e.g. plasma enhanced CVD (PECVD)) is useful as the layer density is lower than silicon dioxide deposited at higher temperatures (e.g. LPCVD) or by thermal oxidation, thus the etch rate can be as much as an order of magnitude greater than that at high temperatures [23]. By heating these oxides at temperatures above 700 ^{o}C, densification occurs resulting in a decrease in film thickness. However, by selecting different material combinations, polysilicon can also be used as the sacrificial material while silicon nitride is used as the structural material [19]. Polysilicon can be removed by KOH but care must be taken because KOH will also etch the silicon wafer. Metals are normally deposited by either sputtering or electroplating depending on the thickness requirement.

Unlike metals and oxides, polymers do not require a high temperature environment for the deposition process, or harsh chemicals for removal. Some polymer materials, such as SU-8, can be directly deposited onto the substrate as the sacrificial layer without any modification, whereas other materials, such as polystyrene [22], needs to be dissolved into a corresponding solvent to achieve a homogenous solution prior to deposition. As most organic sacrificial materials are in liquid form with low viscosities, spin coating is usually employed. Most polymers are synthesised, thus new polymers suitable for different applications can be rapidly developed. In addition, organic materials, with regard to fabrication, can significantly reduce the processing time and complexity compared with inorganic materials when used as the sacrificial material [20].

None of the sacrificial materials reported in this section are suitable for textile applications due to their incompatible deposition process and remover materials or processes. Inorganic materials can be deposited onto most substrates but the deposition conditions are too harsh to the fabrics. In addition to the harsh deposition process of the inorganic materials, removers would degrade or even destroy the fabrics. The subsequent layers can also be damaged. For instance, HF and KOH will significantly

damage the fabric. Even though the removers of organic sacrificial materials are not as harmful as those used in inorganic sacrificial materials, the deposition method is still not compatible with the surface topology of the textiles. For example, a spin coated material may be absorbed by the fabric due to its low viscosity and the porosity of the fabric.

Thermally removable materials:

The common thermally removable materials are polynorbornene and polycarbonate because these materials decompose once the temperature is above their decomposition temperatures. In [24], a 23 wt% solution of polynorbornene (PNB) in mesitylene was spin coated and dried followed by a photolithography step to define the features. Encapsulation layers, which were SiO_2, Si_3N_4 and polyimides, were individually deposited on top of the sacrificial layer to create air channels. The temperature was then increased to 425 ^{o}C and maintained for 2 hours to produce gaseous products which permeate through the top layers leaving behind minimal solid residue. In contrast, polycarbonates were decomposed at a slightly lower temperature range of 200 to 300 ^{o}C depending on the molecular arrangement [25]. The polycarbonate must be fully dissolved to achieve a homogenous solution. A solution with a concentration of 18 wt% was then spin coated and dried at 160 ^{o}C for 30 min. Metal was sputtered onto the polycarbonate layer as a hard mask for the subsequent photolithography process. Silicon dioxide and structural polymer were individually deposited onto the patterned polycarbonate layers by PECVD and spin coating, respectively. Decomposition was performed in a furnace range from 200 to 250 ^{o}C for approximately 2 hours, depending on the kind of structural materials. It showed that polycarbonate was fully decomposed in narrow geometries without any solid residue and the removal temperature was fully compatible with the polymer structural materials, which remains stable and rigid after the temperature treatment.

It has also been demonstrated that wax, a phase changing material, can be used as the sacrificial material for the fabrication of micro channels [26, 27]. Wax is in a solid state at room temperature and it must be melted before deposition. In [26], electrophoresis channels and reservoirs were initially created by an imprinted PMMA substrate and then heated to 85 ^{o}C. A pipette was used to transfer the melted wax from a heated vial to

the reservoirs before it could cool and solidify. A vacuum was applied at all reservoirs to ensure that all channels were completely filled. To remove the wax, a small amount of cyclohexane was pipetted into each reservoir while the entire sample was heated to 75 $^{\circ}$C. A vacuum was applied again to remove the residual wax from the channels.

The decomposable materials polynorbornene and polycarbonate show a good compatibility with silicon dioxide, silicon nitride and some polymers with high glass transition temperatures. However, the removal temperatures and deposition processes are not compatible with the majority of fabrics and the screen printing process. Wax has a low removal temperature of 75 $^{\circ}$C, which is compatible with most fabrics, but wax needs to be liquefied before deposition which is a significant challenge for screen printing. The selection of structural materials is also restricted because only the materials with curing temperatures lower than the melting point of the wax are suitable. In addition, due to the brittle properties of the wax, printed wax layers cannot withstand the pressure used for screen printing resulting in damaged layers.

2.2.4　Screen printed sacrificial materials

Unlike sacrificial materials in MEMS applications, screen printable sacrificial materials have not been widely reported previously. The requirements for a screen printable sacrificial material are:

- o The material should be of a suitable rheology for screen printing
- o When printed, the material must not react with other layers
- o The material should provide a solid foundation once it is dried or fired
- o The materials must be removed at the end of the process and the removal method should not damage other printed layers and the substrate

Table 2-3 summarises existing screen printed sacrificial materials used for fabricating free standing structures on alumina tiles.

Table 2-3: Summary of existing screen printable sacrificial materials.

Printable sacrificial material	Curing condition	Removal condition	Ref
Graphite paste	$120\,^{o}C$	$> 850\,^{o}C$	[28]
$SrCO_3$ paste	$850\,^{o}C$	H_3PO_4 solution	[29]
Gold paste	$850\,^{o}C$	Potassium iodide solution	[30]
Plastic crystal pastes	$80\,^{o}C$	$150\,^{o}C$	[31]

Several researchers have demonstrated that graphite based screen printable paste with a ceramic binder could be used as the sacrificial layer in low temperature co-fired ceramic (LTCC) processes for the fabrication of air channels. When graphite is in contact with sufficient oxygen at a certain temperature, carbon dioxide is generated resulting in a transformation from solid to gas. This reaction is a chemical change because a new substance is generated.

Birol et.al. [28] used graphite powder as part of the sacrificial paste for fabricating chambers on a LTCC tape. Graphite powder with different particle sizes was mixed with ethyl cellulose (EC) (binder), terpinol (solvent) and acetyl acetone (dispersant) followed by a triple-roll milling to achieve a homogenous paste. By printing the graphite layer onto LTCC tape and drying at 120 ^{o}C, the removal process took place while the LTCC tape was being fired. The results showed that the printed graphite layer supported the upper structures, up to its burnout temperature, and was fully burned out at temperatures in excess of 875 ^{o}C. Using the same graphite sacrificial paste, *Kok et.al*. [32] demonstrated free standing piezoelectric cantilevers on alumina tiles for vibration energy harvesting. The ceramic lead zirconate titanate (PZT) and Ag/Pd pastes were printed directly on top of a dried graphite sacrificial layer. There was no reaction between these materials and the sacrificial layer was removed during firing at 950 ^{o}C. It was found that the graphite paste is not only compatible with the LTCC tape but also suitable for use in conjunction with other screen printable pastes printed directly on top. Strontium carbonate ($SrCO_3$) is chemically stable up to 960 ^{o}C and dissolves easily in a weak acidic solution, therefore Laboratoire de l'Intégration du Matériau au Système (IMS laboratory) has identified this as a potential sacrificial material and developed a screen printable paste based on $SrCO_3$ powder [29]. The commercial strontium

carbonate powder was firstly sieved to eliminate the agglomerates. 55 wt% of $SrCO_3$ powder and an epoxy-based vehicle were then mixed in a mortar and homogenised in a ball mill for 12 h. A thermo gravimetric analysis (TGA) showed that a polymerised sacrificial layer could withstand temperatures up to 900 ^{o}C without significant mass loss thus being compatible with a variety of screen printable ceramic pastes. The sacrificial layer can be removed by immersing the sample in H_3PO_4 aqueous solution. Using this paste, *Lakhmi et.al.* [33] fabricated a free standing cantilever structure with a piezoresistive force sensing mechanism. A sacrificial paste was printed onto an alumina tile and dried at 120 ^{o}C. ESL 4702 dielectric paste was then printed on top, followed by an ESL3414 resistive ink as the sensing mechanism. The entire structure was fired at 850 ^{o}C for 10 min. Samples were then immersed in H_3PO_4 solution and results showed that the cantilever was fully released and no reaction was found between H_3PO_4 and the printed layers (except the sacrificial layer).

Gold screen printable paste with a ceramic binder can also be used as the sacrificial material for fabricating pressure sensors, which is reported in [30], shown in Figure 2-3.
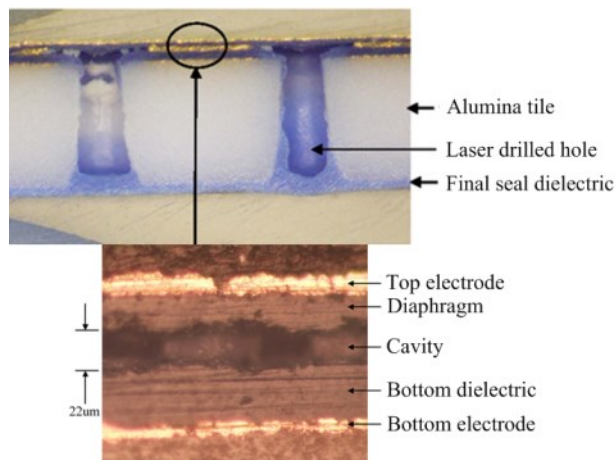
Figure 2-3: A diaphragm fabricated by removing the gold sacrificial layer through laser drilled holes [33].

The bottom gold electrode was firstly printed onto the alumina tile followed by a dielectric layer, which protected it from being removed. A sacrificial gold layer was then printed and dried. Another protective dielectric layer was printed on top, followed by the top gold electrode. Once the samples were fired, the gold sacrificial layer was chemically removed using a potassium iodide solution through holes which were drilled

before printing. Subsequently, a dielectric layer was printed on the back side of the alumina tile to seal the cavity hermetically.

Unlike the materials described above, which require high temperature or harsh liquid for the removal, *Serra et.al.* [31] identified that plastic crystals based sacrificial materials have the ability to sublimate at a relatively low temperature (i.e. 150 ^{o}C) without a liquid phase, which potentially avoids the stiction problem which causes unexpected structural deformations (e.g. bending or sagging) in microscale devices. In this work, three plastic crystals, trimethylolethane (TME), trimethylolpropane (TMP) and neopentylglycol (NPG), were formulated into viscous pastes by partly dispersing and dissolving into a solvent mixture of cyclohexanol (CH), water (H_2O) and propylene glycol (PG) at 100 ^{o}C. Two pastes were formulated with combinations of TME/TMP and TME/NPG. The main compound of TME was finally suspended in the solution once the temperature was cooled down. As TME is the main sacrificial material, TMP and NPG act as the binders in the system. The maximum concentrations of TME/TMP and TME/NPG pastes are 46 wt% and 32 wt%, respectively. These pastes were initially screen printed onto alumina tiles to evaluate the printability and cured at 80~100 ^{o}C for 10 minutes. The results showed that the drying of the printed layers yielded consistent surfaces. However, the TME/TMP layer could not be left in the air because this caused it to dry and consequently become brittle and TME/NPG layer appeared to be relatively hygroscopic resulting in a waxy solid. To investigate the compatibility with potential structural material candidates, epoxy resin, silicone resin and ethyl cellulose (EC) were individually screen printed onto pre-patterned sacrificial layers and dried. The sacrificial layers were subsequently removed at 150 ^{o}C and it was found that the sacrificial layers were fully sublimated. The results showed that the plastic crystals reacted significantly with the epoxy resin because of the –OH groups. However, there was no evidence of any reaction with the silicone or ethyl cellulose layers.

To conclude, the outlined high curing and removal temperatures and harsh removers are not suitable for this research because the fabric cannot withstand these conditions. Screen printable plastic crystal pastes are of interest due to their sublimation mechanism at a temperature around 150 ^{o}C which is suitable for the vast majority of fabrics but the printed surfaces are brittle and hygroscopic which will cause problems in the printing of subsequent layers.

2.3 Structural fabrication technology

2.3.1 Definition of structural technology

The term 'structural material' usually denotes those materials that are used solely for mechanical purposes [34]. Metals, ceramics and polymers have all been used as structural materials Structural materials need to be selected for specific applications because there are no generic structural materials suitable for all applications. The structural materials described in this thesis are mainly materials which are deposited onto substrates, rather than the materials used in industry such as an extruded steel bar.

Materials used as structural materials should have the following properties:

- o Should provide a solid foundation
- o Should be resistant to chemicals and heat used in subsequent processes
- o Should be easy to deposit and compatible with other materials
- o Should have strong adhesion to the substrate or preceding layers

2.3.2 Structural materials used in MEMS

The priority for consideration as a structural material is the ease of deposition. Deposited films should also be self-supporting after solidification and should not be damaged by the subsequent sacrificial removal processes. Structural, sacrificial and functional materials should be compatible with each other, especially their curing conditions. Table 2-4 shows the common structural materials used in microfabrication processes along with their deposition methods.

Table 2-4: Common structural materials used in MEMS.

Structural materials	Deposition methods	Temperature	Ref
Polysilicon	LPCVD	$625\,^{o}C$	[35]
Silicon nitride	PECVD	$230\,^{o}C$	[24]
Silicon carbide	PECVD	$350\text{-}400\,^{o}C$	[36]
Nickel	Electroforming	Unspecified	[18]
Aluminium	RF Sputtering	Unspecified	[37]
Gold	Electroplating	$60\,^{o}C$	[10]
SU-8	Spin coating	RT	[38]
Polyimide	Spin coating	RT	[39, 40]
PDMS	Molding	RT	[41]

RT: room temperature.

Inorganic materials, such as polysilicon, silicon nitride and silicon carbide, are commonly used as the structural material in MEMS. Polysilicon is a useful structural material because integrated circuit processes already exist for depositing and etching polysilicon and its thermal coefficient of expansion is compatible with the silicon substrate [23]. As polysilicon is resistant to HF, it is commonly used in conjunction with silicon dioxide resulting in a selective removal of SiO_2. Polysilicon exhibits a piezoelectric effect and consequently can be used as both a structural and functional material. Ceramic materials are also used as structural materials in microfabrication. Silicon nitride is a widely used ceramic material and it has a higher Young's modulus than silicon. Silicon nitride is resistant to many alkaline etch solutions, thus the structural integrity will not be affected by alkaline chemical removers. Silicon carbide is another ceramic material which offers significant advantages as a structural material, in particular hardness, high wear resistance, high Young`s modulus, resistance to harsh chemicals and mechanical stability at high temperature [23]. Silicon carbide films are commonly achieved by CVD deposition in surface micromachining. They are used in conjunction with silicon dioxide sacrificial layer [42]. Metallic structural materials and their corresponding sacrificial materials can be deposited by sputtering or electroplating.

The layer thickness can be accurately controlled by altering deposition parameters. However, some metallic materials require a seed layer to increase adhesion to the substrates, such as gold layer [10].

Polymer materials include thermosets, thermoplastics and elastomers. Thermosetting polymers are materials that form a cross-linked network yielding a high Young`s modulus and high thermal stability [34]. SU-8 and polyimide are thermosetting polymers that are widely used in microfabrication as structural materials. When cured, SU-8 forms a cross-linked matrix of covalent bonds, which are not weakened by heating or dissolution. As with all photoresist materials, spin coating is used to deposit SU-8. Due to the cross-linking mechanism, cured SU-8 structures have the same thickness as immediately after deposition, thus reducing the shrinkage of deposited layers. Unlike SU-8, which is a brittle material once it is cured, polyimide is a ductile material which allows for a maximum elongation up to 70 % [43]. Polyimide possesses strong mechanical properties and sufficient chemical resistance that it could be a potential structural material. Thermoplastics are defined as polymers which are softened or melt upon the application of heat. They exhibit relatively poor mechanical stability due to their viscoelastic nature resulting in an undesirable plastic deformation when the operating temperature is close or higher than their softening points. Elastomers are cross-linked rubbery polymers which have high stretchability. The most widely used elastomer in MEMS is PDMS as it is chemically inert, thermally stable, permeable to gasses, low cost and simple to handle [41]. Molding PDMS is a common way to achieve desired patterns.

None of the structural materials used in MEMS are suitable for the fabric substrate applications since the deposition processes exclude these materials from being used on fabrics.

2.3.3   Screen printed structural materials

Unlike structural materials used in microfabrication which have a solid foundation after depositing, screen printable materials are in a paste form before and after the deposition process, therefore a curing process is required to solidify the materials. Screen printed structural pastes can be either ceramic pastes, which require a higher curing temperature

(>800 ^{o}C), or polymer pastes which need either a relatively low temperature (< 200 ^{o}C) or ultra violet (UV) light for polymerisation. Table 2-5 summarises existing screen printed structural materials used for the fabrication of free standing structures on alumina tiles.

Table 2-5: Screen printed structural materials used in the literature for the fabrication of free standing structures.

Screen printed structural materials	Curing conditions	Applications	Ref
Gold paste (ESL 8836)	850 ^{o}C 10 min	Cantilever	[29]
Copper paste (DuPont QP153)	960 ^{o}C, nitrogen	Free standing actuator	[44]
Ag/Pt and Ag/Pd pastes	850 ^{o}C 10 min	Free standing resistor/free standing cantilever	[29, 45]
Dielectric paste (ESL4720)	850 ^{o}C 10 min	Cantilever (force sensor)	[46]
PZT-5H paste	950 ^{o}C 10 min	Cantilever (energy harvester)	[45]
Silicone with graphite	80 ^{o}C	Microfluidic channel	[47]
Ethyl cellulose with graphite	80 ^{o}C	Cantilever	[47]

Ceramic pastes are pastes that usually need a high temperature firing profile to melt a glass binder forming a homogeneous solid layer. These kinds of materials are stiff because of the nature of the ceramic. Researchers at the IMS laboratory [29] demonstrated the feasibility of the free standing structure fabrication using different structural materials. A cantilever made of ceramic gold could be achieved by printing the gold paste (ESL8836) onto a $SrCO_3$ sacrificial layer and firing at 850 ^{o}C for 10 min. The gold layer was released by removing the sacrificial layer at the end of the process. Using the same fabrication process, a free standing resistor made of Ag/Pt and a copper actuator can be achieved. The example structures are shown in Figure 2-4.
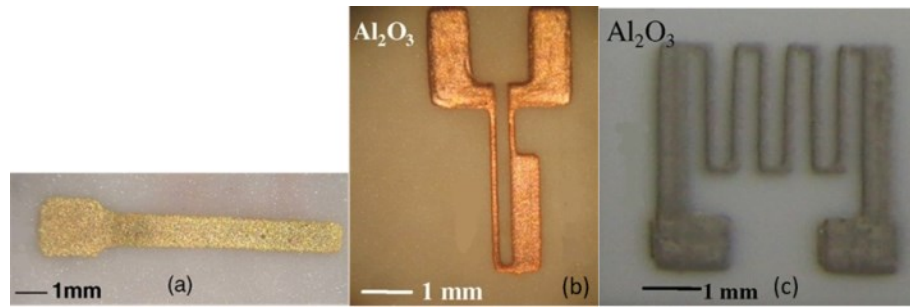
Figure 2-4: Examples of screen printed structural materials: (a) gold cantilever; (b) free standing copper actuator; (c) free standing Ag/Pt resistor [29].

Dielectric ceramic pastes can also be used as a structural material. In [46], piezoresistive force sensors based on a cantilever structure were achieved by printing sacrificial, commercial dielectric (ESL4702) and piezoresistive (ESL3414) pastes, in that order, onto the alumina tile. The sample was then fired at 850 ^{o}C for 10 minutes to achieve solid layers. ESL4702 is used as the structural material because it has good adhesion to the alumina tile. In addition, the displacement produced is higher than other ceramic materials because of its relatively low Young`s modulus (i.e. 35 GPa [48]).
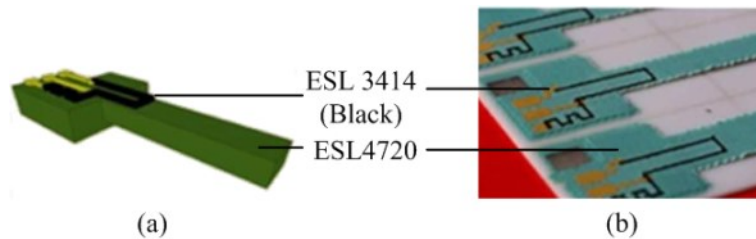
Figure 2-5: Screen printed force sensor based on a cantilever structure with ceramic dielectric paste (ESL4702) as the structural layer. (a) Schematic diagram of the cantilever; (b) photograph of screen printed cantilever [46].

In a similar example, *Kok et.al.* [45] used a combination of piezoelectric and conductive pastes as the structural material. They reported a free standing cantilever structure made up of alternate layer of PZT-5H and Ag/Pd pastes printed onto an alumina tile. The entire structure was fired at 950 ^{o}C during which the sacrificial layer was removed.
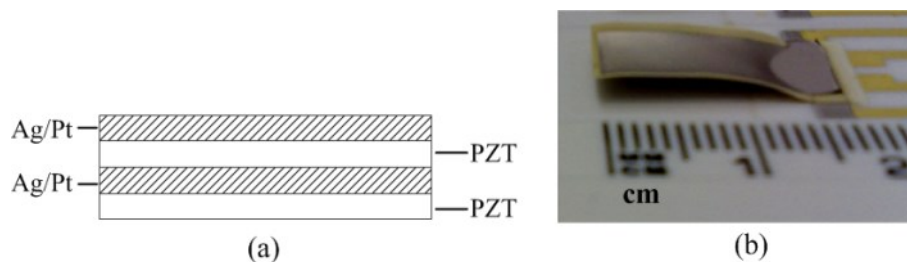
Figure 2-6: Piezoelectric free standing cantilever structure achieved by printing multilayer of PZT and Ag/Pd combination: (a) schematic diagram of the structural layer combination; (b) a photograph of the cantilever [45].

Figure 2-6 shows that the structural layer consists of alternate PZT and Ag/Pd layers. Multilayer printing is used in this research to reduce the thermal mismatch between PZT and Ag/Pd during the firing step and increase the mechanical strength of the resulting cantilever.

Silicone exhibits good flexibility and is resistant to most solvents but is hard to screen print because of its rheology. Research developed in [47] showed that silicone could be screen printed by dissolving it into dodecane/octanol solvent mixture. 20wt% graphite powder was then added into the paste to improve the mechanical properties. Results showed that dissolved silicone had good printability and can be used as the encapsulation layer for the fabrication of microfluidic channels. In a continuation of this research, ethyl cellulose was dissolved into an unspecified solvent mixture and graphite powder was added once ethyl cellulose was fully dissolved. Because ethyl cellulose is stiffer than silicone, it is a more suitable structural material for cantilever structures. Devices fabricated with these structural pastes are shown in Figure 2-7.
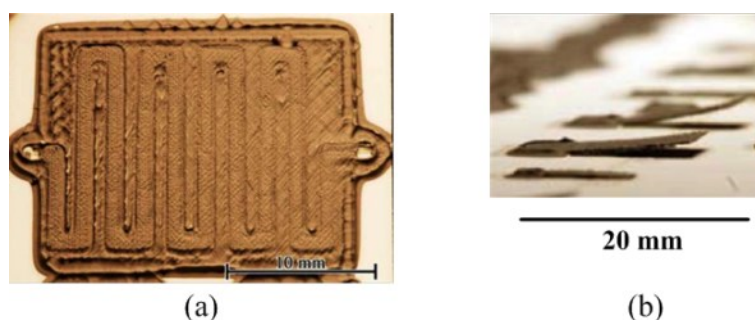
Figure 2-7: (a) Microfluidic channels with a silicone-graphite cover layer and (b) cantilevers with ethyl cellulose-graphite structural layers [47].

According to the curing condition of those materials described above, ceramic pastes will not be considered because of their high firing temperatures which will destroy any fabrics. Silicone and ethyl cellulose based pastes, having a low curing temperature of 80 ^{o}C, are compatible with the majority of fabrics but it is difficult to print other materials on top of the silicone due to its low surface energy.

2.4 Conclusions

By examining the removal mechanism of the materials, it was found that the selection of the sacrificial material is restricted by the fabric substrates. Material selection is limited because most fabrics cannot withstand either temperatures above 200 ^{o}C or a harsh removal environment. Hence, with regard to the material selection, organic materials are more suitable than inorganic in fabric printing applications. Unlike rigid, smooth and flat substrates, which are commonly used in silicon microfabrication, fabric is a soft, highly flexible and porous material with an uneven surface. As a result, most polymer materials used in MEMS cannot be applied onto fabrics due to the incompatible deposition processes. Of particular interest are water soluble materials and low temperature removable materials. Plastic crystals have great potential to be used as the screen printable sacrificial materials but further investigation and improvement are required.

There is a more limited range of screen printed structural materials commercially available compared with MEMS materials. Most screen printed structural materials are based on ceramic which normally have a firing temperature above 800 ^{o}C. Free standing structures based on these pastes are also quite fragile, limiting their use on fabrics. Screen printed polymer pastes are of interest as they are cured at relatively low temperatures compared with ceramic pastes and their ductile properties are compatible with the flexibility of fabrics.

Chapter 3

Literature review: smart fabrics, cantilevers and pump structures

3.1 Introduction

This chapter provides an introduction to smart fabrics followed by reviews of free standing cantilever and pump structures. These reviews consist of free standing structures fabricated on a variety of substrates, from rigid silicon wafers to flexible polyimide sheets.

Making free standing structures on fabrics using sacrificial technology is very challenging. The main challenges are the selection of suitable materials and determination of the appropriate deposition processes. Therefore, this chapter emphasises the fabrication processes used to realise free standing structures, both in MEMS and by screen printing. Free standing cantilevers are appropriate mechanical structures for evaluating the performance of the sacrificial and structural materials because of their simplicity. In contrast to planar structures, cantilever structures have to be realised by the removal of the sacrificial material resulting in a free standing structure.

Pump structures are one of the most complex mechanical structures as they consist of a variety of free standing structures, such as chambers, channels and diaphragms. It is

therefore a good candidate for the further evaluation of the sacrificial and structural materials.

This chapter is comprised of the following sections:

- o Overview of smart fabrics
  - ➢ Definition
  - ➢ Classification
  - ➢ General fabrication processes
- o Introduction to free standing cantilevers
  - ➢ MEMS cantilevers on rigid and flexible substrates
  - ➢ Printed cantilevers on rigid, flexible and fabric substrates
- o Introduction to pump structures
  - ➢ MEMS pump structures on rigid and flexible substrates
  - ➢ Printed pump structures on rigid, flexible and fabric substrates

3.2 Smart fabrics

3.2.1 Definition of smart fabrics

Smart fabrics are defined as conventional fabrics with integrated electronic functionality (e.g. sensors and actuators), potentially offering new functionality in the ubiquitous application of fabrics. Smart fabrics enable the design and production of wearable garments with distributed non-obtrusive sensors. They have been widely researched for healthcare, consumer, fashion and military applications [49]. Wearable sensors integrated into the fabric offer a comfortable approach to achieve sensors on people, with potentially easy integration, since functionalization occurs during the garment manufacture. Smart fabric can be classified into three categories of functional activity [1]:

Passive smart fabrics

Textiles with only a sensing function are referred to as passive smart fabrics. This type of smart fabric has the ability to convert an external stimulus into electrical signals for future data processing. Common stimuli are vibration, temperature and pressure, though the electrical signal has been used for some applications. To convert them into electrical signal, sensing mechanisms, such as piezoelectric, piezoresistive and capacitive, are commonly incorporated into textiles.

Active smart fabrics

Textiles with an actuating function are described as active smart fabrics as they sense stimuli from the environment and then perform actions based on these stimuli. The response could be in the form of movement, sound, colour changing and odour releasing.

Ultra smart fabrics

Textiles with an adaptive function are called ultra smart textiles as they contain sensing, actuating and processing elements to tailor their response. This type of smart fabric can sense and react autonomously to an environmental stimulus.

3.2.2 General fabrication processes and applications

There are two fundamentally different processes currently employed in the fabrication of smart fabrics. One is standard textile fabrication techniques, such as weaving and the other one involves material deposition techniques, such as screen printing.

The standard textile fabrication techniques involve the integration of functional yarns into the fabric structure to form part of the system. This type of fabrication provides garments which are reliable, flexible, elastic and comfortable for wearers [50].

In contrast, screen printing is easy to use and does not need complex initial setup thereby allowing complex designs on fabric. Table 3-1 provides a summary of a number of smart fabric applications along with their fabrication processes.

Table 3-1: Summary of smart fabric applications.

Year	Author	Fabrication process	Application	Ref
2002	Mazzoldi	Printing* and weaving	Motion capture system	[51]
2005	Scilingo	Weaving	Electro cardiography (ECG)	[52]
2006	Meyer	Embroidery	Pressure sensor	[53]
2008	Kang	Screen printing	ECG	[54]
2008	Rothmaier	Weaving	Pressure sensor	[55]
2009	Husain	Knitting	Temperature sensor	[56]
2010	Crowley	Screen and inkjet printing	Gas sensor	[57]
2010	Kim	Screen printing	Passive electronics: resistor, capacitor and inductor.	[58]
2010	Vicente	N/A*	Antenna	[59]
2011	Cho	Knitting	Motion sensor	[60]
N/A*	Peratech Limited	N/A*	Touchpads and switch	[61]

*Information is undisclosed.

3.2.3   Discussion

Smart fabrics manufactured by standard textile processes are durable, resistant to deformation, comfortable to wear and have comparatively good moisture transport properties. However, these fabrication techniques require complex initial setup and yarn preparation. Yarns must also follow the fabric warp and weft yarn structures, thus limiting design options to orthogonal orientations. Moreover, standard textile fabrication techniques are only able to create planar structures, though 3D structures can be achieved using spacer fabric [62]. Multiple layer structures with different patterns and functions are more difficult to achieve if not impossible when free standing structures are needed.

In contrast, screen printing offers an alternative smart fabric fabrication technique in which functional pastes are deposited onto fabric only where they are required. Screen printing provides more design freedom because the printed layers can have any

orientation on fabric and do not need to follow the orthogonal warp and weft directions. In addition, screen printing allows the production of arrays of the same or different devices in a straightforward fashion as screen printing is inherently a batch process, producing multiple devices from a single set of screen designs. A broad range of functional pastes is also commercially available which potentially allows a variety of functionalities to be integrated with the fabric.

3.3 Free standing cantilever structures

A free standing structure is defined as a structure which stands alone or on its own foundation, free of external support or attachment; free standing structures do not rely on any other structures for support. Figure 3-1 illustrates some common free standing structures.
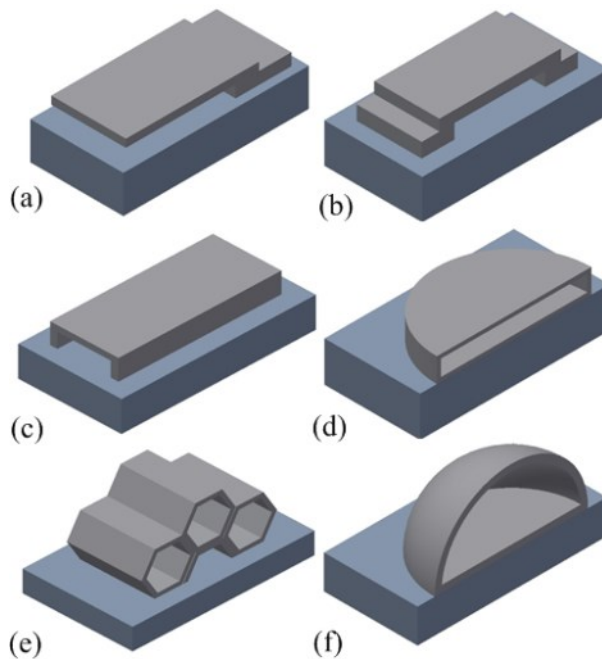
Figure 3-1: Schematic diagram of common free standing structures: (a) cantilever; (b) bridge; (c) channel; (d) chamber; (e) honeycomb; (f) dome.

Based on their mechanical configuration, free standing structures are defined as follows. A cantilever structure (a) is a simple mechanical structure of which one end is clamped and the other end is free to move. When an external stimulus, such as acceleration, acts on the cantilever, the free end of the cantilever is able to move. A bridge structure (b) consists of a beam with both ends clamped. The clamped ends constrain two opposite

edges of the beam and only the middle of the beam is free to move. A channel or tunnel (c) is a structure of which two ends are open with closed surrounding walls. This is usually used for the transportation of fluid. There are two types of channel structure. One has a rectangular cross-section and the other has a circular cross-section. However, the channel with a circular cross-section is not easy to achieve because of the cylindrical sidewall, whereas the rectangular shape is easy to fabricate and has been widely used in microfluidic devices. The chamber (d) is a complex free standing structure which consists of a cavity beneath a membrane with a surrounding sidewall. The chamber structure is the key to the mechanical pump structure. Other free standing structures, such as honeycombs (e) and domes (f), are rarely used, especially for sensor and actuator applications as these are more complex structures which are difficult to fabricate without offering significant advantages over simpler geometries.

3.3.1 MEMS cantilevers on rigid substrates

Cantilevers find widespread application in MEMS based sensors and actuators and have been used as the mechanical structure in a wide variety of sensors (e.g. accelerometers [35], flow sensors [63], pressure sensors and thermopiles [64]) and actuators (e.g. polyimide bimorph actuator [65] and multimorph cantilever actuator [66]).

In MEMS, cantilevers are predominantly fabricated with either silicon or polymer based materials. Although the device design for those materials is similar, the fabrication processes are completely different. Silicon based materials (i.e. mainly of inorganic materials) are predominantly used for the fabrication of cantilever structures because silicon microfabrication is well established and uses technologies developed and proven in the integrated circuit (IC) industry. Materials, such as silicon, silicon dioxide and silicon nitride, are well characterised and stable over time. As a result, cantilevers fabricated with these materials can operate in a large range of temperatures and environmental conditions. Polymer materials have been introduced into the fabrication of cantilever structures as they typically have a Young`s modulus two orders of magnitude lower than that of silicon based materials [34]. This is useful as the sensitivity of the cantilever is increased when the stiffness is reduced.

Cantilevers are usually fabricated using bulk or surface micromachining techniques depending on the design and materials. Bulk micromachining refers to the formation of microstructures by selectively removing material from substrates, mainly silicon, yielding micromechanical structures with a thickness in the region of tens or hundreds of micrometres [23].

The two common types of bulk micromachining are isotropic and anisotropic etching. In isotropic etching, the chemical etches the bulk material at the same rate in all directions resulting in round cross-sectional features. In contrast, anisotropic etching involves etching with different etching rates in different directions and therefore it is possible to obtain angled cavities, diaphragms, cantilevers and bridges. Cantilevers with capacitive [67, 68] and piezoelectric [69-71] transduction mechanisms can be achieved with bulk micromachining. During the fabrication process, the actual cantilever materials are deposited onto the front side of the silicon wafer. The thickness of the deposited layer is the final thickness of the cantilever. The cantilever pattern is defined by subsequent photolithography on a photoresist layer which is spin coated onto the entire substrate. Through the photolithographic process, the pattern is transferred from the mask onto the resist layer. A developing step is required to remove the un-patterned areas. The etching from the back side of the silicon wafer is performed with potassium hydroxide (KOH) and the cantilever is finally released from the substrate. Figure 3-2 shows a simplified fabrication process of a piezoelectric cantilever realised by a bulk micromachining process [72].

a) Deposition of piezoelectric layer

b) Formation of protective layer and bonding pad

c) Cantilever patterning and the formation of etching mask

d) KOH anisotropic etch to release the cantilever
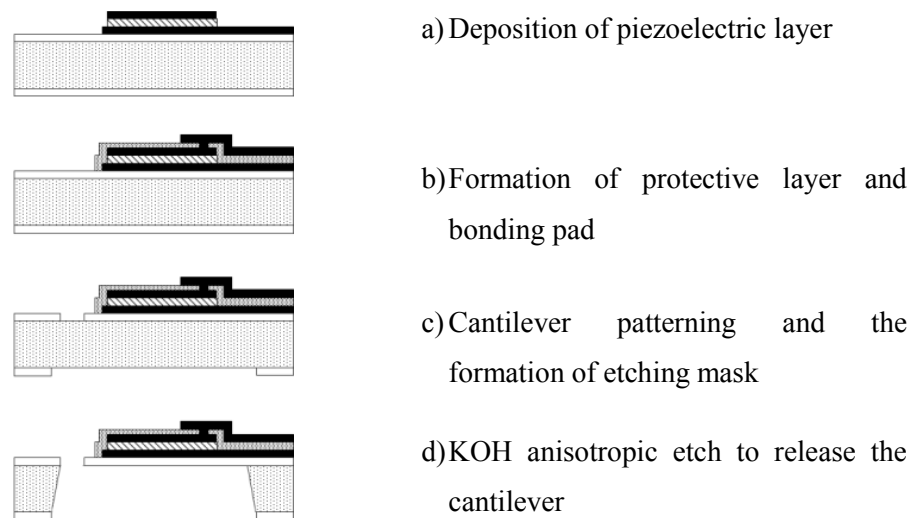
Figure 3-2: A simplified fabrication process of a micro piezoelectric cantilever [72].

37

The fabrication process starts with thermal oxidation of the silicon wafer followed by a thick evaporated Au/Cr layer as the bottom electrode. The piezoelectric ZnO layer was deposited using sputtering. Another Au/Cr layer was deposited and patterned to form the top electrode. ZnO layer was patterned to form the same pattern as the top electrode. Next, the bottom electrode was patterned followed by a sputtered SiO_2 layer to protect the piezoelectric layer during the final etching process. A cantilever shape was created on the front of the substrate and the etching mask was patterned on the back side of the silicon wafer. The entire wafer was then immersed in KOH solution to anisotropically etch the silicon resulting in the release of the cantilever structure. Figure 3-3 shows an scanning electron microscope (SEM) micrograph of the cantilever after release from the silicon wafer.
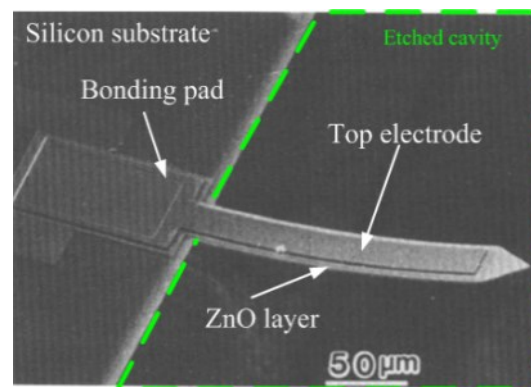
Figure 3-3: An SEM micrograph of a bulk micromachined cantilever released from the silicon wafer [72].

In contrast to bulk micromachining in which structures are formed by etching into substrates, surface micromachining builds up structures through a layer by layer process as materials are deposited on top of the substrate. Therefore, the substrate material is not limited to silicon. The materials deposited on top of the substrate act as either structural layers or sacrificial layers. Dry etching is usually used to define the shape of the layers and a wet etching process releases them from the substrate by removing the sacrificial layer [73]. Compared with bulk micromachining, surface micromachining has the following advantages [74]:

o Materials and etchants used are identical to those used in CMOS (Complementary metal oxide semiconductor) manufacturing.

o It is possible to create a large range of different structures from the same process using only changes in patterning.

o Mechanical elements can be integrated close to electronic circuits, thereby minimising noise, resulting in better performance and higher reliability.

Both silicon and polymer based materials can be used but the deposition methods for each material are different. For silicon-based materials, chemical vapour deposition (CVD) is commonly used, whereas for polymer-based materials, spin coating is employed as these materials are usually in liquid form. A sacrificial layer should first be deposited and patterned. The structural or functional layers are then deposited and patterned. The resist is then spin coated over the entire substrate and baked. A photolithographic process is necessary to define the cantilever patterns. Finally, the cantilever is released from the substrate when the sacrificial layer is removed. The removal speed is relatively slow, as the access of the remover to the sacrificial layer is limited by the gap between the cantilever and the substrate. This results in a longer processing time. In addition, due to this small gap, the chance of stiction between layers is increased. Figure 3-4 shows a simplified fabrication process of a piezoelectric cantilever on top of a silicon wafer.

a) Sacrificial layer deposition and patterning

b) Structural layer deposition

c) Top electrode patterning

d) Functional and bottom electrode patterning

e) Removal of the oxide sacrificial layer
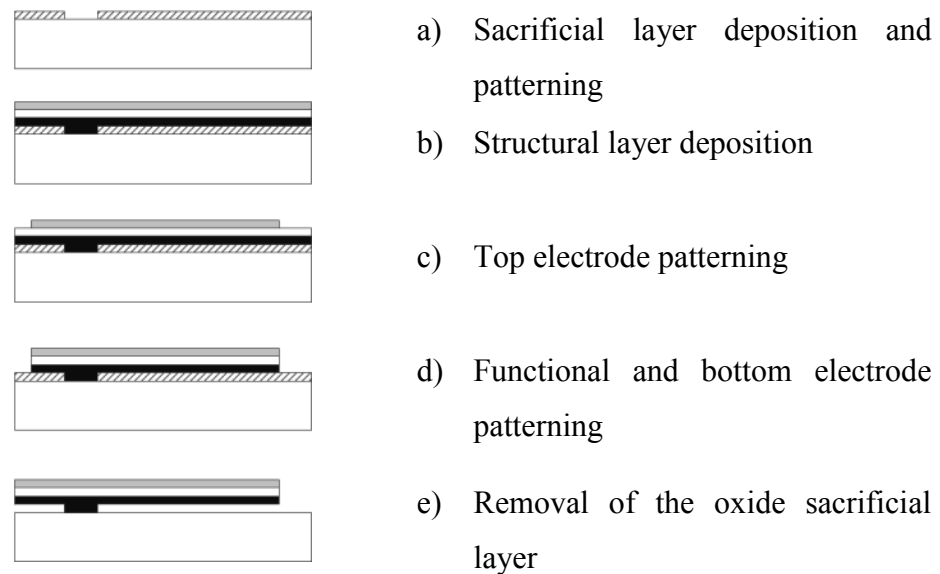
Figure 3-4: A simplified fabrication process of a piezoelectric cantilever using surface micromachining [75].

In work by *Saravanan et.al.* [75], wet oxidation was performed on a silicon wafer to obtain a sacrificial layer, followed by a patterning step to form the anchor position.

Polysilicon, aluminium nitride and chromium layers were individually deposited in the order stated on top of the SiO_2 layer to form the structural layers. These layers were etched to form the final shape of the cantilever. Finally, the SiO_2 sacrificial layer was removed and the cantilever is free to move. Figure 3-5 shows an SEM micrograph of cantilevers released from the silicon substrate after SiO_2 layer was removed by HF.
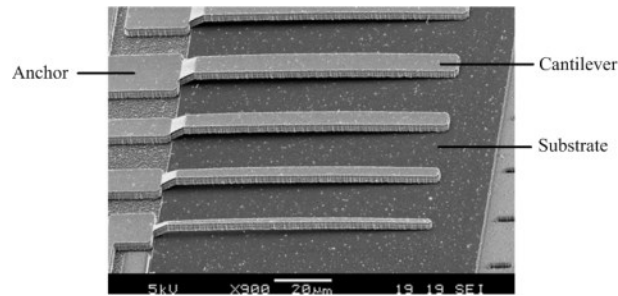
Figure 3-5: A SEM micrograph of surface micromachined cantilevers on a silicon wafer [75].

As well as inorganic materials, free standing structures can also be fabricated using polymer materials, such as SU-8 and polyimide. Due to the rheology of these materials, spin coating is normally employed to achieve a smooth and flat layer. A subsequent photolithographic process defines the cantilever shape. Depending on the fabrication process, an extra sacrificial layer may not be required. Etching directly into the silicon wafer can be used instead. Figure 3-6 shows examples of polymer cantilevers fabricated with SU-8 and polyimide.
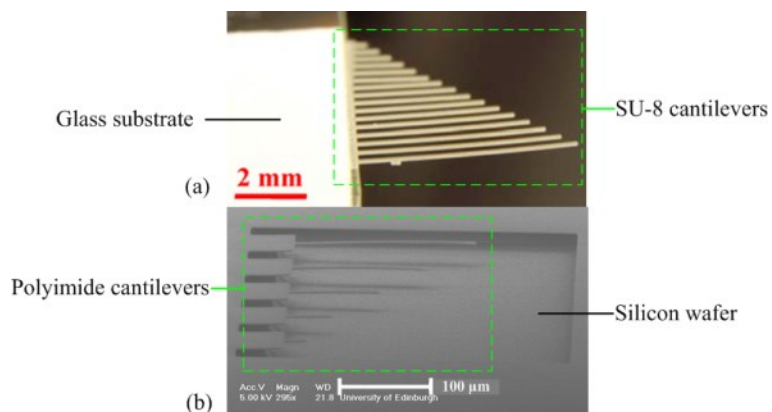
Figure 3-6: (a) SU-8 cantilevers at the edge of a glass wafer; (b) polyimide cantilevers on a silicon wafer [76, 77].

The fabrication processes described in this section are used with rigid substrates (e.g. silicon wafer). Neither bulk micromachining nor surface micromachining in their

standard form are compatible with fabrics because of their incompatible fabrication processes.

3.3.2 MEMS cantilevers on flexible substrates

Cantilevers fabricated on flexible substrates are rarely reported. Figure 3-7 shows the fabrication process of flexible cantilevers on a Kapton sheet by *Petroni et.al*. [78].
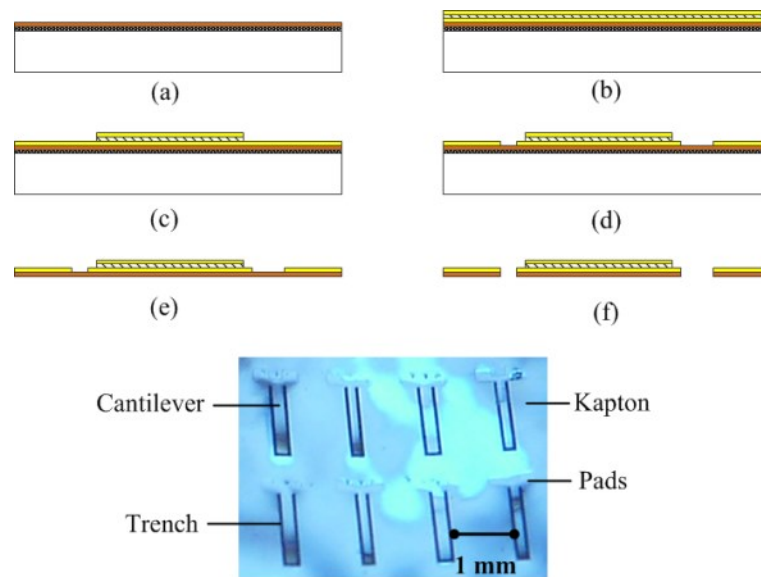
Figure 3-7: The fabrication process of flexible piezoelectric cantilevers on Kapton. [78].

The silicon wafer was used as a temporary supporting platform on which the Kapton film was attached using a thick silicone adhesive (a). Molybdenum/aluminium nitride (AIN)/molybdenum layers were individually sputtered onto Kapton in the order stated (b). Two masks were used to pattern the cantilevers. The first mask was used to define the top electrode and AIN layer by a dry etching, whilst the second mask was used to etch trenches into the bottom electrode layer (c and d). The sample was immersed in a hot isopropyl alcohol (IPA) bath for 1 hour to peel the Kapton film from the silicon wafer (e). Finally, the Kapton constraining the unreleased cantilever structures was processed by oxygen plasma for 50 minutes to etch Kapton through the trenches around the cantilever (f).

The feasibility of fabricating cantilevers on flexible substrates has been described but the fabrication processes, such as spin coating and dry etching, are not compatible with fabrics.

41

3.3.3 Printed cantilevers on rigid substrates

In chapter 2, screen printable sacrificial and structural materials used for fabricating free standing sensors and actuators on rigid substrates have been reported. Alumina tiles are often used as substrates as they can withstand high firing temperatures. In addition, they offer good adhesion and are rigid enough to withstand the tensile stress of the printed paste after curing [45].

Printed free standing structures can be achieved by using the same principle as surface micromachining in that structural and sacrificial materials are deposited on top of a substrate. However, screen printable materials are in a paste form and subsequent drying/firing processes are needed to solidify the materials. Therefore, the compatibility between materials should be carefully considered to avoid any chemical reaction. Several researchers have demonstrated the feasibility of using screen printing for the fabrication of free standing structures on alumina tiles. The process involves a sacrificial layer which must be unaffected by the subsequent printing and curing processes. Finally, this layer is removed by either thermal treatment or an etching process. Microfluidic chambers [28], simple cantilevers [29], bridges and cantilever with capacitive [31] and piezoelectric sensing mechanisms [79] have been achieved using these techniques. These applications are described in detail in the following sections.

3.3.3.1 *Ceramic-based pastes*

For a simple cantilever configuration, conductive pastes are used as the structural layer in conjunction with the sacrificial material. Ceramic pastes are used because these materials are strong enough after curing due to the typical properties of the ceramic. Figure 3-8 shows a simple gold ceramic cantilever on top of the alumina tile used for the evaluation of the sacrificial material by *Lucat et.al*. [29].
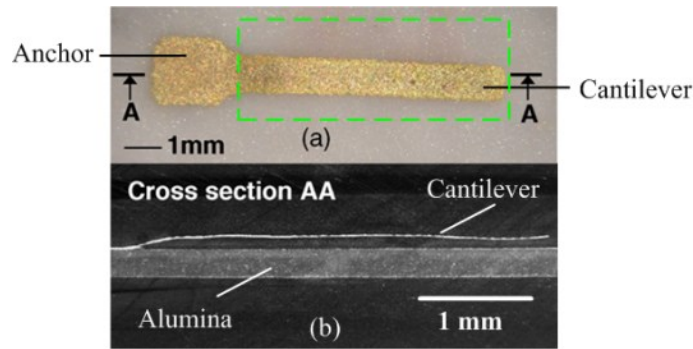
Figure 3-8: A photograph (a) and a SEM micrograph (b) of a ceramic gold cantilever on an alumina tile [29].

The $SrCO_3$ based sacrificial layer was printed onto an alumina tile and fired at 900 ^{o}C. The gold layer was printed on top and fired at 850 ^{o}C for 15 minutes. The entire sample was then immersed into H_3PO_4 solution to release the gold cantilever. It is shown that the sacrificial layer was removed and the gold cantilever was able to support itself on top of the alumina tile.

Another example using a conductive paste as the structural material is also given in [29]. They fabricated a free standing copper electrothermal actuator cantilever structure. It consists of two cantilevers with different widths, connected at the end. Figure 3-9 illustrates the copper actuator and its cross-sectional SEM micrograph.
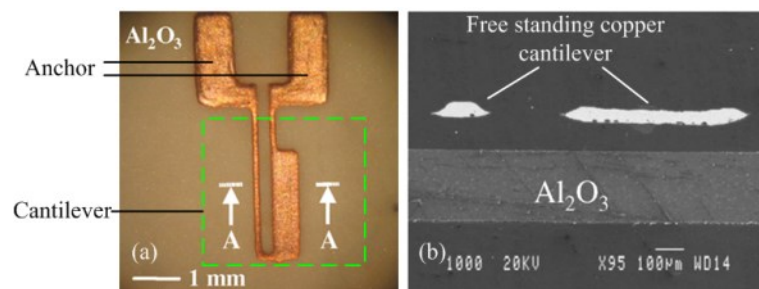
Figure 3-9: (a) A photograph and (b) a SEM micrograph of a copper free standing electrothermal actuator [29].

The actuator was fabricated by screen printing the ceramic copper paste on top of a printed sacrificial layer on an alumina tile. This was followed by a firing step at 900 ^{o}C to solidify the printed copper paste. The free standing copper layer was then released from the substrate in an acidic solution (H_3PO_4) and had enough strength to support itself above the substrate. It is shown that the two cantilevers with different widths are fully released and are free standing on top of the alumina tile.

The above are examples of cantilevers that use a single conductive material. Dielectric materials are an alternative approach to create free standing cantilevers. *Lakhmi et.al.* [46] reported screen printed cantilevers using a ceramic dielectric material for use as force sensors. A piezoresistive material was printed at the clamped end of the cantilever, where a maximum stress variation was produced when the cantilever vibrated.

(a) Sacrificial and dielectric pad deposition

(b) Deposition of cantilever beam

(c) Deposition of piezoresistive layer

(d) Sacrificial layer removal

Gold pads —

— Dielectric cantilever

— Piezoresistive layer
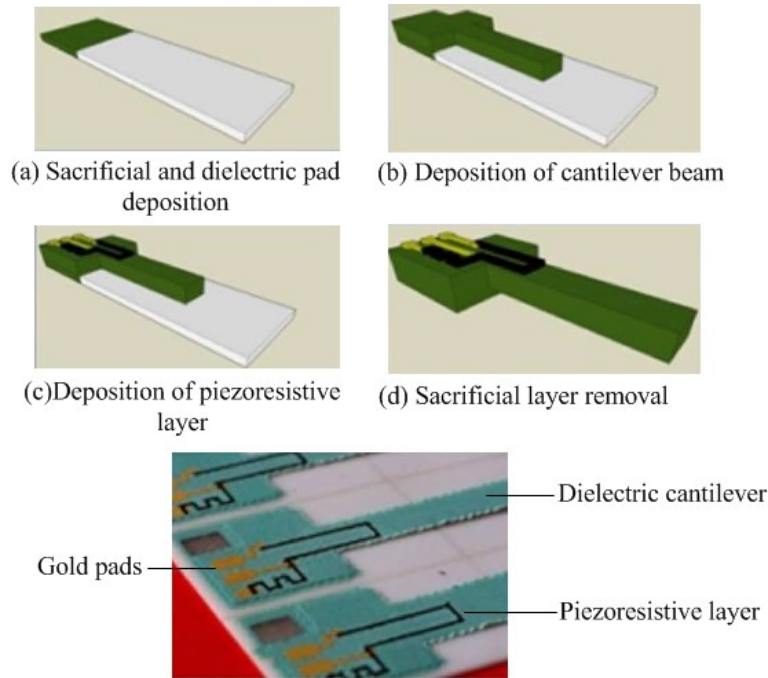
Figure 3-10: Screen printing process of a cantilever force sensor based on ceramic pastes [46].

Figure 3-10 shows the fabrication steps of a screen printed cantilever on an alumina tile. The dielectric pad and sacrificial layer were printed and dried (a). A cantilever design was then printed on top of the sacrificial layer (b) followed by the piezoresistive sensing structure including gold electrodes and a sensing layer (c). Samples were fired at 850 $^{\circ}$C for 10 minutes to solidify the layers and the sacrificial layer was removed in an acidic solution (d). Results showed that the cantilever was fully released from the substrate.

Functional pastes, such as PZT, can also be used as the cantilever layers. *Kok et.al.* [79] reported free standing cantilever structures for harvesting vibration energy that are based on ceramic PZT and Ag/Pd pastes with firing temperatures above 850 $^{\circ}$C. They are shown in Figure 3-11.
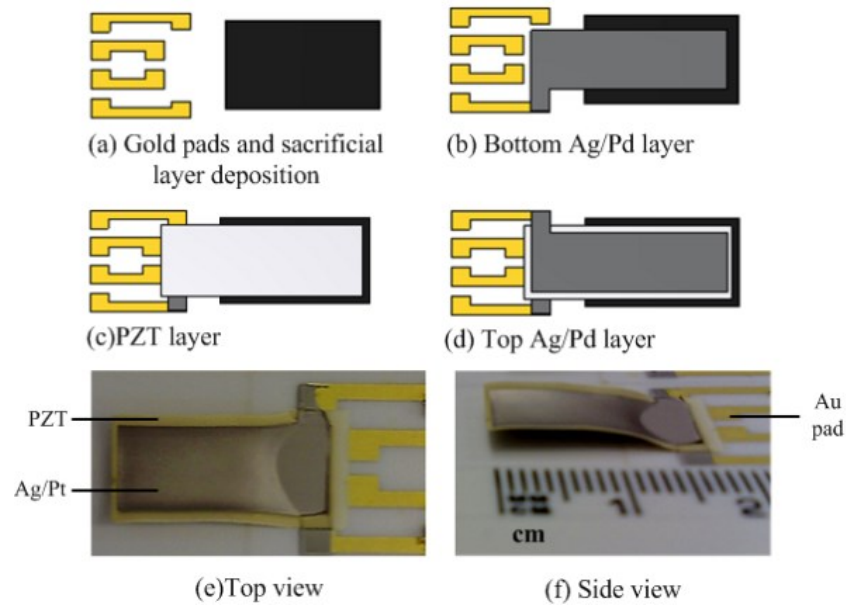
Figure 3-11: Fabrication steps of a free standing piezoelectric cantilever on the alumina tile [45].

During the firing step at 850 ^{o}C, the PZT and Ag/Pd layers were released from the alumina tile when the sacrificial layer was removed. However, the sample was slightly bowed along the spine of the cantilever due to the thermal mismatch between the PZT and Ag/Pd layers [79].

The ceramic pastes described in this section cannot be used for smart fabric applications because their incompatible firing temperature, in excess of 800 ^{o}C, will destroy any fabrics.

3.3.3.2   *Polymer based pastes*

Polymer materials can be used for fabricating free standing cantilevers and have the advantages of low curing temperatures and compatibility with most substrates. *Serra et.al.* [31] demonstrated polymer cantilevers screen printed onto a sacrificial layer on an alumina tile for the evaluation of a sacrificial material. The polymerisation of the polymer material occurs at 80 ^{o}C, which is much lower than for ceramic pastes. The cantilevers are shown in Figure 3-12.
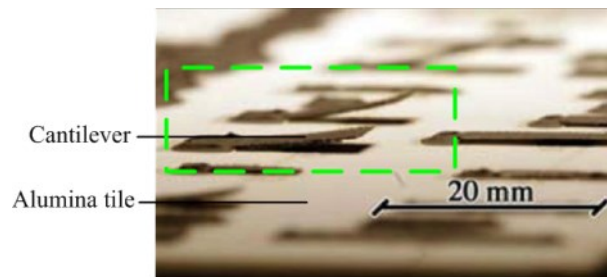
Figure 3-12: Ethyl cellulose based cantilever printed on top of an alumina tile [31].

The cantilever was made of an ethyl cellulose solution loaded with graphite powder to improve the mechanical strength. This paste was cured at 80 ^{o}C and the subsequent sacrificial removal process took place at 150 ^{o}C. Due to the sublimation mechanism of the removal, the stiction phenomenon was avoided. Polymer materials also reduce the likelihood of thermal mismatch compared with materials cured at high temperature.

Inkjet printing is an alternative deposition technique to deposit inks onto a rigid substrate using inks (1-20 mPa.s). Free standing structures created using inkjet printing were reported by *Fuller et.al.* [80]. Figure 3-13 illustrates the fabrication process and the final cantilever released from the substrate.
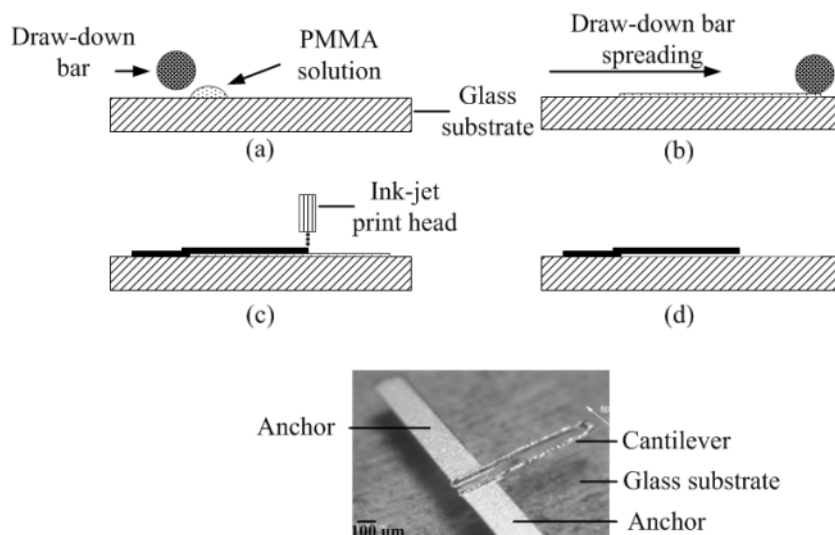
Figure 3-13: The fabrication process of an ink-jet printed free standing cantilever structures used as heatuators [80].

The glass substrate was prepared by coating 50% PMMA solution using a draw-down bar which was suspended 100 μm above the substrate (a-b). The substrate was then placed on a hotplate under the inkjet print head and the temperature was maintained at

250 ^{o}C. Next, a silver colloidal nanoparticle ink was inkjet printed on top of the PMMA layer to form the cantilever shape (c). Once the printing was complete, the sample was sintered at 300 ^{o}C for 10 minutes followed by sonication in an acetone bath to remove the PMMA layer (d). However, this method cannot be used for fabric applications for three reasons:

o It is not possible to apply the PMMA sacrificial layer onto fabric with a precise thickness;

o It is difficult to maintain the printing temperature at 250 ^{o}C because the fabric could not survive at this temperature;

o The sintering temperature of the silver ink is 300 ^{o}C at which the fabric will be damaged.

3.3.4 Printed cantilever structures on flexible substrates

To the best of the author`s knowledge, printed cantilever structures on flexible substrates have never been reported in the literature.

3.3.5 Printed cantilever structures on fabrics

To the best of the author`s knowledge, printed cantilever structures on fabric substrates have never been reported in the literature.

3.3.6 Discussion

Table 3-2 compares the free standing cantilever structures realised using silicon microfabrication and printing techniques.

Table 3-2: Comparison between MEMS cantilevers and printed cantilevers

	MEMS cantilever	*Printed cantilever*
Material selection	Solid:	Pastes:
	Inorganic material or organic material	Ceramic or polymer materials
Material curing	Only polymer materials	Yes
Substrate selection	Silicon, glass, Kapton	Alumina tile
Fabrication approach	Bulk micromachining	Screen printing
	Surface micromachining	Ink-jet printing
Photolithography	Yes	No
Subsequent removal	Yes	Yes
Dimension	Microscale	Macroscale
Functionality	Capacitive	Capacitive
	Piezoelectric	Piezoelectric
	Piezoresisitive	Piezoresisitive

MEMS cantilevers using inorganic materials do not need an additional curing step to solidify the deposited inorganic materials, as the materials are in a solid form once they are deposited. Silicon wafers must be used in bulk micromachining, whereas surface micromachining does not limit to silicon wafers as the entire structure is composed of deposited rather than substrate materials. Both fabrication processes require a photolithographic step to define the cantilever pattern. Subsequent developing and etching processes realise the free standing cantilever from the substrate. By combining different functional materials with the cantilever layer, a variety of functions can also be incorporated in the mechanical structure, thus broadening the use of the cantilever.

Screen printed layers require a curing step to solidify deposited layers before printing subsequent layers. Ceramic pastes need high curing temperatures in excess of 800 $^{\circ}$C which are unsuitable for fabrics, whilst polymer pastes are cured at a relatively low temperature (<200 $^{\circ}$C) but all reported polymer cantilevers are fabricated on rigid substrates (i.e. alumina). Importantly, the screen printing process does not need photolithographic and developing processes to define the cantilever because the design is formed by the screen, thereby reducing the complexity of the fabrication. The

availability of a wide variety of functional pastes, such as piezoelectric, conductive, piezoresistance and electroluminescent pastes, also broadens the available functions of screen printed cantilevers. To the best of the author`s knowledge, there is no relevant prior research on screen printed cantilever structures for either flexible substrates or fabrics.

3.4 Pump structures

Micropumps contain actuators and are used for the transportation of fluids. There are a large variety of operating mechanisms with a variety of actuation elements available to control the precise pumping volume from microscale to macroscale. These offer pumping volumes from several microliters to several millilitres per minute. According to *Nguyen`s* definition [81], micropumps generally fall into one of two classes: mechanical pumps and non-mechanical pumps. Mechanical pumps use movable parts such as valves and oscillating membranes to deliver a constant fluid volume in each pump cycle. Non-mechanical pumps are based on a direct transfer of energy into the movement of the fluid in the form of kinetic energy. Figure 3-14 shows the categorisation of micropumps based on the driving mechanisms.
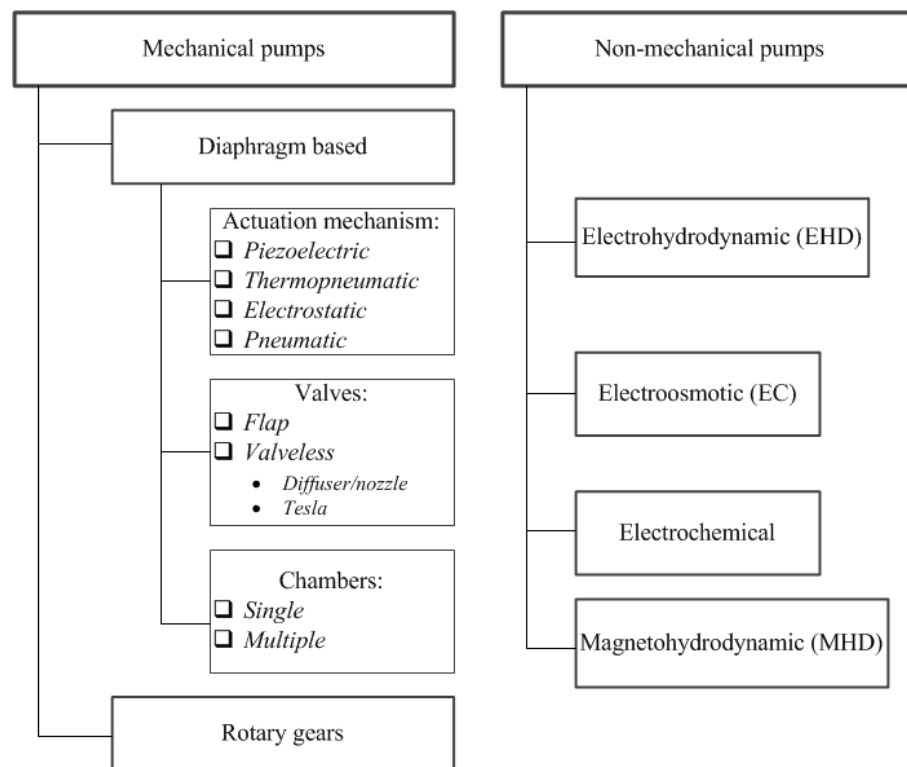
Figure 3-14: Classification of MEMS pump structures [81].

In diaphragm based mechanical pumps, movements of the diaphragm generate a volume change resulting in a pressure change in the chamber. The pumping mechanism can be divided into a supply mode and a pumping mode. During the supply mode, under-pressure is generated in the chamber to fill it with fluid. Usually, the fluid is sucked into the chamber through the inlet while the outlet blocks the backwards flow, though it is also possible the fluid to be sucked from both inlet/outlet in a pump with static valves. During the pumping model, overpressure in the chamber squeezes the fluid to the outlet while the inlet blocks any reverse flow. The common mechanical pumps are check valve, valveless, peristaltic and rotary.

In contrast to mechanical pumps where moving parts drive the pumping effect, non-mechanical micropumps do not need movable parts or use mechanical force to obtain the fluid movement. Non-mechanical pumps use an energy conversion between the external energy, such as electrical and magnetic field, and kinetic energy in the fluid. The external energy provides a steady flow by continuously moving the fluidic ions. In electrochemical pumps, gas bubbles generated from the electrolysis of water are used to push the liquid in the desired direction. The common driving mechanisms are electrohydrodynamic (EHD), electroosmotic (EO), electrochemical and magnetohydrodynamic (MHD) [81, 82].

3.4.1 MEMS pump structures on rigid substrates

3.4.1.1 Mechanical pumps

The main advantages of microfabricated micropumps are the high precision and reproducibility achievable with the materials in use, mainly silicon wafers and glass substrate. Mechanical pumps require flow rectification to produce net flow because these pumps are mechanically symmetric. Valves are necessary to rectify the flow. The valve can be classified by working principle into dynamic geometries and static geometries. Dynamic geometric valves use structural deformation to control flow direction (e.g. check valves), whereas static geometric valves employ a fixed geometry to rectify the flow direction (e.g. diffuser/nozzle). Table 3-3 summarises the common mechanical pumps in MEMS.

Table 3-3: Summary of common mechanical micropumps in MEMS.

Year	Pump type	Pumping mechanism	Pumping media	Fabrication process	Ref
1988	Check-valve	Piezoelectric	Liquid, air	Bulk micromachining, Anodic bonding	[83]
1990	Check-valve	Thermo-pneumatic	Liquid	Bulk micromachining, Anodic bonding	[84]
1995	Check-valve	Electrostatic	Liquid	Bulk micromachining, Bonding	[85]
1995	Rotary	Mechanical movement	Liquid	LIGA	[86]
1996	Valveless	Piezoelectric	Liquid, air	Bulk micromachining, Anodic bonding	[87]
1998	Check-valve	Shape memory alloy	Liquid	Bulk micromachining, Bonding	[88]
2000	Valveless	Thermo-pneumatic	Liquid	Bulk micromachining, Anodic bonding	[89]
2003	Check-valve	Pneumatic	Liquid	Bulk micromachining Bonding	[90]
2004	Peristaltic	Pneumatic	Liquid	Surface micromachining/ Molding	[91, 92]

Check valve micropumps have been widely reported in the literature. In most cases, bulk micromachining and bonding processes are used to fabricate these micropumps. Figure 3-15 shows the pumping principle of a check valve pump.
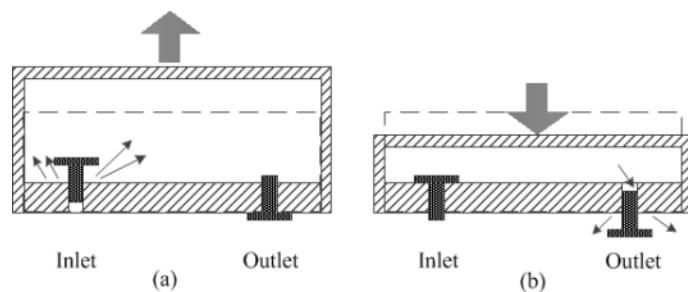
Figure 3-15: Schematic diagram of pumping principle of a check valve pump: (a) supply mode; (b) pumping mode.

When the diaphragm deflects, the chamber expands or compresses resulting in a corresponding pressure change in the chamber. During the supply mode, the chamber pressure is lower than the inlet pressure, thus the inlet valve is open whilst the outlet valve is closed thereby blocking the reverse flow. During the pumping mode, the chamber pressure is higher than outlet pressure and therefore the outlet valve is open and the inlet valve is closed. This generates a net flow from the inlet to the outlet. The first micromachined check-valve micropump was demonstrated by *Lintel, et.al.* [83] in 1988; the pump was fabricated by anodically bonding two glass discs with a silicon wafer on which pump components had been etched. A piezoelectric disc was glued on top of the glass membrane to form the actuation mechanism. The valves only allow flow in one direction. A pumping effect was achieved when the piezoelectric disc was actuated. Researchers have also demonstrated thermo-pneumatic, pneumatic, electrostatic and shape memory alloy actuation mechanisms in check valve micropumps [84, 85, 88, 90]. Problems with moving valves in micropumps are wear and fatigue. Also, small particles can block the valves resulting in a poor pumping performance.

To overcome these problems, valveless micropumps were developed. The structure of valveless micropumps is similar to that of check valve pumps, but instead of using dynamic valves the pump mainly uses static geometry (e.g. diffusers/nozzles and the Tesla valve [87]). The pump is still driven by a membrane. Figure 3-16 shows two types of static geometries used in valveless micropumps. The direction of flow is determined by the geometry.
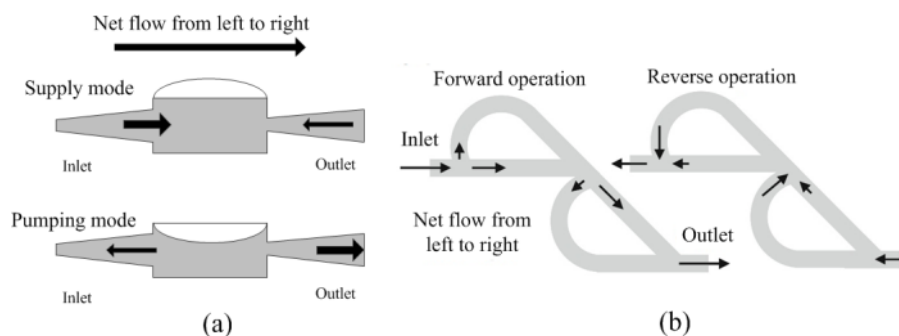
Figure 3-16: Schematic diagrams of static valves used in valveless pump structures. (a) diffuser/nozzle; (b) Tesla [93].

The pump operation is based on the fluid flow rectifying properties of the fixed geometric valves which ensures that the forwards flow is always greater than the

backward flow resulting in a directional net flow. The first valveless micropump was demonstrated by *Stemme et.al.* in 1993 [94] using diffusers and a chamber machined into brass. Further development of the valveless pumps in silicon was demonstrated by several other researchers with the first valveless micropump fabricated on a silicon wafer reported by *Olsson et.al.* [87]. In this research, the chamber and diffusers were isotropically etched into silicon. The silicon wafer was then anodically bonded with a glass wafer to form entire pump structures. Piezoelectric discs were glued onto the diaphragm to provide an actuation mechanism.

The peristaltic pump is based on the peristaltic motion of pump chambers, which are operated in sequence to generate a directional flow. Typically, at least three chambers are required to achieve the pumping effect. Figure 3-16 illustrates the pumping principle of a peristaltic pump.
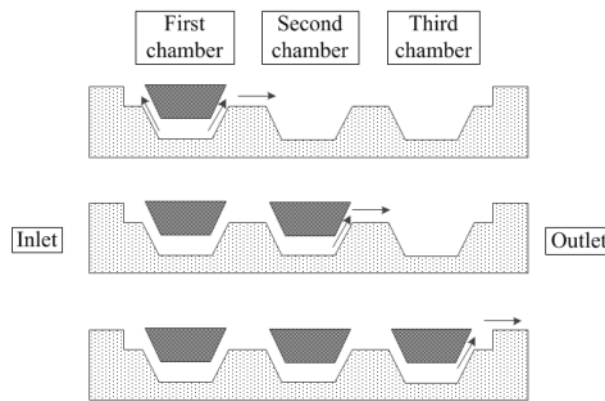
Figure 3-17: Schematic diagram of a peristaltic pumping mechanism.

When the first diaphragm is squeezed, the fluid is pushed towards the second chamber, whilst the flow to the inlet of the pump is blocked. As the second diaphragm is squeezed, fluid is pushed towards the third chamber. Finally, as the third diaphragm is squeezed, fluid is pushed through the outlet of the pump. These chambers can be fabricated by using either bulk micromachining so that the pump structures are anisotropically etched into the silicon wafer [95], or surface micromachining so that the channels and chambers are created on top of the substrate [92]. Moulding can also be used as a fabrication method where PDMS is used as a structural material [96].

A small number of rotary pumps have been reported. Fabricating a rotary pump is difficult because minimising the gap between two gears in microscale is a major

challenge. Rotary pumps normally involve a set of gears which squeezes the fluid towards the outlet. It has the advantage of being able to pump viscous liquids [97]. Figure 3-18 shows an example of a rotary pump fabricated by LIGA (Lithographie, Galvanoformung, Abformung) technique.
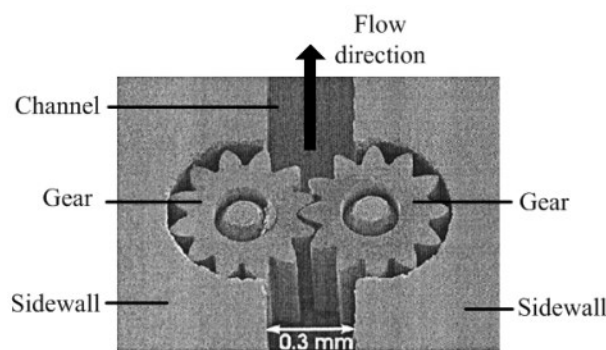
Figure 3-18: An SEM micrograph of a rotary pump with two gears [97].

3.4.1.2 Non-mechanical pumps

Non-mechanical pumps fall mainly into four main categories, which are Electrohydrodynamic (EHD), Magnetohydrodynamic (MHD), electroosmotic (EO) and electrochemical. As described before, these pumping mechanisms do not need movable parts and provide a continuous flow. Table 3-4 summarises the common non-mechanical pumps in MEMS.

Table 3-4: Summary of common non-mechanical micropumps in MEMS.

Pump type	Fabrication	Pumping media	Driving voltage	Ref
Electrohydrodynamic (EHD)	Bulk micromachined	Dielectric liquid	600Vd.c.	[98]
Electroosmotic (EO)	Bulk micromachined	Conductive liquid	2000Vd.c.	[99]
Electrochemical	Bulk micromachined, Anodic bonding	N/A*	N/A*	[100]
Magnetohydrodynamic (MHD)	Bulk micromachined, Anodic bonding,	Conductive liquid	~6V	[101]

*Information is undisclosed.

Electrohydrodynamic (EHD) micropumps are based on the interaction of electrostatic forces with ions in dielectric fluids. They often use an electric field to pull ions into the

pumping channels, in turn pulling the bulk fluid by momentum transfer due to viscosity [102]. The correct operation of these micropumps requires the existence of space charge in a dielectric fluid. As reported in [98], a maximum driving voltage of 600 V was applied between two electrodes to provide the pumping effect. The driving voltage could be reduced by reducing the gap between two electrodes but it is challenging due to fabrication limits. In contrast to EHD pumps, electroosmotic (EO) pumps pump conductive liquid but they need a higher driving voltage compared with EHD pumps. Sometimes the voltage can reach up to 10 kV [103]. Electrochemical pumps use the gas bubbles generated from an electrolysis reaction in water. These pumps typically consist of a pair of electrodes placed in a reservoir which is connected to a channel filled with the liquid to be pumped. When a voltage is applied, oxygen and hydrogen bubbles are generated. These bubbles are then used to push the liquid in the channel to induce flow. Magnetohydrodynamic (MHD) pumps exploit the Lorentz force which is generated when a current-carrying conductor is placed in the magnetic field, resulting in a flow direction perpendicular to both the magnetic and electric fields [93]. In general, the highest flow rate is obtained when current density, magnetic field intensity and electrode length are maximised. However, increasing the magnetic field requires a superconductive magnet which is several meters high [104].

3.4.2 MEMS pump structures on flexible substrates

Chen et.al. [105] demonstrated an electrohydrodynamic (EHD) micropump fabricated on a flexible Parylene substrate, shown in Figure 3-19.
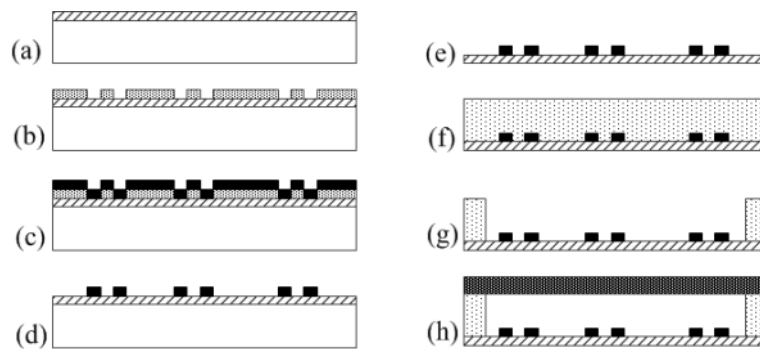
Figure 3-19: Fabrication processes of an EHD pump on a flexible Parylene substrate [105].

Parylene was first deposited onto a silicon wafer (a), followed by a patterned photoresist layer (b). Metal was then evaporated onto the photoresist layer (c). Next, the photoresist layer was peeled from the substrate by hand, leaving the metal layers directly deposited onto the Parylene (d). The entire structure was the peeled from the silicon wafer (e). An SU-8 layer was spin coated and patterned to form the channel walls (f-g). Finally, a PDMS cover layer was bonded on top of the substrate to build an enclosed channel (h). The results are shown in Figure 3-20.
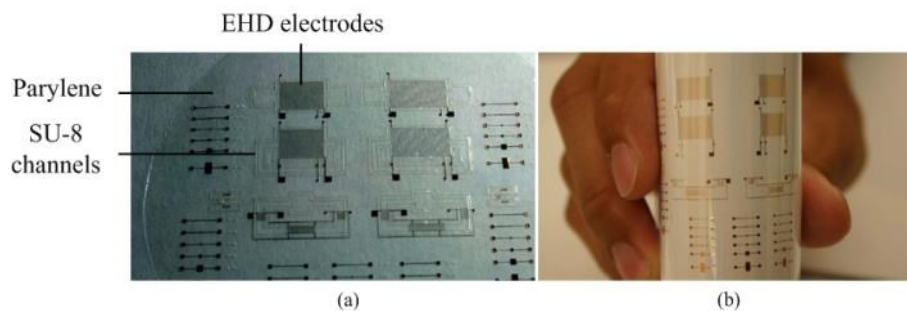
Figure 3-20: (a) photographs of the samples; (b) bending around a paper rod [105].

The defining properties of an EHD micropump are the dimensions and arrangement of the electrodes. In this experiment, the width of the electrode was designed to be 10 μm and the space between two electrodes was 20 μm. These dimensions are difficult to achieve using screen printing technique when used on fabrics. The pump liquid is limited to dielectric materials. As a result, IPA (isopropyl alcohol) was used.

Jahanshahi et.al. [106] demonstrated an electroosmosis micropump which was fabricated by bonding two PDMS layers together forming a flexible micropump. Figure 3-21 shows the simplified fabrication process.
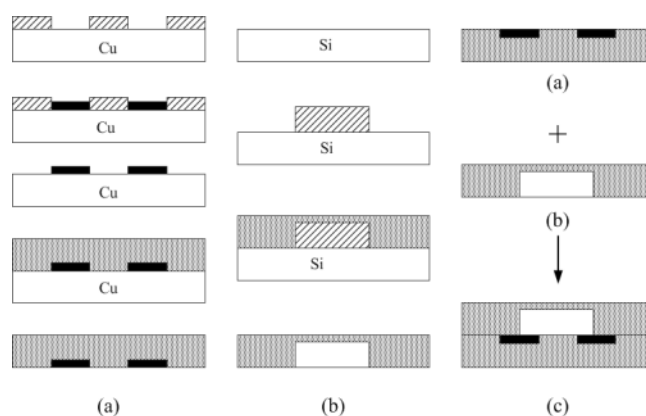
Figure 3-21: The fabrication process of an electroosmosis micropump [106]).

56

A gold layer was deposited and patterned on top of the copper layer followed by casting a PDMS layer to form the bottom electrode layer (a). A photoresist layer was deposited and patterned on a separate silicon wafer followed by casting a PDMS layer to form the channel of the pump (b). Finally, the two PDMS layers were individually peeled from their substrates and bonded together to form the micropump (c). The results are shown Figure 3-22.
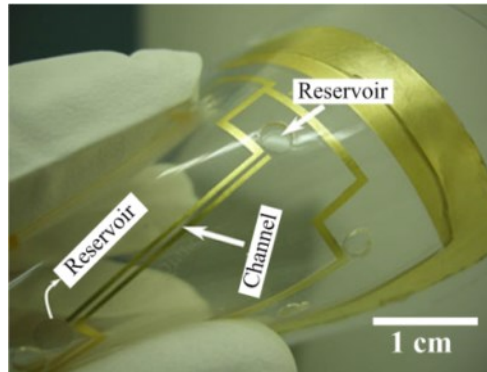
Figure 3-22: Photograph of the electroosmosis micropump [106].

Even though the pump is flexible, the fabrication processes, such as spin coating, etching and casting processes, are not compatible with the fabric applications.

3.4.3 Printed pump structures on rigid substrates

To the best of the author`s knowledge, printed pump structures on rigid substrates have never been reported in the literature.

3.4.4 Printed pump structures on flexible substrates

To the best of the author`s knowledge, printed pump structures on flexible substrates have never been reported in the literature.

3.4.5 Printed pump structures on fabrics

To the best of the author`s knowledge, printed pump structures on fabric substrates have never been reported in the literature.

3.4.6 Discussion

Table 3-5 compares the existing micropumps in MEMS with emphasis on fabrication and configuration.

Table 3-5: Comparison of micropumps in MEMS (*based on the fabrication*).

Pump type	Valve	Minimum chamber	Common actuation	Fabrication*	Substrate	Driving voltage
Check valve	Yes	1	Piezoelectric Electrostatic	Bulk, bonding	Silicon Glass	50-300 V
Valveless	No	1	Piezoelectric	Bulk, bonding	Silicon Glass	50-300 V
Peristaltic	Varying	3	Piezoelectric	Bulk/ surface	Silicon Glass Polymers	50-300 V
Rotary	No	N/A	External motor	LIGA	Silicon	N/A
EHD	No	N/A	Electrical field	Bulk, bonding	Silicon Polymers	40-600 V
Electroosmotic	No	N/A	Electrical field	Bulk, bonding	Silicon Glass Polymers	N/A**
Electrochemical	No	N/A	Electrolysis	Bulk, bonding	Silicon	N/A
MHD	No	N/A	Magnetic field	Bulk, bonding	Silicon Glass	<50 V

*Bulk: bulk micromachining, surface: surface micromachining, bonding: anodic bonding.
**The driving voltage varied from 50 V to 8000 V.

Most mechanical pumps have a movable membrane to change the chamber pressure, thereby driving the liquid through. To ensure the pump flow is always unidirectional, several configurations are applied. Check valve pumps use two valves located in the inlet and outlet to prevent reverse flow. The core of these valves can be a simple cantilever or a diaphragm ring with elastic supports. These valves have problems with wear, fatigue and blockage. Valveless pumps instead use fixed geometric valves which cause different flow rates from each sides of the diffuser. The fabrication process for valveless micropumps is less complicated than check valve pumps. Peristaltic pumps typically use at least three chambers to generate a directional flow but the driving frequency is normally low. The rotary pump is advantageous for pumping viscous liquid but it has a complicated mechanical structure and also requires an external motor as the driving source. Non-mechanical pumps strongly rely on specific properties of driving liquid thus limiting the use of these pumps. The fabrication processes of these

micropumps are not compatible with the fabric. In addition, because of high voltage (EHD and EO), high magnetic field (MHD) and liquid environment (electrolysis), it is difficult to implement these mechanisms on fabrics. To the best of the author`s knowledge, there is no literature on printed pump structures on rigid or flexible substrates.

3.5 Conclusions

Smart fabrics as an emerging technology have been reviewed. Conventionally, smart fabrics are formed by incorporating functional yarns into the fabric structure to form planar sensing and actuating structures as well as interconnections. These techniques are suitable for the fabrication of planar layouts because they can be used to create the same patterns in a large scale fabrication process. However, these fabrication techniques require significant initial machine setup time and yarn preparation. In addition, weaving and knitting yarns must follow the entire length of fabric warp and weft structures and therefore the design is limited to orthogonal orientations. It is also not possible to achieve multiple layers with different material combinations, thus restricting the range of device applications.

This chapter also reviewed free standing cantilever structures and their fabrication processes. The cantilever is the basis of a number of sensing and actuating mechanisms and it has a simple mechanical structure compared with other free standing structures. Most cantilever structures reported in the literature are fabricated using conventional silicon microfabrication. Alternatively, free standing cantilevers can be achieved by screen printing on alumina tiles. Screen printing process does not require photolithography steps, except for the initial screen manufacturing, thereby reducing the time spent on the fabrication. However, most screen printed cantilevers reported in the literature are based on ceramic pastes which have a high curing temperature in excess of 800 ^{o}C which would be unsuitable for the majority of garment fabrics. The curing temperatures of polymer pastes reported in the literature (< 100 ^{o}C) are compatible with the fabric but the performance of these pastes on flexible substrates has not been reported.

In previous studies, pumps are mainly fabricated on rigid substrates, while research on flexible substrates is not often presented. There are currently no examples of pump structures fabricated using only screen printing reported in the literature. Compared with other pump types, valveless micropumps have a simple mechanical structure. They can be combined with different actuation mechanisms thus making them suitable for various applications. Their simple structure also makes it possible to fabricate them by screen printing in a layer by layer process.

To date only planar structures have been demonstrated for smart fabric applications and no attempts have been reported to achieve free standing structures on fabrics. By using the materials developed in this research, the feasibility of realising free standing structures, e.g. cantilevers and micropumps, on fabrics will be demonstrated using only screen printing.

Chapter 4

Screen printable sacrificial materials

4.1 Introduction

This chapter evaluates several potential sacrificial materials, which are selected based on the literature described in chapter 2. The materials reported herein are examined based on their appropriateness for use as the sacrificial material for fabricating free standing structures on fabric.

Water and thermal removal mechanisms are chosen because the curing and removal conditions reported in the literature do not damage the fabric. The water soluble materials selected are Sucragel and Dextran as they each have a relatively low curing temperature. The reported viscosities are too low to screen print so increasing the viscosity is a prerequisite to using these materials.

The plastic crystal materials Neopentyl glycol (NPG), Trimethylolethane (TME) and Trimethylolpropane (TMP) are examined as candidates of thermally removable materials because these materials can be removed through a sublimation mechanism which reduces volume deformation and stiction problems. The problems with these plastic materials are the brittle and hygroscopic properties, which affect the printing quality, thus a thorough investigation of these properties, including the ease of formulation to a screen printable paste, printability and the ease of removal, are

conducted. After an initial investigation of the curing and removal conditions, the selected materials are optimised to minimise damage to the fabric substrate.

4.2 Screen printing and paste formulation process

4.2.1 Equipment and the printing process

A screen printer is a key piece of equipment for depositing materials onto the substrate. A good screen printer is able to repeatedly print the paste through a patterned screen and be able to adjust squeegee speed, pressure and the snap off distance. A schematic diagram of the printing sequence is shown in Figure 4-1.
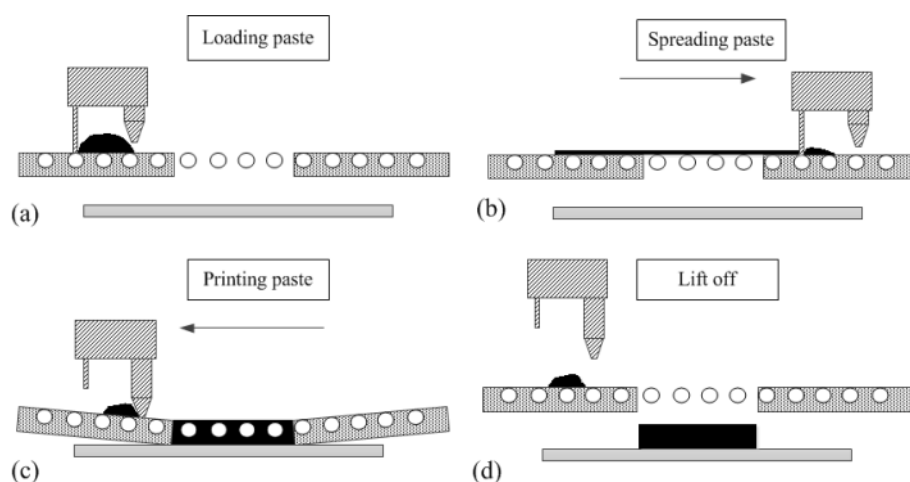
Figure 4-1: General screen printing step: (a) paste loading; (b) paste flooding; (c) paste printing; (d) screen lifting off.

A typical printing step involves loading the paste on top of a screen with an appropriate gap (a) and spreading the paste over the screen using a flood blade (b). A printing squeegee is then applied with appropriate speed and pressure to force the paste through the opening areas (i.e. designs) on the screen (c). The printing process should provide a complete pattern on the substrate so that the movement of the flood blade and printing squeegee should cover entire printing areas. Finally, the screen is lifted off from the substrate leaving the printed patterns behind (d). In this research, a DEK 248 semi-automatic screen printer is used to provide a consistent printing result because the squeegee pressure and speed are controlled by the machine. A stainless steel flood blade and polyurethane printing squeegee are used to spread and print the paste, respectively.

Curing equipment, such as a conventional box oven and UV cabinet are required to solidify the printed materials. The selection of curing equipment is dependent on the kind of the materials, such as polymer or ceramic materials. A box oven (Carbolite PF30) with a maximum temperature of 300 ^{o}C and a UV 400W curing system (UV light technology limited) is used in this research for thermally curable and UV curable materials, respectively.

A triple-roll mill has three metallic rolls geared together and is used to break down large solid agglomerates that may exist in the paste and provides a more homogeneous paste than standard mixing. The paste is passed through the mill several times to obtain a more homogeneous paste. The triple roll mill used in this research is EXAKT 50.

4.2.2 Paste properties

To deposit a material onto a substrate using screen printing, the deposited material should be in a paste form which flows easily during the printing. The definition of 'paste' is different from 'ink' in that paste is commonly used to describe a material which has a high viscosity, such as honey, whereas ink refers to a material with low viscosity which easily flows, such as water.

Paste used in screen printing should be thixotropic, meaning that the viscosity decreases over time at a constant shear strain rate [107]. This means the viscosity changes during the printing process. The decreased viscosity allows the paste to easily flow through the screen mesh when the squeegee pressure is applied. After the printing process, the paste viscosity returns to its original value preventing paste from bleeding over the substrate. The viscosity range of a screen printable paste varies from 1 Pa.s to 10 Pa.s because the viscosity tolerance of the paste can be much greater in screen printing than other printing techniques [108].

4.2.3 Components of a paste

A screen printable paste is composed of four standard components according to *Dorey et.al.*[109]. These are described here.

4.2.3.1   Functional material

This part is composed of the functional material to be deposited. Examples include conductive materials (e.g. silver flakes), dielectric materials (e.g. alumina powder) and piezoelectric materials (e.g. PZT powder). Materials used for this part should be able to survive the curing temperature.

4.2.3.2   Binder part

A binder is used to bond functional particles together during the curing process. The selection of the binder is important because the binder will affect the properties of the paste, such as the viscosity and solubility. For the ceramic paste, this part is normally used to bond functional material particles during the firing process. As a result, a fine glass powder (e.g. glass frit) is generally used as a binder [110]. The glass binder will melt at a specific temperature bonding the functional material together. For polymer pastes, the binder part is typically a polymer which solidifies either at a relatively low temperature (e.g. < 300 ^{o}C) or due to UV light exposure.

4.2.3.3   Carrier part

The carrier normally refers to the solvent in which the functional material is mixed or dissolved. The correct choice of the solvent is critical as this dominates the chemical properties of the final paste. For screen printing, a solvent with a reasonably high boiling point is recommended because it will not evaporate too fast during the transport and the printing process. A solvent with a low boiling point will evaporate quickly resulting in a fast drying material. However, the boiling point cannot be too high because the paste may not be dried at a given temperature and curing time resulting in a wet layer. For solid loaded pastes, the carrier is mixed with the functional part to achieve a desired viscosity, whereas for liquid loaded pastes the functional material is dissolved into the carrier forming a homogeneous mixture.

4.2.3.4   Modifier

Modifiers describe the components of the paste which improve the printability, such as dispersants that are usually used to prevent the agglomeration of functional particles. Typically, a relatively small quantity (<1%) of modifier is required.

4.3 Initial investigation into screen printable materials

Each material will be evaluated based on a progressive procedure, shown in Figure 4-2.
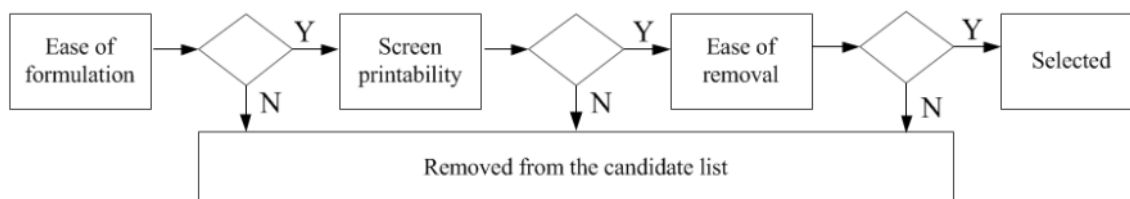
Figure 4-2: The evaluation processes for candidate screen printable materials.

The first stage is to evaluate the ease of formulation of these materials into a paste. The material should be able to be dissolved or mixed with corresponding solvent(s) to form a homogenous paste without agglomeration or separation. If the materials pass the first stage, the second stage involves depositing formulated pastes onto the substrate using screen printing, either with a mesh or stencil screen. Deposited pastes must be cured at a given temperature or other curing mechanisms to form a solid layer. If the materials can be printed and dried, the last stage is to evaluate the removal result in which the printed material should be removed by their corresponding mechanism, such as water or thermal energy. If the materials pass all stages, they will then be selected as the sacrificial materials.

4.3.1 Dextran

Dextran is a high molecular weight glucose and is easily soluble in water, methyl sulphoxide, formamide, ethylene glycol and glycerol because of its hydroxyl (-OH) groups [12]. A single Dextran molecule has a formula of $HO(C_6H_{10}O_5)_nH$, with the molecular weight increases as n is increased. Figure 4-3 shows the molecular structure of a single Dextran group ($n=1$) which includes five hydroxyl (-OH) groups.
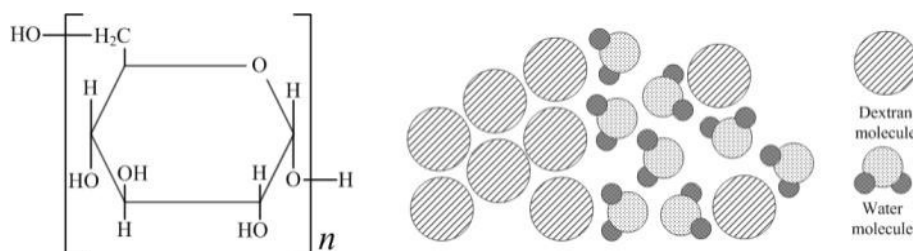
Figure 4-3: Molecular structure of Dextran and water dissolution mechanism.

When Dextran is added to water, Dextran molecules begin to form hydrogen bonds with water molecules because of the polar hydroxyl (-OH) groups present in both materials. Once a Dextran molecule forms a hydrogen bond with a water molecule, it is broken away from other Dextran molecules and surrounded by water molecules drifting in the solution. The dissolution time is strongly dependent on the molecular weight of Dextran (e.g. chain length). The Dextran and water molecules are then mixed together forming a homogenous mixture.

4.3.1.1   Formulation process

A Dextran paste can be formulated at different viscosities with the same concentration by changing the molecular weight of the Dextran powder. Typically, Dextran with a higher molecular weight produces a higher solution viscosity but the dissolution is more difficult. A Dextran powder with a molecular weight of ~12,000 Daltons was purchased from Sigma-Aldrich [111]. Dextran solution was carefully prepared by weighing an appropriate amount of Dextran powder and slowly adding into a beaker with DI water at 80 ^{o}C, increasing the dissolution rate compared with room temperature water. A magnetic stirrer was necessary to mix the powder with water thoroughly. Once the Dextran powder was fully mixed with water, the solution was then left at room temperature for 24 hours to obtain more homogeneous solutions before testing. Using the same preparation step, six Dextran samples with different concentrations (20, 23, 28, 30, 40, 45 wt%) were prepared. There are shown in Table 4-1.

Table 4-1: Dextran samples prepared in DI water at 80 ^{o}C.

Sample name	D1	D2	D3	D4	D5	D6
Concentration (wt%)	20	23	28	30	40	45

4.3.1.2   Test result

The viscosities of the Dextran samples were measured using a BrookField DV-II+Pro viscometer with a fixed spindle speed of 10 rpm which provides a constant shear strain rate. Figure 4-4 summarises the relationship between the concentration and the viscosity of a Dextran solution. It clearly shows that the viscosity is increased when the concentration is increased. However, sample D6 was saturated so that the viscosity could not be measured using this equipment.
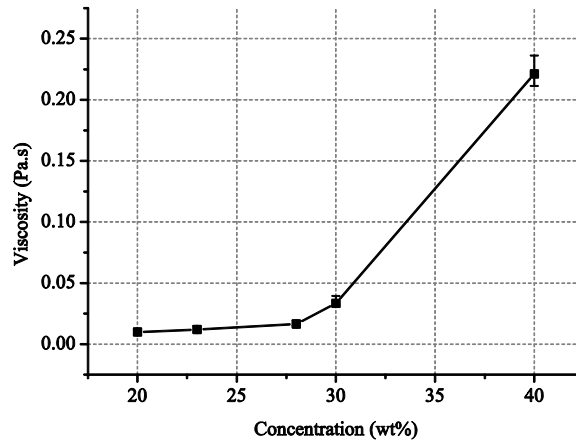
Figure 4-4: Relation between concentrations and viscosities.

The maximum viscosity of the Dextran solution was 0.225 Pa.s at a concentration of 40 wt%, which was too low to deposit using screen printing. It is difficult to increase the viscosity any further than 40 wt% because the solution becomes agglomerated even stirring it over 24 hours resulting in an inhomogeneous solution.

Dextran solutions were then deposited by casting them onto alumina tiles through a plastic stencil mask with the pattern dimensions of 30 x 10 x 1 mm. Sample D1, D4 and D5 with concentrations of 20 wt%, 30 wt% and 40 wt% were individually deposited and dried at 125 $^{\circ}$C for 10 minutes. This temperature was sufficient to evaporate the water and these settings are commonly used for curing polymer based pastes. Figure 4-5 shows the deposition results of the Dextran samples
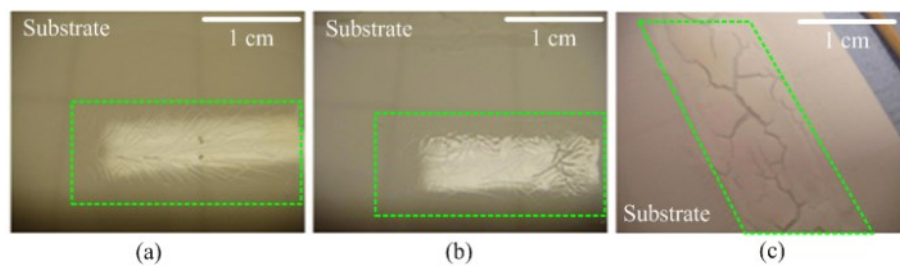
Figure 4-5 Experimental results produced by sample (a) D1, (b) D4 and (c) D5.

The deposited layers have wrinkles on the surface and rounded corners once they are dried. A cracked surface was observed on the Dextran layer which was printed using sample D5. It was also found that the layer thickness was much thinner than the thickness of the stencil due to the low solid loading resulting in high water evaporation. As a result, Dextran cannot be used for a screen printable sacrificial material.

4.3.2 Sucragel

The other water soluble material examined is Sucragel, provided by ALFA Chemical Ltd, because it is soluble in water and can be formulated into a viscous gel. Sucragel is a sugar ester emulsifier that is designed as a thickener for skin care applications such as bath oils, spa products, creams and lotions. Sucragel is a colourless water soluble liquid and its viscosity depends on the type used, as shown in Table 4-2. The liquid Sucragel can potentially be changed to a gel form by adding the appropriate oil. The viscosity of the gel can then be adjusted by changing the relative proportions of Sucragel and oil used. It is designed for use at room temperature but can be also used at temperature below 80 $^{\circ}$C.

Table 4-2: Viscosity comparison among three Sucragel products [112].

Product number*	Viscosity** (Pa.s)	Suitable oil type
Sucragel CF	0.50-1.50	Mineral oils
Sucragel AP	0.15-0.19	Any oil
Sucragel AOF	3.50	Vegetable oils

*All names are the trade name from the manufacturer.
**Viscosity is provided by the ALFA company before mixing with oil.

Sucragel AOF has the highest initial viscosity of the Sucragel types and therefore it is likely to provide the highest viscosity once it is mixed with the corresponding oil.

4.3.2.1   Formulation processes

Vegetable oil is recommended for use with Sucragel AOF. The recommended proportion to form a gel is from 15 wt% to 70 wt% of Sucragel with 30 wt% to 85 wt% of oil [112]. In this test, five samples with 0, 15, 50, 70 and 100 wt% of Sucragel were prepared. First, an amount of Sucragel was mixed in a beaker using a mechanical stirrer at 3000 rpm. Vegetable oil was then added into the beaker whilst the stirring maintained for 30 minutes. Importantly, when formulating, oil must always be added into the Sucragel; adding Sucragel to the oil will not allow the desired gel structure to be formed [112]. Table 4-3 provides the proportions of each Sucragel sample.

Table 4-3: Formulation proportion of each Sucragel sample.

Sample name	Sucragel (wt%)	Vegetable oil (wt%)
S1	0	100
S2	15	75
S3	50	50
S4	70	30
S5	100	0

Sample S1 and S5 were used as references to evaluate the viscosity of the mixtures when only pure material was presented. From sample S2 to S4, proportion of Sucragel was increased from the minimum to maximum based on the recommendation from Alfa Chemical Ltd.

4.3.2.2 Test results

The viscosity of each Sucragel sample was measured using the same equipment as the Dextran solution at a fixed spindle speed of 10 rpm.
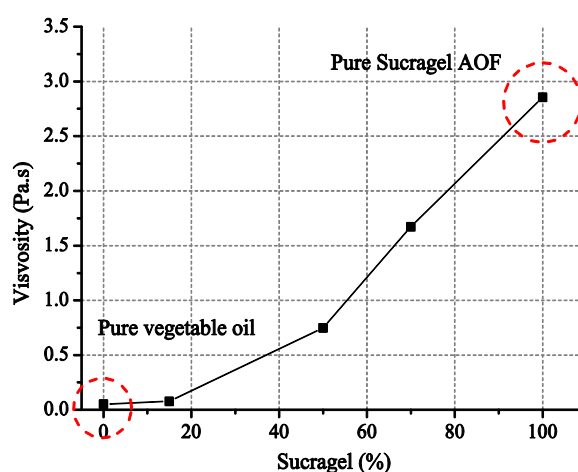
Figure 4-6: Relation between the Sucragel concentration and mixture viscosity.

Figure 4-6 shows the viscosity results of five Sucragel samples, showing the viscosity decreased with increasing vegetable oil. The maximum viscosity was obtained with pure Sucragel AOF, whereas pure oil gave the minimum viscosity. Separation occurred after the mixtures were left more than 30 minutes. Figure 4-7 shows the separation problem affecting samples S2 and S3.
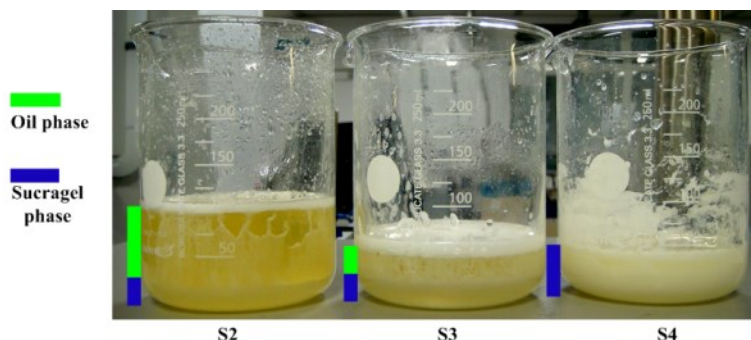
Figure 4-7: Separation of Sucragel mixtures.

Complete separation between vegetable oil and Sucragel was observed in sample S2 and S3, whereas sample S4 did not separate even after 2 hours. Due to the low density, the oil was suspended on top of the solution, shown above for S2 and S3. In contrast, S4 was a homogeneous mixture. To test the printability of pure Sucragel AOF where the viscosity was a maximum, a stencil mask was used to deposit it onto an alumina tile which was subsequently dried at 80 $^{\circ}$C. The Sucragel did not dry even when increasing the drying period from 5 to 20 minutes. The removal temperature was limited to 80 $^{\circ}$C which was the maximum working temperature of Sucragel. These results show that Sucragel and its mixtures are unsuitable as a printable sacrificial material due to the low viscosity and difficulties drying it.

4.3.3 Plastic crystal materials

Plastic crystals are compounds where the molecules have rotational disorder while the lattice structure remains when the temperature exceeds their transition temperatures [113]. At low temperature (i.e. below the transition temperature), materials are crystals in which molecules have both rotational and positional orders. As the temperature exceeds the transition temperature, the materials go into the plastic crystalline phase where the molecules rotate from one orientation to another while the lattice structure is maintained. In this phase, the materials have rotational disorder but keep positional order and the materials remain in a solid state [114]. Once the temperature is above the melting point, molecules absorb energy to break the ordered lattice structures forming an isotropic liquid. In this phase (i.e. molten phase), molecules have both rotational and positional disorder. The most interesting phase for the sacrificial application is the plastic crystal phase because the materials remain in a solid state and their vapour pressure exponentially increases when temperature increases. Therefore, by controlling

the temperature to be between the transition and melting temperatures, causes the material to directly sublimate (i.e. reducing structural deformation) escaping from the structure in a gaseous phase.

Neopentylglycol (NPG), or 2,2-dimethyl-1,3-propanediol, is a white crystalline solid at room temperature and is soluble in many polar solvents. It is partially soluble in water. It has plastic crystalline transition and melting points of 48 $^{\circ}$C and 124 $^{\circ}$C respectively [115]. Trimethylolpropane (TMP), or 1,1,1-tris(hyrdroxymethyl)propane, is a white flake solid at room temperature. TMP is a polar substance which is soluble in water, most alcohols and glycerine, whereas it is insoluble in hydrocarbon solvents (e.g. benzene) because of its polarity. TMP has a very low melting point ($\sim$ 56 $^{\circ}$C) and the transition point is even lower although unspecified in the literature [116]. Trimethylolethane (TME), or 1,1,1-tris(hydroxymethy)ethane, is a white crystalline powder at room temperature which undergoes a plastic crystalline transition at 85 $^{\circ}$C [117]. The melting point of TME is higher than TMP and NPG at 187 $^{\circ}$C [118]. Figure 4-8 presents their molecular structures and the vapour pressure of these materials as a function of the temperature.
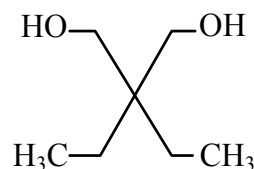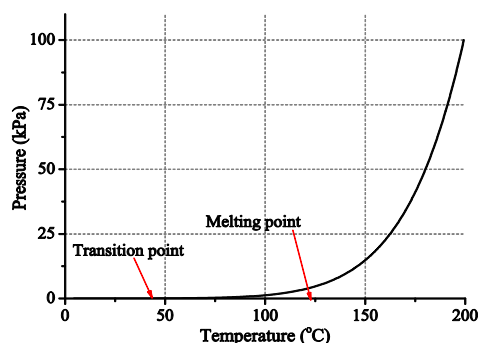
(a)
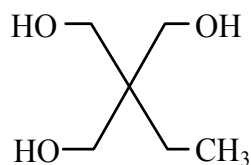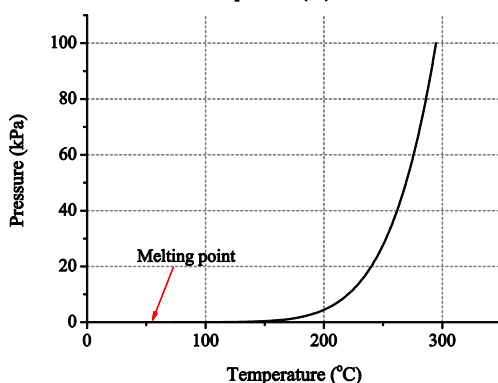
(b)
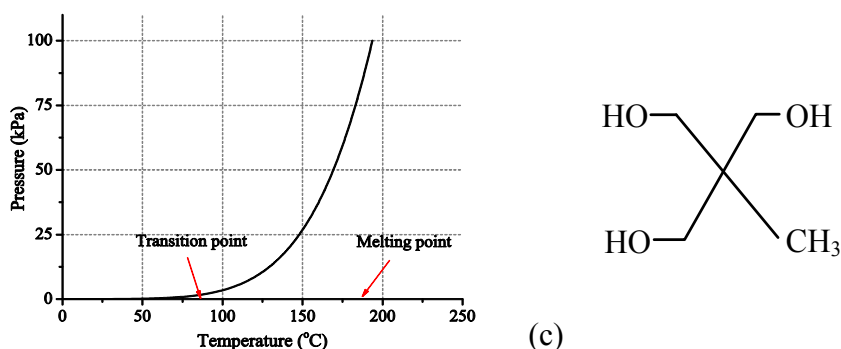
Figure 4-8: Vapour pressure of plastic crystals versus temperature, (a) NPG, (b) TMP and (c) TME [119].

NPG has a low vapour pressure of 40 Pa at its transition point. This pressure increases with temperature until its melting point at which the vapour pressure is 4 kPa. NPG has a relatively small vapour pressure increase between its transition and melting points. Even at temperatures above the melting point of TMP, there is no significant pressure increase until its boiling point (i.e. 160 ^{o}C) resulting in an inefficient sublimation mechanism. The vapour pressure of TME increases significantly after the temperature exceeds its transition point and this increasing tendency keeps going until it becomes liquid. Before the transition point, its vapour pressure is small, thus the mass loss is minimal. At the transition point, it has a low vapour pressure 1.4 kPa but this exponentially increases, generating a maximum vapour pressure of 82 kPa before it reaches the melting point. A higher vapour pressure gradient indicates a fast sublimation mechanism. Compared with NPG and TMP, TME has the highest pressure gradient, ensuring a fast sublimation mechanism.

4.3.3.1 *Formulation process*

Since the plastic crystalline materials selected here are polar substances, corresponding polar substances, such as alcohols, should be the solvents. No formulation process information has been reported in the literature other than the type of solvent used. Consequently the author will only use the selected solvents, cyclohexanol (CH) and propylene glycol (PG), from the literature [31] and develop the formulation processes from scratch. Cyclohexanol (CH), which is a viscous liquid with a boiling point of 160 ^{o}C, was used as the solvent for the dissolution of plastic crystals. However, CH is a solid at room temperature because it has a melting point of ~23-25 ^{o}C. Propylene glycol (PG), which has a melting temperature of -60 ^{o}C, was added into CH to decrease its melting point resulting in liquid CH at room temperature. The amount of PG used with

72

CH for the formulation was experimentally determined by gradually adding PG into CH in a beaker until the CH was no longer in a solid form at room temperature. The amount of PG used should be approximately 14 % by weight of CH. A lower PG quantity would result in a solid CH at room temperature, whereas the paste was hard to dry if too much PG was added as it has a higher boiling point than CH.

Before formulating, each plastic crystal should be ground in a mortar and pestle to obtain a fine powder. This step is important to avoid any agglomeration during the mixing process. A screen printable paste was formulated based on the following procedures. Firstly, the CH was heated to 100 ^{o}C in a 250 mL beaker and was stirred by a magnetic stirrer. 14 % PG was then added into the beaker. Next, the plastic crystal powder was carefully weighed out and added to the beaker. The hot beaker was then half immersed in a cold water bath to achieve a plastic crystal precipitation.

4.3.3.2   Test results

Neopentylglycol (NPG)

NPG is a translucent crystal at room temperature and is harder than TMP and TME so that several grinding cycles were required to obtain a fine powder. The concentration of the NPG paste was determined by adding the NPG powder into the solvent mixture. It was found that NPG separated and precipitated at the bottom of the beaker when stirring was discontinued and that NPG tended to form a crystalline structure once the solution was cooled down, shown in Figure 4-9.
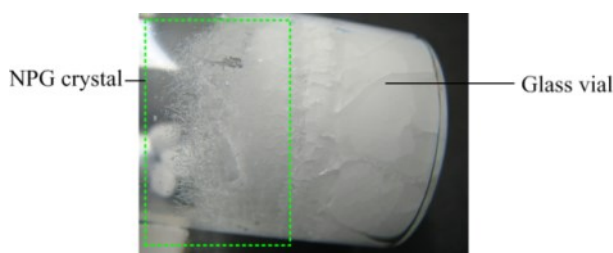
Figure 4-9: Crystallisation problem of NPG when the solution was cooled down.

No homogeneous liquid mixture was obtained after mixing due to NPG crystallisation and therefore it was not possible to perform any further testing.

Trimethylolpropane (TMP)

As the melting point of TMP is lower than the mixing temperature of 100 ^{o}C, TMP became liquid phase once it was added into the solvent mixture. A liquid-liquid mixing was performed and concentrations up to 70 wt% were obtained before saturation occurred. The mixture was a homogenous and transparent liquid at 100 ^{o}C. A higher concentration would lead to the saturation of TMP resulting in TMP precipitating at the bottom of the beaker. Once the mixture cooled down, it was a white liquid but its viscosity was low. The viscosity was then examined using a Brookfield CAP 1000+ viscometer with a fixed spindle speed of 10 rpm and an average value of 3.50 Pa.s was measured. An initial attempt at printing was performed by printing the TMP solution using a polyester screen (32 threads per cm) with 40 μm emulsion and it was found that the paste could not form a consistent pattern with defined edges. As the melting point of TMP is 56 ^{o}C, it is difficult to dry the mixture at a temperature below its melting point. An alternative fabrication technique was examined by smearing a thin layer of TMP solution onto an alumina tile which was left at room temperature for 24 hours. Figure 4-10 shows a TMP sample dried at room temperature.

Figure 4-10: TMP paste deposited by smearing onto an alumina tile and dried at room temperature.

The surface was smooth but this material had several problems. This thin layer would be melted again when the temperature was higher than its melting point. It could not be printed by using either the mesh screen or the stencil screen due to its viscosity.

Trimethylolethane (TME)

TME powder dissolved easily into the solvent mixture in a variety of concentrations without saturation. TME powder was weighed out directly and added into the beaker in which the solvent mixture was heated to 100 ^{o}C. Unlike TMP, the melting point of TME

is higher than the mixing temperature, thus a solid-liquid mixing was performed. Once the paste had cooled down, the solution formed a waxy solid precipitation in the beaker, thus it was essential to grind it up using a triple roll mill. A white viscous paste was achieved once the solid precipitation was broken. Five samples with concentrations of 40, 50, 55, 60 and 70 wt% were prepared using the process stated above. All samples were left at room temperature for 24 hours before measuring the viscosity. Each sample was individually tested using a Brookfield CAP1000+ viscometer at a fixed spindle speed of 10 rpm at room temperature. Table 4-4 presents the formulation details and the viscosities of the five samples.

Table 4-4: Formulation of the TME paste with five concentrations.

Paste name	T1	T2	T3	T4	T5
Concentration	40 wt%	50 wt%	55 wt%	60 wt%	70 wt%
TME	40 %	50 %	55 %	60 %	70 %
CH	52.6 %	44 %	39.5 %	35 %	26.4 %
PG	7.4 %	6 %	5.5 %	5 %	3.6 %
Viscosity (Pa.s)	2.1	3.78	6.32	8.70	21

To evaluate the printability of these samples, a polyester screen (32 threads per cm) was used to deposit these formulated pastes onto alumina tiles. The screen design and printing parameters are shown in Figure 4-11.
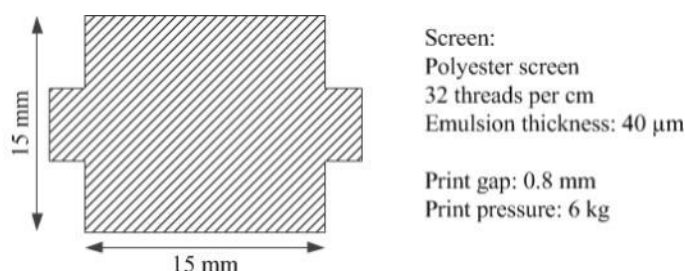
Figure 4-11: Screen design for initial test for TME pastes.

Sample T1 (40 wt%) was difficult to screen print as the viscosity was too low causing it to spread all over the screen and flow through the pattern without being forced. Sample T5 (70 wt%) was too viscous for a screen printing process because the paste stuck to the blade of the squeegee and did not pass through the screen mesh. Samples T2, T3 and T4

could be screen printed onto alumina tiles and cured at 80 ^{o}C for 15 minutes with varying quality, shown in Figure 4-12.
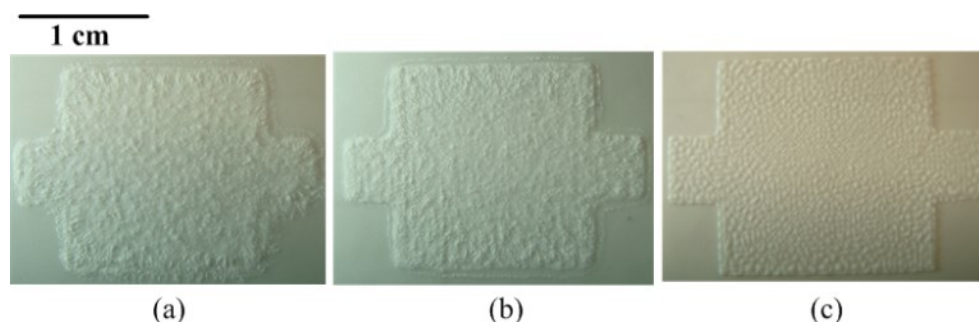
Figure 4-12: Printing results of TME pastes with the samples, (a) T2, (b) T3 and (c) T4.

Figure 4-12 shows that printed layers obtained with sample T2 and T3 had ragged edges and corners. The paste bled once the screen was lifted from the substrate and there were also some wrinkles located on the corners of sample T2. These problems were due to the lower viscosities of these formulations which could not maintain the definition of the printed patterns. Paste T4 had the best printing quality of those tested. The printed pattern was clearly defined and the surface was relatively consistent without any wrinkles.

The ease of removal of sample T4 was examined by screen printing a silver layer (ElectroPolymers ELX30) on top which was dried at 125 ^{o}C for 10 min. This silver was chosen since it was previously used to achieve conductive tracks. The compatibility between the silver and sacrificial materials can also be evaluated because the final device will require electrical connections. The removal temperature of the sacrificial material was 150 ^{o}C based on the literature [31]. Figure 4-13 shows photographs of the sample before and after removal. It was found that the TME layer was fully removed, releasing the silver layer from the substrate.
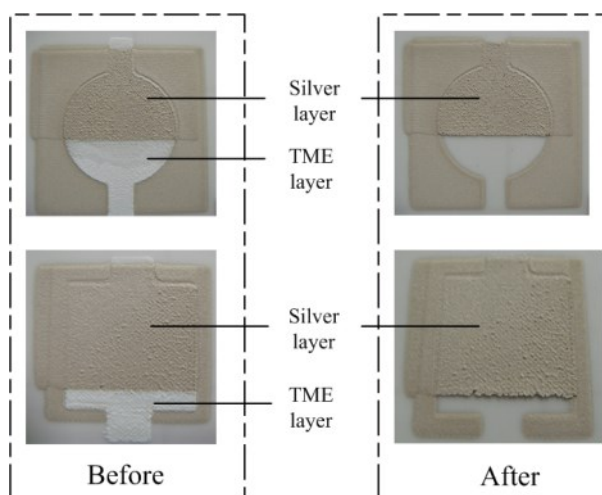
Figure 4-13: Initial removal evaluation of a sample T4 with circular and square cover layers.

Removal residue was checked by peeling back the free standing silver layer using tweezers. It is clearly shown in Figure 4-14 that the TME layer was completely removed through the sublimation mechanism.
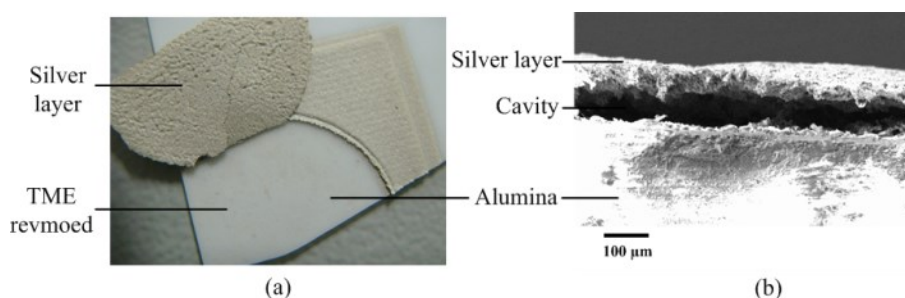
Figure 4-14: (a) Free standing silver layer peeled off from the alumina tile and (b) A cross-sectional SEM micrograph of the printed sample.

Results also showed that there was no significant chemical reaction; thereby the mechanical properties of the silver layer were not affected. In addition, a cross-sectional SEM micrograph was used to further confirm the removal of TME layer.

4.3.3.3   Other plastic crystal combinations

Other formulation attempts, such as mixtures of TME/TMP and TME/NPG, were examined. Various concentrations, from 40 wt% to 60 wt% of the mixture, were examined using the formulation steps described previously. However, neither the formulation nor the printing results were comparable with those achieved with the pure TME paste, which was able to produce a consistent layer with a smooth surface. The

details of the formulation and printing results of these mixtures are included in appendix A.

4.3.4 Summary of sacrificial material selection

Potential water and thermally removable sacrificial materials were evaluated in this section based on the ease of formulation, printability and ease of removal. Table 4-5 provides a comparison of sacrificial materials evaluated in this section.

Table 4-5: Comparison of potential sacrificial materials.

	Dextran	*Sucragel*	*NPG*	*TMP*	*TME*
Dissolvable	Y	Y	Y	Y	Y
Curable	Y	N	N/A	Y*	Y
Viscosity (Pa.s)	0.2	2.8	N/A	3.5	2.1~21
Deposition technique	Stencil print	Stencil print	N/A	N/A	Screen print
Selected	N	N	N	N	Y

Only at room temperature for a period of 24 hours.

For the water soluble materials;

o Dextran solution had a maximum concentration of 40 wt% and any higher concentration caused the solution to saturate. Dextran solutions had low viscosities which were impractical for screen printing. A stencil printed Dextran layer cracked as it dried because of weak cohesion force between Dextran molecules. In addition, Dextran is significantly more expensive, thus no further evaluation will be performed.

o Sucragel exhibited a relatively high viscosity compared with Dextran but the viscosity could not be increased above 3 Pa.s. It was difficult to dry the Sucragel mixture at its maximum operating temperature and it was not possible to print with mesh based or stencil based screens due to its low viscosity.

For the thermally removable materials;

  o NPG could not be formulated into a paste form because it separated from the solution as it cooled down. It also crystallised during the cooling process forming crystals which adhered to the side wall of the beaker.

  o TMP was soluble in the mixture of CH and PG, and a final concentration of 70 wt% was achieved but this solution was useless for screen printing because of the low viscosity and low melting temperature. Even though a smeared TMP was dried at room temperature for 24 hours, it was still unusable because any temperature higher than its melting point would cause a liquid TMP thereby destroying the upper structures.

  o Initial evaluation showed that TME was easy to formulate compared with the other materials reported in this section. TME with a concentration of 60 % gave the best printing properties. The removal results for TME were examined by printing an additional silver layer on top that was dried in a conventional box oven at 125 $^{\circ}$C. It was shown that TME was able to support the subsequent layer of cured silver layer during the printing and curing, and could be removed by sublimation at 150 $^{\circ}$C leaving no residue. However, the printing surface quality of a TME layer was not smooth and flat so a further optimisation process of both the formulation and processing was required.

4.4 Optimisation of plastic crystal sacrificial paste

TME paste was selected as the best screen printable thermally removable material examined in the previous section because it was easy to formulate into a paste, had good printability and was easier to remove compared with the other materials investigated. The initial curing and removal temperatures were 80 $^{\circ}$C and 150 $^{\circ}$C, respectively. These temperatures were sufficient to solidify the paste and then remove the TME at the end of the process. However, the printed TME layer had an uneven surface which reduced the print quality of the subsequent layer. The operating temperature of the fabric and the sublimation mechanism of TME were not fully considered or analysed while selecting these temperatures. This section will therefore focus on improving the print quality of the TME layer and identify the optimum curing and removal processes for a Trimethylolethane (TME) based sacrificial paste.

4.4.1 Evaluation of a TME 60wt% paste

Before optimisation, the cause of the uneven surface problem with the TME material should be identified. A black alumina tile with dimensions of 10 cm by 10 cm was selected as the substrate to provide a smooth substrate surface and because the printed TME layers are white and can therefore be more easily distinguished. A polyester mesh screen, which has same screen parameters as the one described in Figure 4-11, was used as the testing screen to identify the problems of the printed TME layer. The same printing parameters were used as with the initial TME selection prints. The screen design and printing parameters are shown in Figure 4-15.
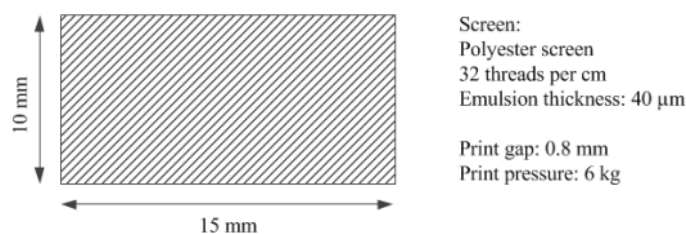
Figure 4-15: Screen design for the evaluation of the TME 60wt% paste.

TME paste was printed onto the alumina tile and then dried in a box oven at 80 $^{\circ}$C for 15 min. Four complete print cycles with a subsequent curing step after all the prints were performed to evaluate the surface quality of the layer and assess the maximum achievable thickness. Figure 4-16 shows that the surface quality was improved by increasing the number of prints.
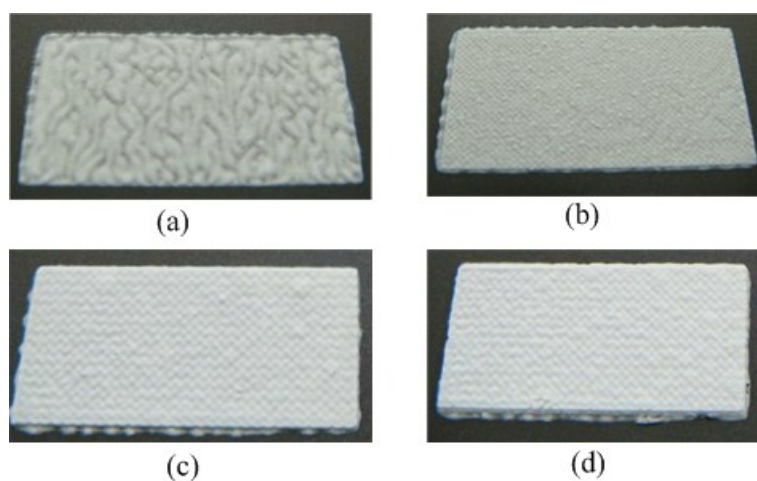
Figure 4-16: 60 wt% TME paste printed on an alumina tile with (a) one print, (b) two prints, (c) three prints and (d) four prints.

For the first print, the layer surface had many agglomerates because the paste would not wet the substrate properly to form a uniform film. However, this problem was reduced with an increasing numbers of deposits. With two prints, this problem was reduced but some agglomerations were located on the surface. After the third and fourth prints, it was found that there was a height variation across the sample. The undulations in the film were periodic and coincided with the shape of the weave in the screen mesh.

The reason for the imprint of weave onto the surface was that the TME paste did not reflow properly after the squeegee passed through the screen and the mesh retracted. This would commonly be caused by a high ink viscosity, high powder loading, poor powder dispersion or inappropriate printer setting [108]. The printing gap and pressure were adjusted from 0.8 mm to 1.5 mm, and 4 kg to 7 kg, respectively. The surface quality was not significantly improved, thus it was most likely caused by the poor powder dispersion because the TME powder may not be fully dissolved and dispersed in the solvents during formulation. Figure 4-16 (b) illustrates that small agglomerations were found on the surface of the printed layer. It was also found that the printed pattern had a serrated edge. This problem was most likely caused by the coarse screen mesh.

The number of deposits could not be increased any further because delamination occurred on some samples after the fourth cure, as shown in Figure 4-17.

(a)   (b)
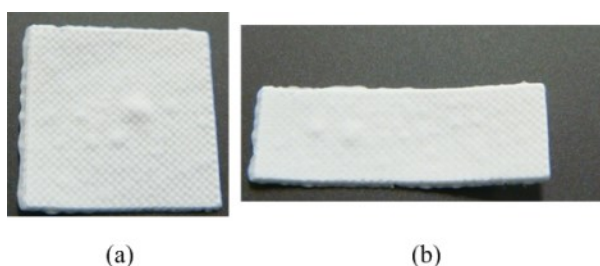
Figure 4-17: Wave shapes and layer separation of printed sacrificial layers.

This problem could be due to the curing profile, which may have evaporated too much solvent, and therefore it is incompatible with the paste. As a result, only solid TME, which had a poor adhesion to the substrate, was left. Temperature or curing period could be the reasons causing this problem.

4.4.2 Formulation improvement

To produce a homogenous paste, the TME powder must be fully dissolved into the solvent. To confirm this, the final solution at the dissolution temperature should be transparent without any agglomeration. Any cloud or agglomeration will affect the paste properties and result in poor print quality. To achieve a transparent solution, a slightly higher dissolution temperature (i.e. 110 °C) was used compared with the previous temperature (i.e. 100 °C). The reason for increasing the temperature is that the solubility of a plastic crystal is higher in its plastic crystal phase than in its normal crystalline phase; dissolution at a temperature higher than the transition temperature would result in acceleration of dissolution and reduce agglomeration during formulation [114]. This temperature should be carefully selected because the CH will evaporate if the temperature is close to its boiling point. In addition, a fast stirring speed also improved the TME dispersion. The significant differences between the previous and improved dissolution processes are as follows.

- o TME was mixed with the solvents producing a cloudy solution at 100 °C, whereas the improved TME solution was transparent at 110 °C resulting in full dissolution of TME.
- o TME paste should be left in a refrigerator to homogenise the paste and prevent the solvents from evaporating
- o TME paste should also be left in a refrigerator after the milling process to achieve a more homogeneous paste.

The thixotropic properties of the improved TME paste was examined using a BrookField CAP1000+ viscometer at a fixed spindle speed of 10 rpm. The measurement was performed continuously and the viscosity was recorded every minute. Figure 4-18 show shows the viscosity of a TME paste at a constant shear strain rate over 10 minutes.
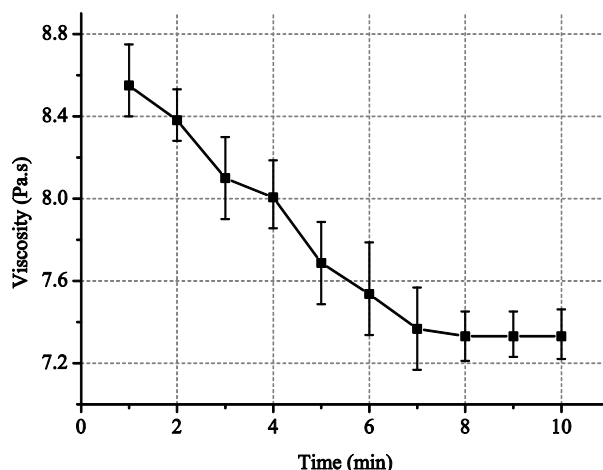
Figure 4-18: Thixotropic property of the improved TME paste.

It was found that the viscosity gradually reduced over time at a constant shear strain rate. It was not possible to measure the viscosity at 0 minutes as any stirring mechanism would introduce a shear stress reducing the viscosity accordingly. The viscosity remained constant after 8 minutes at a constant shear strain rate. Two commercial thermally curable polymer dielectric screen printable pastes, DuPont 8153 and Electra Polymers ELX80, were also measured using the same process to compare their thixotropic properties with the TME paste. Figure 4-19 shows the comparison of thixotropic properties among these three pastes using a normalised viscosity.
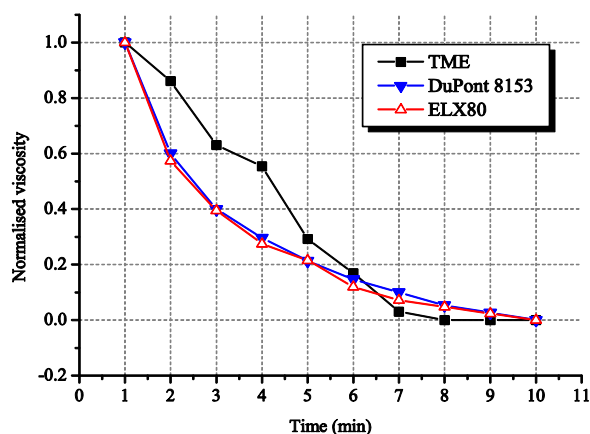
Figure 4-19: Comparison of thixotropic properties between the TME paste and two commercial polymer dielectric pastes DuPont 8153 and ELX80 (TME: 8.5 Pa.s; DuPont 8153: 10 Pa.s; ELX80: 20 Pa.s).

DuPont 8153 and ELX80 pastes had a similar rate of reduction over time while viscosities were decreased. TME paste also had a reduction over time but this reduction was not as smooth as the results obtained from DuPont 8153 and ELX80.

It was found that the viscosity of the TME paste also changed over a long period of storage. Figure 4-19 shows that the viscosity of the TME paste measured every two months.
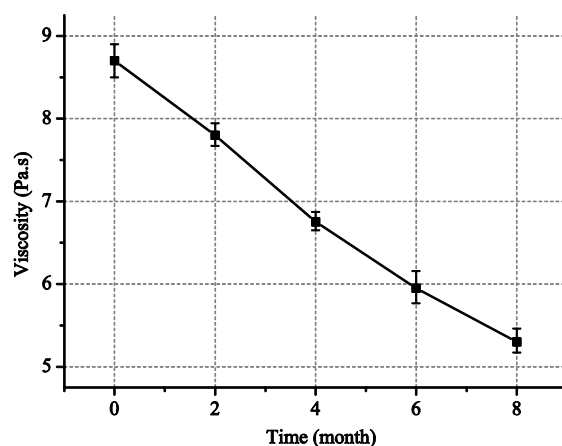
Figure 4-20: Viscosity drifts as the function of time.

This shows that the viscosity drifted at a constant rate over eight months since it was initially formulated. It is believed that viscosity reduction is caused by the increase in particle size during the storage period. However, printing results were only affected when the viscosity was lower than 6 Pa.s at which poorly defined patterns were formed.

4.4.3   Curing temperature adjustment

To achieve maximum evaporation of CH and minimal sublimation of the TME during the curing process, the plastic crystalline transition point of TME should be identified. To achieve this, differential scanning calorimetry (DSC) was used. DSC is a technique in which the heat absorbed or released from a sample with known mass is measured whilst being subjected to a controlled heating or cooling program. DSC can be used to measure the information about physical and chemical changes, such as transition, melting and boiling points, which involve an endothermic or exothermic process. Figure 4-21 shows a schematic diagram of a DSC measurement.
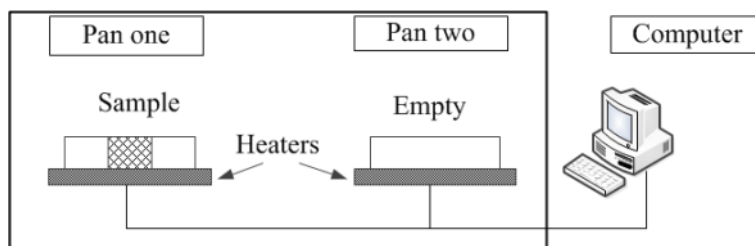
Figure 4-21: Schematic diagram of a DSC operation

There are two heaters in a DSC measurement, one of which is used to heat up a reference empty pan and the other one is to heat up the sample pan. The heating rates of the two heaters are maintained by the computer. The presence of the extra sample means that the heater needs to generate more energy to maintain the heating rate as the same as the reference pan. By measuring how much extra heat is generated, a DSC measurement can be performed.

Energy will be absorbed when TME is transferred from a normal crystalline structure to a plastic crystal structure, thus an endothermic reaction is expected around the transition point. Detection of this energy absorption peak will therefore provide the specific TME transition temperature for this particular powder. A small amount of the TME powder was weighed on a precision balance and was hermetically sealed in an alumina pan. A reference pan without any material inside was also hermetically sealed and placed on the reference heater. The temperature range was selected from 50 $^{\circ}$C to 230 $^{\circ}$C with a heating rate of 20 $^{\circ}$C/min increasing from the minimum to the maximum testing temperature. Any temperature lower or high than the testing range was considered unimportant due to the requirement for fabric compatibility.
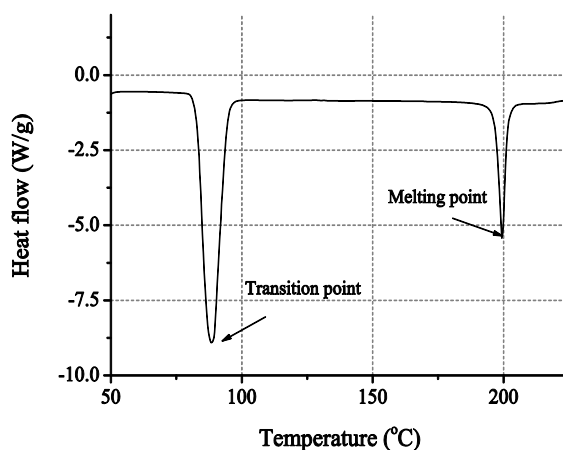
Figure 4-22: DSC result of TME powder showing transition and melting points.

Plastic crystal phase transition and melting are endothermic mechanisms so that the sample heater needs to generate more energy to maintain the same heating rate and therefore the heat flow is higher than the heat flow on the reference heater. Figure 4-22 shows that TME has a plastic crystalline transition point of around 87 $^{\circ}$C at which point the TME becomes orientationally disordered whilst maintaining positional order. Once the temperature exceeds this point, vapour pressure exponentially increases with temperature. This increases the rate of TME sublimation. As long as this temperature is lower than its melting point, sublimation dominates the removal mechanism, whereas liquefaction will take place once the TME is melted. The curing temperature of TME must be below its transition point to avoid unexpected removal.

Since TME was used in conjunction with solvents in the printing process, the primary solvent (i.e. cyclohexanol) must be removed from the paste to form a solid layer. A compromise between maximising the evaporation of CH and minimising the loss of TME during the curing process was achieved by combining the DSC results with the vapour pressure data for each compound in the TME paste. Figure 4-23 shows that the vapour pressure is a function of temperature for TME, CH and PG.
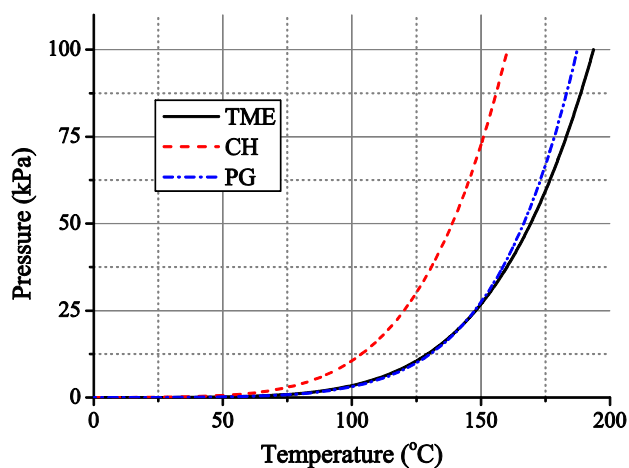
Figure 4-23: Vapour pressure of each compound for TME paste formulation [11].

TME and PG have a similar pressure gradient at all temperatures below 150 $^{\circ}$C while CH has a higher vapour pressure compared with TME and PG. The initial curing condition was 80 $^{\circ}$C for 15 minutes which was sufficient to solidify the TME paste. However, delamination occurred when the thickness of the sacrificial layer was more than 200 μm (i.e. four prints). It was believed that both CH and PG were completely

evaporated resulting in a pure TME solid, which had weak substrate adhesion. In addition, a thicker layer has higher cross-sectional area than a thin layer and therefore more stress is generated resulting in peeling layer from the substrate.

The vapour pressure of CH is twice than that of PG resulting in different evaporation rates. By controlling the curing temperature and period, CH can be sufficiently evaporated whilst the PG will be left with the TME, potentially improving the adhesion. From the vapour pressure graph, the vapour pressure of TME does not change significantly at its transition point of 87 ^{o}C compared with the initial curing temperature of 80 ^{o}C; the curing temperature was therefore increased to 85 ^{o}C. A curing temperature of 85 ^{o}C provided a maximum evaporation rate of CH and also ensured the TME was below its transition point so that the mass loss was minimal. The curing period was also reduced to 5 minutes to reduce the evaporation of PG.

4.4.4 Removal process evaluation

Thermo gravimetric analysis (TGA) was used to evaluate the mass loss of TME due to sublimation at different temperatures. TGA is a technique in which the mass of a substance is monitored as a function of temperature or time as the sample is subjected to a controlled temperature in a controlled atmosphere [120]. TGA measurements are used to determine the composition of materials and to predict their thermal stability at various temperatures. The technique can characterise materials that exhibit weight loss or gain due to decomposition, oxidation, or dehydration.
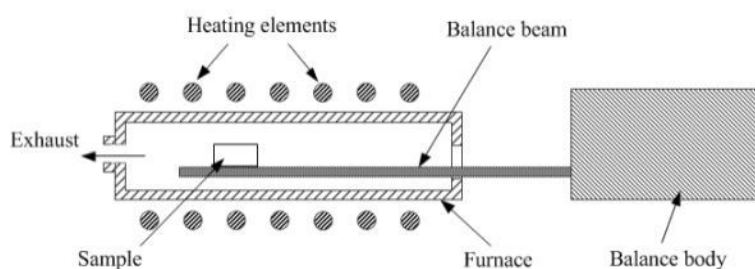
Figure 4-24: Schematic diagram of a TGA operation.

A TGA consists of a sample pan that is supported by a precision balance beam. The balance body is located outside of the furnace to avoid thermal damage. The balance configuration can be either in a horizontal direction (shown in Figure 4-24) or in a

vertical direction where the balance body is located on top of the furnace. The pan is inside the furnace and is heated or cooled during the experiment. To control the sample environment, the sample purge gas may be inert or reactive. This gas flows over the sample and exits through an exhaust.

The mass loss of TME was evaluated by weighing small amounts of TME in an alumina crucible which was then placed in a sample holder of the TGA. Nitrogen gas was initially blown into the TGA furnace to clean up any air residue and a test was then performed with a temperature range from 30 ^{o}C to 300 ^{o}C whilst the chamber was filled by air.
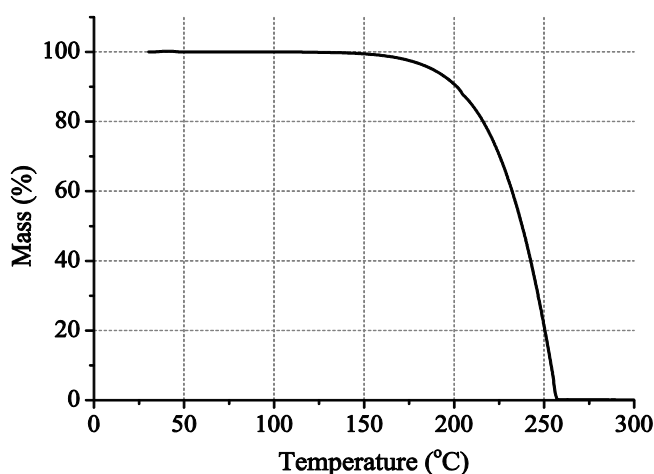
Figure 4-25: Mass loss of TME with a temperature range from 30 ^{o}C to 300 ^{o}C.

Figure 4-25 shows that there was no mass loss below the transition point. The TME started to reduce its mass once the temperature was above its transition temperature. Between its transition point and 150 ^{o}C, the mass loss was small, resulting in a slow removal. Once the temperature exceeds 150 ^{o}C the mass loss was accelerated until it was fully sublimated. As the liquid phase must be avoided, the upper limit of the removal temperature should be lower than the measured TME melting point of 200 ^{o}C.

To examine the mass loss rate of TME at certain temperatures, TGA was performed at 130 ^{o}C, 160 ^{o}C and 190 ^{o}C for one hour. Figure 4-26 presents the mass loss rates of TME samples at these temperatures.
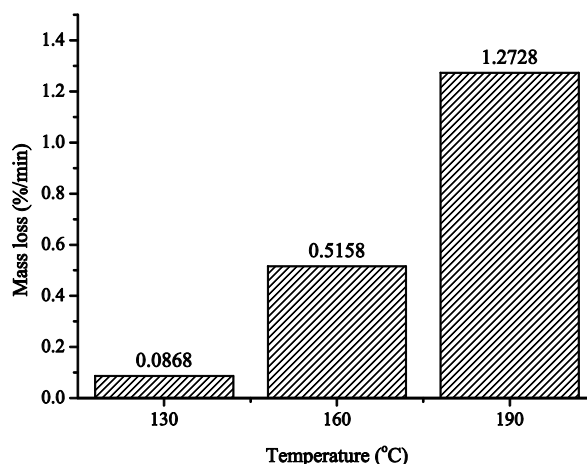
Figure 4-26: Mass loss of TME at 130, 160 and 190 ^{o}C.

The mass loss rate of TME at 160 ^{o}C is six times faster than that at 130 ^{o}C. The maximum mass loss rate was obtained at 190 ^{o}C before TME became liquid. As a result, the mass loss rate was 15 times higher than that at 130 ^{o}C. No further tests were performed at temperatures higher than 200 ^{o}C since the TME was then in liquid form. The removal temperature is also limited by the particular fabric used. In addition, the actual removal rate of TME will be influenced by other factors when printing, such as layer thickness, pattern surface area and airflow.

4.4.5 Optimisation of printing parameters

One of the reasons that poor printing quality occurred was the screen selection which resulted in periodic undulations in the layer. The polyester screen with 32 threads per cm increases the amount of the paste loaded onto the screen but reduces the surface quality. In this section, a polyester screen with 120 threads per cm was therefore selected for the deposition of TME paste. The TME layer was dried at 85 ^{o}C for 5 minutes, which was optimised in section 4.4.3. Figure 4-27 shows the improved screen and printing parameters.

Screen:
Polyester screen
120 threads per cm
Emulsion thickness: 40 μm

Gap: 1.5 mm
Pressure: 6 kg
Deposit: 2
Prints: 4
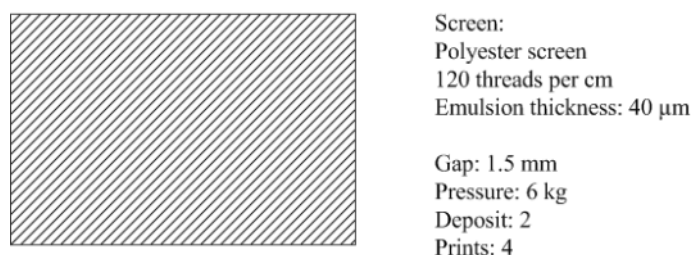
Figure 4-27: Printing parameters and modified screen design.

TME layer

Alumina tile

1 cm

(a)   (b)
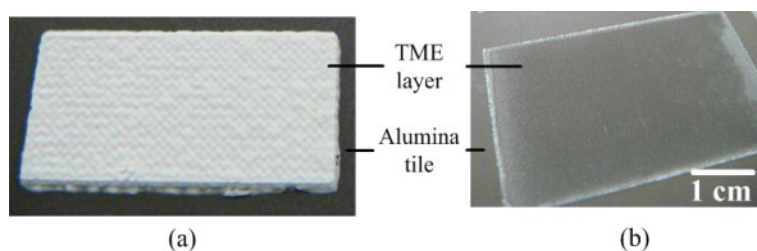
Figure 4-28: Printing results, (a) before optimisation and (b) after optimisation.

Visual examination shows that the surface was flatter and smoother than before optimisation. Compared with the sample produced with a screen with 32 threads per cm, the screen with 120 threads per cm produced a sample with a smoother surface, with no undulations observable on the surface. The serrated edges were also eliminated. In addition, increasing the printing gap to 1.5 mm also improved the printing quality. The colour of the layer was pure white in previous results and was translucent under the improved curing temperatures. By using the improved curing temperature and also reducing the curing period, it was believed that CH was removed while PG was left with TME resulting in a translucent appearance.

4.4.6 Summary

This section analysed and identified the problems with the TME paste, which was initially evaluated in the previous section. An undulated surface, serrated edges and poor adhesion were improved by changing the printing and curing parameters and the formulation process.

Full dissolution was required to achieve a homogeneous TME paste with no particle agglomeration. Transparency indicated that TME was fully dissolved in the solvent. A higher temperature accelerated the dissolution process. Increasing the dissolution

temperature by 10 $^{\circ}$C improved the TME dissolution but the TME powder should be added as slow as possible. Adding the TME powder too quickly resulted in agglomerations which were hard to break.

The optimum curing temperature was identified at 85 $^{\circ}$C. This was a compromise between the maximising the evaporation of CH and minimising the sublimation of TME. TME started to sublimate at 87 $^{\circ}$C but the mass loss was low until it reached 150 $^{\circ}$C at which point a significant mass loss was observed. The vapour pressure of CH was more than double than that of TME and PG at 85 $^{\circ}$C and therefore only the CH was completely evaporated leaving a mix of PG and TME.

The removal temperature was evaluated using TGA, allowing the mass losses of TME to be observed at different temperatures. To be used as a sacrificial material, TME must maintain a solid foundation to support the printing and curing of the subsequent layer. Any liquid TME will result in structural deformation and stiction problems. An upper limit of the removal temperature has been identified to be 200 $^{\circ}$C before liquefaction. The removal temperature will be further limited depending on the maximum operating temperature of the selected fabric.

4.5 Adjusting the removal temperature of a TME based paste

In the following section, the objective was to achieve an adjustable removal temperature by combining two plastic crystalline materials thereby achieving the same removal rate at any required temperatures. In the previous section, TME was entirely removed at 150 $^{\circ}$C in 30 minutes. However, some applications may need a higher temperature for curing the materials. In these cases, TME paste is not able to provide a solid foundation during the subsequent curing process if it requires temperatures higher than the removal temperature of TME. Due to the transition point of TME, which limits the removal temperature to 200 $^{\circ}$C, the aim was to increase this temperature by mixing TME with another plastic crystal with a higher transition point than TME. The transition point of the mixture can then be increased by changing the proportions of the two.

4.5.1   Potential plastic crystalline materials

A single plastic crystal exhibits a solid-solid transition in which vapour pressure is abnormally high. Their mixtures also present a plastic crystalline transition when the external temperature is above its transition point. This makes a plastic crystal mixture of special interest for applications in which the subsequent layers require a curing temperature higher than the transition temperature of pure TME.

Pentaerythritol (PE), which has a plastic crystalline transition point of 187 ^{o}C, was used because TME is a derivative of PE. Table 4-6 summarised the transition and melting temperatures of TME and PE.

Table 4-6: Theoretical transition and melting points of plastic crystals [121].

Compound name	Transition temperature (^{o}C)	Melting temperature (^{o}C)
Pentaerythritol (PE)	187	250
Trimethylolethane (TME)	87	187

According to the literature [118, 122-124], the transition temperature of a TME-PE mixture is determined by the proportion of each individual plastic crystal. Pure TME has a transition temperature of 87 ^{o}C and this temperature can be increased by adding Pentaerythritol (PE). The adjustable range of the transition temperature of TME-PE mixture is from 87 ^{o}C to 187 ^{o}C. By changing the transition temperature, the melting point of the mixture will also be changed. *Benson et. al.* [118] have measured the possible transition temperatures for a TME-PE mixture, the results are shown in Figure 4-29.
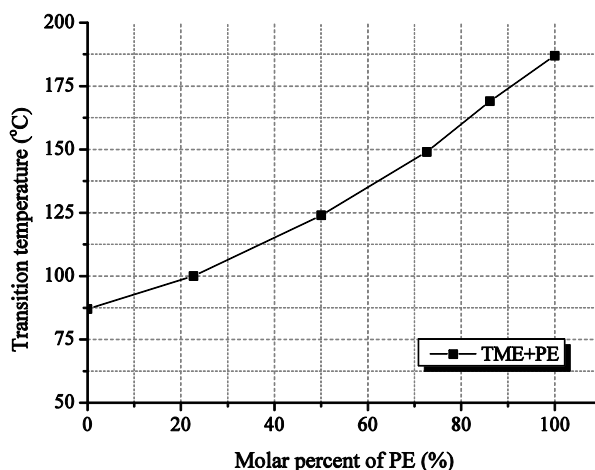
Figure 4-29: Transition temperature of TME and PE mixture [118].

When the proportion of PE is 0 %, the transition temperature is the same as the transition temperature of TME which is 87 $^{\circ}$C. As the amount of PE is increased, the transition temperature is gradually increased until the upper limit, which is the transition temperature of pure PE (i.e. 187 $^{\circ}$C). The transition temperature is function of the amount of PE hence the transition temperature is linearly controllable between 87 $^{\circ}$C and 187 $^{\circ}$C, thus the sublimation region is also shifted towards higher temperatures.

4.5.2 Mixing methods evaluation

Benson.et.al. [118] stated that the transition point of TME can be adjusted by mixing another plastic crystal to form a homogeneous mixture. According to *Benson*`s work, plastic crystalline samples should be prepared by melting and then solidifying to form a consistent mixture before any measurements are made. In *Benson's* work, TME and PE powders were ground together. A few milligrams of TME-PE mixtures were hermetically sealed in aluminium foil pans, and were melted and then solidified before any measurements. *Yan et.al.* [124] used a dissolution method in which the mixture was prepared by dissolving plastic crystals into an alcohol which was finally removed using an infrared heater. According to the literature reported in [125], PE has a high solubility in hot water; 77.2 g in 100 g water at 97 $^{\circ}$C. TME is soluble in water at any temperatures, so it is possible to dissolve TME and PE in hot water to form a mixture. For the purpose of comparison, the TME-PE mixture was prepared using three different methods described below; 1) melting, 2) dissolution in ethanol and 3) dissolution in hot water.

4.5.2.1   Experimental procedure

To examine the mixing approaches, the desired transition temperature was chosen as 100 ^{o}C from Figure 4-29. To achieve this temperature, 77.3 mol% of TME and 22.7 mol% PE are mixed. The experimental data are shown in Table 4-7.

Table 4-7: Materials used for each preparaion method.

Sample name	PE (22.7 mol%)	TME (77.3 mol%)
Melting method	1.54g	4.64g
Ethanol dissolution	1.55g	4.63g
Hot water dissolution	1.5g	4.6g

The three mixing procedures for combining TME and PE are as follows:

a) **Melting method**

To obtain a large amount of the mixture, a 45 ml autoclave (Parr 4744) from Parr Instrument Company was used. PE and TME powders were weighed using a precision scale and transferred into the Polytetrafluoroethylene (PTFE) container of the autoclave. A screw cap hermetically seals the autoclave so that the internal pressure created by the melting will not escape, thus the material mass will not reduce. The autoclave was placed in a box oven which was pre-heated to 250 ^{o}C, which is the melting point of PE. The melting process occurred by maintaining the autoclave at 250 ^{o}C for 1 hour and cooling down to room temperature. Three melting cycles were performed to form a homogenous mixture.

b) **Ethanol dissolution***

PE and TME powders were dissolved into 500 ml of ethanol at room temperature. A magnetic stirrer was used to stir the solution until the powders were fully dissolved. The solution was then placed in an oven at 60 ^{o}C for 24 hours to evaporate the ethanol and precipitate the mixture.

(*Because the solubility of PE (0.33 g/100g) is much lower than TME (28 g/100 g) in ethanol [125], the use of 500 ml ethanol provided a maximum dissolution of 1.5 g PE in this experiment.)

c) **Hot water dissolution**

100 ml of water was pre-heated to 90 ^{o}C prior to using. PE and TME powders were gradually added into hot water until the dissolution was completed. A beaker cover was

used to avoid the variation of the concentration due to evaporation. This solution was moved into a box oven and heated at 60 ^{o}C for 24 hours to remove the water.

4.5.2.2   Results

A pestle and a mortar were used to break down the precipitations produced from three methods before performing a DSC measurement. The DSC measurements were made using a temperature range from 50 ^{o}C to 230 ^{o}C at a rate of 20 ^{o}C/min.
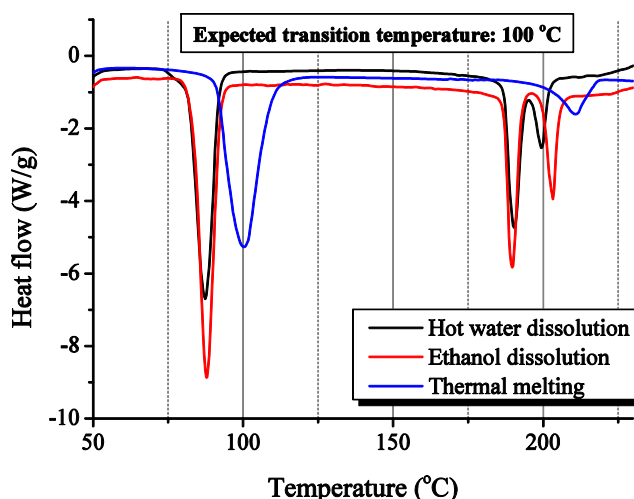
Figure 4-30: DSC results evaluating the three preparation methods for TME:PE mixtures.

From Figure 4-30, only the sample prepared using the melting method had a transition peak at 100 ^{o}C with a melting peak at approximately 210 ^{o}C. However, the other two samples prepared by dissolution methods had a first peak around 85~87 ^{o}C, which was the transition temperature of the pure TME. Each of these samples also had a second peak between 180 ^{o}C and 210 ^{o}C compared. The first peak within this range shows the melting point of TME and the second peak is likely the combination of the melting point of TME and transition point of PE. The reason for the double peaks was that both ethanol and hot water dissolutions could not sufficiently mix the TME and PE together. As the solubility of PE is much lower than TME in both water and ethanol and also PE has a different polarity than TME, it is believed that the most PE particles were not completely dissolved and mixed to form a homogenous solution but instead only formed a binary mixture. It was concluded that the melting method provided the best mixing compared with dissolution methods.

4.5.3 Preparation of TME and PE mixture

According to the experimental results from the previous sections, the melting method was the best approach to form a homogenous plastic crystal mixture. The transition temperature was proportional to the amount of PE in the mixture. To evaluate transition temperatures of different mixtures, several samples with different predicted transition temperatures were prepared.

4.5.3.1   Sample preparation for DSC measurement

Six samples prepared using the melting method are listed in Table 4-8. The proportions of TME and PE were selected based on [118].

Table 4-8: Sample preparation of TME and PE mixture.

Sample name	Predicted transition temperature	TME (mol%)	PE (mol%)
TME100:PE0	$87\,^oC$	100	0
TME77.3:PE22.7	$100\,^oC$	77.3	22.7
TME50:PE50	$125\,^oC$	50	50
TME27.4:PE72.6	$149\,^oC$	27.4	72.6
TME13.9:PE86.1	$169\,^oC$	13.9	86.1
TME0:PE100	$187\,^oC$	0	100

The melting procedure was same as the one used in section 4.5.2.1. Three melting cycles were performed. After melting, samples were crushed and ground to form fine powders for use in the DSC measurement.

4.5.3.2   DSC results

The transition temperatures of six samples were examined using DSC. The results are shown in Figure 4-31.
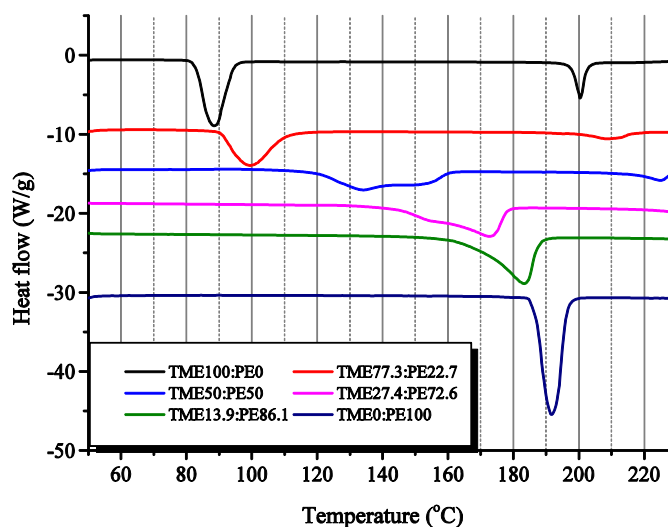
Figure 4-31: Transition temperatures for different mixtures of TME and PE.

The first peak of each curve represents the plastic crystalline transition temperature and the second peak is the melting temperature of the mixture (only for first three samples). Results show that the transition temperature of TME is increasing when increasing the proportion of PE.

4.5.3.3   TGA sample preparation

Mass loss evaluations of the previous six samples were obtained using TGA. Samples were prepared as follows:

- o Samples were carefully ground using a pestle and a mortar to obtain a fine powder prior to testing.
- o Individual sample was transferred into a 60 µL alumina crucible.
- o Air was pumped into the TGA furnace as the test environment.
- o Test profiles were set at 130 $^{\circ}$C, 160 $^{\circ}$C, 190 $^{\circ}$C and 220 $^{\circ}$C.
- o Test period was set for 1 hour.

4.5.3.4   TGA results

As the melting points of the TME-PE samples are increased after adding PE, it is of interest to evaluate these samples at a temperature higher than 200 $^{\circ}$C, which is the melting point of pure TME. As a result, 220 $^{\circ}$C was selected. The mass loss of each sample at 130 $^{\circ}$C, 160 $^{\circ}$C, 190 $^{\circ}$C and 220 $^{\circ}$C were analysed using TGA. The results are shown in Figure 4-32.
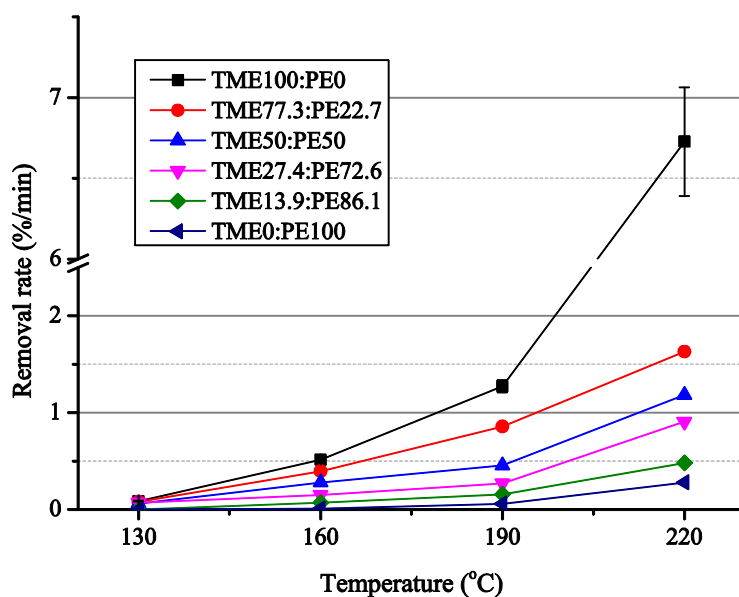
Figure 4-32: Mass loss of TME-PE mixtures.

It was found that the removal rate of each sample increased with temperature. The maximum removal rate was obtained with 100 % TME at all temperatures. At 220 $^{\circ}$C, the removal rate of the 100 % TME sample increased significantly due to the combination of sublimation and evaporation.

4.5.4 Discussion

In this section, the transition temperature of TME was increased by adding PE to form a TME-PE mixture which also has a plastic crystalline transition mechanism. It was difficult to obtain a homogenous TME-PE mixture using the dissolution methods because TME and PE have different polarities and solubility. At the melting temperature of PE, TME and PE were mixed in liquid phases so that the final mixture would be more homogenous compared with mixing in a solid phase.

DSC results showed that the transition temperatures were successfully changed by mixing PE into TME. The transition point of the final mixture depends on the amount of PE added into TME. Changing the transition point changes the sublimation temperature. TGA results showed that removal rates were inversely proportional to the amount of PE. To achieve the same rate of mass loss at higher levels of PE, the removal temperature had to be increased.

An adjustable removal rate can be useful whether or not a fabric substrate is used. Firstly, if using fabric substrates which have different operating temperatures, the removal temperature can be kept low to improve compatibility. Secondly, if using non-fabric substrates, the removal temperature of the mixture can be adjusted to increase the range of materials that can be included in this process so that the sacrificial layer can withstand higher temperatures before sublimation. Finally, to obtain the adjustment, only PE and TME are used thereby reducing the complexity of seeking alternative materials. However, the removal rate was affected by some factors, such as the layer thickness and the pattern surface area, because of the difference in mass. For instance, a thinner layer with a large surface area will sublimate faster than that of a thick layer with a small surface area.

4.6 Conclusions

In this chapter, potential sacrificial materials were evaluated through a three stage evaluation. The first stage was to find suitable sacrificial materials. The results showed that Dextran and Sucragel were unsuitable for use as a screen printable sacrificial material in their current form. Plastic crystal materials, NPG, TMP and TME were investigated with TME showing the most promising results. TME exhibited an ease of formulation compared to NPG and TMP in which a variety of concentrations could be achieved. Initial printing showed that a TME paste with 60 % concentration gave the best printing results. It was also shown that the TME paste could be removed by heating to 150 $^{\circ}$C leaving a free standing layer.

The second stage was the optimisation of the TME paste. By fully dissolving the TME powder in the solvent mixture, using a screen with a finer mesh and increasing the printing gap, the printing quality was improved. To provide a compromise between the maximum evaporation of cyclohexanol and a minimum sublimation of TME during curing, the curing temperature was increased to 85 $^{\circ}$C and the curing period was reduced to 5 minutes. The printed TME layer can be removed below 200 $^{\circ}$C but the actual removal temperature is dependent on the maximum operating temperature of a particular fabric and other relevant materials.

The third stage was the adjustment of the removal temperature of the TME paste by adding PE. The transition temperature was increased when the proportion of PE was increased. As a result, to achieve the same removal rate, the removal temperature was increased. This is a great advantage of the TME sacrificial material if used for different removal processes, because only the proportions of TME and PE need to be changed, thus reducing the complexity of seeking alternatives.

Chapter 5

Investigation into screen printable structural materials

5.1 Introduction

This chapter evaluates structural materials which could potentially be used in conjunction with the TME based sacrificial material identified in chapter 4 to fabricate free standing structures on fabrics. Materials with low temperature thermal and UV curing mechanisms are essential because these curing mechanisms will not damage the vast majority of fabrics.

The work described in this chapter was divided into two stages. The first stage was the selection of a suitable structural material which is compatible with the TME sacrificial material and the screen printing process. Since the structural material must be screen printable, potential materials are split into bespoke pastes and commercially available pastes. Bespoke pastes consist of materials which need to be formulated into a printable paste before using, such as silicone and ethyl cellulose. In contrast to bespoke pastes, commercially available pastes are ready to use. There are no commercial available pastes specific for structuring applications so the following sections evaluate the feasibility of using commercial screen printable pastes (i.e. dielectric paste) as the structural material. Three low temperature thermally curable pastes and four UV curable pastes are selected from different manufacturers to compare their properties and compatibility with fabrics. The second stage is the testing of the compatibility of the

selected sacrificial and structural materials with a printed interface layer for the fabrication of cantilever structures. Any structural deformation will be noted and subsequent optimisation may be required.

5.2 Evaluation method

The evaluation process is split into three stages, shown in Figure 5-1, based on the types and properties of the materials.
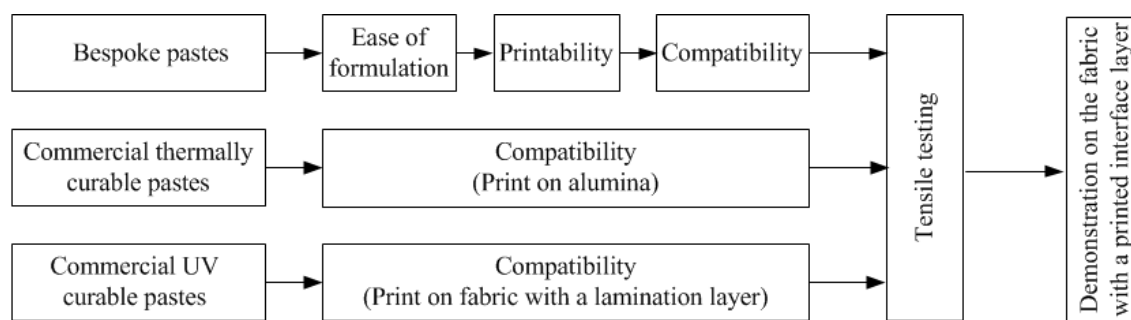
Figure 5-1: Evaluation method of a structural material.

For bespoke pastes, the evaluation processes are the same as that used for the selection of the sacrificial material, including the ease of formulation, printability and compatibility. If the materials fail in one of these stages, they will be dismissed from the candidate list. For commercially available pastes, the compatibility with the substrate and the sacrificial material will be evaluated.

Alumina tiles are used as substrates to evaluate the compatibility between all thermally curable pastes and the TME sacrificial paste. In contrast, fabrics are used as substrates for all UV curable pastes because the fabrics are unlikely to be damaged by UV light. The specific fabric used in this research is a polyester/cotton fabric which is the most prevalent fabric used in everyday clothing. It is supplied by Klopman International and consists of 65 % polyester and 35 % cotton yarns woven together [126]. All layers should be printed on the front side of the fabric which has a relatively smooth surface. Photographs of the front and back sides of this fabric are shown in Figure 5-2.
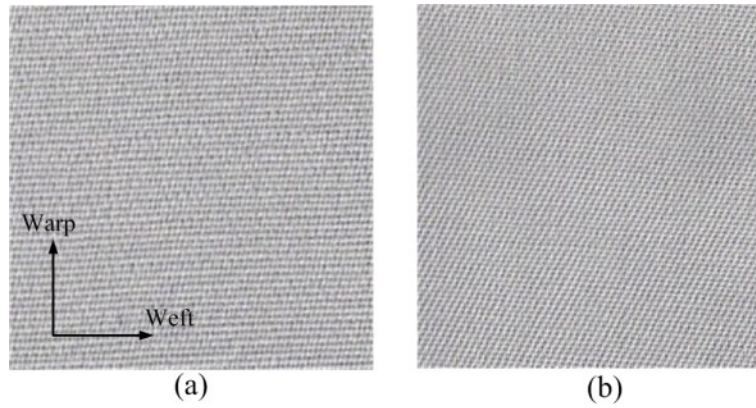
Figure 5-2: Photograph of a fabric: (a) Front side; (b) back side.

The yarns woven in the horizontal direction are called weft and those in the vertical direction are called the warp. The length of the weft is determined by the size of the weaving machine, whereas the length of the warp is dependent on the customer`s requirements. A significant difference between the front and back sides of the fabric for this particular fabric is the appearance in which yarns tend to align on orthogonal directions on the front, while a diagonal aligned appearance appears on the back side.

Due to the porosity, roughness and pilosity of the fabric surface, the printing definition can be poor compared with smooth substrates. A lamination film is therefore applied to provide a smooth platform for the deposition of structural and sacrificial materials, thereby reducing the likelihood that differences in the fabric surface will affect the evaluation results.

After the selection of a suitable structural material is completed, a demonstrator, in the form of a cantilever on a printed interface layer, is produced.

5.3 Bespoke pastes

5.3.1 Silicone rubber

Silicone is a polymer of which the chain length is a function of the silicone group number. The presence of a large number of silicone groups means a long chain in the final polymer. Usually, one or more organic groups are attached to silicone atoms to

meet the specific properties, such as resistance, stability/inertness and flexibility [127]. The viscosity of the silicone varies with different types of attached organic groups.

Silicone formulations can be split into three groups: oils, resins and elastomers [127]. Silicone oil is a non-flammable substance and has excellent electrical insulation properties. It is commonly used as the compound of lubricants. Silicone resin is for sealing, adhesive and coating applications to provide protection. Silicone elastomer is primarily used for moulding and flexible coating due to its flexibility and transparency. In a previous study by *Serra et. al.* [31], silicone was mixed with graphite powder to create a structural material with improved mechanical properties. The viscosity of the mixture is determined by the proportion of graphite and the initial viscosity of the silicone. Generally, the more graphite added, the higher the viscosity obtained; a higher viscosity can reduce the printability.

5.3.1.1 *Formulation and deposition processes*

The specific silicone used in this research was Q5-8401 silicone adhesive, which was ordered from Dow Corning. Q5-8401 has a viscosity of 77.43 Pa.s and a high tensile strength once cured [128]. It does not contain additive solvents, thereby reducing the likelihood of chemical reactions between the additional solvents and the sacrificial material. Q5-8401 consists of two parts with a mixing ratio 1:1. Once mixed, the material takes 24 hours to solidify at room temperature which is sufficient time for the printing process. Curing can also be achieved at 120 $^{\circ}$C for 90 minutes. Graphite powder, purchased from TIMCAL, was used as the additive to improve the mechanical properties (e.g. stiffness) of the silicone. No attempt was made to reduce the viscosity using solvents at this stage because of uncertainty about chemical reactions between additional solvents and the sacrificial material. Therefore, the following experiment is based on a mixture of the pure silicone adhesive and the graphite powder.

The two parts of the silicone were mixed in a beaker in a ratio of 1:1 using a spatula. Graphite powder was weighed and then gradually added into the silicone. The final mixture was homogenised using a triple roll mill. The formulation details are shown in Table 5-1.

Table 5-1: Silicone structural paste formulations.

Sample name	Graphite	Q5-8401
SG1	5 %	95 %
SG2	10 %	90 %

Initial experiments showed that the concentration of silicone-graphite mixture could not be increased higher than 10 wt% because of the agglomeration. Silicone samples were individually deposited onto alumina tiles using a spatula and cured at 85 ^{o}C. This temperature was selected based on the curing temperature of the sacrificial material. The curing period was experimentally determined during the testing. As cured silicone is noted in the literature as having a low surface energy, an adhesion test was performed to examine the surface adhesion of the two mixtures. Polymer silver (Johnson Matthey S-20) and carbon (DuPont[TM] 7102) pastes were selected as the test materials. These pastes have good adhesion to the substrates, thus they are appropriate materials for the surface adhesion test. Two pastes were individually deposited on top of cured silicone layers and cured at 125 ^{o}C for 10 minutes, as recommended in their datasheets. If the two materials bond to the cured silicone layer, the silicone paste is deemed to have passed the test.

5.3.1.2 *Experimental results and discussion*

Sample SG2 was too viscous to deposit as it formed agglomerates which adhered to the spatula. SG1 could be deposited using a spatula and was cured at 85 ^{o}C for a period of 2 hours which was long enough to solidify the mixture. It was found that the cured silicone layer bonded with the alumina tile and had a relatively smooth surface. However, it was easily damaged by scratching using a spatula. The damaged silicone layer is shown in Figure 5-3.
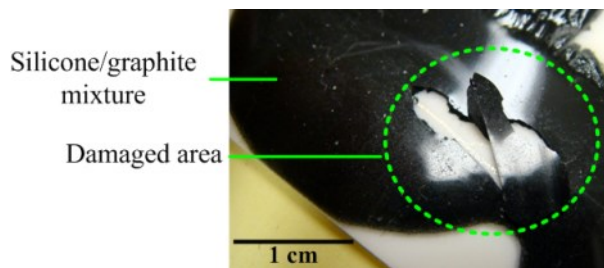
Figure 5-3: Scratching test of silicone/graphite layer.

Surface adhesion testing showed that silver and carbon pastes could be deposited onto the silicone layer and solidified to form continuous layers, but these pastes did not bond with the silicone layer. As a result, these layers were easily peeled from the silicone surface, shown in Figure 5-4. This would be a problem when subsequent layers were needed and printed on top.
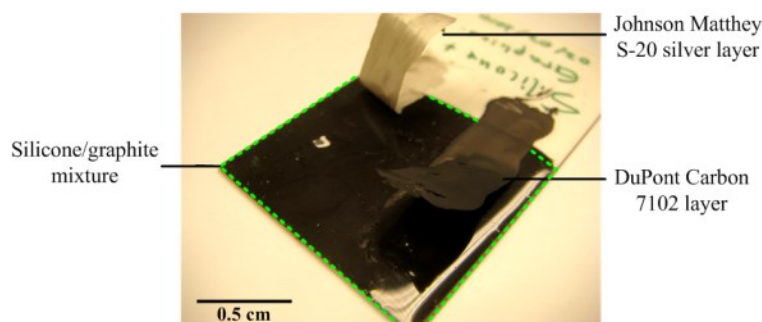
Figure 5-4: Adhesion test on silicone/graphite layer.

Pure silicone does not bond well with other materials; the silicone-graphite mixtures also exhibit the same results. In addition, the silicone-graphite mixture could not be printed because the viscosity was too high.

5.3.2   Ethyl cellulose

Ethyl cellulose (EC) is a colourless, odourless and rigid material with good thermal stability at temperatures below its melting point (135 ^{o}C) [129]. Ethyl cellulose also has good chemical stability because of its low reactivity [129-131]. Ethyl cellulose is one of the cellulose derivatives in which the hydroxyl groups (-OH) are substituted by ethoxyl groups (-CH$_2$CH$_3$). Figure 5-5 shows the molecular structures of ethyl cellulose and cellulose molecules.
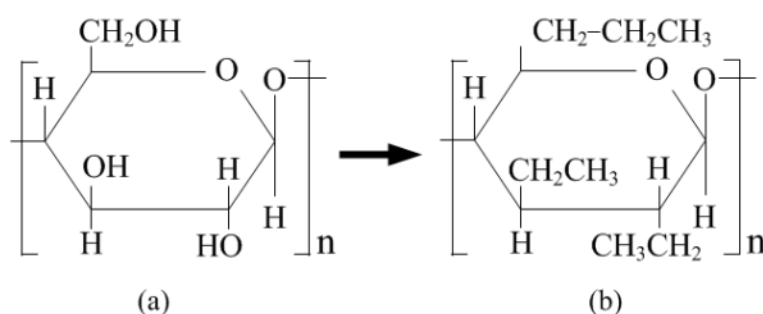
Figure 5-5: Molecular structure of cellulose (a) and ethyl cellulose (b).

Ethyl cellulose is classified into two grades based on the proportion of ethoxyl groups: the standard grade has an ethoxyl content from 48 to 49 % and the medium grade has an ethoxyl content from 45 to 47 %. Ethyl cellulose is soluble in a wide range of solvents, such as alcohols, esters, hydrocarbons and ketones, but practically insoluble in water [129]. The viscosity of the ethyl cellulose solution is determined by the length of the cellulose molecular chain and the type of dissolution solvent used.

5.3.2.1   Formulation and deposition processes

Ethyl cellulose (No. 433837), purchased from Sigma-Aldrich, is a standard grade which has an ethoxyl content of 48 %. As ethyl cellulose is soluble in a variety of solvents and their mixtures, specific chemicals had to be selected for this purpose. The possible solvents selected from each solvent type to dissolve the ethyl cellulose are shown in Table 5-2.

Table 5-2: Dissolution solvent selection.

Solvent type	Chemicals
Alcohols	Ethanol, cyclohexanol
Esters	ethyl lactate
Ether	2-Butoxyethyl ether
Hydrocarbons	Cyclohexane
Ketones	Acetyl acetone

The formulation was obtained by mixing the ethyl cellulose powder with each solvent or solvent combination. A magnetic stirrer was used to blend the mixtures thoroughly. The ethyl cellulose powder had to be added into the solvents slowly due to its thickening properties which increase viscosity dramatically. After ethyl cellulose was fully dissolved, graphite powder was weighed and then added while continuously stirring for an extra 30 minutes. Finally, the ethyl cellulose-graphite mixtures were homogenised at room temperature for 24 hours before testing.

Ethyl cellulose-graphite mixtures were deposited using a spatula onto alumina tiles and dried at 85 $^{\circ}$C. In addition, a surface adhesion test was performed to evaluate the adhesion properties of cured ethyl cellulose-graphite layers. Silver and carbon pastes

were then deposited on top of dried ethyl cellulose-graphite layers and were cured at 125 ^{o}C for 10 minutes in the same procedure used for the silicone tests.

5.3.2.2 *Experimental results and discussion*

A homogeneous solution was achieved by dissolving the ethyl cellulose powder into cyclohexanol, which was also used as the dissolution solvent for the sacrificial material. Full dissolution was achieved after 1 hour. The maximum concentration of ethyl cellulose in cyclohexanol was 10 wt%, increasing this concentration resulted in a gelatinous gel. Graphite powder was then gradually added into the dissolved ethyl cellulose mixture and was stirred simultaneously until the mixture became viscous. As a result, a maximum concentration of 15 wt% of graphite was achieved before agglomeration occurred.

The mixture was deposited onto an alumina tile using a spatula. After drying at 85 ^{o}C for 15 minutes, the ethyl cellulose-graphite mixture formed a rigid layer with a bubbled surface. Figure 5-6 shows the deposited mixture with the silver and carbon layers printed on top.
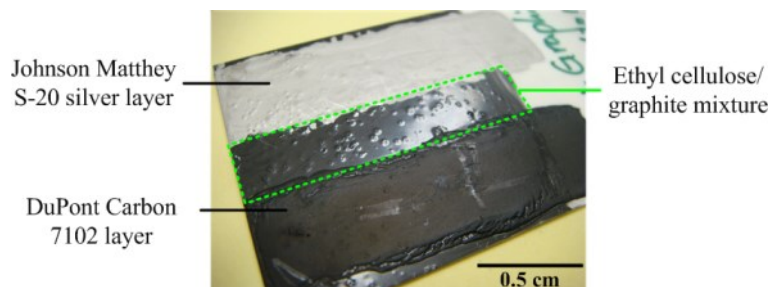
Figure 5-6: Adhesion test on ethyl cellulose-graphite layer with deposited silver and carbon layers.

A vacuum container in which the pressure was maintained at -80 kPa for 20 minutes was used to attempt to remove these bubbles from the mixture; however, this appeared to have no impact. An adhesion test showed that the ethyl cellulose-graphite mixture provided a strong bond to subsequent layers because the deposited silver and carbon layers are difficult to remove after curing. The results produced by mixing ethyl cellulose with other solvents were not as good as those using cyclohexanol. For instance, a mixture obtained by mixing ethyl cellulose with ethanol had a fast dissolution and low viscosity, but it reacted with the sacrificial layer. A mixture

achieved by mixing ethyl cellulose with acetyl acetone had cracked surface after curing. When mixing ethyl cellulose with cyclohexane, 2 hours dissolution period was required resulting in a viscous mixture that could not be used. The formulation details and photographs of these mixtures are shown in appendix B.

Ethyl cellulose was dissolved in a variety of solvents and the best result was achieved using cyclohexanol. By adding graphite powder into the dissolved ethyl cellulose, the viscosity was further increased. Deposition results showed that the ethyl cellulose-graphite mixture strongly bonded with the substrate and adhesion tests showed that silver and carbon layers also firmly bonded with the solidified ethyl cellulose-graphite layer. However, bubbles on the surface affected the printing quality of subsequent layers. It is believed that these bubbles were due to thickening properties of ethyl cellulose, thus the air was trapped in the mixture. Overcoming this problem at this stage would be difficult and other easier options were available. Therefore ethyl cellulose was dismissed.

5.4   Commercially available pastes

There are many types of commercially available screen printable materials, such as conductive, dielectric and piezoelectric pastes. These pastes are typically classified by their composition as either a ceramic or polymer paste. Ceramic pastes require high firing temperatures in excess of 800 ^{o}C to solidify the printed layers. These temperatures will destroy the majority of fabrics and other printed polymer layers. In contrast, polymer pastes can be solidified by using either low temperature (<150 ^{o}C) or UV light. Usually, UV curable materials have a relatively small shrinkage after curing compared with thermally curable materials. As polymer pastes have more fabric compatible curing mechanisms, they have greater potential to be used for smart fabrics.

5.4.1   Material selection and deposition parameters

To avoid interference with the operation of the sensors and actuators, a non-conductive material would be appropriate as the structural material. There are a wide range of non-conductive pastes available so that this is a good starting point. Unlike the bespoke pastes, commercially available pastes already have appropriate rheology and therefore it

is unnecessary to evaluate the ease of formulation. Three thermally curable pastes and four UV curable pastes were selected as candidates because they are commonly used for the fabrication of printed electronics. It is of interest to evaluate the compatibility of the silver paste with the sacrificial material because the silver paste is commonly used as the electrode material. Table 5-3 shows the selected thermally curable materials and their printing and curing parameters.

Table 5-3: Printing and curing parameters of thermally curable pastes.

Paste name	Printing parameters	Curing condition	Substrate
Johnson Matthey S-20	Print speed: 50 mm/s, Gap: 0.8mm, Pressure: 5 kg, Deposits: 2, Prints: 5.	Box oven, 125 ^{o}C 15min	Alumina
DuPont 8153	As above	As above	As above
Electra Polymers ELX80	As above	As above	As above

Four UV curable dielectric pastes were selected because they have a relatively low solvent content in contrast to the thermally curable pastes. As a result, the volume shrinkage is typically small compared with the thermally curable pastes. The material details and deposition parameters are shown in Table 5-4.

Table 5-4: Printing and curing parameters of UV curable pastes.

Paste name	Printing parameters	Curing condition	Substrate
Johnson Matthey K-920	Print speed: 70 mm/s, Gap: 0.8mm, Pressure: 5 kg, Deposits: 2, Prints: 5.	60 seconds UV	Fabric with a laminated interface layer
Electra Polymers ELX40T	As above	As above	As above
Electra Polymers EFV4/2647T	As above	As above	As above
Electra Polymers EFV4/4965	As above	As above	As above

To deposit these pastes, a polyester screen (120 threads per cm) with 40 μm emulsion was used. Screens were designed to fabricate cantilevers in different lengths to examine

the suitability of materials for use as structural materials. The screen design and the printing structure, and the dimensions for cantilevers are shown in Figure 5-7 and Table 5-5, respectively.
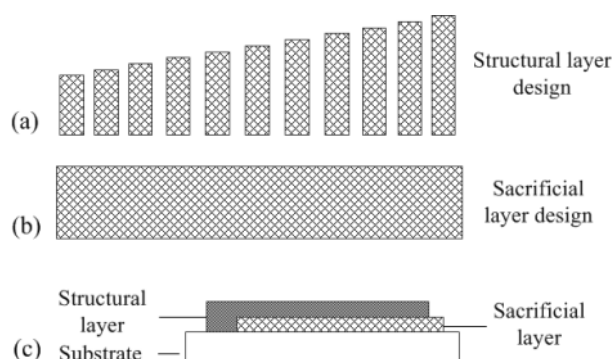
Figure 5-7: (a) Structural layer screen design (top-down); (b) sacrificial layer screen design (top-down); (c) printed structure (cross-section).

Table 5-5: Cantilever dimensions.

Cantilever No.	1	2	3	4	5	6	7	8	9	10	11
Width (mm)	5	5	5	5	5	5	5	5	5	5	5
Length (mm)	3.0	4.5	6.0	7.5	9.0	10.5	12.0	13.5	15	16.5	18

For thermally curable materials, alumina tiles were used as substrates, whereas polyester/cotton fabrics with laminated interface layers were used for UV curable materials. Fabric substrates were prepared by laminating a plastic film (i.e. acetate) with a thickness of 80 μm onto the front side of the fabric using a Digital Knight 20S laminator. The lamination temperature and period were 160 $^{\circ}$C and 6 seconds, respectively. The selection of the laminated interface layer was determined by its surface energy which was measured using a Krüss DSA30 tensiometer at room temperature. The measurements show a surface energy of 40 mN/m which was comparable with the measured surface energy of Kapton (43 mN/m), which is widely used for printing flexible electronics. Once the lamination was completed, the fabric substrates were individually mounted onto alumina tiles using 3M spray glue. This glue provides a temporary bond between the fabric and the alumina tile which provides rigidity and support during the printing process. Finally, the alumina tiles are removed after fabrication.

The TME sacrificial layers were printed and dried at 85 °C for 5 minutes. The structural materials were individually printed on top of the sacrificial layers and dried at their corresponding curing conditions. The final removal process was achieved by individually placing the sample in a box oven at 150 °C for 30 minutes. Metal clips were used on each side of the fabric substrate to prevent the fabric from peeling from the tile as the high temperature weakens the 3M adhesive.

5.4.2 Experimental results and discussion

5.4.2.1 Thermally curable pastes

Johnson Matthey S-20 silver paste

Figure 5-8 shows the silver cantilevers before and after the removal process.
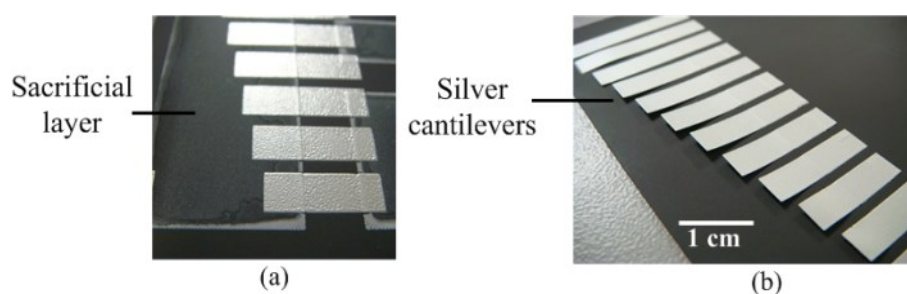
Figure 5-8: S-20 silver cantilevers on alumina tile before (a) and after (b) removal.

All silver cantilevers were released from the substrate when the TME was removed. The longer cantilever, No. 11, sagged onto the substrate because the cantilever could not support itself under gravity, however, the shorter cantilevers, from No. 1 to 10 remained free standing, shown in Figure 5-8 (b).

Electra Polymers ELX80 pastes

Figure 5-9 shows the ELX80 cantilevers before and after the removal process.
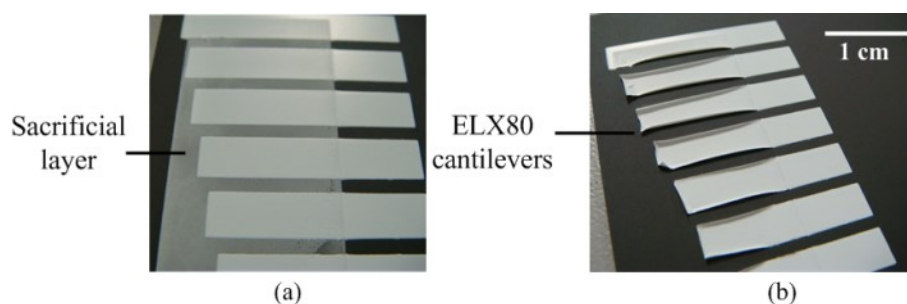
Figure 5-9: ELX80 on an alumina tile before (a) and after (b) removal.

Cantilevers fabricated by using the ELX80 paste were difficult to release as these cantilevers adhered to the alumina tile, after the removal of the sacrificial layer. It could be the reaction between the ELX80 and the TME sacrificial materials. The side edges of the cantilevers curled and bent out away from the substrate, as shown in Figure 5-9 (b).

An additional test was performed to examine the influence of gravity. Figure 5-10 shows the configuration of the experiment.
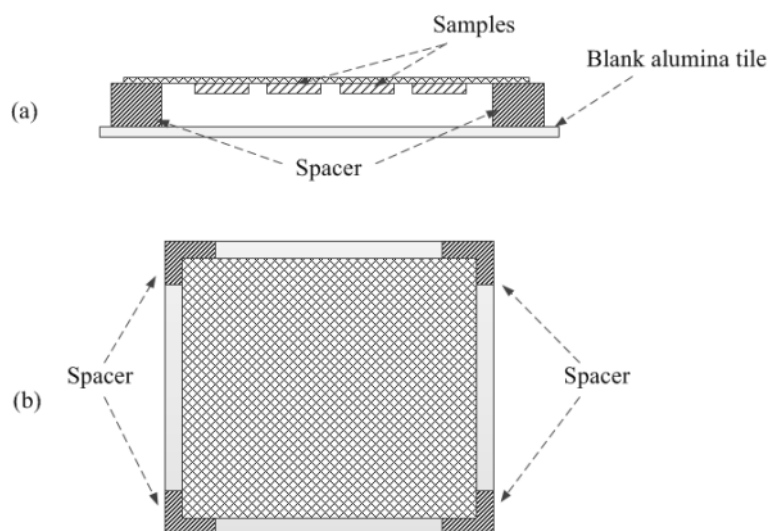
Figure 5-10: An alternative removal configuration for ELX80 cantilevers: (a) side view; (b) top view.

Four 1 cm thick spacers were used to support the samples during the removal process. Samples were placed upside down so that gravity would pull away the cantilevers once the sacrificial layer was removed. The circulating airflow in the oven is able to pass across the sample from all directions through the gap between the sample and the blank alumina tile. However, after a 30 minutes removal process, the ELX80 cantilevers still adhered to the alumina tile.

As the Johnson Matthey S-20 silver cantilevers were fully released from the alumina tile, a further experiment to release the ELX80 cantilevers involved printing a silver barrier layer between the sacrificial layer and the ELX80 cantilevers. If the silver and ELX80 layers could be released simultaneously, a chemical reaction between the ELX80 and TME could be the cause of the problem. Figure 5-11 shows ELX80 cantilevers when using a silver barrier layer before and after the removal process.
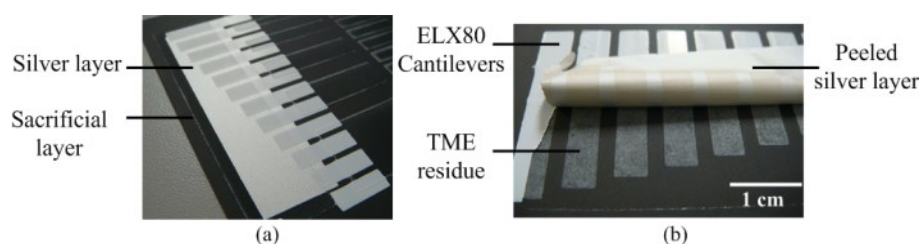
Figure 5-11: Printing results of ELX80 with a silver barrier layer: (a) before removal; (b) after removal.

The results showed that ELX80 cantilevers were not removed even with a silver barrier layer. By peeling the silver layer from the substrate, it was found that the sacrificial material remained beneath the silver layer. It is believed that the adhesion problem was due to the reaction between ELX80 and the sacrificial material. This reaction prevented the TME from being removed and therefore TME residue was left on the substrate.

DuPont 8153 dielectric paste

DuPont 8153 showed similar behaviour to ELX80; the cantilevers adhered to the alumina tile after removal. Figure 5-12 shows the results of DuPont 8153 cantilevers before and after the removal process.
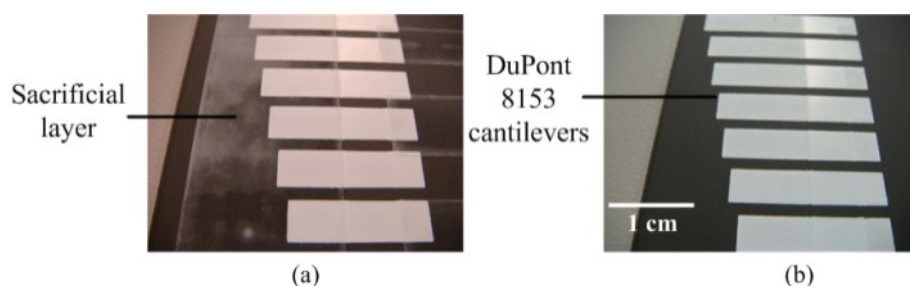
Figure 5-12: DuPont 8153 cantilevers on an alumina tile before (a) and after (b) removal.

No curled edges were observed on DuPont 8153 cantilevers. By flipping the sample and printing an extra silver barrier layer, these cantilevers still adhered to the alumina tile suggesting that a chemical reaction could occur between DuPont 8153 and the sacrificial material.

5.4.2.2   UV curable pastes

Johnson Matthey K-920

Figure 5-13 shows printed cantilevers composed of K-920 UV curable paste on a laminated fabric.
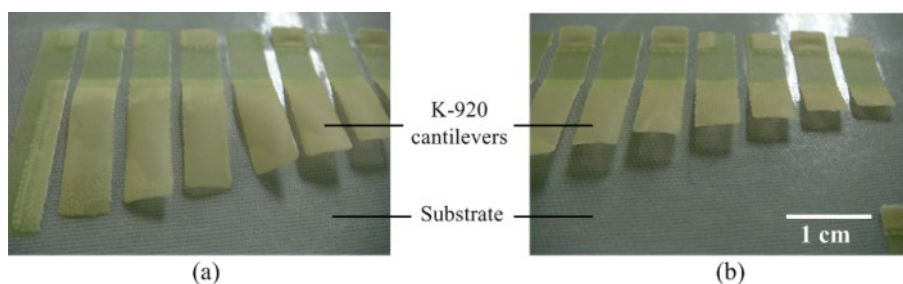
Figure 5-13: K-920 cantilevers: (a) No. 6~11 cantilevers; (b) No. 1~7 cantilevers.

The sacrificial layer was fully removed and no residue was left beneath these cantilevers. No significant damage was observed on either the fabric or the interface layer. However, it was found that the longer cantilevers (No. 8-11) tended to sag onto the substrate and curl at the edges after the removal process, whereas the shorter cantilevers (No. 1-7) were relatively flat.

Electra Polymers EFV4/4965

Cantilevers fabricated using EFV4/4965 on a laminated fabric are shown in Figure 5-14.
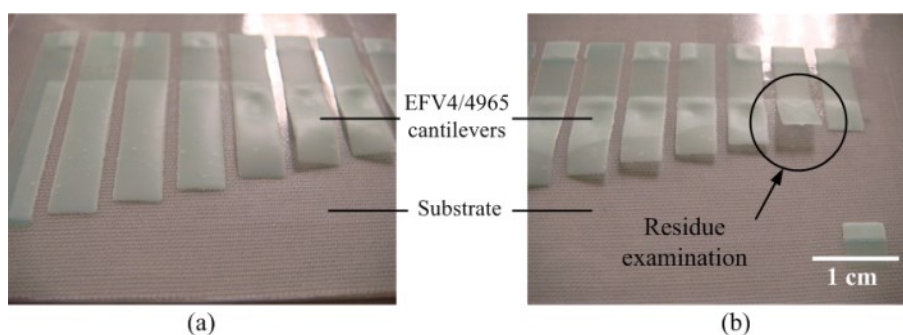
Figure 5-14: EFV4/4965 cantilevers: (a) No. 6~11 cantilevers; (b) No. 1~7 cantilevers.

All eleven cantilevers were completely released from the substrate when the sacrificial layer was removed. The amount of residue was examined by bending the cantilever upwards using tweezers. It was found that no TME residue remained. In contrast to the results obtained with K-920, the longer cantilevers (No. 9-11) were flat and smooth, whereas the shorter cantilevers (No. 1-8) had curled edges and bent inwards. It was

believed that the bending of the cantilever was caused by the difference between stress and gravity. For instance, a longer cantilever has higher gravity than the generated stress thereby pulling entire cantilever towards the substrate; whereas, the stress generated on a short cantilever may be higher than its gravity, therefore, pulling the cantilever upwards.

Electra Polymers ELX40

Cantilevers fabricated using ELX40 on a laminated fabric were shown in Figure 5-15.
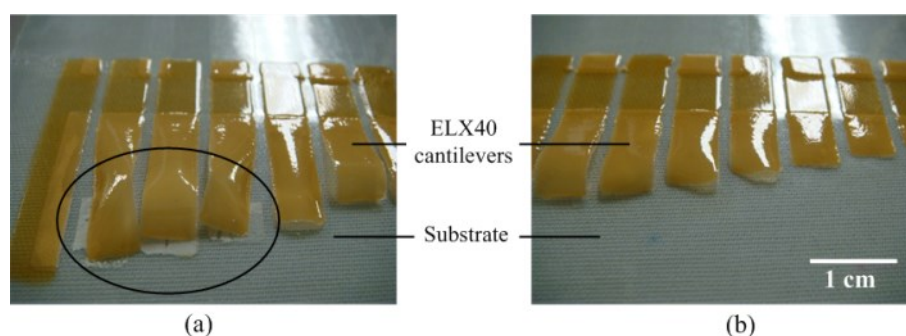
Figure 5-15: ELX40 cantilevers: (a) No. 7~11 cantilevers; (b) No. 1~7 cantilevers.

Most cantilevers significantly curled and sagged onto the substrate. This could be due to the thermal plastic behaviour of the ELX40 as it can be softened while heating up. As a result, cantilevers were bent during the removal process. TME residue was found beneath the longer cantilevers (No. 7-11), whereas no residue was observed beneath the shorter cantilevers (No. 1-6). The reason could be a reaction between the sacrificial material and ELX40 during the printing process. In addition, it is likely that the printing areas cause the sacrificial layer to be sealed beneath the larger printed ELX40 layers. ELX40 also had poor adhesion to the substrate which could be the result of its thermal plastic behaviour in that the layer was softened during the removal process resulting in poor adhesion, shown in Figure 5-16.
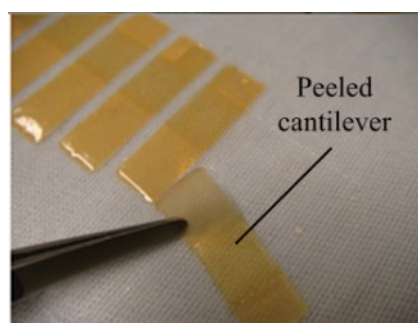
Figure 5-16: An ELX40 cantilever peeled from the substrate.

Electra Polymers EFV4/2647T

EFV4/2647T has a similar appearance to ELX40 but has the different formulation provided by the manufacturer. The results of using EFV4/2647T are shown in Figure 5-17.
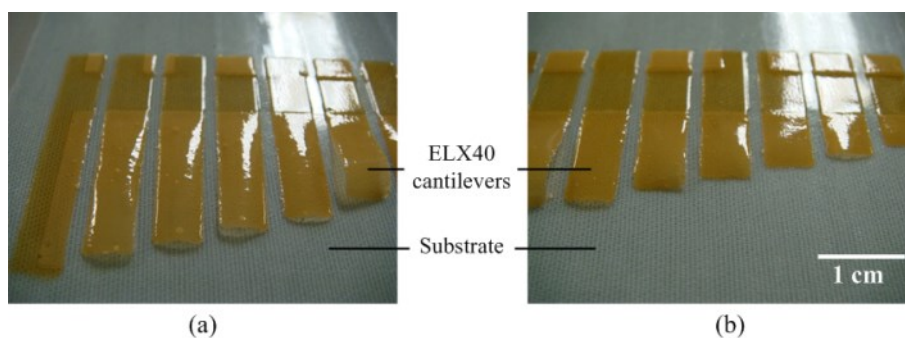
Figure 5-17: EFV4/2647T cantilevers: (a) No. 7~11 cantilevers; (b) No. 1~6 cantilevers.

No material residue was found beneath these cantilevers. The longer cantilevers (No. 7~11) curled and the shorter cantilevers (No. 1~6) sagged onto the substrate after removal. Small bubbles were also observed on the surface of the cantilever. In addition, EFV4/2647T cantilevers also had poor adhesion to the substrate and the cantilevers were easily peeled from the substrate.

5.4.2.3   *Summary*

In this section, three thermally curable materials and four UV curable materials were evaluated. Of the thermally curable materials, Johnson Matthey S-20 silver paste had the best removal result, whereas ELX80 and DuPont 8153 had chemical reactions with the sacrificial material. As a result, the TME layer was not able to sublimate. Of the UV curable materials, K-920 and EFV4/4965 had strong adhesion to the substrate, while ELX40 and EFV4/2467T were easy to remove from the substrate. Cantilevers created by using K-920 had a smooth and flat surface when the length was from 3 mm to 12 mm (No. 1~7), whereas cantilevers fabricated using EFV4/4965 had a smooth and flat surface when the length was from 13.5 mm to 18 mm (No. 8~11).

It was found that the fabric was not damaged by sacrificial removal at 150 $^{\circ}$C, confirming that the removal condition is compatible with the polyester/cotton fabric. In addition, no delamination, deformation, or damage to the laminated interface layer was

observed; thus the removal condition was also suitable for this particular laminated interface layer material.

5.4.3 Tensile test of structural materials

A tensile testing machine is a machine whose primary function is to obtain a stress-strain curve by extending a sample and recording the force and the extension length. In this test, the tensile testing machine used was an INSTRON electro plus 1000, shown in Figure 5-18. The grippers were mechanical clamps with serrated edges to hold the sample.
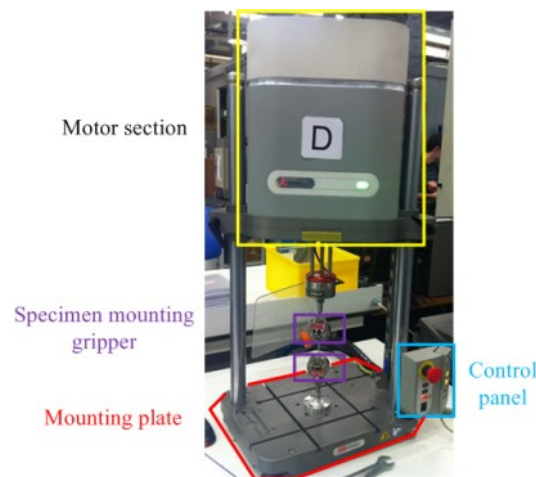
Figure 5-18: INSTRON Electro plus 1000 tensile test equipment.

A tensile test was performed to select the most suitable structural material from the remaining candidates based on their measured mechanical properties. K-920 and EFV4/4965 were examined because these materials produced the best printing results.
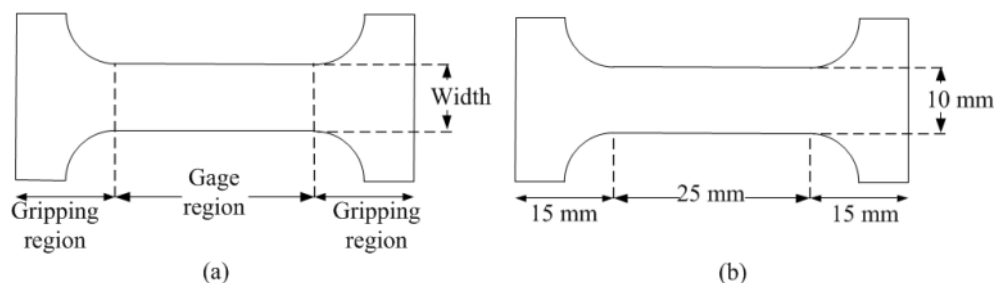
Figure 5-19: (a) schematic diagram of the specimen; (b) actual dimensions for the tensile test.

Figure 5-19 (a) shows the design for a tensile test sample. It has two enlarged ends to grip during extension of the sample. The middle area is called the gauge area. The cross-sectional area of the gauge section in this test is a rectangle. The cross-sectional area of the gauge section should be half smaller relative to the two enlarged areas so that the deformation and failure will be located in the gauge region rather than gripping areas [132]. The gripper keeps the sample in position during the testing without slippage or failure. The dimensions of the testing specimen are shown in Figure 5-19 (b). It had a gauge region with length 25 mm long and width 10 mm. The gripping areas had length 15 mm, reducing the risk of deformation in these areas.

The screen printable materials are provided in a paste form which cannot be tested directly on a tensile machine. These materials must therefore be solidified prior to testing. To achieve the testing shape, a mould is required. Due to the UV curing mechanism which does not require high temperatures, PTFE is suitable as the mould material because it has poor adhesion to the materials. The mould was created by machining the specimen shape into a thick PTFE sheet which was then glued into an aluminium frame to provide extra support, shown in Figure 5-20 (a).
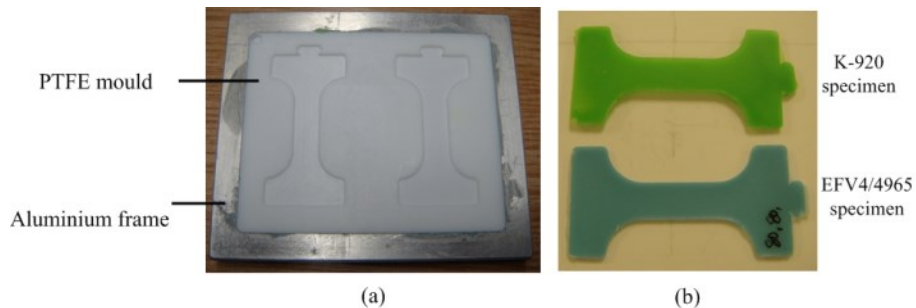
Figure 5-20: (a) A photograph of the PTFE mould and (b) casted samples.

Specimens were prepared by stencil printing, by hand, two pastes onto the PTFE mould using a squeegee blade and curing in a UV cabinet for 300 seconds (7.7 J/cm^2) to ensure full curing. Solidified materials were then peeled from the mould and were ready for test, as shown in Figure 5-20 (b). Five specimens were used for each material to obtain an accurate result. The results are given in Figure 5-21.
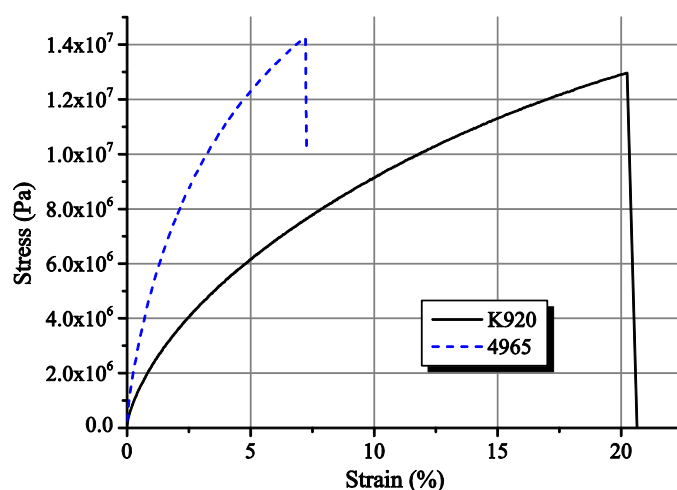
Figure 5-21: Stress-strain curves of four UV curable materials.

EFV4/4965 has a steeper strain-stress curve than K-920, which shows that the Young's modulus of EFV4/4965 is higher than that of K-920. The Young's modulus of the two materials is then calculated based on the ratio of stress over strain when the strain is increased to 0.5 %. Table 5-6 summarises the tensile test results of EFV4/4965 and K-920 pastes as well as their measured viscosities.

Table 5-6: Young`s modulus and viscosities of two UV curable materials.

Material name	Young's modulus*	Viscosity**
Electra Polymers EFV4/4965	638 MPa	9.50 Pa.s
Johnson Matthey K-920	293 MPa	5.30 Pa.s

*6 samples for each material were tested. Standard deviation of EFV4/4965: 23; Standard deviation of K-920: 9.

**Viscosities were measured using BrookField CAP 1000+ viscometer at a fixed spindle speed of 10 rpm.

The Young's modulus of EFV4/4965 is twice than that of K-920, so the cantilevers created using EFV4/4965 would have greater strength and be more likely to be self-supporting on top of the substrate once the sacrificial layer is removed. In addition, the viscosity of EFV4/4965 is higher than that of K-920, making it easier build up a thick layer.

5.5 Discussion

Table 5-7 provides a comparison of materials evaluated in this section.

Table 5-7: Summary of evaluated structural materials.

Material name	Ease of formulation	Printability	Compatibility*	Notes
Silicone	Poor	No	Not tested	Poor adhesion
Ethyl cellulose	Poor	No	Not tested	Bubbled surface
S-20	N/A	Yes	Yes	Expensive/unexpected conductivity
ELX80	N/A	Yes	No	Reaction
DuPont 8153	N/A	Yes	No	Reaction
K-920	N/A	Yes	Yes	Low viscosity, low E
EFV4/4965	N/A	Yes	Yes	High viscosity, high E
ELX40	N/A	Yes	Yes	Poor adhesion
EFV4/2647T	N/A	Yes	Yes	Poor adhesion

*It describes the compatibility between the sacrificial material and the candidate.

Cured silicone has poor adhesion to other material and other materials have poor adhesion to silicone. The ethyl cellulose-graphite mixture has a surface which can be printed on. However, air bubbles in the mixture were difficult to remove, resulting in poor surface smoothness. Thermally curable S-20 silver paste was compatible with the sacrificial material. Eleven silver cantilevers, of lengths 3~18 mm, were completely released from the alumina tile after the sacrificial material was sublimated. However, its conductivity, which may be unwanted, and the high cost of the silver prevent it being used as a structural material. EFV4/4965 could be used to fabricate well defined cantilevers when the cantilever length is longer than 12 mm. It also has a high Young's modulus compared with K-920. The viscosity of EFV4/4965 is higher than K-920 which could potentially reduce the time taken to fabricate thick layers. Other UV curable materials were significantly less compatible with this process than EFV4/4965 and therefore these materials will not be evaluated any further.

5.6 Evaluation of EFV4/4965 on fabrics with a printed interface layer

An evaluation was previously undertaken on fabric with a laminated interface layer. The disadvantage was that the entire fabric had to be covered by a lamination film. The flexibility and breathability of the fabric is affected by adding this extra layer. The benefit of a printed interface layer is that it is only printed where needed and consequently the flexibility/breathability of the fabric is not significantly affected. The interface paste used in this research was developed by the University of Southampton and is based on polyurethane. This paste is called Fabinks-UV-IF1. UV curing allows a faster printing/curing process which can be used to build a thick layer in a short period. UV curing mechanism reduces the risk of removing the sacrificial material during the fabrication process. To demonstrate the feasibility of using the selected materials for fabricating free standing structures, cantilevers were printed onto a fabric with a printed interface, sacrificial and structural layers.

The screen design and the dimensions of each layer are shown in Figure 5-22 and Table 5-8, respectively. These dimensions were chosen to produce macro-scale devices which were easier handle and evaluate any problem.
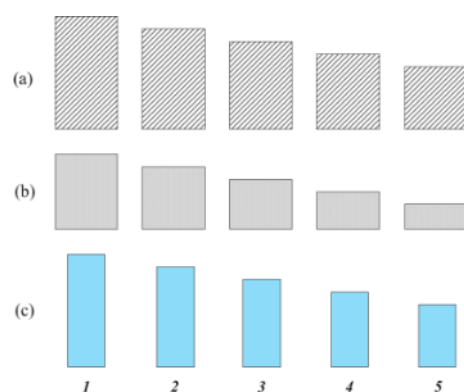
Figure 5-22: Screen design: (a) interface layer; (b) sacrificial layer; (c) structural layer.

Table 5-8: Testing dimensions for cantilevers on fabric with a printed interface layer.

Sample No.	1	2	3	4	5
Interface layer (mm)	13×26	13×23	13×20	13×17	13×14
Sacrificial layer (mm)	9×17	9×14	9×11	9×8	9×5
Cantilever (mm)	5×16	5×13	5×10	5×7	5×4
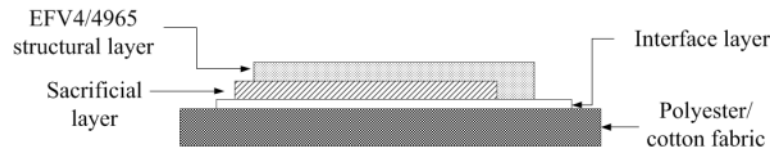
Figure 5-23: Cross-section of the printed layers for cantilevers on fabric with a printed interface layer.

Figure 5-23 shows the printing sequence to produce cantilevers on fabric. Polyester/cotton substrates were prepared as before. The interface layers were printed only where needed. The number of prints was experimentally determined by applying complete printing/curing cycles until a smooth and flat surface was obtained. A sacrificial layer was then printed on top, followed by the structural layer.

To achieve a smooth printed interface layer, two printed and cured layers were needed. The first print involved six deposits to fill the fabric structure before curing and the second print had only four deposits to obtain a smooth surface after curing. The TME sacrificial material was then printed on top of the interface layer and dried at 85 $^{\circ}$C for 5 minutes. Next, EFV4/4965 was printed on top of the sacrificial layer and UV cured for 60 seconds. Once the printing was finished, the sacrificial layer removal process was performed in a conventional box oven at 150 $^{\circ}$C for 30 minutes. Figure 5-24 shows that the resulting cantilevers are completely released from the interface layer.
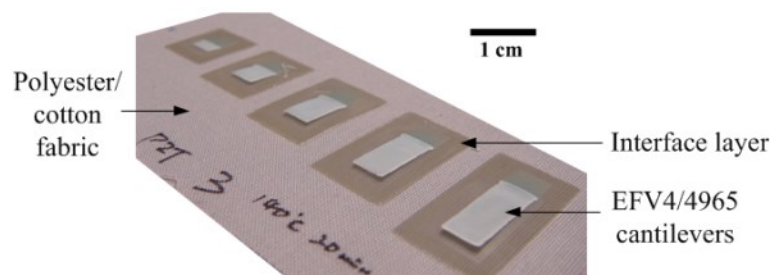
Figure 5-24: EFV4/4965 cantilevers fabricated on top of the printed interface layers.

No curling or deformation was observed on the interface layer after the sacrificial layer was removed. It was also found that there was no chemical reaction between the sacrificial and interface materials, confirming their compatibility.

The interface paste exhibited good compatibility with the fabric, sacrificial and EFV4/4965 structural materials and no chemical reaction appeared to have occurred

between these materials during the printing, curing and removal processes. Sacrificial and structural layers could be printed on top of the interface layer without any adhesion problems. The sacrificial layer could be fully removed from between the interface and structural layers and all cantilevers were successfully released from the fabric substrate.

5.7 Conclusions

Nine different structural materials and their associated mixing, printing and curing processes were evaluated in this chapter. The silicone-graphite mixture was not able to print and had a surface to which other materials did not adhere. Ethyl cellulose-graphite mixture had low solid content and also bubbles in the material reducing the surface smoothness. Of the thermally curable pastes, the polymer silver paste Johnson Matthey S-20 was compatible with the sacrificial material and its cantilevers were fully released once the sacrificial material was removed. ELX80 and DuPont 8153 had chemical reactions with the sacrificial material, preventing their cantilevers being released. Of the UV curable pastes, ELV4/4965 had better adhesion to the substrate than ELX40 or EFV4/2647T and a significantly higher Young's modulus than K-920. In addition, no residue remained beneath the cantilevers created by EFV4/4965, whereas TME residue did remain when ELX40 and EFV4/2647T were used as structural materials.

The evaluation of EFV4/4965 on fabric showed that EFV4/4965 was compatible with the interface layer, which was only printed where needed, whereas the laminated interface layer had to cover the entire area of the fabric meaning that a printed interface layer would increase the flexibility and decrease breathability of the fabric compared with a laminated interface layer. By printing sacrificial and structural materials on top of the interface layer and removing the sacrificial layer in an oven, free standing cantilevers were achieved, confirming the compatibility of these materials. It was concluded that EFV4/4965 was an appropriate structural material for use in conjunction with the TME sacrificial material. It was also confirmed that cantilevers could be fabricated on fabrics using only screen printing.

Chapter 6

Screen printed cantilevers on fabrics

6.1 Introduction

This chapter demonstrates the feasibility of fabricating free standing cantilevers with multiple layers on fabrics using the selected materials. In chapter 5, a simple cantilever with only one structural layer was fabricated using the interface, sacrificial and structural materials. The feasibility of the fabrication process was evaluated. In this chapter, by adding additional functional layers, more complex cantilevers are presented.

This chapter is comprised of two sections; the first section presents capacitive free standing cantilevers which require an interface layer, top/bottom electrodes, a structural layer and a sacrificial layer. The sensing mechanism is the change in capacitance due to a change in the distance between two electrodes. The second part presents cantilevers with a piezoelectric layer on top of the cantilever as the sensing mechanism. Both types of sensing mechanisms can be employed in sensing acceleration, motion, or pressure.

This chapter mainly focusses on the fabrication process for each cantilever and discusses the problems and the complexity of printing cantilevers onto fabric. A test application using these cantilevers as the basis for a motion sensor is undertaken at the end of each section to demonstrate the capability of the printed devices.
This chapter includes the following:

o   An introduction to the capacitive sensing mechanism

o   Fabrication and testing of a capacitive cantilever

o   An introduction to the piezoelectric sensing mechanism

o   Fabrication and testing of a cantilever with a piezoelectric layer

6.2   Free standing cantilevers

Many wearable applications require smart sensors that are able to convert stimuli, such as movement, into electrical signals for data processing and evaluation. These signals could be used to infer physical parameters or potential risks for the wearers. Conventionally, these sensors are manufactured by silicon microfabrication techniques on a rigid substrate and attached on to the clothing [2]. However, these wafer-based fabrication technologies are not compatible with fabrics as these processes or materials may damage the fabric (e.g. acid or high temperature). In addition, it is not possible to use conventional photolithography processes because the material will be absorbed into the fabric structure while spin coating. Since these sensors are rigid, they have the potential to cause the wearer discomfort. Additionally, each sensor is individually mounted which can be time consuming and costly. Conventional knitting and weaving manufacturing methods are limited by the need to follow the fabric warp and weft yarn structure, thus patterns can only have orthogonal arrangements. In addition, knitting and weaving methods are unable to produce a free standing cantilever or a cavity on top of the fabric. Screen printing, an alternative solution for smart fabric applications, provides more design freedom and the ability to create multiple layers with different designs. In addition, a wide range of screen printable pastes are commercially available.

6.2.1   Capacitive free standing cantilevers

6.2.1.1   Capacitive sensing mechanism

The device described in this section is a capacitive free standing cantilever which is entirely screen printed on fabric. Capacitive sensing has been widely used because of its simple configuration and ease of implementation. A variety of applications (e.g. flow and pressure measurement, liquid level analysis, switches and accelerometers) can be achieved using the capacitive sensing mechanism.

A simple capacitor consists of two parallel metal plates separated by a dielectric material. The capacitance is given by:

$$C = \frac{\varepsilon_0 \epsilon A}{d} \qquad\qquad Eq.\ 6\text{-}1$$

where ε_0 is the permittivity of free space, ε is the relative permittivity of the dielectric material, A is the overlap area of the plate and d is the distance between two plates. By changing ε, A or d, the capacitance can be changed accordingly. A schematic diagram of changing capacitance based on each parameter is shown in Figure 6-1.
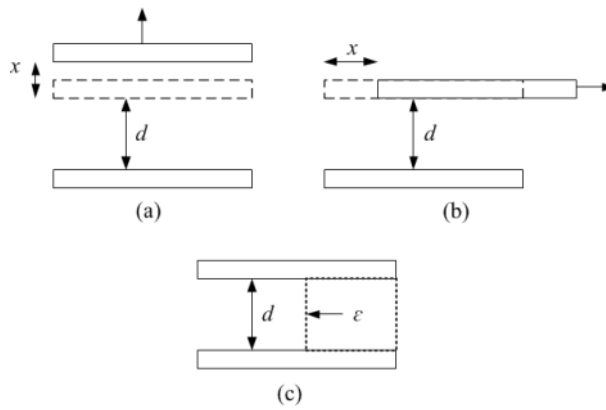
Figure 6-1: Capacitive sensing mechanisms: (a) distance change, (b) area change and (c) dielectric change.

Baxter [133] stated that the capacitive sensing mechanism can be used to sense proximity with a precision of 10^{-14} m. From equation 6-1, the capacitance is inversely proportional to the distance between the two electrodes. Due to the linear relationship between the capacitance and the overlap area of the electrode, large displacements are detectable but the distance between the two electrodes must be small [133]. Compared with changing the distance and the area, changing the dielectric material between two electrodes is less common but can be used, such as for measuring the level of a liquid [134]. In this research, plate separation distance is selected as the basis of capacitive measurement mechanism because it is compatible with the achievable screen printed geometries.

6.2.1.2   Cantilever design and fabrication

Figure 6-2 shows the screen printing sequence of a capacitive cantilever printed on fabric.
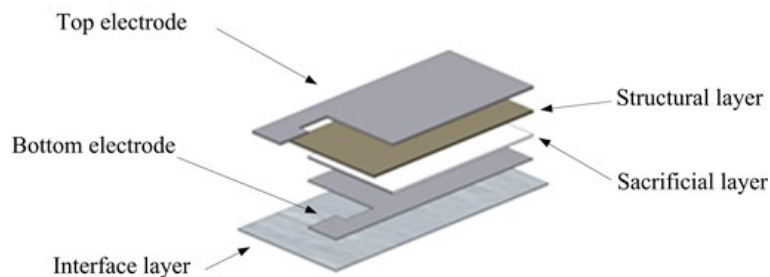
Figure 6-2: Schematic diagram of printing sequence for a capacitive cantilever on fabric.

To characterise the sacrificial material removal results versus the cantilever length on fabric, four designs with different beam lengths of 9, 12, 15 and 18 mm were designed. A separate screen is required for each layer and the full dimensions of the cantilever beam and electrode layers are shown in Table 6-1. A slightly smaller top electrode avoids short circuits between each electrode which can occur due to bleeding of the silver paste during the printing.

Table 6-1: Dimensions for the four cantilevers.

Design	1	2	3	4
Cantilever (mm) $L \times W$	9×10	12×10	15×10	18×10
Top electrode (mm) $L \times W$	8×8	11×8	14×8	17×8
Bottom electrode (mm) $L \times W$	15×12	15×15	15×18	15×21

These dimensions were chosen to produce macro-scale devices to allow straightforward visual examination and handling of the device during the process development. The ultimate resolution of this technology should produce devices of dimensions ≥ 200 μm which is expected to be sufficient for the majority of fabric-based applications.
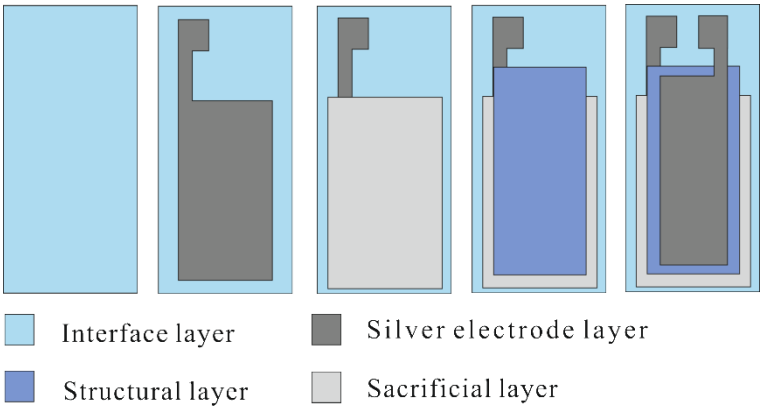
Figure 6-3: Screen designs for the capacitive cantilever.

Figure 6-3 shows the screen design of each layer. Screen selection is based on the recommendations and experiments conducted in chapters 4 and 5. A 250 threads per inch stainless steel screen was identified during the MICROFLEX project as the optimum screen for the deposition of the interface paste. Polyester screens with a 120 threads per cm mesh and 40 μm emulsion screen are used for the rest of the layers which are the sacrificial, structural and conductive layers. The sizes of these screens are designed to be 12 inch by 12 inch to ensure they can be mounted onto the DEK 248 screen printer.

Johnson Matthey S-20 thermally curable silver conductive polymer paste was used for the two electrodes because the conductivity is higher than the UV curable pastes identified. This paste can be cured at 80 $^{\circ}$C for 5 minutes providing a compromise between sufficient conductivity and low mass loss from the sacrificial layer. S-20 also has good compatibility with the TME sacrificial layer demonstrated in chapter 5.

Initially, polyester/cotton fabrics were cut to a desired size (i.e. 4 inch by 4 inch) and glued onto alumina tiles. The Fabinks-UV-IF1 interface paste was printed on top of the fabric substrate and was UV cured for 60 seconds. Two prints with six and four deposition for each print respectively were required to fill the rough fabric surface and provide a smooth surface for the subsequently printed layers. The bottom electrode was then printed followed by the sacrificial layer. Next, EFV4/4965 structural layer and top electrode layer were printed in that order. The details of the process parameters are summarised in Table 6-2 as well as the screen printing sequence are shown in Figure 6-4.

Table 6-2: Material selection and curing conditions for each layer.

Layer	Paste	Curing conditions
Interface	Fabinks-UV-IF1	UV 60 second
Bottom electrode	Johnson Matthey S-20	$80\,^oC$ 5 min
Sacrificial	TME based	$85\,^oC$ 5 min
Structural	EFV4/4965	UV 60 second
Top electrode	Johnson Matthey S-20	$80\,^oC$ 5 min
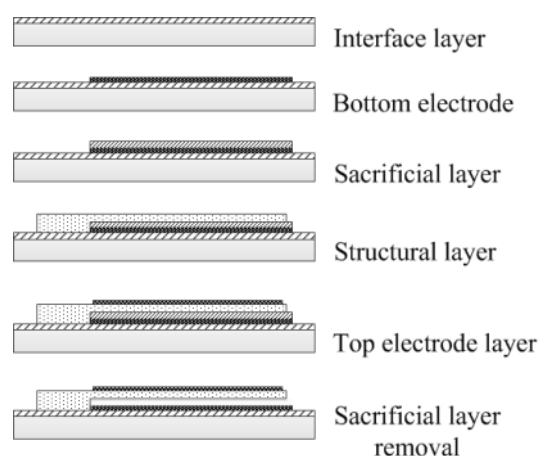
Figure 6-4: Printing sequence of a capacitive cantilever.
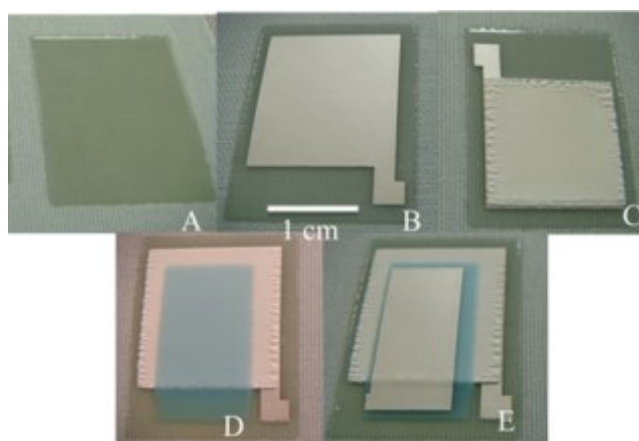
Figure 6-5: Printing steps for a capacitive cantilever: A. Interface layer, B. Bottom electrode layer, C. Sacrificial layer, D. Structural layer, E. Top electrode layer.

Figure 6-5 shows photographs of each printing stage. For the removal process, cantilevers were placed in a box oven at 150 °C for 30 minutes. The selection of curing and removal conditions of the above pastes was determined by the results of the removal temperature examinations reported in chapter 4.

6.2.1.3   Testing results and discussion

6.2.1.3.1   Cantilever examination

Figure 6-6 shows a 15 mm long cantilever after the removal of the sacrificial material from the fabric substrate. The cantilevers were completely released from the fabric substrate when the sacrificial layer was sublimated. No significant damage to the fabric was observed and therefore the removal temperature was suitable for fabric applications. In addition, there was no delamination or cracks in the final printed structure, shrinkage or wrinkling of the fabric.
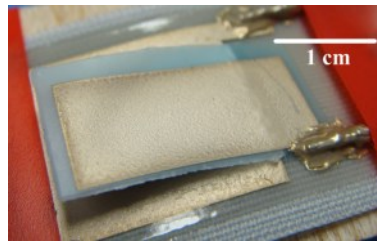
Figure 6-6: Screen printed capacitive cantilever with 15 mm long beam.

The cantilevers were examined using a Zeiss SEM which confirmed that the sacrificial layer was fully removed leaving no residue, shown in Figure 6-7. The structures were therefore completely released from the substrate to create free standing cantilevers.
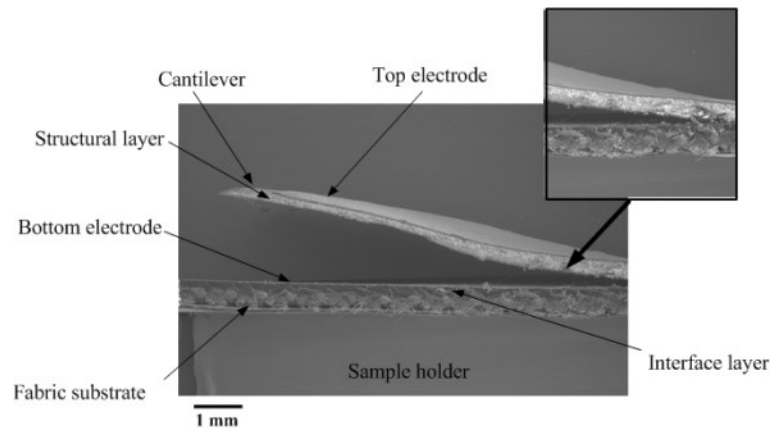
Figure 6-7: SEM cross-section micrograph of a printed cantilever on fabric.

Bowing of the cantilever, shown in Figure 6-7, is believed to be due to different thermal expansion coefficients of the silver and dielectric layers, thus the lower dielectric layer expands more than the upper silver layer. This could potentially be improved by printing an additional silver layer at the back side of the dielectric layer to balance the

deformation. Bowing also affected the capacitance of each cantilever. The capacitances measured using a Wayne Kerr 4350 LCR meter are shown in Table 6-3.

Table 6-3: Capacitances measured by Wayne Kerr LCR meter

Cantilever design	1	2	3	4
Measured value (pF)	3.94	6.02	6.29	7.59
Calculated value (pF)*	5.6	7.7	9.9	12

*Capacitive value was calculated using equation 6-1 with a plate separation distance of 100 μm.

The results shown in Table 6-3 show that the measured value is smaller than the calculated value. The calculated value was based on an ideal parallel capacitor with a plate separation distance of 100 μm, which is the thickness of the sacrificial layer. It is believed that the differences are caused by the bowing of the cantilever which increase the distance between two electrodes, thus the capacitance reduces.

6.2.1.3.2   Mechanical analysis

To evaluate the dynamic performance of the released cantilevers, a purpose built electromechanical shaker rig was used to measure the cantilever deflection as a function of frequency. The shaker rig can generate a range of acceleration levels and frequencies up to 8.5 kHz with the acceleration level at each frequency being limited by the maximum displacement of the shaker plate (~19 mm). A laser displacement meter (KEYENCE LC-2450) with a resolution of 0.5 μm controlled by LabView was used to measure the cantilever deflection. Each cantilever was individually tested by mounting it on the shaker and focusing the laser on the tip of the cantilever to measure the deflection. Figure 6-8 shows a sample cantilever mounted on top of the shaker rig.
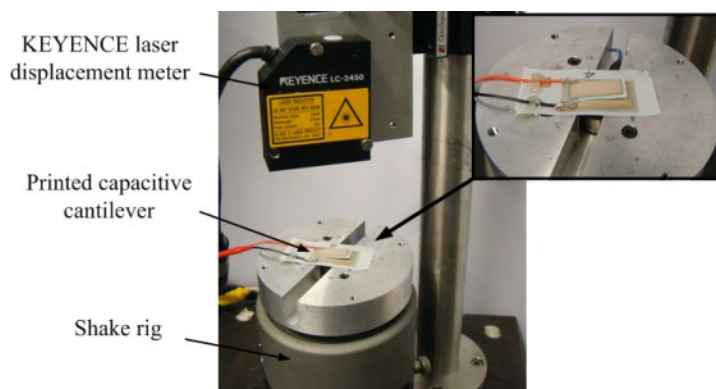
Figure 6-8: The shaker rig with a cantilever mounted on top.

For a thin cantilever, the natural vibration frequency of the ith mode can be found using equation (6-2) [135]:

$$f_r = \frac{\lambda_i^2}{2\pi} \left(\frac{t_c}{2L^2} \right) \sqrt{\frac{E}{\rho}} \qquad Eq.\ 6\text{-}2$$

where λi is a coefficient based on clamping conditions, t_c and L are the thickness and length of the cantilever respectively and E and ρ are the Young`s modulus and density of the cantilever material, which are 0.5 GPa and 950 kg/m^3, respectively.

The resonant frequency of each cantilever was simulated using ANSYS finite element modelling, shown in Figure 6-9.
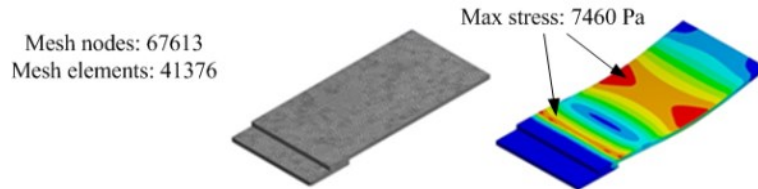
Figure 6-9: ANSYS model and stress distribution of a cantilever in mode 1.

Figure 6-10 shows the experimentally observed normalised displacements of the cantilever versus the frequency with a vibration acceleration of 19.62 m/s^2.
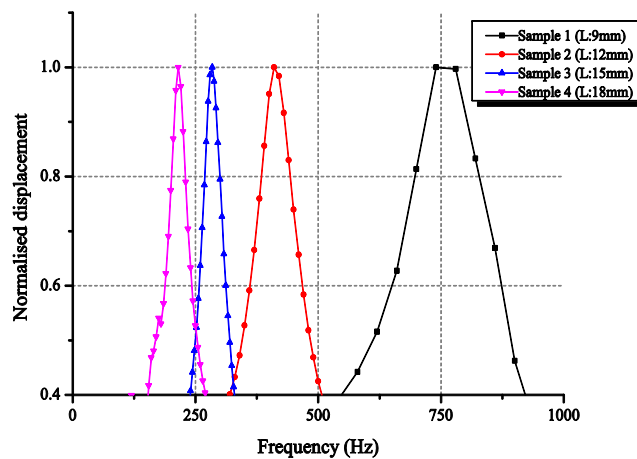
Figure 6-10: Frequency responses of four cantilevers.

A comparison of the measured and harmonic modelling results is given in Table 6-4 as well as maximum displacements measured using LabView. As expected, the resonant frequency increases with decreasing cantilever length.

Table 6-4: Comparison between modelling and experimental results of the resonant frequency.

Sample name	1	2	3	4
Measured resonant frequency (Hz)	760	410	280	215
Analytical predicted frequency*	508	285	182	127
ANSYS modelled frequency** (Hz)	700	380	240	160
Measured maximum displacement (μm)	10	63	164	350

*Predicated frequency was calculated using equation 6-2 without considering the silver layer.
**Modelled frequency was achieved with considering the silver layer.

Figure 6-11 shows that the resonant frequency is inversely proportional to the length-squared of the cantilever.
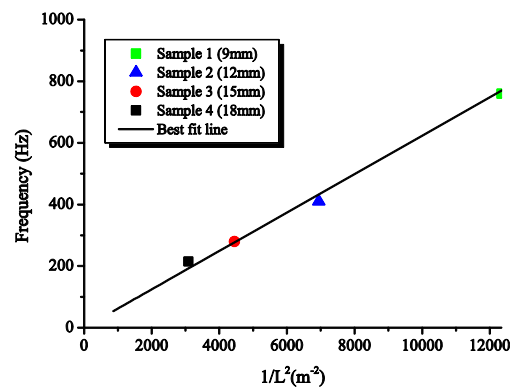
Figure 6-11: Consistency of four cantilevers' fabrication.

It also shows that cantilever thickness t, Young`s modulus E and density ρ of the material are reasonably consistent between different cantilevers and that the sacrificial material has been completely removed from under the cantilevers.

6.2.1.3.3   Motion test circuit configuration

Since the capacitance of each cantilever is very small (~3-8 pF), the most significant problem in measuring dynamic capacitance is the parasitic capacitance introduced by the connection wires. These parasitic capacitors are normally several orders of

magnitude larger than the capacitor to be measured [136]. *J. da Rocha et al.* [137] reported a capacitance measuring circuit, shown in Figure 6-12, reduces this parasitic effect. In this figure, v and ω are the voltage and the angular frequency of the voltage source and C_x is the capacitance to be measured. C_{w1} and C_{w2} are parasitic capacitances of the wires.
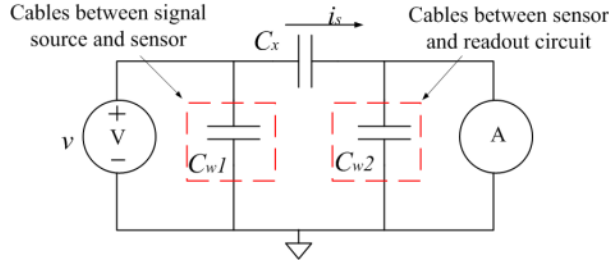
Figure 6-12: Schematic diagram of capacitance measurement.

As C_{w1} is in parallel with the voltage source, its current is not measured by the ammeter. However, as C_{w2} is in parallel with the ammeter and the impedance of the ammeter is very small, the current through C_{w2} is zero. Therefore, the ammeter only measures the current passing through the capacitive cantilever C_x and this current is given by:

$$i_s = v\omega C_x \qquad \qquad Eq.\ 6\text{-}3$$

To implement this circuit, the voltage source and ammeter are replaced by a signal generator and a current-to-voltage converter respectively. A TTi TGA1241 signal generator ($f = 100$ kHz and $V_{pp} = 3.8$V) replaces the voltage source and the current-to-voltage converter is a transimpedance amplifier, as shown in Figure 6-13.
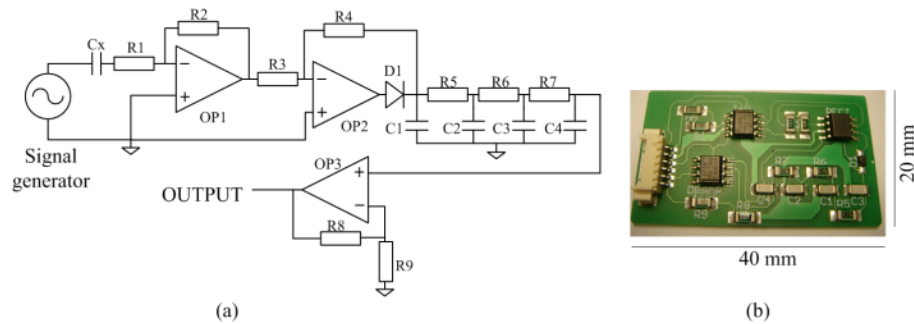
Figure 6-13: (a) circuit diagram of the readout circuit and (b) Printed circuit board (PCB).

The capacitive cantilevers (C_x) are connected between the signal generator and the transimpedance amplifier that is followed by an active full wave rectifier. A three-stage

low pass filter removes the high frequency noise from the signal generator. Finally, a non-inverting op-amp amplifies the voltage signal. The circuit was tested using commercial capacitors (2, 4, 12, 22, 33 and 47 pF) and the results confirmed that the readout circuit is able to detect changes in capacitance up to 33 pF with a linearly increasing output signal with increasing capacitance. Preliminary capacitance testing of each cantilever involved shaking the cantilever by hand whilst observing the capacitance change using a Wayne Kerr LCR meter and the results showed that the capacitive changes are smaller than the maximum detectable range of 33 pF. Therefore, it is suitable to use this circuit to detect the change in capacitance.

6.2.1.3.4 *System testing on the shaker rig*

Ideally, only the performance (i.e. linear area of the output) at low frequencies (<10 Hz) is of interest because these cantilevers are evaluated on the basis of a motion sensor on human bodies. However, due to the limitation of the shaker, the lowest frequency that can be used is limited to 30 Hz at an acceleration sweep from 9.8 m/s^2 to 24.5 m/s^2. To perform this testing, each sensor was individually mounted onto the shaker rig and the output voltage was recorded using a USB-6008 DAQ (Data acquisition) card controlled by National Instrument's LabView software. A frequency sweep from 30 Hz to 40 Hz with an interval of 0.5 Hz was performed at different vibration accelerations from 9.8 m/s^2 to 24.5 m/s^2. The results are shown in Figure 6-14.
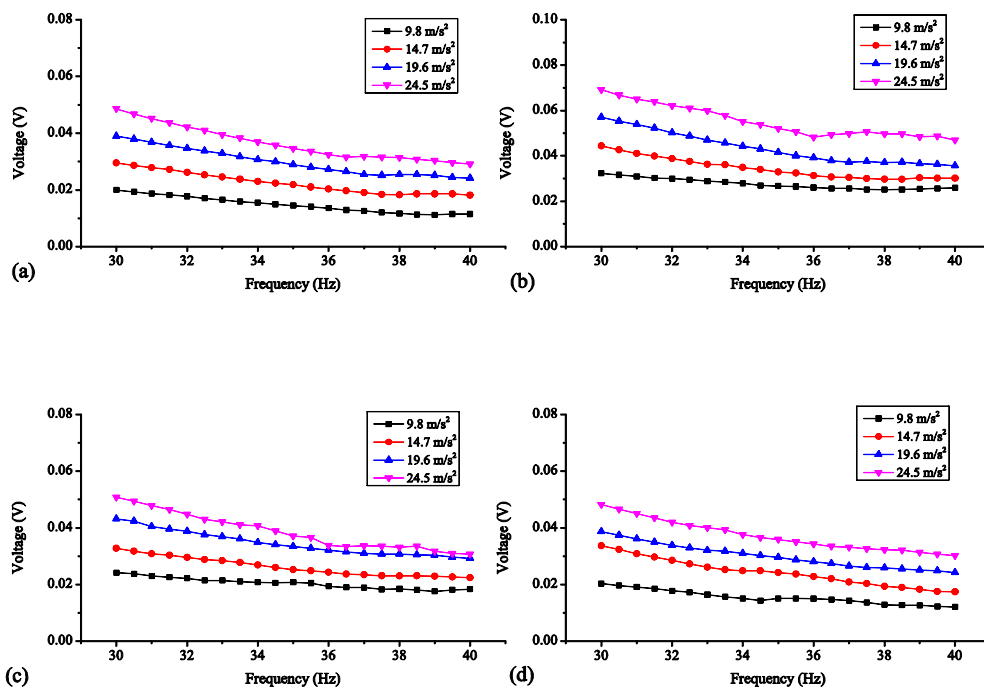
Figure 6-14: Frequency sweep from 30 Hz to 40 Hz against the voltage output at different accelerations: (a) design 1 (9 mm); (b) design 2 (12 mm); (c) design 3 (15 mm); (b) design 4 (18 mm).

Between 30 Hz and 40 Hz, voltage outputs at different accelerations have a similar decreasing gradient, particularly in design 1 (9 mm) and 4 (18 mm) which have the shortest and longest beam lengths, respectively. In this linear area, a given frequency produces a unique voltage at a constant acceleration. For designs 2 (12 mm) and 3 (15 mm), outputs at lower accelerations are more linear than those at higher accelerations. For design 3 (15 mm), the output is not unique at accelerations of 19.6 m/s^2 and 24.5 m/s^2 as these overlap at frequencies higher than 40 Hz.
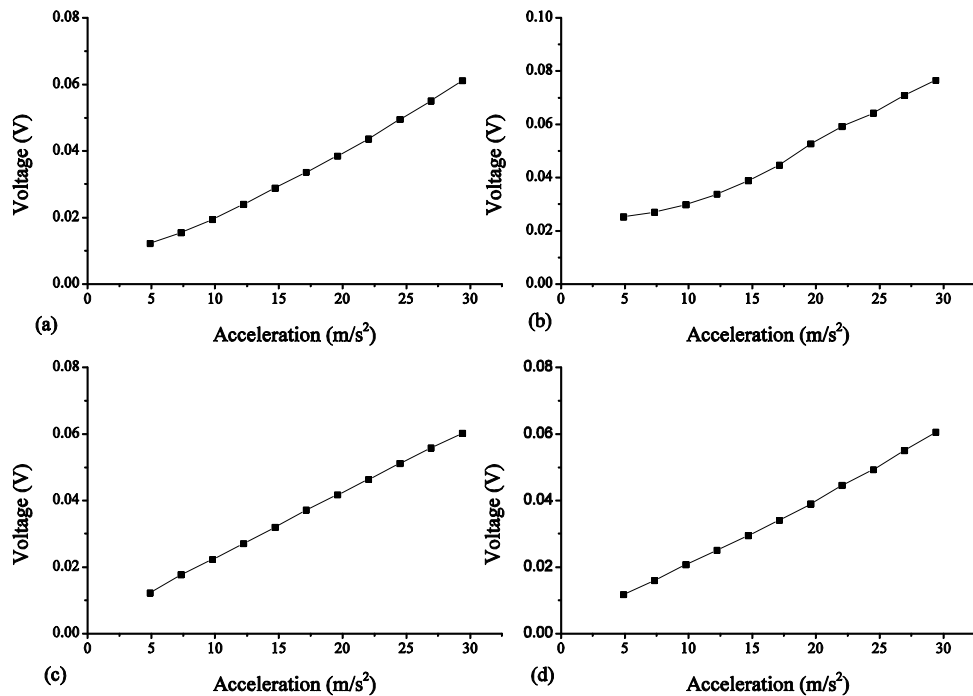
Figure 6-15: Acceleration sweep of each design versus the voltage output at 30 Hz: (a) design 1 (9 mm); (b) design 2 (12 mm); (c) design 3 (15 mm); (d) design 4 (19 mm).

The sensitivity of each design was evaluated by sweeping the vibration accelerations from 4.9 m/s^2 to 29.4 m/s^2 in a step of 2.45 m/s^2 at a constant frequency of 30 Hz (i.e. the lowest frequency of the shaker) while the voltage output was recorded simultaneously by LabView. From Figure 6-15, the voltage output of each design has a linear increase when the acceleration is increased. The sensitivity of each is therefore calculated and shown in Table 6-5.

Table 6-5: Sensitivity of each capacitive cantilever design.

Design	1 (9 mm)	2 (12 mm)	3 (15 mm)	4 (18 mm)
Sensitivity (V.m^{-1}·s^{-2})	0.0020	0.0022	0.0019	0.0019

The sensitivity of each design is similar but the linearity of design 2 tends to become worse when the acceleration is smaller than 10 m/s^2. It is found that at a fixed frequency, there is no significant difference in sensitivity.

6.2.1.3.5   System testing on a human forearm

Initial trials to evaluate the performance of the cantilever on human bodies have been performed. At this stage, the cantilever is unencapsulated but the future version would need to include a printed encapsulation over the cantilever so the sensor is unaffected by contacts such as might occur from covering by additional fabric overlayers. The encapsulation will require the use of the second sacrificial layer to ensure sufficient space between the top of the cantilever and the encapsulation to allow the cantilever to move. Cantilevers with different designs were individually mounted on the forearm of a human participant and the arm was moved up and down in front of the body. The direction perpendicular to the forearm, defined as the z-direction, is the direction of measurement. For comparison purposes, a commercial wireless accelerometer (MicroStrain G-link), with an accuracy of 0.098 m/s^2 and sampling rate of 512 Hz, was mounted alongside the printed cantilever and only the acceleration in the z-direction was recorded. The mounting position is shown in Figure 6-16.
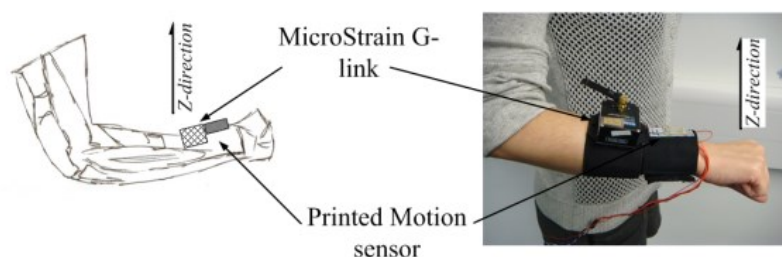
Figure 6-16: Printed capacitive cantilever and the G-link accelerometer mounted on the forearm.
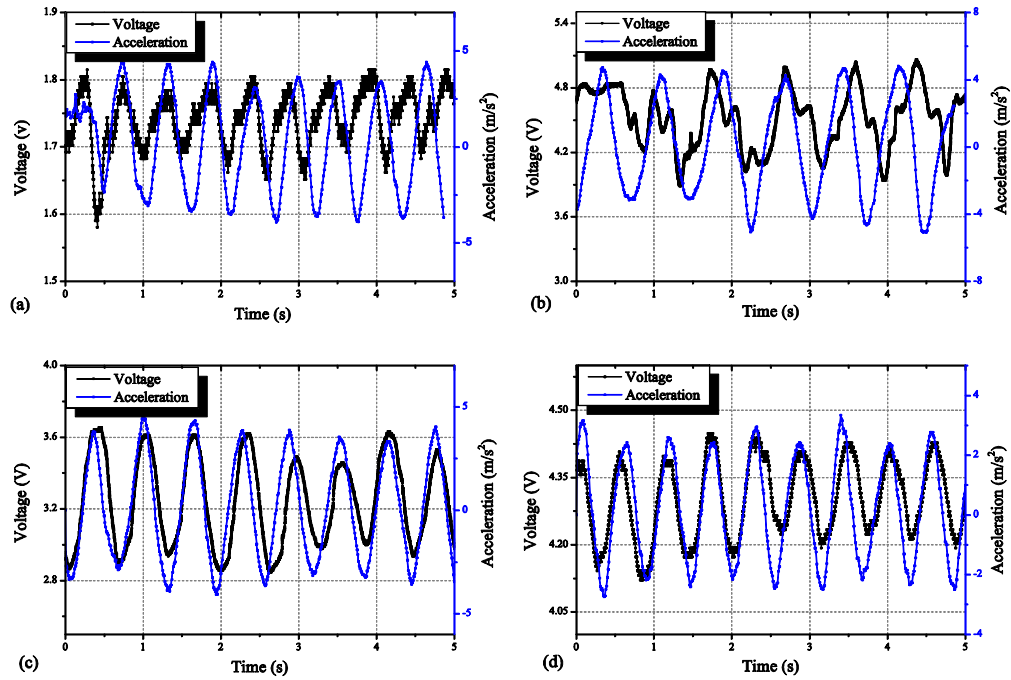
Figure 6-17: Comparisons between the output voltage from the cantilever readout circuit and acceleration data from the G-link accelerometer: (a) design 1 (L: 9 mm); (b) design 2 (L: 12 mm); (c) design 3 (L: 15 mm); (d) design 4 (L:18 mm).

Data from the printed cantilevers and G-link accelerometer was recorded for five seconds with the forearm moving up and down. Acceleration data from the Microstrain G-link was transmitted wirelessly to a PC and the output voltage from the circuit was recorded. The data from the accelerometer and printed cantilevers are shown in Figure 6-17. The results show that the screen printed capacitive cantilevers have a similar motion response to the commercial G-link accelerometer and the printed capacitive cantilevers are capable of being used as a motion sensor on garments. However, as the resolution of the available DAQ card is low (11 bits), there are some quantisation errors in designs 1 and 4 due to the small change in motion.

6.2.1.4   *Summary of capacitive cantilevers*

Capacitive cantilevers with four different designs were fabricated by screen printing and curing the interface, silver, sacrificial and structural materials onto fabric. The removal process was obtained by putting these cantilevers in a box oven at 150 $^{\circ}$C for 30 minutes. Removal results were visually examined, confirming that the cantilevers were released from the substrate. An SEM micrograph showed that the sacrificial layer was fully sublimated leaving no residue. The resonant frequency of each cantilever was measured using a shaker. The experimental resonant frequencies were close to that

obtained using ANSYS simulation. Discrepancies in these values are thought to be due to the bowing of the cantilever and the neglecting of the top silver layer.

The resonant frequency is inversely proportional to the length of the cantilever, confirming that cantilevers are completely released from the substrate. The measured capacitance is smaller than the calculation result because of the bowing of the cantilever. Test results produced by the shaker show that cantilevers have a linear voltage output at a low frequency range (30 - 40 Hz) and there is no significant difference in sensitivity. Testing results on a human forearm shows that the printed capacitive cantilevers are comparable with a commercial accelerometer, thereby demonstrating that such cantilevers can be used to detect human movement.

6.2.2   Piezoelectric free standing cantilevers

In this section, two designs with different lengths are achieved by screen printing the interface, sacrificial, structural, conductive and piezoelectric pastes onto fabric. The addition of a piezoelectric layer to the process enables electronics that are simpler (i.e. only a charge amplifier is required) than the previous capacitive approach which needs more amplifiers and an external input signal source.

6.2.2.1   *Piezoelectric sensing mechanism*

Piezoelectricity was first discovered by Pierre Curie and Jacques Curie in 1880 [138]. They demonstrated that certain crystalline materials, such as tourmaline, quartz and Rochelle salt, became electrically polarised and the degree of polarisation was proportional to the applied strain. The materials generate electrical charge when stress is applied. Inversely, the materials deform under the influence of an electric field. This phenomenon is known as piezoelectricity.
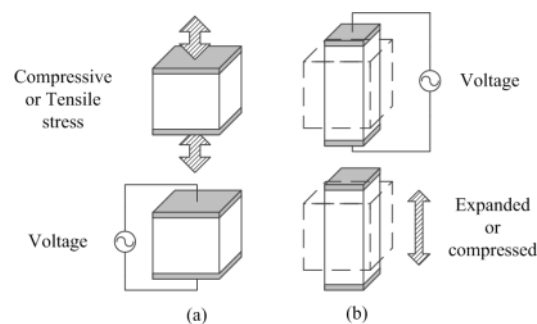
Figure 6-18: Reversible piezoelectric effect: (a) sensing function, (b) actuating function.

Figure 6-18 shows schematic diagrams of the reversible piezoelectric effect applied to a sandwich structure. When a compressive or tensile stress acts on the electrodes located opposite one another on two side of the piezoelectric material, a corresponding voltage is generated. It is also reciprocal; if the piezoelectric material is exposed to an electric field, it will experience an elastic strain causing its length to increase or decrease depending on the field polarity. Piezoelectricity can be used either for a sensing or for an actuating mechanism due to this reversible property.

A piezoelectric mechanism can be operated in either d_{31} or d_{33} mode depending on the arrangement [45]. For d_{31} mode, the poling direction is perpendicular to the direction of the stress, whereas in d_{33} mode the poling direction is in the same direction of the stress. In implementing these modes on a free standing cantilever, planar and interdigital electrode (IDE) arrangements are involved.
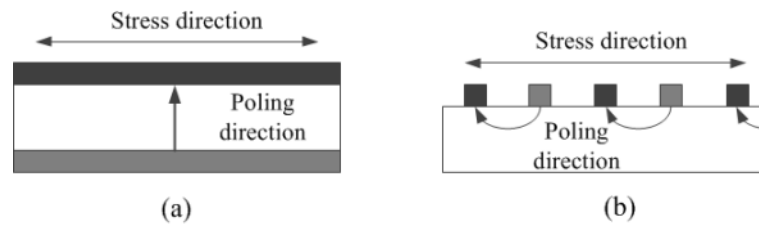
Figure 6-19: Cross-section of free standing cantilevers: (a) on d_{31} mode; (b) on d_{33} mode.

Figure 6-19 (a) shows a planar electrode arrangement which includes a piezoelectric layer sandwiched between two electrodes. It performs on a d_{31} mode because the poling direction is orthogonal to the stress direction applied to the cantilever. In contrast, as shown in Figure 6-19 (b), an IDE arrangement consisting of two comb-shaped electrodes interlocked together on top of the piezoelectric material obtains a d_{33} mode. The poling direction is roughly in the same direction as the stress applied.

6.2.2.2   Design and fabrication

The cantilevers are part of a structure in which the piezoelectric layer is sandwiched between two electrodes. The cantilever is fabricated using the same steps as the capacitive free standing structure. However, additional layers are needed to create a cantilever with a piezoelectric sensing layer. Figure 6-5 gives the screen printing sequence of a cantilever with a piezoelectric layer.
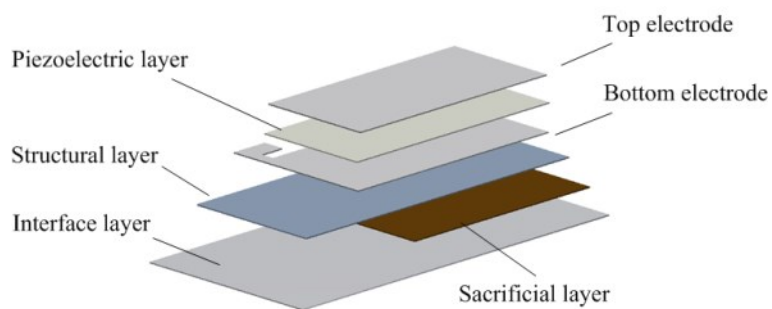
Figure 6-20: Schematic diagram of a cantilever with a piezoelectric layer (not to scale).

The dimensions of each design are shown in Table 6-6. These designs are the same as those used for the capacitive cantilevers (i.e. design 2 and 3).

Table 6-6: Dimensions for each cantilever design.

	Design one	*Design two*
Top electrode (mm) L×W	*11×8*	*14×8*
Bottom electrode (mm) L×W	*15×15*	*15×18*
Cantilever (mm) L×W	*12×10*	*15×10*
PZT (mm) L×W	*12×10*	*15×10*

Figure 6-21 shows the screen design of each layer for a free standing cantilever with a piezoelectric layer. A 250 stainless steel screen was used for the interface paste. Polyester screens with a 120 mesh count and 40 µm emulsion were used for the sacrificial, structural, piezoelectric and conductive layers.
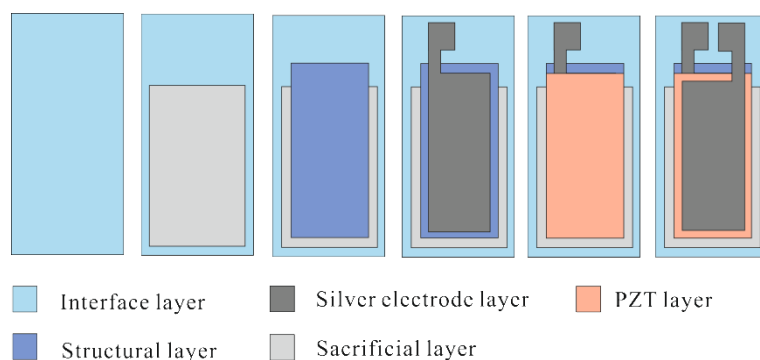
Figure 6-21: Screen design of a cantilever with a piezoelectric layer.

There are a wide variety of piezoelectric materials. These materials exist in either crystal/polycrystalline forms (e.g. quartz and lead zirconate titanate (PZT)) or polymer

form (e.g. Polyvinylidene fluoride (PVDF)) [139]. Normally, PZT is widely used for screen printing as it can be formulated into a ceramic paste, whereas PVDF is spin coated onto the substrate. However, as PZT usually needs a high firing temperature (>800 ^{o}C), it cannot be used with fabrics. PVDF is difficult to screen print because it exists either in a sheet form or in liquid form with a viscosity that is too low for screen printing. To achieve a material with a low curing temperature and a higher piezoelectric coefficient compared with inherently piezoelectric polymer materials, a screen printable piezoelectric polymer paste was obtained from Meggitt A/S [140]. This paste combines the advantages of ceramic PZT (i.e. high piezoelectric coefficient d_{33}) with those of polymers (i.e. low curing temperature and flexible). The curing process is 100 °C which is compatible with the selected fabric.

First, the interface paste was printed onto the fabric and cured; following this, the sacrificial layer was then printed and cured. Next, the structural layer was printed on top followed by a Johnson Matthey S-20 polymer silver layer as the bottom electrode. Meggitt PZT was then printed three times to achieve a thickness of ~100 μm. Finally, Johnson Matthey S-20 was printed as the top electrode of the piezoelectric layer. The curing parameters of each layer and fabrication sequence are shown in Table 6-7 and Figure 6-22, respectively.

Table 6-7: Material selection and curing conditions for each layer.

Name	*Paste*	*Curing conditions*
Interface layer	*Fabinks-UV-IF1*	*UV 60 seconds*
Sacrificial layer	*TME based*	*85 ^{o}C 5 minutes*
Structural layer	*EFV4/4965*	*UV 60 seconds*
Electrode layer	*Johnson Matthey S-20*	*80 ^{o}C 5minutes*
Piezoelectric layer	*Meggitt Piezoelectric paint*	*100 ^{o}C 5 minutes*
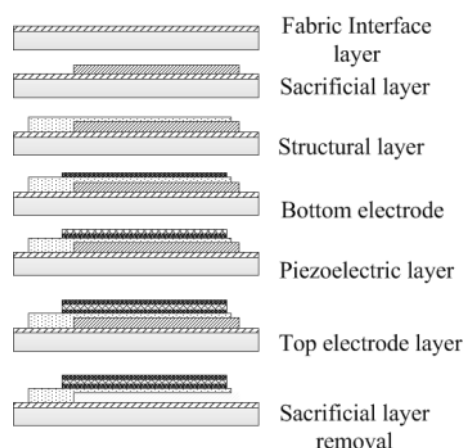
Figure 6-22: The fabrication sequence for a free standing cantilever with a piezoelectric sensor layer.
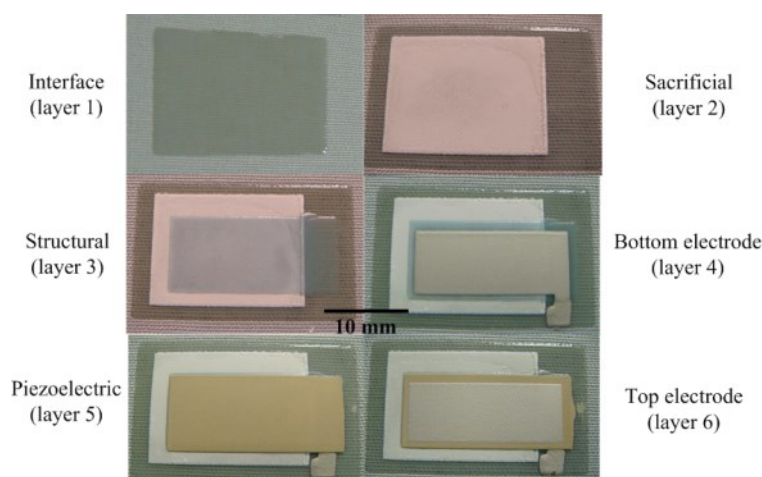
Figure 6-23: Printing sequence of a cantilever with a piezoelectric layer on top of the fabric.

The curing conditions of these pastes are compatible with the sacrificial material and do not significantly reduce the mass of the sacrificial layer during the subsequent layer printing and curing. For the removal process, the cantilevers were placed in an oven at 150 ^{o}C for 30 minutes.

6.2.2.3   Testing results and discussion

6.2.2.3.1   Cantilever examination

The piezoelectric layer was initially cured at 80 ^{o}C for 5 minutes to match the curing conditions with those of the sacrificial and silver pastes. However, this curing temperature was insufficient for the piezoelectric material because the solvent in the paste was not completely removed and continued to evaporate during subsequent drying

and removal processes. This evaporation caused cracking, delamination and an uneven surface resulting in short circuits between the two electrodes. Figure 6-24 shows examples of cantilevers, which were cured at 80 ^{o}C for 5 minutes.
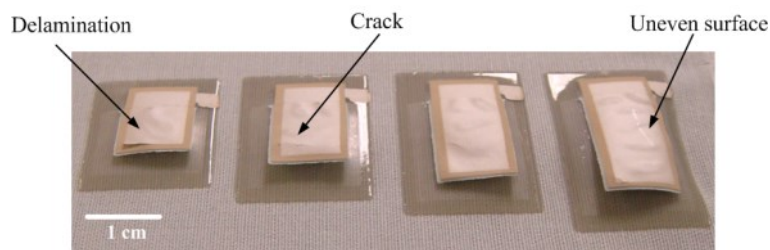
Figure 6-24: Example of defective cantilevers caused by incomplete curing of the piezoelectric layer before the removal process.

The delamination, uneven surface and bending of the silver and piezoelectric layers caused by solvent evaporation during the removal process can clearly be seen. Therefore, the curing temperature was increased to 100 ^{o}C but the curing time remained at 5 minutes. The piezoelectric paste was completely dried out at 100 ^{o}C providing a flat and smooth cantilever surface. Examples of successful cantilevers cured at the optimum temperature and time are shown in Figure 6-25.
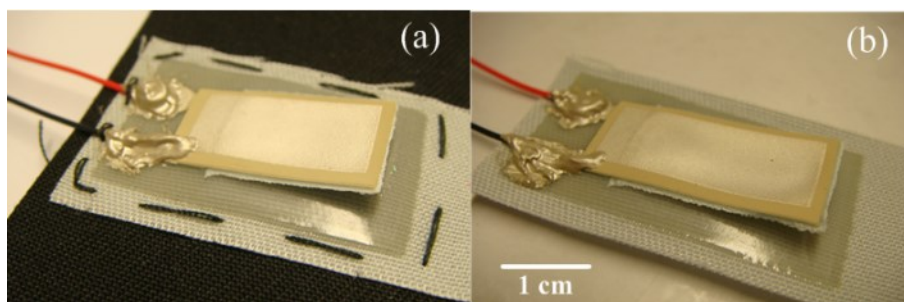
Figure 6-25: Piezoelectric cantilevers after the removal process: (a) sample one (L:12 mm); (b) sample two (L:15 mm).

Figure 6-26 show that the sacrificial layers have been completely removed and that no residue remains. In addition, no significant sagging or bending of the cantilever was observed. The key result is that there is no significant damage to the polyester/cotton fabric thereby confirming the compatibility of the curing and removal temperatures of these materials with the fabric substrate.
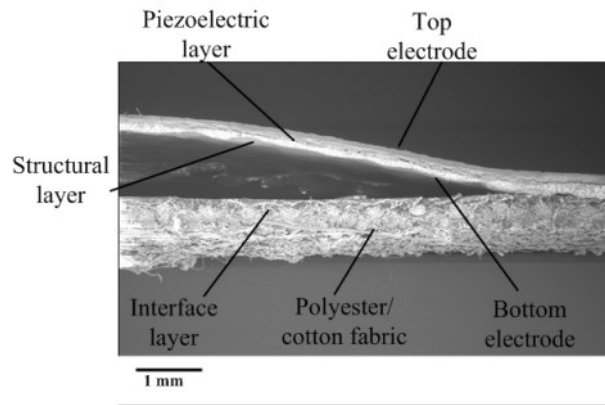
Figure 6-26: Cross-sectional micrograph of a piezoelectric cantilever.

6.2.2.3.2   *Mechanical analysis*

Before testing, wires were attached using silver epoxy (RS Components – Part No. 186-3616) to each electrode and the cantilevers were polarised using a bespoke polarisation station. The electric field and the temperature were 4 MV/m and at 100 $^\circ$C, respectively. The temperature was then reduced whilst maintaining the electric field. Once the cantilevers were polarised, the piezoelectric coefficient (d_{33}) was measured using a PIEZOTEST PM300 piezometer; an average d_{33} of 45 pC/N was measured. This confirmed that the printing process was successful because there were no short circuits in the printed piezoelectric sandwich structure. In addition, it is shown that the d_{33} obtained from the piezoelectric layers is higher than that of conventional PVDF film. Therefore, these results prove that the piezoelectric material is compatible with fabric applications.

To evaluate the dynamic performance of the piezoelectric layer and further check whether the cantilever was completely released from the substrate, the cantilevers were tested on the shaker rig as before. Figure 6-27 shows a schematic diagram of a charge amplifier used to amplify the charge output from the piezoelectric layer.
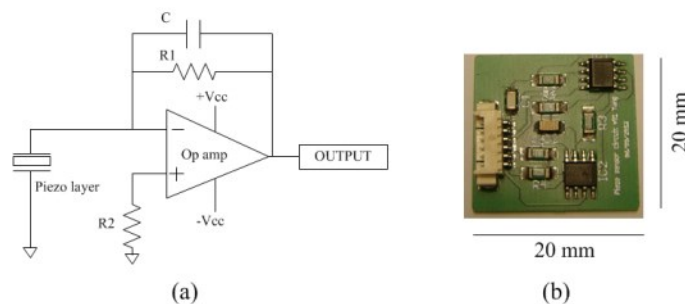
Figure 6-27: (a) schematic diagram of a charge amplifier and (b) the PCB.

Figure 6-28 shows that the root mean square (R.M.S.) voltages of each design against vibration frequency as input acceleration is changed, ranging from 0.98 m/s^2 to 11.76 m/s^2.
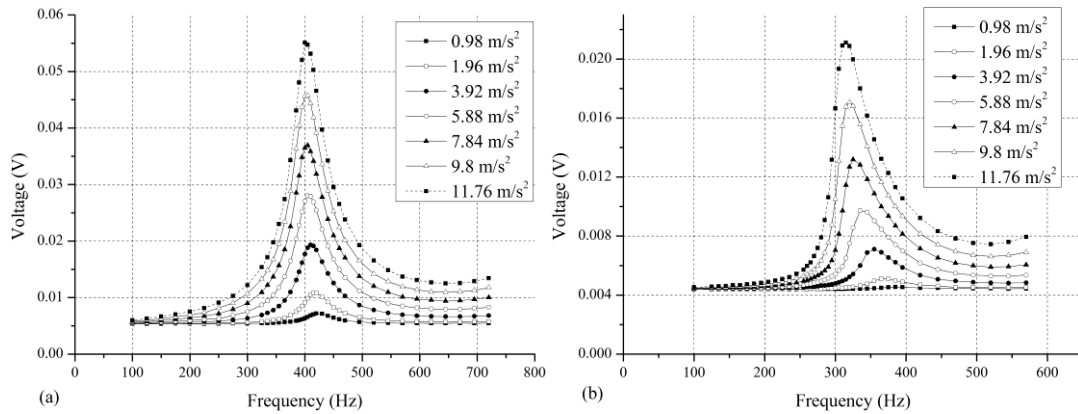
Figure 6-28: Output voltage versus frequency sweep: (a) design one (L:12 mm); (b) design two (L: 15 mm).

The mechanical resonant frequencies of two designs at an acceleration of 11.76 m/s^2 are 400 Hz and 320 Hz due to their different beam lengths (i.e. 12 mm and 15 mm). Both designs show a soft non-linear response but design two is more non-linear than design one. The two designs show a decrease of 20 Hz and 50 Hz in resonant frequency respectively, with increasing amplitude of acceleration. This non-linear response could affect the repeatability of the cantilever for future applications so a broadband design may need to be considered.

6.2.2.3.3   System test on human arm

Preliminary tests to evaluate the performance of these cantilevers on the human forearm have been performed. Two designs were individually mounted on the forearm of a participant. The participant then moved the arm up and down in front of the body in an arc of ~40 cm whilst the sensor output was recorded (same mounting configuration as capacitive cantilevers, shown in Figure 6-16). For comparison purposes, a commercial wireless accelerometer (Shimmer 9DOF) was mounted alongside the printed cantilever. Acceleration data from the accelerometer were transmitted via Bluetooth to a PC whilst the voltage output from the charge amplifier was recorded through an NI DAQ card (USB-6008) using the LabView software. The comparison between the voltages and accelerations is shown in Figure 6-29.

147
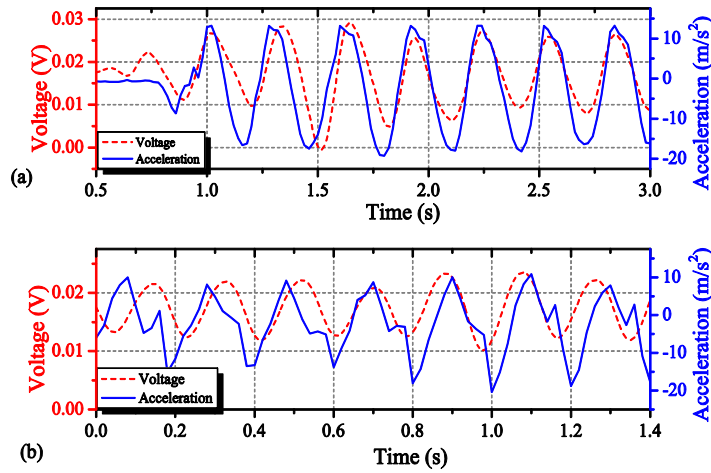
Figure 6-29: Preliminary arm test results of two designs: (a) design one; (b) design two.

The results show that these cantilevers do respond to arm movements but also have a phase difference compared with the commercial accelerometer. However, this phase difference does not affect the periods of the acceleration or voltage output. The acceleration data presented in Figure 6-29 (b) shows quantisation errors because the accelerometer only has a sampling rate of 50 Hz compared with the NI DAQ card, which has a sampling rate of 1 kHz.

6.2.2.4   Summary of cantilevers with a piezoelectric layer

In this section, cantilevers with a piezoelectric sensing layer were achieved using the same screen printing process and materials as those used for the fabrication of capacitive cantilevers. A piezoelectric layer was printed on top of the cantilever and cured. Initial curing at 80 ^{o}C was not sufficient to solidify the piezoelectric paste resulting in cracking and delamination. By increasing the curing temperature to 100 ^{o}C, the piezoelectric layer was completely dried leaving a smooth surface.

The results also show that the printed piezoelectric material has good compatibility with the other printed materials and that curing at 100 ^{o}C does not significantly affect the sacrificial layer. Poling the piezoelectric layer at 100 ^{o}C with an electrical field of 4 MV/m resulted in an average d_{33} of 45 pC/N. The harmonic tests was performed on a shaker rig at different accelerations and results showed that both designs have a soft non-linear response when the acceleration amplitude was increased resulting in a decrease in resonant frequency. Testing results on a human forearm shows that the printed cantilevers with a piezoelectric layer are able to detect human movements.

6.3 Conclusions

This chapter demonstrates a novel way of realising free standing microstructures directly onto fabrics which can be used in a wide variety of sensing or actuating smart fabric devices. The screen printing approach provides more design freedom and the ability to produce arrays of the same or different devices in a straightforward fashion. Using an interface layer reduces the fabric surface roughness and achieves a smooth and flat layer for the subsequently printed layers. The sacrificial material with low curing and removal temperatures demonstrates sufficient mechanical strength to support subsequent layer printing and complete removal by sublimation at a temperature which is not harmful to the fabric. The measurement circuit of the piezoelectric mechanism is simpler than the capacitive mechanism which requires more amplifiers and also a signal source, thus it may be possible in the future to print on entire readout circuit tracks alongside these cantilevers on fabric during the printing process, which would enhance the integration of the device into future smart fabric designs. These cantilevers demonstrate the feasibility of performance in that the human motion can be detected. In addition, these cantilevers can be potentially fabricated during the garment manufacture, thus an array of the cantilevers could be achieved.

Chapter 7

Screen printed micropumps on flexible substrates

7.1 Introduction

This chapter demonstrates the fabrication of a valveless micropump, which presents the challenge of fabricating a cavity using the materials and the screen printing process identified in the previous chapters. A pump involves channels and chambers and is a challenging structure to further evaluate the sacrificial material and the fabrication process. Entire printed pump structures have yet to be reported in the literature due to the lack of suitable sacrificial material.

The device presented in this chapter is a valveless micropump, shown in Figure 7-1.
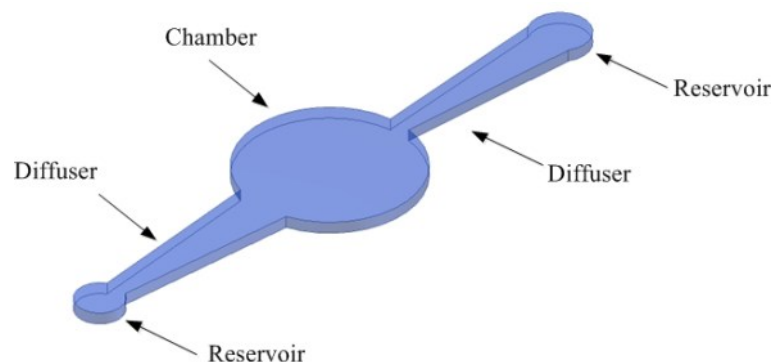
Figure 7-1: Schematic diagram of a valveless micropump.

Unlike other pump types, the valveless micropump has a simple mechanical structure, which is comprised of two diffusers/nozzles, a chamber and an actuator. It does not require complicated active valves or long channels. In addition, the pumping liquid is not limited in contrast to some pumps, such as EHD and MHD pumps. By combining the sacrificial technology with the screen printing technique, diffusers and chambers are formed once the sacrificial layer is removed.

For the actuator, a piezoelectric mechanism is used for the printed pump structure as the capacitor sandwich structure identified in chapter 6 can be created by screen printing the conductive and PZT layers on top of the membrane.

This chapter contains the following subsections:

- o   Selection of the diffuser geometry
- o   Fabrication of the pump structure
- o   Testing of the pump structure

7.2   Selection of the diffuser geometry

A valveless micropump usually contains two diffusers and one chamber. An actuator is located on top of the membrane to displace the membrane resulting in a volume change. The liquid is then pumped from the inlet to the chamber and pushed out from the chamber to the outlet. The key component of a micropump is the fluidic rectification mechanism which ensures a net flow in one direction.

Unlike other mechanical pumps which have dynamic valves, valveless micropumps use static valves to rectify the flow. As described in chapter 3, two types of static valve are used in literature: the diffuser/nozzle and the Tesla. The diffuser/nozzle element has a simple mechanical structure in contrast to the Tesla valve which has long and complex channels. The presence of a long channel in the printing process may cause problems, such as channel deformation. Therefore, for this study, the diffuser/nozzle static valve has been selected.

7.2.1 Theoretical analysis

Diffuser elements are fluidic channel constrictions where the fluidic resistance is higher in one direction than in the other, causing the flow rate to be different in each direction for the same applied pressure. A diffuser is characterised by a gradual widening of the fluidic channel cross-section in the direction of the flow which gives a smaller fluidic resistance; a nozzle is characterised by a gradual reduction of the fluidic channel cross-section in the direction of the flow leading to an increased fluidic resistance [141]. During the supply mode when the membrane moves upwards, more fluid flows through the inlet element than through the outlet element. During the pump mode when the membrane moves downwards, more fluid flows through the outlet element than through the inlet element. Hence, a net flow is generated towards the outlet.

Different diffuser geometries have been used in valveless micropumps, shown in Figure 7-2.
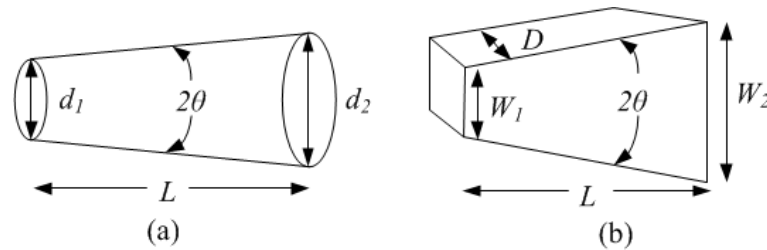
Figure 7-2: (a) Conical and (b) flat-walled diffusers.

A conical diffuser consists of a circular expanding cross-section, whereas a flat-walled diffuser includes a rectangular cross-section with four surrounding walls. The narrowest area of the diffuser is defined as the 'throat'. The choice of diffuser shape is mainly dependent on the fabrication capabilities. In most recent studies, the flat-walled diffuser was used because it is easier to fabricate. Another advantage of using the flat-walled diffuser is that, under the same inlet boundary condition, the best flat-walled diffuser is 10~80 % shorter than the best conical design [142]. Therefore, if space is limited in the pump design, the flat-walled diffuser gives better performance. In addition, the flat-walled diffuser is the best choice for screen printing rather than the conical shape because the conical shape cannot easily be achieved by printing.

An estimate of the flow directing efficiency of the diffuser elements can be achieved using the pressure loss data. The pressure drop through a diffuser is usually given as the loss coefficient K, which is related to the pressure drop ΔP given in equation 7.1 [94]:

$$\Delta P = \frac{1}{2}\rho\bar{v}^2 K \qquad \qquad Eq.\ 7\text{-}1$$

where ρ and $\bar{v}$ are the density and the flow velocity of fluid at the throat, respectively. A workable diffuser has a lower pressure loss coefficient in the diffuser direction than in the nozzle direction. The ratio of the latter to the former is denoted as a diffuser efficiency η, which is defined as [143]:

$$\eta = \frac{K_n}{K_d} \qquad \qquad Eq.\ 7\text{-}2$$

where K_n and K_d are pressure loss coefficients in nozzle and diffuser directions, respectively. To obtain a net pumping action, η must be greater than one so that the pressure loss in the nozzle direction is higher than the pressure loss in the diffuser direction resulting in a net flow. To achieve better performance, the efficiency should be as large as possible.

Several researchers [144-146] reported that, for a rectangular cross-sectional diffuser with a small opening angle ($< 20^{\circ}$), the losses in the diffuser direction are small and the minimum losses occur for a diffuser angle close to $2\theta = 10^{\circ}$. To select suitable diffuser parameters, a stability map of the diffuser is used, shown in Figure 7-3.
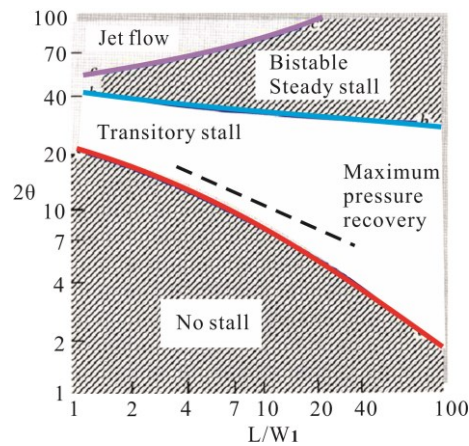
Figure 7-3: Stability map of a diffuser [142].

A diffuser operates in four regions based on the stability map. The first region is called the no stall region where the area is below the red line. In this region, the flow is steady without separation at the diffuser walls and moderate performance is achieved. The second region, which lies between the red and blue lines, is called a transitory stall region in which the flow is unsteady. In this region, the minimum pressure loss and the maximum pressure recovery occur. The third region is located between the blue and purple lines, called a bistable steady stall region. A bistable steady stall can flip-flop from one part of the diffuser wall to another and performance is poor. The fourth region is called the jet flow region where the area is above the purple line. In this region, flow completely separates from the diffuser walls making performance extremely poor. To achieve a maximum pressure recovery, the diffuser dimension needs to be located in the second region, which is a transitory stall area [147].

The achievable diffuser dimension is strongly determined by the screen printing resolution. The width of the throat is the minimum printing area of the pump and it must be designed to meet the requirement of the screen printing. The dimensions of the diffusers examined in this research are shown in Table 7-1.

Table 7-1: Parameters for two diffuser designs.

Parameters	Design one	Design two
W_1	1 mm	2 mm
L	15 mm	15 mm
2θ	10°	10°
L/W_1	15	7.5

To ensure the diffuser is working in the transitory stall region, the inlet width W_1 is designed to be 1 mm and the length of the diffuser is 15 mm so that L/W_1 ratio can be maintained at 15. The divergence angle of the diffuser is 10° which generates the smallest pressure loss. The second diffuser design, which only enlarged the inlet width (W_1) to 2 mm, was used for comparisons. These dimensions were chosen to produce macro-scale devices to allow straightforward visual examination, evaluation and handling of the devices during their development.

7.2.2 Numerical analysis

To evaluate the selected dimensions, the two designs were simulated using Comsol Multiphysics software. The simulations were used to examine the performance of the proposed diffuser designs based on the pressure loss coefficient and the efficiency. Simulations were based on 2D modelling with a variety of Reynolds numbers. The Reynolds number for a diffuser is defined as [141]:

$$Re = \frac{\bar{v}W_1}{v_k} \qquad\qquad Eq.\ 7\text{-}3$$

where v_k is the kinematic viscosity, which is 1.0×10^{-6} m^2/s. The Reynolds numbers for flow through micropumps are generally in the range of 100~500 [143]. The simulation considers flow Reynolds numbers of 200, 300, 500 and 1000 and the results are used to examine the flow rectification ability of the proposed diffuser designs.

The mesh distribution for a diffuser model with 4932 elements was used. Uniform velocities are applied at the diffuser inlet and the pressure at the outlet is set to zero. No-slip boundary conditions are imposed on the wall. Water was used as the fluid for the simulation because it is often used as the testing liquid.
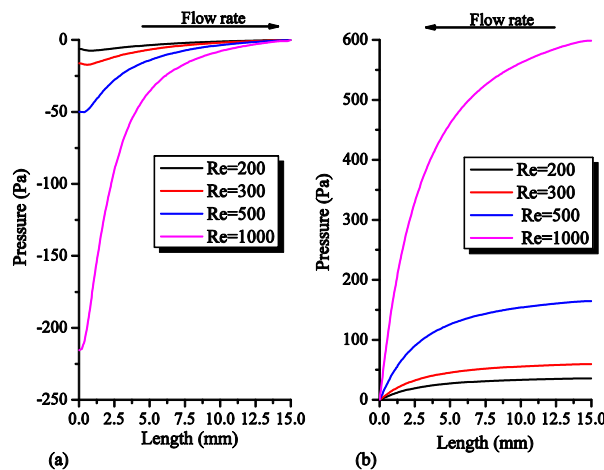
Figure 7-4: Pressure simulation results for the design one acting as (a) a diffuser element, (b) a nozzle element at different Reynolds numbers.

Figure 7-4 shows the pressure distribution of the diffuser and nozzle elements for design one. It was found that the pressure difference in the diffuser direction is approximately

three times lower than the pressure difference in the nozzle direction at all Reynolds numbers.

For design two, the same simulations were performed with different Reynolds numbers. The results are shown in Figure 7-5.
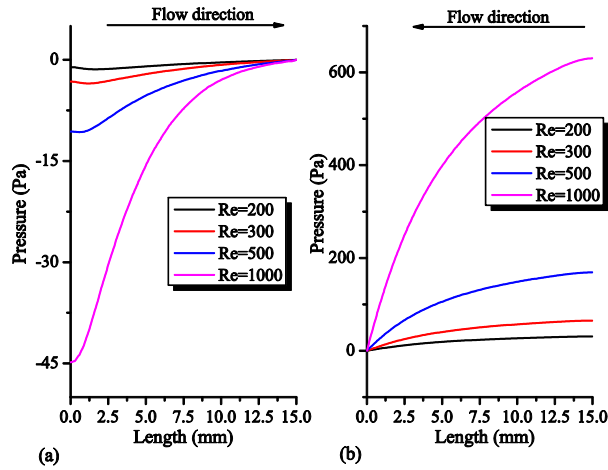
Figure 7-5: Pressure simulation results of the design two acting as (a) a diffuser element, (b) a nozzle element at different Reynolds numbers.

To compare the results between two designs, pressure loss coefficients and efficiencies were calculated based on equations 7-1 and 7-2. The results are shown in Table 7-2.

Table 7-2: Simulation results of two diffuser designs.

	Re=200	Re=300	Re=500	Re=1000
Design one:				
K_d	0.311	0.360	0.398	0.431
K_n	0.939	0.926	0.927	0.929
η	3.02	2.57	2.31	2.15
Design two:				
K_d	0.216	0.286	0.339	0.358
K_n	0.860	0.856	0.850	0.847
η	3.97	2.98	2.50	2.36

The pressure loss coefficients of both designs are higher in the nozzle direction compared with in the diffuser direction at all Reynolds numbers confirming that the pumping action is in diffuser direction.
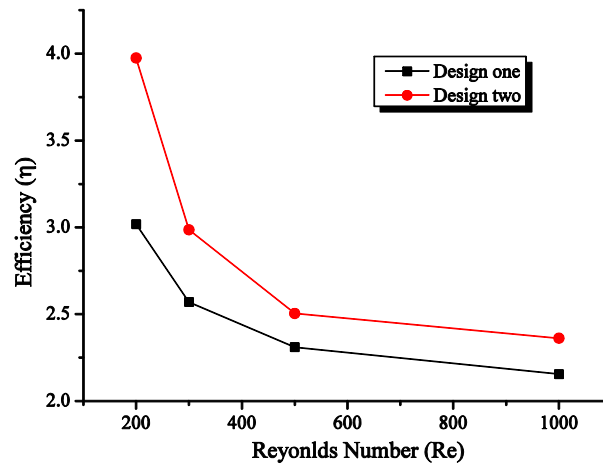
Figure 7-6: Efficiency comparison between two designs at a various Reynolds numbers.

Figure 7-6 compares the efficiencies of both designs. It shows that the pumping efficiency decreases with an increase in Reynolds numbers for both designs. It was found that the efficiency of design two was higher than that of design one over different Reynolds numbers. A higher efficiency implies that a higher flow volume can be pumped through the diffuser during each pumping cycle. With regard to screen printing, design two has wider throat width, which potentially increases the ease of printing and reduces the risk of blockage during the printing process. Design two was therefore selected as an appropriate design for the printing process development.

Figure 7-7 shows a CAD (Computer aided design) drawing of the proposed pump shape. The chamber size is determined by the size of the exit width of the diffuser so that diffusers and the chamber are connected smoothly.
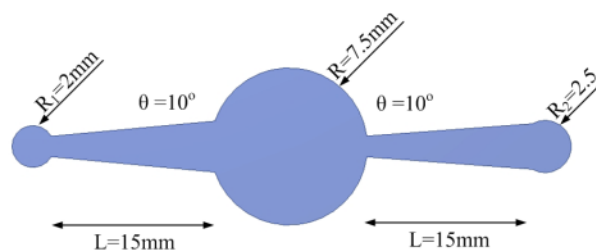
Figure 7-7: Proposed pump design.

The chamber size was designed with a radius of 7.5 mm and two reservoirs with radius of 2 mm and 2.5 mm were added to the inlet and outlet of the diffuser, respectively. These macro-scale dimensions ensure a straightforward examination and evaluation during the printing stage.

7.3 Pump fabrication

7.3.1 Screen design

To screen print a valveless micropump, the entire structure is split into layers. The thickness of each layer is determined by the number of prints. Figure 7-8 shows a schematic diagram of the layers of the valveless micropump.
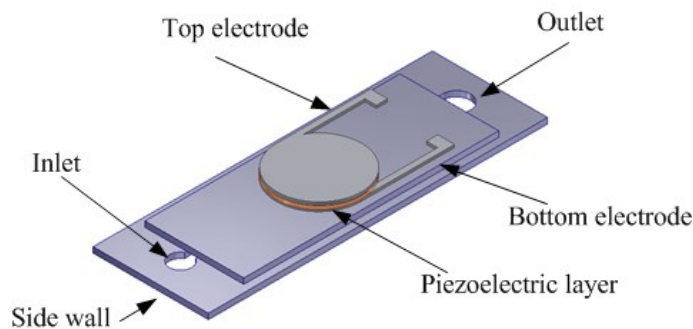
Figure 7-8: Schematic diagram of a valveless micropump.

The first layer is the interface layer which produces a smooth surface for the subsequently printed layers and reduces the usage of the more expensive functional materials to be printed. The second layer is the sacrificial layer which defines the dimensions of the pump chamber and diffusers as well as the reservoirs. This layer is critical because the performance of the diffuser is dependent on the printed shape. The third layer is the side wall layer which is the same height as that of the sacrificial layer. It also ensures the membrane has a uniform thickness around the edges and the middle area. The fourth layer is the membrane which acts as the part of the actuation component for the valveless micropump. This layer also provides covers on top of the diffusers to form the channels. The fifth layer is the bottom electrode. The sixth layer is the piezoelectric layer which produces the actuation mechanism on the membrane. The last layer is the top electrode.

The layer patterns designed using Auto CAD inventor 2012 are shown in Figure 7-9.
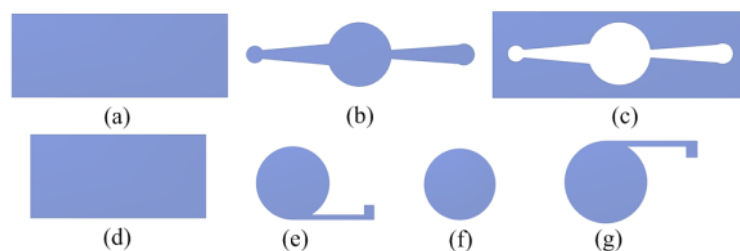
Figure 7-9: Pattern designs of screens: (a) interface layer, (b) sacrificial layer, (c) side wall layer, (d) membrane layer, (e) bottom electrode, (f) piezoelectric layer, (g) top electrode (not to scale).

The dimensions of each pattern are summarised in Table 7-3.

Table 7-3: Dimensions for each printed micropump layer.

Layer name	Dimensions	Screen selection
Interface layer*	L:60mm W: 24mm	Stainless steel, 250, 40 μm emulsion
Sacrificial layer	As described in Figure 7-7	Polyester screen, 120, 40 μm emulsion
Side wall layer	L:55mm W:20mm	Polyester screen, 120, 40 μm emulsion
Membrane layer	L:40mm W:17mm	Polyester screen, 120, 40 μm emulsion
Bottom electrode	r:7.5mm	Polyester screen, 120, 40 μm emulsion
Piezoelectric layer	r:8.5mm	Polyester screen, 120, 40 μm emulsion
Top electrode	r:7.5mm	Polyester screen, 120, 40 μm emulsion

This layer is only used when the fabric substrate is presented.

7.3.2   Material and substrate preparations

The materials used for the fabrication of micropumps have been previously tested in chapter 6. Table 7-4 summarises the materials used for printing a pump.

Table 7-4: Material selections for printing a pump structure.

Layer name	Material	Curing conditions
Interface layer*	Fabinks-UV-IF1	UV 60 seconds
Sacrificial layer	TME based	$85\,^oC$ 5 minutes
Side wall	EFV4/4965	UV 60 seconds
Membrane	EFV4/4965	UV 60 seconds
Bottom electrode	Johnson Matthey S-20	$80\,^oC$ 5 minutes
Piezoelectric layer	Meggitt Piezoelectric paint	$100\,^oC$ 5 minutes
Top electrode	Johnson Matthey S-20	$80\,^oC$ 5 minutes

*This layer is only used when the fabric substrate is presented.

7.3.3 Fabrication evaluation process

The purpose of this section is to realise the pump structure designed in the previous section using screen printing. An incremental fabrication process was used, as shown in Figure 7-10
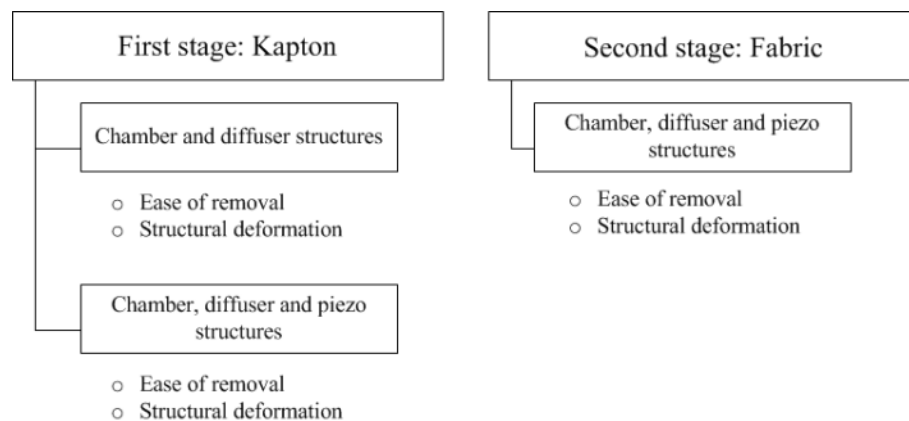
Figure 7-10: An incremental fabrication process used for evaluating the pump structure.

The first stage is to print the pump structure onto a Kapton, which is an appropriate flexible substrate to examine the printing process because it is easier to print on than the fabric so that it eliminates potential problems which will allow for easier identification of design issues before the migration of the design to the more difficult fabric substrates. At the beginning, only the sacrificial, side wall and membrane layers are printed. The purpose of printing these layers is to evaluate the ease of removal of the

sacrificial layer in a complex structure and also to determine the number of printed layers required to achieve an un-deformed membrane after removal. A deformed membrane would not provide an effective pumping mechanism. Once the chamber and diffuser are successfully fabricated, the piezoelectric structure is then added on top of the membrane. By adding extra layers, the structural deformation is examined again as these layers may create additional stresses which could cause deformation.

The second stage is to migrate the entire pump structure onto fabric using the evaluation results identified in the first stage, such as the number of prints and the removal conditions. A printed interface layer on the fabric is then required before printing other layers. The compatibility between the printing parameters and the removal conditions on fabrics are examined.

7.3.4 First stage investigation

7.3.4.1 Printing process of the chamber and diffusers

7.3.4.1.1 Printing

The first stage is to print only the chamber and diffusers onto a Kapton substrate and evaluate the any results obtained after the removal. The printing sequence is shown in Figure 7-11.
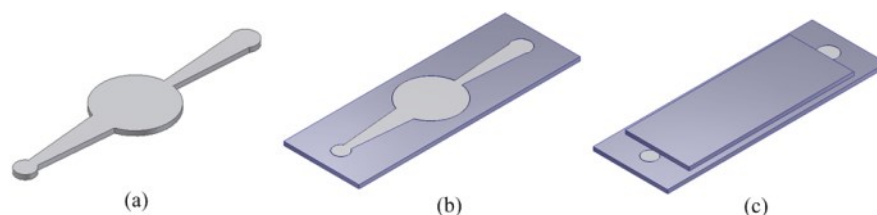
Figure 7-11: Screen printing sequence of a valveless micropump on Kapton; (a) sacrificial, (b) side wall, (c) membrane layer.

Kapton substrates with a thickness of 75 μm were glued on alumina tiles to provide extra support and rigidity. The sacrificial layer was then printed four times to achieve a layer thickness of 100 μm. The side wall layer was printed to the same height as the sacrificial layer to provide support and a uniform surface height for the subsequently printed membrane layer. The printing parameters for each layer are shown in Table 7-5.

Table 7-5: Printing parameters of each layer on Kapton substrate.

Layer name	Printing parameters
Sacrificial layer	Gap: 1.5 mm, pressure: 5 kg, 4 prints
Side wall	Gap: 1.0 mm, pressure: 6 kg, 4 prints
Membrane layer	Gap: 1.0 mm, pressure: 6 kg, 5 prints
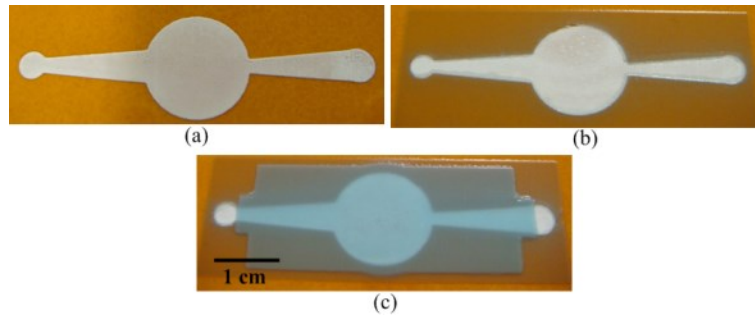
Figure 7-12: Printing sequence of the first stage investigation.

Figure 7-12 shows the printing process of each layer. Finally, the sacrificial layer was removed by placing the pump samples in a box oven at 150 $^{\circ}$C for 30 minutes.

7.3.4.1.2   Results and discussion

An example of the removal results are shown in Figure 7-13.
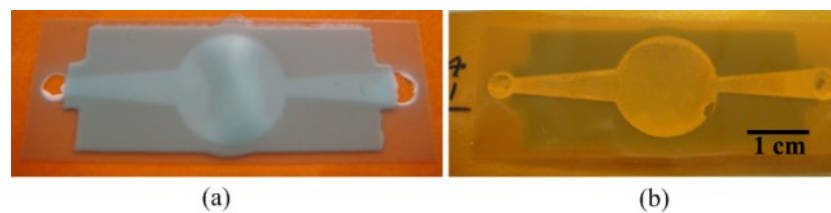
Figure 7-13: Example removal results of a single device viewed from (a) the top and (b) bottom (5 prints).

It was found that the membrane layer, with five prints, was significantly deformed on the chamber area. It is believed that the deformation is due to the temperature which softens the structural material during the removal. Whilst the membrane is softened, it is expanded by the internal pressure which is generated due to the sublimation. Once the temperature reduces, the expanded chamber shrinks, resulting in the deformation.

To overcome the deformation, the thickness of the membrane was increased. As a result, the number of prints for a membrane layer was increased to 10 and 15 to investigate the influence of increased membrane stiffness. The results are shown in Figure 7-14 and Figure 7-15.
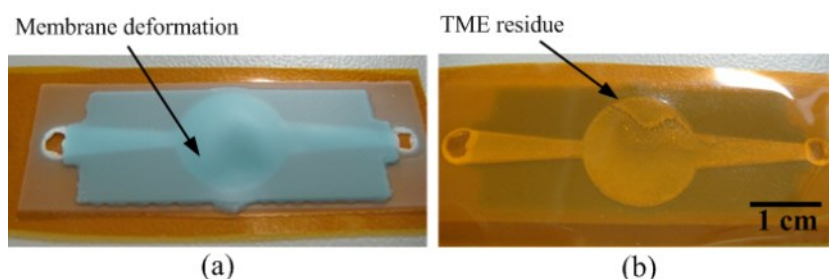
Figure 7-14: Example removal results of a single device viewed from (a) the top and (b) bottom (10 prints).
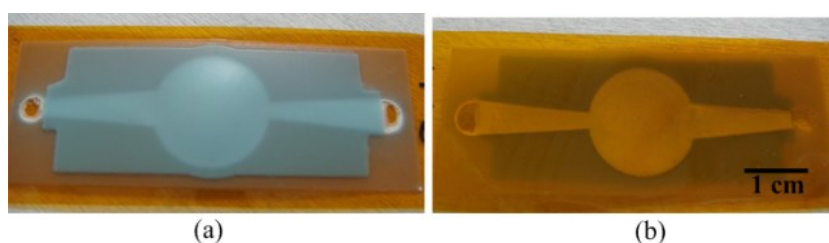
Figure 7-15: Example removal results of a single device viewed from (a) the top and (b) bottom (15 prints).

Increasing the number of prints to 10 still resulted in some deformation but 15 prints produced a chamber that was relatively flat and smooth after the removal.

Compared with the thickness of the membrane with 5 (i.e. 100 µm) and 10 (i.e. 150 µm) prints, the resultant layer after 15 prints was approximately 200 µm. This thickness ensures a membrane free of deformation therefore, in the following sections, 15 prints are used to achieve the membrane.

7.3.4.2 Printing process of entire pump structure

7.3.4.2.1 Printing

In this section, a piezoelectric actuation structure was printed on top of the membrane layer using the materials shown in Table 7-4 and with a printing sequence of bottom electrode, PZT layer and top electrode. The printing sequence is shown in Figure 7-16.
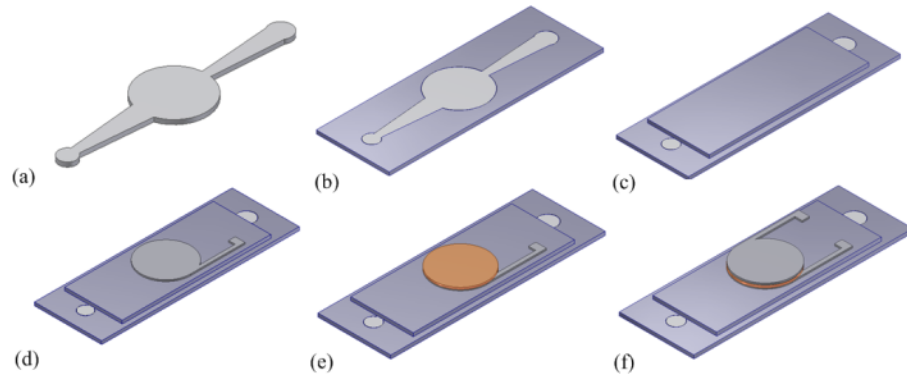
Figure 7-16: Printing sequence with a piezoelectric layer; (a) sacrificial, (b) side wall, (c) membrane, (d) bottom electrode, (e) piezoelectric, (f) top electrode layers.

Beside the parameters reported in Table 7-5, the printing parameters of the rest of layers are summarised in Table 7-6.

Table 7-6: Printing parameters and curing conditions of piezoelectric layers.

Layer name	Parameters
Bottom electrode	Gap: 1.0 mm, pressure: 5.5 kg, 1 print
Piezoelectric layer	Gap: 1.0 mm, pressure: 6 kg, 3 prints
Top electrode	Gap: 0.8 mm, pressure: 6.5 kg, 1 print

Figure 7-17 illustrates the printing process of each layer on Kapton.
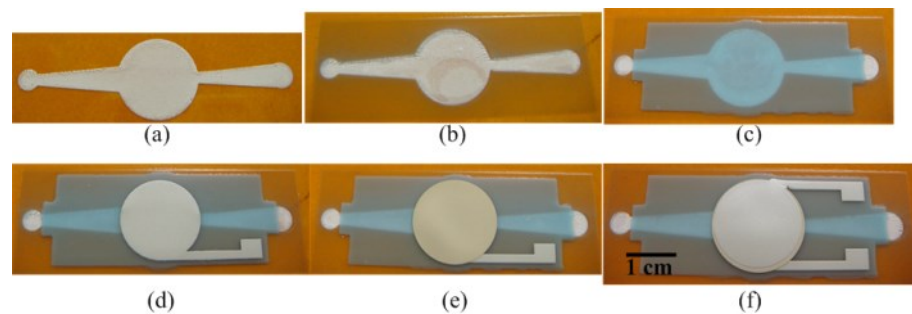
Figure 7-17: Photographs of the printing sequence for a piezoelectrically actuated pump.

7.3.4.2.2   Results and discussion
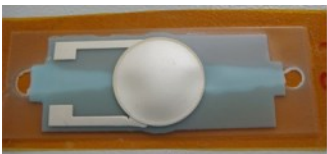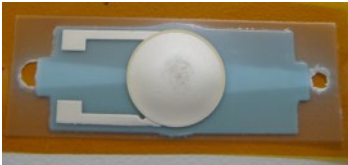
Initially, the removal temperature of 150 ^{o}C was used for 30 minutes. It was found that the chamber seriously deformed and sagged onto the substrate. The silver layer on top of the membrane also cracked and the piezoelectric layer delaminated. The removal temperature was then reduced to 140 ^{o}C for 30 minutes but the deformed chamber still

existed. At this temperature, the sacrificial layer has a lower vapour pressure resulting in a slower rate of sublimation. A longer removal period (i.e. >30 minutes) was not expected because the structural material could be softened further during the long curing process, resulting in a deformed chamber. Temperatures lower than 140 ^{o}C were not investigated because of the low mass loss of TME.

An alternative removal solution, combining the water and thermal removal methods, was introduced. TME is a polar substance and is soluble in most polar substances, including water. The principle is to remove the TME layer from the sample using water in an ultrasonic bath which accelerates the TME dissolution. The thermal removal process then evaporates water from the sample at the last stage. To implement this method, a 500 mL beaker was used as the container and was filled with DI water. The individual sample was clamped onto a piece of alumina tile using two clips and was then placed in this beaker. The beaker and its content were placed on a tray and half immersed in the water of the ultrasonic bath. Once the TME was removed by water, the sample and its supporting alumina tile were placed in a box oven at 150 ^{o}C, 140 ^{o}C and 130 ^{o}C for 5 minutes to evaporate the water. The results are shown in Table 7-7.

Table 7-7: Results with a piezoelectric actuation mechanism at different removal conditions.

Removal conisations	Results
Ultrasonic bath 10 minutes, 150 ^{o}C 5 minutes	
Ultrasonic bath 10 minutes, 140 ^{o}C 5 minutes	
Ultrasonic bath 10 minutes 130 ^{o}C 10 minutes	

It is important to avoid damage to the diffuser structure during the removal process as a deformed diffuser would not provide the optimum fluid rectification. Removal and drying at 150 ^{o}C resulted in a bulging that the chamber area and the side walls of the diffusers were deformed and damaged, respectively. Despite the structural deformation, it could be seen that the sacrificial layer was fully removed and no residue was observed. Drying at 140 ^{o}C showed that no significant bulges were found on the membrane. The sidewalls of the diffusers were not damaged by the deformation so that the rectification performance would not be affected. Water could be evaporated at 140 ^{o}C for five minutes. The removal process obtained at 130 ^{o}C had no significantly difference compared with the sample removed at 140 ^{o}C, but 10 minutes was required for the evaporation of water.

The cross-sectional photograph of the sample dried at 140 ^{o}C shows that the sacrificial layer was fully removed and no significant deformation occurred, shown in Figure 7-19.
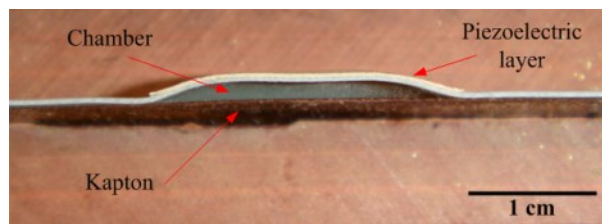
Figure 7-18: Cross-sectional photograph of a pump on a Kapton substrate.

SEM micrographs presented in Figure 7-19 confirm the release of the membrane and the removal of the sacrificial layer. The cracking of the surfaces was due to the cutting of the sample for SEM inspection.
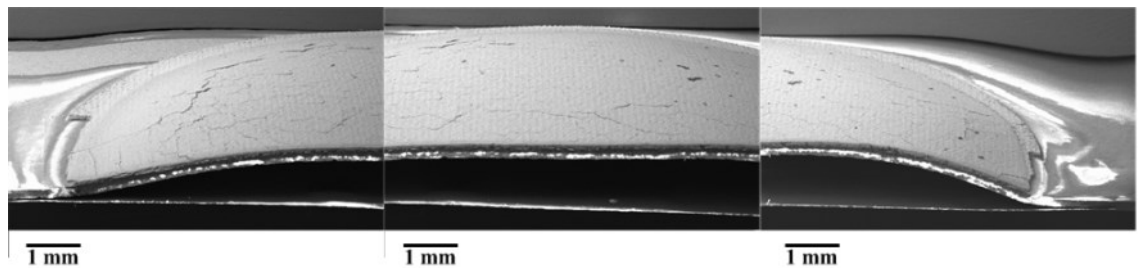
Figure 7-19: Cross-sectional micrograph of a pump on Kapton.

A water removal method combined with a thermal process was identified as a suitable method to remove the sacrificial material without damaging the geometries of the

membrane and diffusers. The removal results obtained at 140 °C enable any TME residue to be removed quickly and a short removal period reduces the risk of chamber deformation due to the softened membrane. Therefore, the chamber shape has less deformation and is relatively flat. However, the bulged membrane cannot be reduced any further because of the properties of the structural material (i.e. thermal plastic).

7.3.5 Second stage investigation

The second stage performs a migration of the fabrication and removal parameters onto the polyester/cotton fabric. The interface layer, which is described in chapter 5 and 6, is used to produce a smooth layer for printing subsequent layers.

7.3.5.1 Printing

Polyester/cotton fabric was glued on top of an alumina tile using the materials and procedure described in chapter 6. The screen selections were reported in Table 7-3. The interface layer was printed onto fabric with 2 prints (i.e. 6 and 4 deposit each print) resulting in a total thickness of 150 μm. The sacrificial layer was then printed on top of the interface layer. The side wall and the membrane layer were subsequently printed and dried in the order stated. The PZT actuation structure was printed with a printing order of bottom electrode, PZT layer and top electrode. The printing sequence and screen selections are the same as those reported in Figure 7-16 and Table 7-3, respectively. The printing parameters are summarised in Table 7-8.

Table 7-8: Printing parameters and curing conditions for each layer on fabric.

Layer name	Printing parameters	Curing conditions
Interface layer	Gap: 1.0 mm, pressure: 6 kg	UV, 60 sec
Sacrificial layer	Gap: 1.5 mm, pressure: 5 kg	85 °C, 5 min
Side wall	Gap: 1.0 mm, pressure: 6 kg	UV, 60 sec.
Membrane layer	Gap: 1.0 mm, pressure: 6 kg	UV, 60 sec
Bottom electrode	Gap: 1.0 mm, pressure: 5.5 kg	80 °C, 5 min
Piezoelectric layer	Gap: 0.8 mm, pressure: 6 kg	100 °C, 5 min
Top electrode	Gap: 0.8 mm, pressure: 6.5 kg	80 °C, 5 min
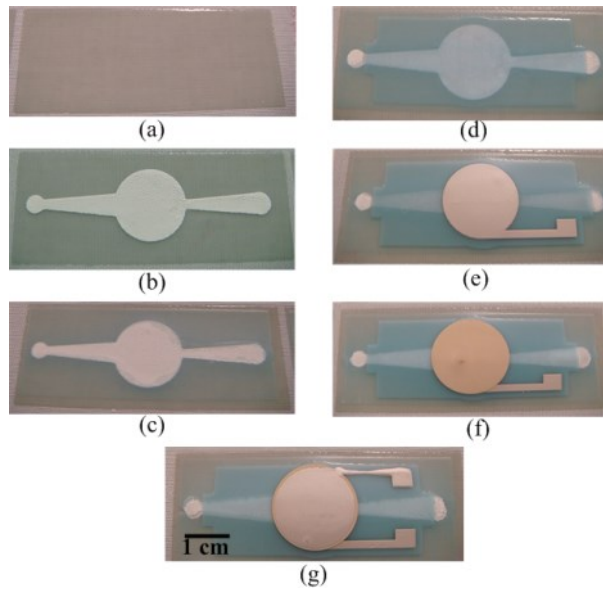
Figure 7-20: Photographs of the printing sequence on polyester/cotton fabric for a micropump.

The removal process was to immerse the sample in a beaker which was half immersed in an ultrasonic bath for 10 minutes. The configuration was the same as the one described in section 7.3.4.2.2. The sample was then placed in a box oven at 140 $^{\circ}$C for 5 minutes. During the two removal steps, the sample was constrained on a piece of alumina using two clips to avoid any deformation during the process.

7.3.5.2   *Results and discussion*

The removal results are shown in Figure 7-21.
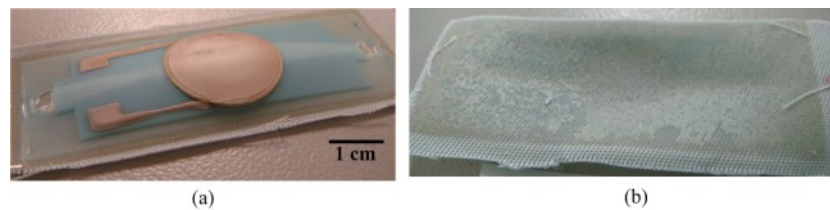
Figure 7-21: Front (a) and back (b) sides of a pump structure after the removal.

Figure 7-21 shows that no bulges were observed on the membrane and the shapes of the diffusers were not damaged. However, the fabric substrate was found to curl forming a 'bowl' shape on the back side of the sample, shown in Figure 7-21 (b). This shape bent the layers on the front side of the fabric resulting in a squeezed chamber. Figure 7-22 shows a cross-sectional photograph of a micropump printed onto fabric with an interface layer. The reduction in the height of the chamber meant the sacrificial layer

was sealed between the membrane and the interface layers. It was then difficult for the water to enter the channel and the chamber during the removal process.
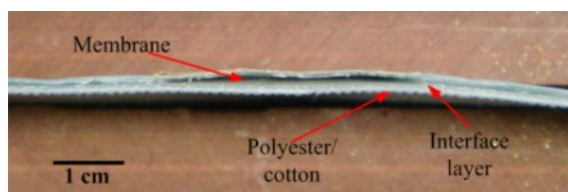
Figure 7-22: Cross-sectional photograph of a pump printed onto the polyester/cotton fabric with a Fabinks-UV-IF1 interface layer.

Alternative removal conditions to remove the sacrificial layer are summarised in Table 7-9 but none of these were completely successful.

Table 7-9: Alternative removal conditions used.

Alternative removal	*Note*
Pure thermal removal:	
150 ^{o}C, 10 minutes and 20 minutes	*Chamber deformed*
140 ^{o}C, 10 minutes and 20 minutes	*Chamber deformed*
Combinations:	
Ultrasonic bath 10 min, 150 ^{o}C 5 minutes	*Sample bent*
Ultrasonic bath 10 min, 130 ^{o}C 5 minutes	*Less bending but sacrificial layer left*
Ultrasonic bath 10 min, 120 ^{o}C 5 minutes	*Less bending but sacrificial layer left*

To examine the deformation problem, EFV4/4965 paste was used to replace the Fabinks-UV-IF1 paste as the interface layer. Ideally, by using the same material as in the structural and interface layers, the deformation due to the difference in thermal expansion coefficients could be minimised. However, the results obtained still had a deformed membrane and the entire sample formed a 'bowl' shape, shown in Figure 7-23.
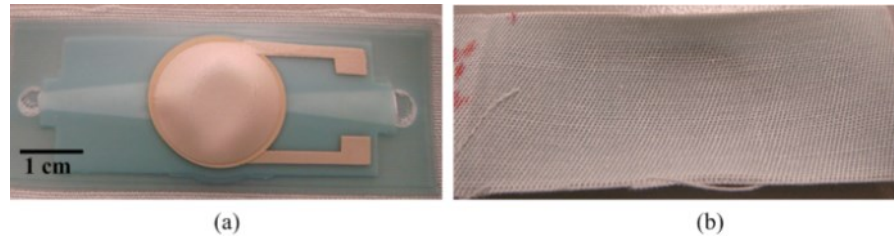
Figure 7-23: Front (a) and back (b) sides of a pump structure with an EFV4/4965 interface layer after removal.
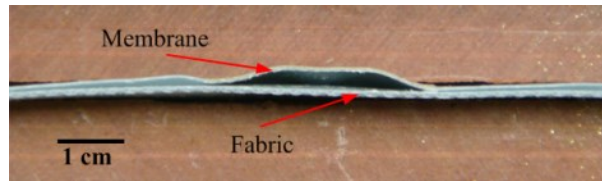
Figure 7-24: Cross-sectional photograph of a pump printed onto the polyester/cotton fabric with an EFV4/4965 interface layer.
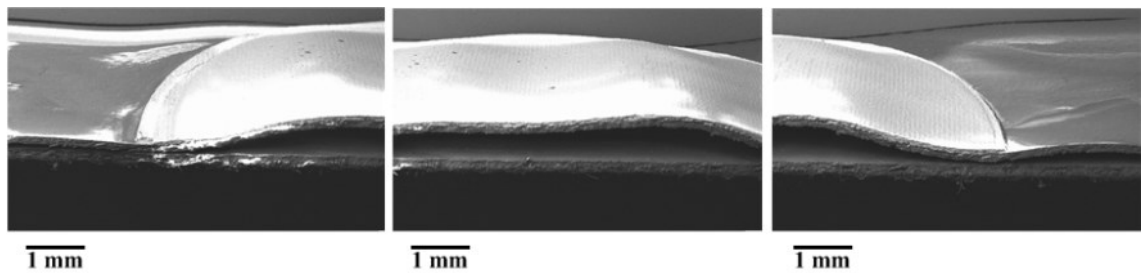
Figure 7-25: Cross-sectional micrograph of a pump on the polyester/cotton fabric with an EFV4/4965 interface layer.

From both the cross-sectional photograph and the SEM micrograph shown in Figure 7-24 and Figure 7-25, respectively, the chamber deformed and bulged outward from the substrate. However, the membrane was released from the substrate in contrast to the results obtained using the Fabinks-UV-IF1 interface layer.

A further experiment involved printing the entire pump structure on a polyester fabric (100% polyester yarns) with a Fabinks-UV-IF1 interface layer. Polyester fabric (~ 65 µm) is thinner than the polyester/cotton fabric (~320 µm) so that any resistance introduced by the thicker fabric can be minimised. Figure 7-26 shows the photographs of the pump sample on the polyester fabric.
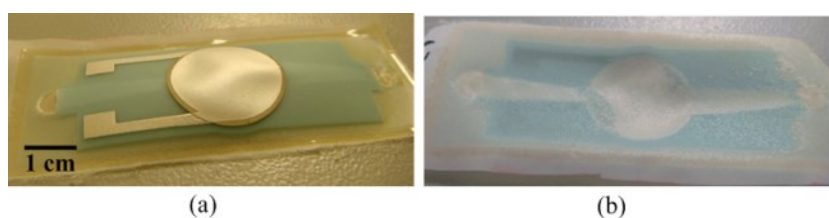
Figure 7-26: Front (a) and back (b) sides of a pump structure on the polyester mesh fabric.

A bulge on the membrane occurred resulting in a 'bowl' shape being formed after the removal, shown in Figure 7-26 (b).
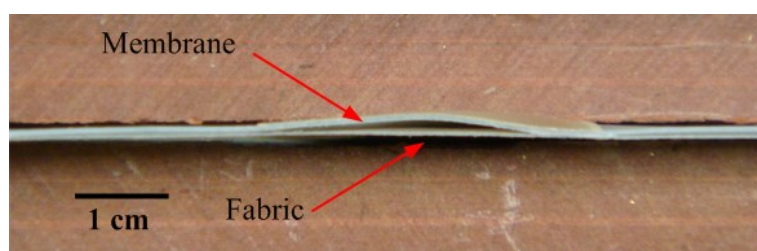
Figure 7-27: Cross-sectional photograph of a pump on polyester mesh fabric.
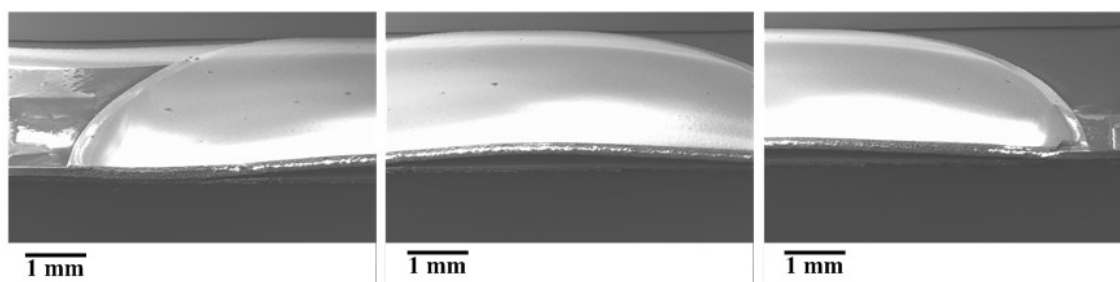
Figure 7-28: Cross-sectional micrograph of a pump on the polyester fabric with an EFV4/4965 interface layer.

The cross-sectional photograph and SEM micrograph in Figure 7-27 and Figure 7-28 show that the removal of the sacrificial layer was prevented by the deformation of the entire sample. Compared with the results obtained using EFV4/4965 and on the polyester/cotton fabric, the membrane was more consistent with less deformation.

7.3.6 Discussion

For the first stage, the chamber and diffusers were completely released and formed after removal. No significant bulges and deformation were observed. The sacrificial layer can be removed by the dissolution of TME in a water bath followed by evaporation of the

water at 140 ^{o}C for 5 minutes. For the second stage, the evaluation did not achieve comparable results in contrast to the results obtained in the first stage.

Various methods were employed to try to reduce the deformation of the interface layer. These include changing the dissolution period and varying the thermal removal period and temperature. However, results showed that significant bulges occurred on the membrane and a 'bowl' shape deformation appeared on all samples on fabrics. This deformation bends the layers printed on top and prevents the sacrificial layer from being removed. It is believed that the 'bowl' shape was formed due to the difference in thermal expansion coefficients between the interface and the structural layers. The structural layer expanded more than the expansion of the interface layer resulting in an inward bending to the fabric substrates. In addition, residual stress could also be the reason of causing the unexpected bending.

7.4 Pump testing

Only the pumps printed on Kapton substrates are tested because a complete pump system on fabric was not achieved. However, these results provide an indication of the expected performance of the printed pump on fabric if the processing compatibility problem can be overcome.

To test the pump, the piezoelectric layer was polarised with a poling field of 4 MV/m at 100 ^{o}C for 10 minutes. The voltage was then maintained when the temperature was cooled down to room temperature. Once the poling was finished, two plastic tubes each with a diameter of 7 mm were glued on the positions where the inlet and outlet holes were using Bostik all-purpose glue. An assembled sample is shown in Figure 7-29.
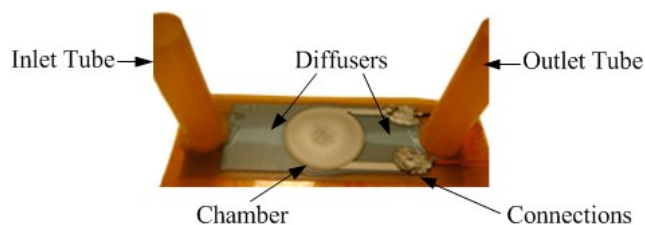
Figure 7-29: A pump with inlet/outlet tubes glued on top.

To drive the piezoelectric layer, a signal generator and a power amplifier were used to produce a sinusoidal signal and amplified driving power, respectively. The signal generator was a TTi TG2000 20 MHz DDS function generator. The power amplifier was a Labworks Inc. PA-138 with a frequency range from DC to 10 kHz. The output voltage of the power amplifier is 80 V_{pp} which is used to drive the printed piezoelectric layer [148]. An oscilloscope (Tektronix TDS2014) was used to observe the waveform of the output signal to ensure that a sinusoidal wave is applied all the time.

The thickness of the membrane was measured using an SEM and an average total thickness of 300 μm was obtained. The theoretical resonant frequency of the membrane was estimated using finite element analysis ANSYS simulation. Since there is no mechanical data available for the Meggitt piezoelectric and Johnson Matthey silver pastes, the entire membrane was simplified as a pure structural material, EFV4/4965. A harmonic analysis was performed on a membrane with a diameter and a thickness of 15 mm and 0.3 mm, respectively. The frequency sweep was performed from 5 Hz to 6 kHz to identify the first model frequency. This simulation also verified the suitability of the selected power amplifier for the required drive frequency. As a result, the simulated resonant frequency was 2.2 kHz, which was below the maximum driving frequency of the power amplifier.

Water was used as the testing liquid. The test involves pumping the liquid from the inlet to the outlet through the chamber. The flow rate was calculated by the following methods, shown in Figure 7-30.
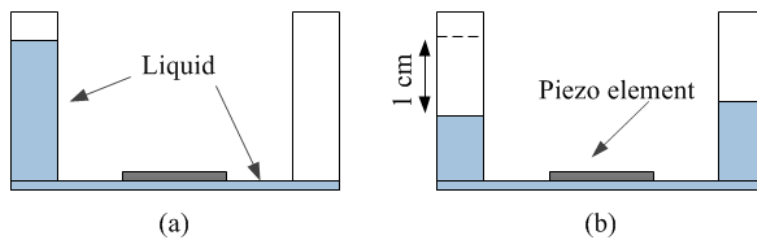
Figure 7-30: The test principle of the pump; (a) before testing, (b) after testing.

For the first test, the pressure on the inlet is higher than the pressure on the outlet because of the different liquid level. This difference drives the liquid, which slowly moves to the outlet side until the liquid levels on both sides are the same. The flow rate is then calculated based on the time at which the liquid reaches the same level. The

experiment was undertaken for 10 minutes whilst the liquid level dropped by 10 mm. The flow rate was then calculated to be:

$$\varphi = \frac{V}{t} = \frac{\pi R^2 h}{t}$$

Eq. 7-4

As a result, 38 µL/min flow rate, which was generated by gravity due to the potential difference between the two liquid levels, was achieved.

In the second test, the inlet tube and the chamber are filled with the liquid and no liquid is in the outlet tube. The driving voltage with a certain frequency is then applied to the piezoelectric layer. The flow rate is calculated based on the time at which the liquid level in the inlet tube drops by 10 mm, shown in Figure 7-30. The resultant flow rate as a function of frequency from 5 Hz to 6 kHz is shown in Figure 7-31.
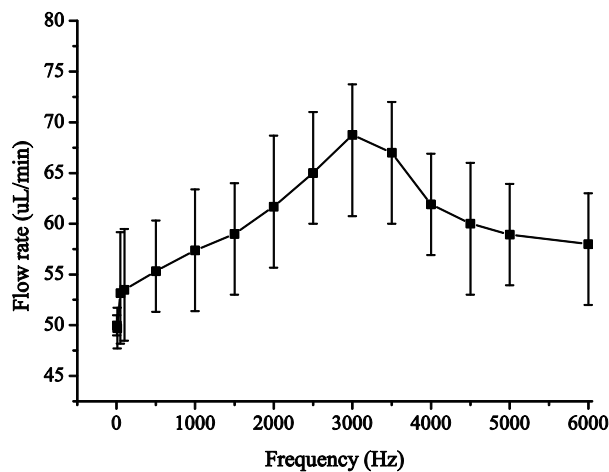
Figure 7-31: Flow rate versus driving frequency.

The net flow rate of the pump shows a maximum at a driving frequency of 3 kHz of 30 µL/min at 80 V_{pp}.

For the third test, the piezoelectric layer is driven at 3 kHz in which the maximum flow rate occurs. The pressure head, which is the maximum level difference between the outlet and the inlet at which the liquid level in the outlet tube no longer increases, was examined. As a result, a maximum average height difference of 1 mm was observed, which was equivalent to 10 Pa.

The theoretical resonant frequency of the membrane was 2.2 kHz which was different from the experimentally determined frequency of the fabricated membrane 3 kHz. It is believed that the printed silver and piezoelectric layers have higher Young's moduli`s than EFV4/4965, thus the experimental resonant frequency is higher than the theoretical results. However, it is difficult to measure the real Young's moduli`s because of limited supply of the piezoelectric paste and the cost of the silver paste.

7.5 Conclusions

Valveless micropumps have been successfully fabricated using screen printing on the Kapton substrate. The cavities within the diffusers and chamber are created after the sacrificial layer is removed. It is shown that the sacrificial material developed in this research can be used to achieve complex mechanical structures, thereby demonstrating the feasibility of the fabrication process.

An un-deformed pump membrane is achieved by printing the structural layer 15 times to achieve a membrane thickness of 200 μm. A lower thickness results in a deformed membrane once the sacrificial layer is removed. A combination of the water dissolution and the thermal evaporation was sufficient to remove the sacrificial material without damaging the membrane and subsequent layers. Even though the combination removal process achieves an un-deformed membrane at this stage it is not an ideal method for garment manufacture because it is unexpected to submerge the entire garment into water and dry in an oven. Migration of the pump structure onto the polyester/cotton fabric shows that the entire sample is deformed after the removal. Replacing the interface layer and changing the fabric substrate did not reduce the deformation. It was believed that the structural material EFV4/4965 could have higher thermal expansion than the Fabinks-UV-IF1 interface layer. As a result, the entire sample was therefore bent inwards of the fabric.

The results show that a maximum flow rate of 68 μL/min and a pressure head of 1 mm were achieved at a driving frequency of 3 kHz 80 V_{pp}. This work has shown that screen printed pumps can be achieved during garment manufacture and could be used in actuator applications, such as drug or bactericide delivery and the release of deodorant or perfume.

Chapter 8

Conclusions and future work

8.1 Conclusions

The aim of this research, which is the development of screen printable sacrificial and structural materials compatible with fabrics and their potential applications, has been accomplished. The following technical areas have been investigated in detail:

- o Development and optimisation of the sacrificial material and processes compatible with fabrics.
- o Identification of the fabric compatible structural materials and process optimisation.
- o Demonstration of the sacrificial and structural materials and fabric compatible processing by fabrication of free standing cantilevers and micropump structures.
- o Demonstration of the feasibility of using screen printed free standing structures on fabrics as the basis of a sensor (i.e. motion sensor) and an actuator (i.e. pump).

The sacrificial material developed in this research is a screen printable paste with a viscosity of 8.5 Pa.s. It is based on the plastic crystalline material Trimethylolethane (TME). The formulation of this material is achieved by fully dissolving 60 wt% TME in a solvent mixture that includes the cyclohexanol (CH) and propylene glycol (PG). As CH is the primary solvent, the proportion of the PG is approximately 14 wt% of CH used. Triple roll milling is necessary to achieve a more homogeneous paste before

printing. The curing temperature of the paste is 85 ^{o}C for 5 minutes and the removal temperature is around 150 ^{o}C for 30 minutes, which is compatible with the majority of fabrics.

The removal temperature can be adjusted by increasing the proportion of PE. This is a great advantage of the TME sacrificial material if used for different removal processes, because only the proportions of the TME and PE need to be changed, thus reducing the complexity of seeking alternatives. A UV curable dielectric material EFV4/4965 is used as the structural material because it is compatible with the TME and the selected fabric. This material can be replaced by other materials depending on future applications.

By depositing these materials on fabric and removing the sacrificial material at the end of the process, various free standing structures can be achieved, such as cantilevers and cavities. Cantilevers with both capacitive and piezoelectric sensing mechanisms can be used as the basis of motion sensors. The measured signals from these cantilevers have a similar motion response to commercial accelerometers.

In addition, a cavity structure is demonstrated in the formation of a valveless micropump which is fabricated entirely using screen printing and the materials. As a result, a maximum flow rate of 68 uL/min while using water can be achieved at the driving frequency of 3 kHz. It is therefore shown that complex structures can also be fabricated using the sacrificial material developed in this research.

8.1.1   Material development

Potential sacrificial materials were evaluated through a three stage evaluation. **The first stage** was to find suitable sacrificial materials.

Dextran could be mixed with water to form a solution which had a maximum concentration of 40 %. Viscosity analysis showed that it was impractical to use the Dextran solution as a screen printable paste because of its low viscosity. The Dextran solution with 40 % concentration also cracked when it was cured.

Sucragel formed a gel when mixed with vegetable oil but the viscosity was reduced when the proportion of the oil increased. Although pure Sucragel was viscous, it was difficult to dry at its maximum operating temperature.

Plastic crystal materials, NPG, TMP and TME were investigated. NPG and TMP could not be formulated into pastes because of their crystallisation and the melting temperature which was too low to be compatible with other screen printable pastes. TME shows the most promising results due to its ease of formulation into a variety of concentrations. Printing evaluation shows that a TME paste with 60 wt% concentration exhibits the best printing results compared with other concentrations. It also shows that the cured TME paste can be removed by heating to 150 $^{\circ}$C leaving no residue. It was therefore found that the thermally removal material TME was the best sacrificial material in this research.

The second stage was to optimise the TME paste by improving the formulation procedure, identifying the transition temperature using DSC, examining the removal rate through TGA and improving the printing quality using a screen with a finer mesh. The formulation of TME paste was improved to make the paste more homogenous. The viscosity of the paste is 8.5 Pa.s and this viscosity decreases with time at a constant shear strain rate, confirming that the paste is thixotropic. The curing temperature was increased to 85 $^{\circ}$C to provide a maximum evaporation of CH and a minimum sublimation of TME during curing. The removal temperature was identified to be below 200 $^{\circ}$C to maintain TME in a solid phase which reduces the chance of stiction problems compared with higher temperatures.

The third stage was to adjust the removal temperature of TME by adding PE. The removal temperature was increased when the proportion of PE was increased. To achieve the same removal rate, the removal temperature was increased. This is a great advantage of the sacrificial material if used for different removal processes, because only the proportions of the materials need to be changed, thus reducing the complexity of seeking alternatives. As a result, the removal temperature can be increased from 150 $^{\circ}$C to any temperatures up to 220 $^{\circ}$C. Since the melting point of PE is 250 $^{\circ}$C, it is expected that the temperature is beyond 200 $^{\circ}$C, up to 250 $^{\circ}$C will be achievable.

8.1.2 Fabrication process development

The chosen fabrication technique is screen printing. Free standing structures are printed on top of the substrate layer by layer similarly to surface micromachining. Different materials, including conductive and piezoelectric materials, can be printed onto fabric to form micro devices. Subsequent drying or curing processes solidify the printed layers. The simplicity of the fabrication procedure means that sensors and actuators can be easily integrated into existing clothing using the same methods as T-shirt printing, by anyone from industrial printing companies to small print shops. Compared with silicon MEMS and weaving/knitting techniques, the key advantage of this technology is that it can be used with any screen printing equipment and does not require expensive specialist technology.

8.1.3 Demonstration and characterisation

A two stage process was used to demonstrate the developed sacrificial technology on fabric.

The first stage demonstrates the feasibility of using the sacrificial technology for the fabrication of cantilevers on a fabric substrate using only screen printing. By printing additional conductive and piezoelectric layers onto the cantilevers, capacitive and piezoelectric sensing mechanisms can be implemented. The capacitive mechanism was first evaluated as it had a simpler mechanical structure and fewer printed layers compared with the cantilever with a piezoelectric layer. Removal results showed that cantilevers could be completely released from the substrate after the sacrificial material sublimated. It was also confirmed that the removal temperature was compatible with the interface and structural materials as well as the chosen fabric. Subsequently, the piezoelectric material was printed onto the top of cantilevers for the evaluation of an alternative sensing mechanism. It was shown that curing the piezoelectric layer at 100 ^{o}C, which was higher than its sublimation point, would not affect the cured TME layer. Arm testing results showed that both types of the cantilever had the potential to be used as the basis of motion sensors on fabric.

The second stage demonstrated the feasibility of using the sacrificial material for the fabrication of a cavity on fabrics using screen printing. This is demonstrated by fabricating valveless micropumps on Kapton. After the printing process, the sacrificial layer can be removed to release the membrane and form the diffusers. The removal process used was a two-stage approach, differing from that used for cantilevers. The first stage was to remove the sacrificial material using water and the second stage was to evaporate the water using thermal energy. Removal results showed that a complete pump structure could be achieved by removing the sacrificial material in a water ultrasonic bath for 10 minutes followed by an evaporation of water at 140 $^{\circ}$C for 5 minutes. The testing results showed that the printed pumps could pump water with a maximum flow rate of 68 uL/min at 3 kHz, conforming the functionality of the device. However, pumps printed on fabrics are not successful because of the deformation of the entire sample during exposure to high temperature and water whilst removal.

8.2   Future work

8.2.1   Material formulation

As described in chapter 4, the removal temperature of the TME sacrificial paste can be adjusted by mixing with PE to achieve a homogeneous mixture. DSC results show that the transition point of the TME-PE mixture is increased by adding more PE. TGA results also show that the mass loss rate is decreased when increasing the amount of PE. However, the formulation of these mixtures into a suitable paste form has not been achieved. As the TME and PE have opposite polarities, the dissolution solvent needs to be investigated to ensure both materials can be dissolved. One possibility for dissolving two materials with different polarities is to mix two different solvents which also have different polarities.

8.2.2   Cantilever designs

In chapter 6, printed cantilevers with the capacitive and piezoelectric sensing mechanisms are shown to have potential use as motion sensors with sensing mechanisms that are excited by human movement. As the dimensions of these

cantilevers were not designed to be motion sensors, further optimisation could be conducted, such as detecting small human movement (e.g. < 1 m/s^2).

For capacitive cantilevers, the first improvement could be changing the size of the cantilever as a smaller cantilever potentially reduces the risk of damage. The second improvement could be reducing the resonant frequency by adding an additional proof mass layer at the free end of the cantilever. In addition, an encapsulation layer could be added on top of the cantilever to prevent it being damaged.

For cantilevers with a piezoelectric layer, the phase difference needs to be compensated by changing the detection circuit. Because the cantilever is operated in the d_{31} mode, the size of the piezoelectric layer should be reduced and relocated to where the maximum stress is generated when vibrating. In addition to the testing, low frequencies (e.g. <100 Hz) will be used to evaluate the performance of these cantilevers in accurately sensing human movement.

The PCB designs show that both capacitive and piezoelectric readout circuits only require a single layer of conductive tracks. It is therefore possible to print the readout circuit tracks on fabric at the same time as the sensor fabrication. The readout circuit and the sensors should be located as close as possible to reduce the noise introduced by the connection wires.

8.2.3   Investigation of micropump fabrication on fabrics

The problem with printing the pump structure onto fabrics is the deformation caused by the difference in thermal expansion coefficients. The structural layer expands faster compared with the interface layer. Bending will reduce the sublimation of the sacrificial material as the upper layers are squeezed. This contraction could be balanced by printing an additional structural layer onto the back side of the fabric so that the stress may reduce, thus reducing the bending. In addition to the pump operation, a lower driving voltage than existing 80 $V_{pp.,}$ would be preferable for wearable applications. Reducing the driving voltage or seeking an alternative driving mechanism (e.g. thermo pneumatic mechanism [84]) could be implemented.

Appendix A:

Other TME formulations

TME and TMP paste evaluation

*TME and TMP (**90:10**)*

Concentration of the paste	TME	TMP	CH	PG	Printability
40 wt%	36% (13.5)	4% (1.5)	52.6% (19.7)	7.4% (2.7)	No
50 wt%	45% (20.2)	5% (2.2)	43.9% (19.7)	6.1% (2.7)	Poor
60 wt%	54% (30.3)	6% (3.3)	35% (19.7)	5% (2.7)	Yes

*The valves shown in the bracket are experimental data used in the evaluation process. Unit: gram.
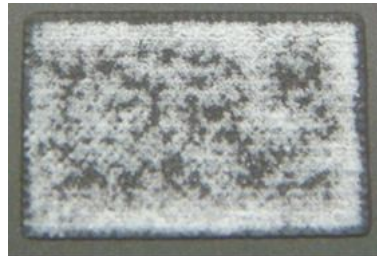
1 cm

50 wt% TME/TMP paste

1 cm

60 wt% TME/TMP paste

183
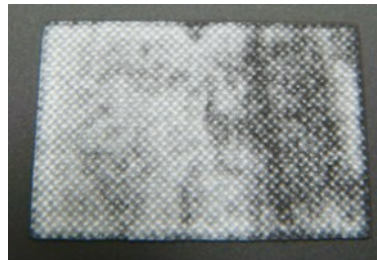
*TME and TMP (**80:20**)*

Concentration of the paste	TME	TMP	CH	PG	Printability
40 wt%	32% (12.0)	8% (3.0)	52.6% (19.7)	7.4% (2.7)	No
50 wt%	40% (19.9)	10% (4.4)	43.9% (19.7)	6.1% (2.7)	No
60 wt%	48% (26.88)	12% (6.72)	35% (19.7)	5% (2.7)	Poor

*The valves shown in the bracket are experimental data used in the evaluation process.
Unit: gram.

1 cm
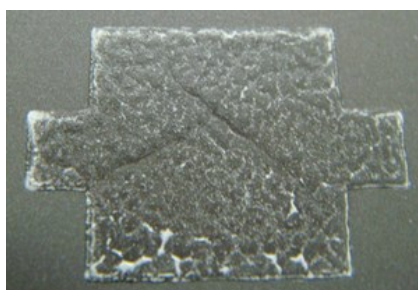
60 wt% TME/TMP paste

TME and TMP (70:30)

Concentration of the paste	TME	TMP	CH	PG	Printability
40 wt%	28% (10.5)	12% (4.5)	52.7% (19.7)	7.3% (2.7)	No
50 wt%	35% (15.7)	15% (6.7)	43.86% (19.7)	6.4% (2.8)	No
60 wt%	42% (23.5)	18% (10)	35% (19.7)	5% (2.7)	Poor

The valves shown in the bracket are experimental data used in the evaluation process. Unit: gram.

1 cm
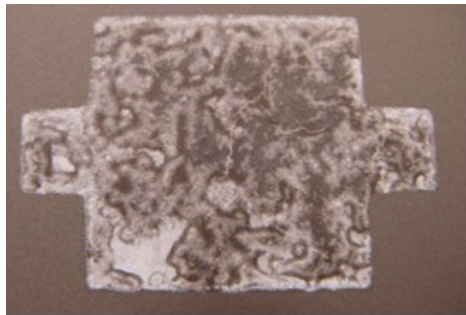
<u>60 wt% TME/TMP paste</u>

TME and NPG paste evaluation*					

TME and NPG (90:10)

Concentration of the paste	TME	NPG	CH	PG	Printability
60wt%	54% (10.26)	6% (1.14)	35.1% (6.7)	4.9% (0.9)	Poor

The valves shown in the bracket are experimental data used in the evaluation process. Unit: gram.

1 cm

60 wt% TME/NPG paste

*TME and NPG (**80:20**)*

Concentration of the paste	TME	NPG	CH	PG	Printability
60wt%	48% (9.4)	12% (2.3)	35% (6.9)	5% (0.9)	Poor

*The valve shown in the bracket are experimental data used in the evaluation process.
Unit: gram.

1 cm

60 wt% TME/NPG paste

TME and NPG (70:30)

Concentration of the paste	TME	NPG	CH	PG	Printability
60wt%	42% (8.1)	18% (3.5)	35% (6.9)	5% (0.9)	Poor

*The valve shown in the bracket are experimental data used in the evaluation process.
 Unit: gram.*
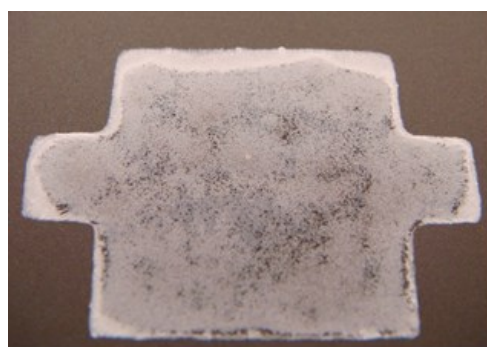
60 wt% TME/NPG paste

Appendix B:

Other ethyl cellulose mixtures

Ethyl cellulose + ethanol	
Composition	Ethyl cellulose and ethanol
Concentration	10 wt%
Formulation	1.2 g ethyl cellulose was mixing with 14 mL ethanol at room temperature
Dissolution	Fully dissolved, 1 hour
Paste state	Clear liquid
Note	Chemical reaction with TME.
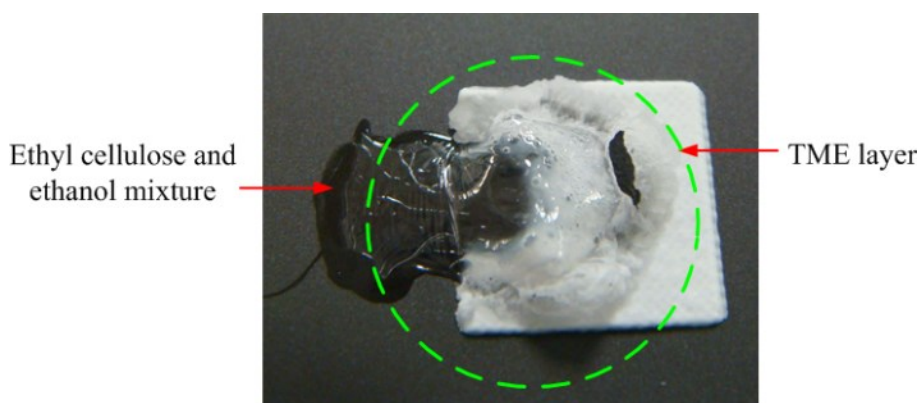
Ethyl cellulose + cyclohexane	
Composition	Ethyl cellulose and cyclohexane
Concentration	10 wt%
Formulation	1.2 g ethyl cellulose was mixing with 14 mL cyclohexane at room temperature
Dissolution	Swelling at room temperature, 1 hour
Paste state	Viscous liquid with bubbles
Note	The viscosity of the mixture is not compatible with the screen printing and it cannot be printed.

Ethyl cellulose + Acetyl acetone	
Composition	Ethyl cellulose and acetyl acetone
Concentration	10 wt%
Formulation	1.2 g ethyl cellulose was mixing with 11 mL acetyl acetone at room temperature
Dissolution	Fully dissolved, 2 hour
Paste state	Clear yellow liquid
Note	The viscosity of the mixture is too low to print.

Ethyl cellulose + ethyl lactate	
Composition	Ethyl cellulose and ethyl lactate
Concentration	10 wt%
Formulation	1.2 g ethyl cellulose was mixing with 10 mL ethyl lactate at room temperature
Dissolution	Fully dissolved, 1 hour
Paste state	Clear liquid
Note	The viscosity of the mixture is too low to print.

Ethyl cellulose + 2-butoxyethyl ether	
Composition	Ethyl cellulose and 2-butoxyethyl ether
Concentration	9 wt%
Formulation	1g ethyl cellulose was mixing with 11 mL 2-butoxyethyl ether at room temperature and 100 $^{\circ}$C 1g ethyl cellulose was mixing with 11 mL 2-butoxyethyl ether at 100 $^{\circ}$C
Dissolution	Swelling at room temperature, 0.5 hour Fully dissolved at 100 $^{\circ}$C, 1 hour
Paste state	Clear gel
Note	The viscosity of the mixture is too low to print.

Ethyl cellulose + solvent mixture	
Solvent mixture	20% Acetyl acetone 80% 2-Butoxyethyl ether
Concentration	3 wt%
Formulation	0.4 g ethyl cellulose was mixing with 15 mL solvent mixture at room temperature
Dissolution	Swelling at room temperature, 0.5 hour
Paste state	Swelling gel

Ethyl cellulose + solvent mixture	
Solvent mixture	80% Acetyl acetone 20% 2-Butoxyethyl ether
Concentration	6 wt%
Formulation	0.6 g ethyl cellulose was mixing with 11 mL solvent mixture at room temperature
Dissolution	Swelling at room temperature, 0.5 hour
Paste state	Swelling gel

Ethyl cellulose + solvent mixture	
Solvent mixture	70% Acetyl acetone 30% 2-Butoxyethyl ether
Concentration	9 wt%
Formulation	1 g ethyl cellulose was mixing with 11 mL solvent mixture at room temperature
Dissolution	Swelling at room temperature, 0.5 hour
Paste state	Swelling gel

References

[1]   X. Tao,"*Smart fibres, fabrics and clothing*", Woodhead Publishing Ltd and CRC Press LLC, 2001.

[2]   C. Baber, A. Schwirtz, J. Knight, H. Bristow, T. N. Arvanitis and F. Psomadellis, "SensVest-onbody physiological monitoring system", in *IEE Eurowearable*, Birmingham,UK, 2003, p. 93-98.

[3]   Y. I. Lee, K. H. Park, J. Lee, C. S. Lee, H. J. Yoo, C. J. Kim and Y. S. Yoon, "Dry release for surface micromachining with HF vapor-phase etching", *Journal of Microelectromechanical Systems,* vol.6, 1997, p. 226-33.

[4]   J. M. Bustillo, R. T. Howe and R. S. Muller, "Surface micromachining for microelectromechanical systems", *Proceedings of the IEEE,* vol.86, 1998, p. 1552-74.

[5]   H. C. Nathanson, W. E. Newell, R. A. Wickstrom and J. R. Davis, "The resonant gate transistor", *IEEE Transactions on Electron Devices,* vol.14, 1967, p. 117-33.

[6]   R. T. Howe and R. S. Muller, "Polycrystalline silicon micromechanical beams", *Journal of the Electrochemical Society,* vol.130, 1983, p. 1420-1423.

[7]   R. Lewis and W. Evans,"*Chemistry*", 2 ed., Palgrave Fundations, 2001.

[8]   P. W. Atkins and J. A. Beran,"*General chemistry*", 2 ed., Scientific American Library, 1992.

[9]   L. Jones and P. Atkins,"*Chemistry: molecules, matter, and change*", 4 ed., W.H. Freeman and Company, 2000.

[10]   Q. Liu, B. Liu and Z. Li, "Improvement of Au cantilever fabrication process with Cu as a sacrificial layer", in *4th IEEE International Conference on Nano/Micro Engineered and Molecular Systems*, Shenzhen, China, 2009, p. 872-76.

[11]   J. Dykyj, J. Svoboda, R. Wilhoit, M. Frenkel and K. Hall,"*Vapor pressure of chemicals: vapor pressure and antoine constants for oxygen containing organic compounds*". " New York, Springer Verlag Berlin Heideberg, 2000.

[12]   V. Linder, B. D. Gates, D. Ryan, B. A. Parviz and G. M. Whitesides, "Water-soluble sacrificial layers for surface micromachining", *Small Journal,* vol.1, 2005, p. 730-36.

[13]   E. B. Steager, M. S. Sakar, D. H. Kim, V. Kumar, G. J. pappas and M. J. Kim, "Electrokinetic and optical control of bacterial microrobots", *Journal of Micromechanics and Micoengineering,* vol.21, 2011, p. 1-8.

[14]   N. Ferrell, J. Woodard and D. Hansford, "Fabrication of polymer microstructures for MEMS: sacrificial layer micromolding and patterned substrate micromolding", *Biomedical Microdevices,* vol.9, 2007, p. 815-821.

[15]   K. A. Addae-Mensah, R. S. Reiserer and J. P. Wikswo, "Poly(vinyl alcohol) as a structure release layer for the microfabrication of polymer composite structures", *Journal of Micromechanics and Microengineering,* vol.17, 2007, p. 41-46.

[16]   L. Tao, X. M. Zhao, J. M. Gao and W. Hu, "Lithographically defined uniform worm-shaped polymeric nanoparticles", *Nanotechnology,* vol.21, 2010, p. 1-6.

[17]   W. Sparreboom, J. C. T. Eijkel, J. Bomer and A. van den Berg, "Rapid sacrificial layer etching for the fabrication of nanochannels with integrated metal electrodes", *Lab on a Chip,* vol.8, 2008, p. 402-07.

[18]   X. Huang, G. Liu, X. Ying, J. Wang, Y. Guo, C. Kang and Y. Tian, "Applications of thick sacrificial-layer of zinc in LIGA process", in *Microsystem Technologies*, Germany, 2008, p. 1257-61.

[19]   J. W. Berenschot, N. R. Tas, T. S. J. Lammerink, M. Elwenspoek and A. van Den Berg, "Advanced sacrificial poly-Si technology for fluidic systems", *Journal of Micromechanics and Microengineering,* vol.12, 2002, p. 621-24.

[20]   C. Chung and M. Allen, "Uncrosslinked SU-8 as a sacrificial material", *Journal of Micromechanics and Microengineering,* vol.15, 2005, p. N1-N5.

[21]   I. G. Foulds, R. W. Johnstone and M. Parameswaran, "Polydimethylglutarimide (PMGI) as a sacrificial material for SU-8 surface-micromachining", *Journal of Micromechanics and Microengineering,* vol.18, 2008, p. 1-11.

[22]   C. Luo, A. Govindaraju, J. Garra, T. Schneider, R. White, J. Currie and M. Paranjape, "Releasing SU-8 structures using polystyrene as a sacrificial material", *Sensors and Actuators A: Physical,* vol.114, 2004, p. 123-28.

[23]   N. Maluf and K. Williams,"*An introduction to microelectromechanical systems engineering*", Artech hous Inc., 2004.

[24]   D. Bhusari, H. A. Reed, M. Wedlake, A. M. Padovani, S. A. B. Allen and P. A. Kohl, "Fabrication of air-channel structures for microfluidic, microelectromechanical, and microelectronic applications", *Journal of Microelectromechanical Systems,* vol.10, 2001, p. 400-08.

[25]   H. A. Reed, C. E. White, V. Rao, S. A. B. Allen, C. L. Henderson and P. A. Kohl, "Fabrication of microchannels using polycarbonates as sacrificial materials", *Journal of Micromechanics and Microengineering,* vol.11, 2001, p. 733-37.

[26]   R. T. Kelly, T. Pan and A. T. Woolley, "Phase changing sacrificial materials for molvent bonding of high performance polymeric capillary electrophoresis microchips", *Analytical Chemistry,* vol.77, 2005, p. 3536-41.

[27] H. V. Fuentes and A. T. Woolley, "Phase changing sacrificial layer fabrication of multilayer polymer microfluidic devices", *Analytical Chemistry,* vol.80, 2008, p. 333-39.

[28] H. Birol, T. Maeder and P. Ryser, "Processing of graphite-based sacrificial layer for microfabrication of low temperature co-fired ceramics (LTCC)", *Sensors and Actuators A: Physical,* vol.130-131, 2006, p. 560-67.

[29] C. Lucat, P. Ginet, C. Castille, H. Debeda and F. Menil, "Microsystems elements based on free-standing thick-films made with a new sacrificial layer process", *Microelectronics Reliability,* vol.48, 2008, p. 872-75.

[30] C. B. Sippola and C. H. Ahn, "A hermetic thick film screen-printed ceramic cavity for harsh environment sensing applications", *IEEE Transactions on Components and Packaging Technologies,* vol.30, 2007,

[31] N. Serra, T. Maeder, C. Jacq, Y. Fournier and P. Ryser, "Screen-printed polymer-based microfluidic and micromechanical devices based on evaporable compounds", in *2009 European Microelectronics and Packaging Conference,* Italy, 2009.

[32] S. L. Kok, N. M. White and N. R. Harris, "Free-standing thick-film piezoelectric device", *Electronics Letters,* vol.44, 2008, p. 280-82.

[33] C. B. Sippola and C. H. Ahn, "A thick film screen-printed ceramic capacitive pressure microsensor for high temperature applications", *Journal of Micromechanics and Microengineering,* vol.16, 2006, p. 1086-91.

[34] S. A. Wilson, R. P. J. Jourdain, Q. Zhang, R. A. Dorey, C. R. Bowen, M. Willander, Q. U. Wahab, M. Willander, S. M. Al-hilli, O. Nur, E. Quandt, C. Johansson, E. Pagounis, M. Kohl, J. Matovic, B. r. Samel, W. v. d. Wijngaart, E. W. H. Jager, D. Carlsson, Z. Djinovic, M. Wegener, C. Moldovan, R. Iosub, E. Abad, M. Wendlandt, C. Rusu and K. Persson, "New materials for micro-scale sensors and actuators: an engineering review", *Materials Science and Engineering: R,* vol.56, 2007, p. 1-129.

[35] J. H. Chung and J. J. Pak, "A surface-micromachined accelerometer using a movable polysilicon gate FET", in *Smart electronics and MEMS,* Adelaide, Australia, 1997, p. 96-104.

[36] L. Tong, M. Mehregany and W. C. Tang, "Amorphous silicon carbide films by plasma-enhanced chemical vapor deposition", in *Micro Electro Mechanical Systems, 1993, MEMS '93, Proceedings An Investigation of Micro Structures, Sensors, Actuators, Machines and Systems. IEEE.,* 1993, p. 242-47.

[37] A. Bagolini, L. Pakula, T. LMScholtes, H. TMPham, P. J. French and P. M. Sarro, "Polyimide sacrificial layer and novel materials for post-processing surface micromachining", *Journal of Micromechanics and Microengineering,* vol.12, 2002, p. 385-89.

[38] A. Hartley, R. Miles, N. Dimitrakopoulos and R. D. Pollard, "SU-8 beams and membranes", in *1st EMRS DTC technical conference,* Edinburgh, UK, 2004.

[39]   A. B. Frazier, "Recent applications of polyimide to micromachining technology", *IEEE Transactions on Industrial Electronics,* vol.42, 1995,

[40]   *HD MicroSystems*. Available: http://hdmicrosystems.com (08/07/2013).

[41]   J. C. McDonald and G. M. Whitesides, "Poly(dimethylsiloxane) as a material for fabricating microfluidic devices", *Accounts of Chemical Research,* vol.35, 2002, p. 491-99.

[42]   M. Mehregany, C. A. Zorman, N. Rajan and W. Chien Hung, "Silicon carbide MEMS for harsh environments", *Proceedings of the IEEE,* vol.86, 1998, p. 1594-1609.

[43]   M. Ree, T. L. Nunes and K. J. R. Chen, "Structure and properties of a photosensitive polyimide: Effect of photosensitive group", *Journal of Polymer Science Part B: Polymer Physics,* vol.33, 1995, p. 453-65.

[44]   C. Lucat, P. Ginet and F. Menil, "New sacrifical layer-based screen printing process for free standing thick films applied to MEMS", *International Microelectronics and Packaging Society,* vol.4, 2007, p. 86-92.

[45]   S. L. Kok, "Design, fabrication and characterisation of free standing thick-film piezoelectric cantilevers for energy harvesting", PhD thesis, School of Electronics and Computer Science, University of Southampton, 2010.

[46]   R. Lakhmi, H. Debéda, I. Dufour and C. Lucat, "Force sensors based on screen-printed cantilevers", *IEEE Sensors Journal,* vol.10, 2010, p. 1133-37.

[47]   N. Serra, "Epoxy-graphite resistive composites: formulation, characterization and applications", PhD thesis, École polytechnique federale de lausanne, 2012.

[48]   R. Lakhmi, H. Debéda, I. Dufour and C. Lucat, "Determination of Young's Moduli for free-standing screen-printed thick film layers used in MEMS", in *20th Workshop on Micromachining, Microechanics and Microsystems*, Toulouse, France, 2009.

[49]   A. Schwarz, L. V. Langenhove and D. Deguillemont, "A roadmap on smart textiles", *Textile Progress,* vol.42, 2010, p. 99-180.

[50]   X. Tao,"*Wearable electronic and photonics*", Woodhead Publishing Ltd and CRC press LLC, 2005.

[51]   A. Mazzoldi, D. D. Rossi, F. Lorussi, E. P. Scilingo and R. Paradiso, "Smart textiles for wearable motion capture systems", *AUTEX Research Journal,* vol.2, 2002,

[52]   E. P. Scilingo, A. Gemignani, R. Paradiso, N. Taccini, B. Ghelarducci and D. D. Rossi, "Performance evaluation of sensing fabrics for monitoring physiological and biomechanical variables", *IEEE Transactions on Information Technology in Biomedicine,* vol.9, 2005, p. 345-52.

[53]   J. Meyer, P. Lukowicz and G. Troster, "Textile pressure sensor for muscle activity and motion detection", in *10th IEEE International Symposium on Wearable Computers*, 2006, p. 69-72.

[54]   T. H. Kang, C. R. Merritt and E. Grant, "Nonwoven fabric active electrodes for biopotential measurement during normal daily activity", *IEEE Transactions on Biomedical Engineering,* vol.55, 2008, p. 188-95.

[55]   M. Rothmaier, M. P. Luong and F. Clemens, "Textile pressure sensor made of flexible plastic optical fibers", *Sensors,* vol.8, 2008, p. 4318-29.

[56]   M. D. Husain and T. Dias, "Development of Knitted Temperature Sensor (KTS)", Textiles & Paper, School of Materials, University of Manchester, UK, 2009.

[57]   K. Crowley, A. Morrin, R. L. Shepherd, M. i. h. Panhuis, G. G. Wallace, M. R. Smyth and A. J. Killard, "Fabrication of polyaniline-based gas sensors using piezoelectric inkjet and screen printing for the detection of hydrogen sulfide", *IEEE Sensors Journal,* vol.10, 2010, p. 1419-26.

[58]   Y. Kim, H. Kim and H. Yoo, "Electrical characterization of screen printed circuits on the fabric", *IEEE Transactions on Advanced Packaging,* vol.33, 2010, p. 196-205.

[59]   J. Vicente and A. A. Moreira, "Electro-textile printed slot antenna over finite EBG structure", in *International Workshop on Antenna Technology (iWAT)*, 2010, p. 1-4.

[60]   G. Cho, K. Jeong, M. J. Paik, Y. Kwun and M. Sung, "Performance evaluation of textile-based electrodes and motion sensors for smart clothing", *IEEE Sensors Journal,* vol.11, 2011,

[61]   *Peratch company ltd.* Available: http://www.eleksen.com/?page=products/elektexproducts/touchscreen.php (08/07/2013).

[62]   S. Bruer, N. Powell and G. Smith, "Three-dimensionally knit spacer fabrics: a review of production techniques and applications", *Journal of Textile and Apparel, Technology and Management,* vol.4, 2005, p. 85-113.

[63]   Z. Fan, J. Chen, J. Zou, D. Bullen, C. Liu and F. Delcomyn, "Design and fabrication of artificial lateral line flow sensors", *Journal of Micromechanics and Microengineering,* vol.12, 2002, p. 655-61.

[64]   J. G. Korvink and O. Paul,"*MEMS: A practical guile to design, analysis and applications*", Brent Beckley/William Andrew Inc., 2006.

[65]   M. Ataka, A. Omodaka, N. Takeshima and H. Fujita, "Fabrication and operation of polyimide bimorph actuators for a ciliary motion system", *Journal of Microelectromechanical Systems,* vol.2, 1993, p. 146-50.

References

[66]   X. Sun, K. R. Farmer and W. N. Carr, "A bistable microrelay based on two-segment multimorph cantilever actuators", in *International conference on Micro-Electro-Mechanical Systems (MEMS)*, 1998, p. 154-59.

[67]   Y. C. Li, M. H. Ho, S. J. Hung, M. H. Chen and M. S. Lu, "CMOS micromachined capacitive cantilevers for mass sensing", *Journal of Micromechanicals and Micoengineering,* vol.16, 2006, p. 2659-65.

[68]   S. Chatzandroulis, A. Tserepi, D. Goustouridis, P. Normand and D. Tsoukalas, "Fabrication of single crystal Si cantilevers using a dry release process and application in a capacitive-type humidity sensor", *Journal of Microelectronics Engineering,* vol.61-62, 2002, p. 955-61.

[69]   S. Dongna, P. Jung-Hyun, A. Jyoti, C. Song-Yul, C. W. Howard, III and K. Dong-Joo, "The design, fabrication and evaluation of a MEMS PZT cantilever with an integrated Si proof mass for vibration energy harvesting", *Journal of Micromechanics and Microengineering,* vol.18, 2008, p. 1-7.

[70]   P. Ivaldi, J. Abergel, M. H. Matheny, L. G. Villanueva, R. B. Karabalin, M. L. Roukes, P. Andreucci, S. Hentz and E. Defay, "50 nm thick AlN film-based piezoelectric cantilevers for gravimetric detection", *Journal of Micromechanics and Microengineering,* vol.21, 2011, p. 1-8.

[71]   S. S. Lee and R. M. White, "Self-excited piezoelectric cantilever oscillators", *Sensors and Actuators A: Physical,* vol.52, 1996, p. 41-45.

[72]   T. ltoh and T. Suga, "Development of a force sensor for atomic force microscopy using piezoelectric thin films", *Nanotechnology,* vol.4, 1993, p. 218-24.

[73]   F. Chollet and H. Liu,"*A (not so) short introduction to MEMS*", http://memscyclopedia.org/introMEMS.html, 2012 (08/07/2013).

[74]   F. Yalcinkaya and E. T. Powner, "Intelligent Structures", *Sensor Review,* vol.16, 1996, p. 32-37.

[75]   S. Saravanan, E. Berenschot, G. Krijnen and M. Elwenspoek, "Surface micromachining process for the integration of AlN piezoelectric microstructures", in *7th Annual Workshop on Semiconductor Advances for Future Electronics*, Veldhoven, Netherlands, 2004.

[76]   D. Sameoto, S. H. Tsang, I. G. Foulds, S. W. Lee and M. Parameswaran, "Control of the out-of-plane curvature in SU-8 compliant microstructures by exposure dose and baking times", *Journal of Micromechanics and Microengineering,* vol.17, 2007, p. 1093-98.

[77]   D. Thuau, V. Koutsos and R. Cheung, "Stress relaxation of polyimide (PI) cantilevers using low energy ion bombardment", *Soft Materials,* 2012,

[78]   S. Petroni, G. Maruccio, F. Guido, M. Amato, A. Passaseo and M. T. Todaro, "Flexible piezoelectric cantilevers fabricated on polyimide substrate", *Microelectronic Engineering,* vol.98, 2012, p. 603-06.

[79]   S. L. Kok, N. White and N. Harris, "Fabrication and characterisation of free-standing thick-film piezoelectric cantilevers for energy harvesting", *Measurement Science and Technology,* vol.20, 2009, p. 1-13.

[80]   S. B. Fuller, E. J. Wilhelm and J. M. Jacobson, "Ink-jet printed nanoparticle microelectromechanical systems", *Journal of Microelectromechanical Systems,* vol.11, 2002, p. 54-60.

[81]   N. Nguyen, X. Huang and T. Chuan, "MEMS-micropumps: a review", *Journal of Fluids Engineering,* vol.124, 2002, p. 384-92.

[82]   S. Beeby, G. Ensell, M. Kraft and N. White,"*MEMS mechanical sensors*", Artech House, 2004.

[83]   H. T. G. V. Lintel, F. C. M. V. D. Pol and S. Bouwstra, "Piezoelectric micropump based on micromachining of silicon", *Sensors and Actuators,* vol.15, 1988, p. 153-67.

[84]   F. C. M. Pol van de, H. T. G. Lintel van, M. Elwenspoek and J. H. J. Fluitman, "A thermopneumatic micropump based on micro-engineering techniques", *Sensors and Actuators A Physical,* vol.21, 1990, p. 198-202.

[85]   R. Zengerle, S. Kluge, M. Richter and A. Richter, "A bidirectional silicon micropump", in *IEEE Micro Electro Mechanical Systems*, 1995, p. 19-24.

[86]   C. H. Ahn and M. G. Allen, "Fluid micropumps based on rotary magnetic actuators", in *IEEE Micro Electro Mechanical Systems Conference*, Netherlands, 1995, p. 408-12.

[87]   A. Olsson, P. Enoksson, G. Stemme and E. Stemme, "Valve-less planar pump isotropically etched in silicon", *Journal of Micromechanics and Microengineering,* vol.6, 1996, p. 87-91.

[88]   W. L. Benard, H. Kahn, A. H. Heuer and M. A. Huff, "Thin-film shape-memory alloy actuated micropumps", *Journal of Microelectromechanical Systems,* vol.7, 1998, p. 245-51.

[89]   O. C. Jeong and S. S. Yang, "Fabrication and test of a thermopneumatic micropump with a corrugated p+ diaphragm", *Sensors and Actuators A: Physical,* vol.83, 2000, p. 249-55.

[90]   W. H. Grover, A. M. Skelley, C. N. Liu, E. T. Lagally and R. A. Mathies, "Monolithic membrane valves and diaphragm pumps for practical large-scale integration into glass microfluidic devices", *Sensors and Actuators B: Chemical,* vol.89, 2003, p. 315-23.

[91]   Y. Hsu, J. Li and N. Le, "An experimental and numerical investigation into the effects of diffuser valves in polymethylmethacrylate (PMMA) peristaltic micropumps", *Sensors and Actuators A: Physical,* vol.148, 2008, p. 149-57.

[92]   J. Xie, J. Shih, Q. Lin, B. Yang and Y. Tai, "Surface micromachined electrostatically actuated micro peristaltic pump", *The Royal Society of Chemistry,* vol.4, 2004, p. 495-501.

[93]   D. I. Brian and S. V. Garimella, "Recent advances in microscale pumping technologies: a review and evaluation", *Microfluid Nanofluid,* vol.5, 2008, p. 145-74.

[94]   E. Stemme and G. Stemme, "Valveless diffuser/nozzle-based fluid pump", *Sensors and Actuators A: Physical,* vol.39, 1993, p. 159-67.

[95]   H. Mizoguchi, M. Ando, T. Mizuno, T. Takagi and N. Nakajima, "Design and fabrication of light driven micropump", in *Micro Electro Mechanical Systems,* Travemunde, 1992, p. 31-36.

[96]   O. C. Jeong, T. Morimoto, Y. Watanabe and S. Konishi, "Peristaltic PDMS pump with perfect dynamic valves for both gas and liquid", in *19th IEEE International Conference on Micro Electro Mechanical Systems,* Istanbul, 2006, p. 782-85.

[97]   J. Dopper, M. Clemens, W. Ehrfeld, S. Jung, K. Kamper and H. Lehr, "Micro gear pumps for dosing of viscous fluids", *Journal of Micromechanics and Microengineering,* vol.7, 1997, p. 230-32.

[98]   A. Richter, A. Plettner, K. A. Hofmann and H. Sandmaier, "A micromachined electrohydrodynamic (EHD) pump", *Sensors and Actuators A: Physical,* vol.29, 1991, p. 159-68.

[99]   S. Zeng, C. H. Chen, J. C. M. Jr and J. G. Santiago, "Fabrication and characterization of electroosmotic micropumps", *Sensors and Actuators B Chemical,* vol.79, 2001, p. 107-14.

[100]   S. Bohm, W. Olthuis and P. Bergveld, "A bi-directional electrochemically driven micro liquid dosing system with integrated sensor/actuator electrodes", in *13th Micro Electro Mechanical Systems,* 2000, p. 92-95.

[101]   A. V. Lemoff and A. P. Lee, "An AC magnetohydrodynamic micropump", *Sensors and Actuators B,* vol.63, 2000, p. 178-85.

[102]   D. J. Laser and J. G. Santiago, "A review of micropumps", *Journal of Micromechanics and Microengineering,* vol.14, 2004, p. R35-R64.

[103]   D. J. Harrison, K. Seiler, A. Manz and Z. Fan, "Chemical analysis and electrophoresis systems integrated on glass and silicon chips", in *5th IEEE Solid-State Sensor and Actuator Workshop,* USA, 1992, p. 110-13.

[104]   A. Homsy, V. Linder, F. Lucklum and N. F. d. Rooij, "Magnetohydrodynamic pumping in nuclear magnetic resonance environments", *Sensors and Actuators B Chemical,* vol.126, 2007, p. 636-46.

[105]   C. Chia-Ling, S. Selvarasah, C. Shih-Hsien, A. Khanicheh, C. Mavroidis and M. R. Dokmeci, "An electrohydrodynamic micropump for on-chip fluid pumping

on a flexible parylene substrate", in *2nd IEEE International Conference on Nano/Micro Engineered and Molecular Systems*, 2007, p. 826-29.

[106] A. Jahanshahi, F. Axisa and J. Vanfleteren, "Fabrication of a biocompatible flexible electroosmosis micropump", *Microfluid Nanofluid,* vol.12, 2012, p. 771-77.

[107] M. Prudenziati,"*Thick Film Sensors*", vol. 1, Elsevier science, 1994.

[108] R. Dorey,"*Ceramic Thick Films for MEMS and Microdevices*", Elsevier Inc., 2012.

[109] R. A. Dorey and R. W. Whatmore, "Electroceramic thick film fabrication for MEMS", *Journal of Electroceramics,* vol.12, 2004, p. 19-32.

[110] N. Grabham, "Development of a thick film magnetostrictive material: formulation and characterisation", PhD thesis, Electronics and Computer Science, University of Southampton, Southampton, 2002.

[111] Sigma-Aldrich. *Dextran*. Available: http://www.sigmaaldrich.com/ (03 July 2013).

[112] *ALFA Chemicals*. Available: http://www.alfa-chemicals.co.uk/default.aspx (03 July 2013).

[113] L. E. Humphrey,"*Plastic Crystal* ", Claud Press, 2012.

[114] J.N.Sherwood,"*The plastically crystalline state: orientationally disordered crystals*", John Wiley & Sons, 1979.

[115] J. Font and J. Muntasell, "Pressure-temperature equilibrium curves in plastic crystals derived from neopentane", *Materials Research Bulletin,* vol.30, 1995, p. 479-489.

[116] *Trimethylolpropane*.   Available: http://www.perstorp.com/upload/tmp_eng_20080901.pdf (03/07/2013).

[117] K. Suenaga, T. Matsuo and H. Suga, "Heat capacity and phase transition of trimethylolethane", *Thermochimica Acta,* vol.163, 1990, p. 263-270.

[118] D. K. Benson, R. W. Burrows and J. D. Webb, "Solid state phase transitions in pentaerythritol and related polyhydric alcohols", *Solar Energy Materials,* vol.13, 1986, p. 133-52.

[119] J.Dykyj, J.Svoboda, R.C.Wilhoit, M.Frenkel and K.R.Hall,"*Vapor pressure of chemicals: vapor pressure and antoine constants for oxygen containing organic compounds*", vol. 20, Springer, 2000.

[120] *TA   Instruments*.   Available: http://www.tainstruments.com/default.aspx?siteid=11 (08/07/2013).

References

[121] J. Font and J. Muntasell, "Sublimation measurements on plastic crystals. Influence of the hydroxyl group on the sublimation enthalpy and vapour pressure", *Materials Research Bulletin,* vol.29, 1994, p. 1091-1100.

[122] J. Font and J. Muntasell, "Comparative study on solid crystalline–plastic–vapour equilibrium in plastic crystals from pentaerythritol series", *Journal of Materials Chemistry,* vol.5, 1995, p. 1137-40.

[123] M. Barrio, J. Font, D. O. Lopez, J. Muntasell, J. L. Tamarit and Y. Haget, "Thermal-expansion tensors of pentaerythritol (PE) and pentaglycerin (PG) and compositional deformation tensor of PG1-xPEx molecular alloys", *Journal of Applied Crystallography,* vol.27, 1994, p. 527-31.

[124] Q. Yan, "The volatility and the thermal storage performance of binary polyalcohols systems used in the wall", *Envelope Technologies for Building Energy Effeciency,* vol.II, 2006, p. 1-4.

[125] W. N. Hunter, "Alcohols, Polyhydric", in *Kirk-othmer encyclopedia of chemical technology*. vol. 2, ed: John Wiley & Sons, 2000, pp. 46-58.

[126] *Klopman International* Available: http://www.klopman.com/ (08/07/2013).

[127] *Techsil Limited*. Available: http://www.techsil.co.uk/ (08/07/2013).

[128] DowCorning. *Data sheet of Dow Corning brand Silicone Encapsulants*. Available: http://www.dowcorning.com (08/07/2013).

[129] G. S. Rekhi and S. S. Jambhekar, "Ethyl cellulose -- A polymer review", *Drug Development and Industrial Pharmacy,* vol.21, 1995, p. 61-67.

[130] *Ethyl cellulose-Physical and chemical properties*. Available: http://www.ashland.com (08/07/2013).

[131] *Ethylcellulose polymers technical handbooks*. Available: http://www.dow.com (08/07/2013).

[132] J.D.Davis,"*Tensile testing*", 2 ed., ASM International, 2004.

[133] L.K.Baxter. *Capacitive Sensors*. Available: http://www.capsense.com/capsense-wp.pdf (08/07/2013).

[134] K. Matsumoto, M. Sobue, K. Asamoto, Y. Nishimura, S. Abe and T. Numazawa, "Capacitive level meter for liquid hydrogen", *Cryogenics,* vol.51, 2011, p. 114-15.

[135] R. D. Blevins,"*Formulas for natural frequency and mode shape*", Krieger Pub Co., 1995.

[136] F. M. van der Goes and G. C. Meijer, "A universal transducer interface for capacitive and resistive sensor elements", *Analog Integrated Circuits and Signal Processing,* vol.14, 1997, p. 249-60.

[137] J. da Rocha, P. da Rocha and S. Lanceros-Mendez, "Capacitive sensor for three-axis force measurements and its readout electronics", *IEEE Transactions on Instrumentation and Measurment,* vol.58, 2009,

[138] "Piezoelectric ceramics data book for designers", Morgan Electroceramics.

[139] T. Papakostas and N. White, "Screen printable polymer piezoelectrics", *Sensor Review,* vol.20, 2000, p. 135-38.

[140] *Meggitt PLC*. Available: http://www.meggitt.com (08/07/2013).

[141] C. Yamahata, C. Lotto, E. Al-Assaf and M. A. M. Gijs, "A PMMA valveless micropump using electromagnetic actuation", *Microfluidics and Nanofluidics,* vol.1, 2005, p. 197-207.

[142] P. W. Runstadler, F. X. Dolan and R. C. Dean,"*Diffuser Data Book*", Springer, 1975.

[143] V. Singhal, S. V. Garimella and J. Y. Murthy, "Low Reynolds number flow through nozzle-diffuser elements in valveless micropumps", *Sensors and Actuators A: Physical,* vol.116, 2004, p. 226-35.

[144] G.H.Patterson, "Modern diffuser design", *Aircraft Engineering,* vol.10, 1938, p. 267-73.

[145] D.J.Cockrell and E.Markland, "A review of incompressible diffuser flow", *Aircraft Engineering,* vol.35, 1963, p. 286-92.

[146] Y. Cheng and J. Lin, "Manufacture of three-dimensional valveless micropump", *Journal of Materials Processing Technology,* vol.192-193, 2007, p. 229-36.

[147] A. Olsson, "Valve-less diffuser micropumps", PhD thesis, School of Electronical Engineering, Royal Institute of Technology, 1998.

[148] M. Koch, N. Harris, R. Maas, A. G. R. Evans, N. M. White and A. Brunnschweiler, "A novel micropump design with thick-film piezoelectric actuation", *Measurement Science and Technology,* vol.8, 1997, p. 49-57.